University of Southampton

Faculty of Engineering and Physical Sciences

School of Engineering

Development and characterisation of an aqueous aluminium-ion battery

by

Alexander Wicaksana Holland

Thesis for the degree of Doctor of Philosophy

November 2018

University of Southampton

Abstract

Faculty of Engineering and Physical Science

School of Engineering

Thesis for the degree of Doctor of Philosophy

Development and characterisation of an aqueous aluminium-ion battery

by

Alexander Wicaksana Holland

Aqueous intercalation batteries, using Earth-abundant electrode materials such as TiO_2, present the possibility of high rate, safe, non-toxic and potentially cheap energy storage. Though the low potential stability window of water hinders energy density, the need for this is reduced for certain applications, such as grid storage, hybridised systems or e-textiles. The present work focused on the development and characterisation of an aqueous aluminium-ion (Al-ion) battery using TiO_2 nanopowders as the negative electrode, copper hexacyanoferrate (CuHCF) as the positive and aqueous $AlCl_3$ solutions as electrolytes.

For the first time, TiO_2 and CuHCF were combined into both a full cell and a 2-cell battery, using aluminium containing aqueous electrolytes, and their electrochemical performance characterised. A proof-of-concept aqueous Al-ion cell was capable of 1750 cycles with energy efficiency remaining between 70-80% when cycled at a 20 C rate. Degradation of the CuHCF electrode resulted in cell failure, though this in turn was shown to be a result of the <100% coulombic efficiency of TiO_2.

TiO_2 electrodes were shown to have reversible capacities of approximately 15-20 mA h g^{-1} and reasonable cycle lives of up to 5000 cycles. It was found that electrode performance could be improved through both an electrochemical treatment and the vacuum impregnation of electrolyte into electrodes. Both techniques were found to improve TiO_2 rate capability, in addition to improving the stability of capacity and efficiency during initial cycling. The electrochemical treatment consisted of holding the electrode at -1.4 V vs SCE in 1 mol dm^{-3} KOH and was found to decrease the IR-drop between charge and discharge, especially at higher currents. Mott-Schottky analysis suggested that the treatment resulted in an increase in the electron charge carrier density, which would be consistent with the introduction of Ti^{3+} and a change in the band gap of TiO_2,

expected from the cathodic treatment. The treatment, in conjunction with the use of PVDF as binder (as opposed to Nafion), allowed for a discharge capacity of >30 mA h g^{-1} at 1 A g^{-1} with coulombic efficiency being nearly 95%. A capacity of 27.5 mA h g^{-1} was measured from the same electrode at 4 A g^{-1}.

The vacuum impregnation technique allowed for greater electrode wetting by releasing trapped air and forcing electrolyte into the pores of the electrode. Greater electrode-electrolyte contact was deemed to be the cause of the improved rate capability, where a capacity of 15 mA h g^{-1} could be maintained at the high specific current of 40 A g^{-1} (260 mA cm^{-2}) from an electrode with a mass loading of 6.5 mg cm^{-2}. This is only a 25% drop in capacity to the 20 mA h g^{-1} measured at 1 A g^{-1}. The specific currents and cycle lives demonstrated are therefore higher than have previously been reported for TiO_2 in aqueous Al^{3+}-containing electrolyte. Furthermore, the vacuum impregnation technique was also shown to improve the rate capability of CuHCF electrodes.

Additionally, charge storage mechanisms of TiO_2 in 1 mol dm^{-3} $AlCl_3$ were explored via cyclic voltammetry studies, which implied a surface contribution to charge storage capacity. The coulombic efficiency of TiO_2 was also found to decrease with decreasing specific current during constant-current cycling. This had been implicit in the data from previous publications on TiO_2, in aqueous Al^{3+}-containing electrolytes, though not explicitly discussed. Therefore, the nature of this was explored through a systematic study of potential self-discharge mechanisms. Purging electrolytes with N_2 gas improved coulombic efficiency and reduced self-discharge at open circuit potential, while the effect of electrolyte pH and charge redistribution within the electrode were also studied.

Table of Contents

Table of Tables

Table of Figures

Table of Figures

Table of Figures

Research Thesis: Declaration of Authorship

Print name:	ALEXANDER WICAKSANA HOLLAND

Title of thesis:	Development and characterisation of an aqueous aluminium-ion battery

I declare that this thesis and the work presented in it are my own and has been generated by me as the result of my own original research.

I confirm that:

1. This work was done wholly or mainly while in candidature for a research degree at this University;
2. Where any part of this thesis has previously been submitted for a degree or any other qualification at this University or any other institution, this has been clearly stated;
3. Where I have consulted the published work of others, this is always clearly attributed;
4. Where I have quoted from the work of others, the source is always given. With the exception of such quotations, this thesis is entirely my own work;
5. I have acknowledged all main sources of help;
6. Where the thesis is based on work done by myself jointly with others, I have made clear exactly what was done by others and what I have contributed myself;
7. Parts of this work have been published as:

   A. Holland, R. D. Mckerracher, A. Cruden, R. G. A. Wills, *An aluminium battery operating with an aqueous electrolyte,* Journal of Applied Electrochemistry, 2018, **48**, p243-250

   A. Holland, R. D. Mckerracher, A. Cruden, R. G. A. Wills, *TiO_2 nanopowder as a high rate, long cycle life electrode in aqueous aluminium electrolyte,* Materials Today Energy, 2018, **10**, p208-213

   A. Holland, R. D. Mckerracher, A. Cruden, R. G. A. Wills, *Electrochemically treated TiO_2 for enhanced performance in aqueous aluminium-ion batteries*, Materials, 2018, **11 (11)**, p2090

Signature:		Date:	

Acknowledgements

Firstly, I would like to thank my supervisor Dr Richard Wills for his encouragement and optimism over the duration of the project, as well as for his input and suggestions on papers and thesis drafts. Thank you also to Ewan Fraser, Ben Craig, Harriet Kimpton and Rachel McKerracher for your various contributions and proof reading of thesis chapters and papers. I must also thank Professor Andy Cruden, Sharon Brown and everyone involved in the delivery of the CDT in Energy Storage and its Applications. It has kept me involved and interested in a wide variety of topics outside of my core studies.

I want to thank my office mates, especially Tom Bryden and George Hilton, who have been valuable sounding boards and a great source of humour throughout. To everyone in the CDT and the electrochemical engineering lab, I wish you all the success in the future. And to anyone I have played squash with over these past years, thanks, you provided an enjoyable distraction from work.

Thank you also to my friends who have left me alone to hermit during these final months. In a similar vein, I must also thank my parents who have had to wait patiently for messages, phone calls and visits. Terima kasih. And finally to Cristina, I can only say that your support, company and understanding have helped immeasurably. Thank you.

Abbreviations

AC	Alternating current or activated carbon
Al-ion	Aluminium-ion
CB	Carbon black
CoHCF	Cobalt-hexacyanoferrate
CuHCF	Copper-hexacyanoferrate
CV	Cyclic voltamettry
DC	Direct current
EIS	Electrochemical impedance spectroscopy
EPR	Electron paramagnetic resonance
ESR	Equivalent series resistance
EV	Electric vehicle
GHG	Greenhouse gas
ICE	Internal combustion engine
Li-ion	Lithium-ion
Mtoe	Million tonnes of oil equivalent
MnHCF	Manganese-hexacyanoferrate
NiHCF	Nickel-hexacyanoferrate
NMP	N-Methyl-2-pyrrolidone
NTA	Nanotube array
OCP	Open circuit potential
PTFE	Polytetrafluoroethylene
PV	Photovoltaic

Abbreviations

PVA	Polyvinyl alcohol
PVDF	Polyvinylidene fluoride
RFB	Redox flow battery
RPM	Rotations per minute
SCE	Saturated calomel electrode
SEM	Scanning electron microscopy
SHE	Standard hydrogen electrode
SoC	State-of-charge
TEM	Transmission electron microscopy
TiNT	Titanate nanotubes
UV-vis	Ultraviolet visible
XRD	X-ray diffraction
XPS	X-ray photoelectron spectroscopy

List of Symbols

Symbol	Meaning	Units
a	Unit cell lattice constant	Å
A	Surface area	m^2
c	Unit cell lattice constant	Å
C	Capacitance	F
C_s	Theoretical specific capacity of an electrode material	C kg^{-1}
C_{cell}	Cell capacity	mA h g^{-1}
C_{-ve}	Negative electrode capacity	mA h g^{-1}
C_{+ve}	Positive electrode capacity	mA h g^{-1}
d	Distance	m
d_{hkl}	Distance between adjacent lattice planes	m
D	Diffusion efficient	cm^2 s^{-1}
ε	Permittivity	F m^{-1}
ε_0	Vacuum permittivity	F m^{-1}
ε_r	Relative permittivity	Dimensionless
E	Half-cell potential	V
E^0	Half-cell potential under standard conditions	V
E_{cell}	Cell potential	V
$E_{cell,OC}$	Cell open circuit potential	V
f	Alternating current frequency	Hz
F	Faraday's constant	mol^{-1}
ΔG_{cell}	Change in Gibbs free energy of an electrochemical cell	kJ mol^{-1}
h	Miller indices integer	Dimensionless
i	Imaginary number	Dimensionless

List of Symbols

I	Current	A
I_p	Peak current	A
$i(V)$	Current at a specified potential	A
k	Miller indices integer	Dimensionless
k_1	Solvable constant	Dimensionless
k_2	Solvable constant	Dimensionless
k_B	Boltzmann's constant	J K^{-1}
l	Miller indices integer	Dimensionless
M	Molar mass	kg mol^{-1}
N_A	Avogadro's constant	mol^{-1}
N_d	Charge carrier density	m^{-3}
η	Overpotential	V
q	Accumulated charge	C (Coulombs)
Q	Reaction quotient	Dimensionless
R	Electrical resistance	Ω
t	time	s
U	Energy stored	J
T	Temperature	K
V	Applied potential or voltage	V
V_{FB}	Flat band potential	V
ν	Scan rate	mV s^{-1}
z	Electron stoichiometry	Dimensionless
Z	Impedance	Ω
Z'	Real part of impedance	Ω
Z''	Imaginary part of impedance	Ω

Chapter 1 Introduction

1.1 Background and motivation for energy storage

The negative impact of CO_2 and greenhouse gases (GHG) on the global climate has resulted in legislated cuts to GHG emissions by many nations. The UK has set a legally binding target of reducing emissions by 80% below 1990 levels by 2050 and requires the use of sustainable and carbon free energy throughout society [1]. Due to the great difficulty in decarbonisation of certain areas of transport (e.g. aviation) and heating, responsibility has fallen primarily on the power sector to reduce reliance on polluting and often geopolitically sensitive fossil fuels. Worldwide, renewable energy consumption (excluding hydropower and nuclear) has increased from approximately 40 million-tonnes-of-oil-equivalent (Mtoe) in 1995 to over 400 Mtoe in 2016 [1]. Wind and solar are responsible for the majority of this growth. However, while significantly larger portions of renewable power generation will be needed to mitigate the worst effects of climate change, the increasing utilisation of renewables can cause a number of problems for electricity grids. Not least, the variable nature of wind and solar increases the difficulty with which supply and demand can be continuously matched. Additionally, issues surrounding grid stability and power quality increase with high levels of renewables. Distributed energy storage, primarily in the form of electrochemical batteries, can reduce these problems by storing and releasing energy at specific times and locations within certain timeframes. In addition to long duration storage, high power devices become necessary to smooth transient power fluctuations. To better understand the different characteristics required from energy storage technologies, the following section will briefly surmise key energy storage applications, including grid applications, electric vehicles (EV) and consumer electronics.

1.2 Energy storage applications

1.2.1 Electric vehicles

The relative success of the Nissan Leaf and Tesla S is indicative of the increasing popularity of EVs. These cars rely on Li-ion batteries, generally nickel-manganese-cobalt (NMC) though Tesla's chemistry* of choice is based on the nickel-cobalt-aluminium (NCA). Both have maximum cell level

* The positive electrode, with the negative electrode being graphite, is used to define Li-ion cell chemistries. The exception is the lithium titanate (LTO) battery, which describes the negative electrode used.

energy densities approaching 500-600 W h L^{-1} and specific energies around 200 W h kg^{-1} [2-6]. This high energy density allows the class-leading cars to travel around 200 miles per charge while cycle lives of ca. 2000 mean the life of the car is likely to be sufficient at around 10 years [7]. High DC-DC efficiency of up to 90% and the relatively low cost of electricity ensure that the low "re-fuelling" costs can go some way to offsetting the high initial cost of battery EVs, which is primarily a result of the high cost of the Li-ion batteries [5, 8, 9].

While Li-ion battery technology looks set to provide the first wave of electrified personal vehicles, H_2 fuel cell technologies are still being pursued as alternatives. Their comparatively low uptake is a result of high costs, primarily due to prohibitively expensive platinum catalysts, and limited H_2 infrastructure. It also needs to be noted that the majority of current H_2 production comes from non-renewable sources such as steam reformation of methane. Nevertheless, fuel cell vehicles possess the significant advantages of driving ranges comparable to internal combustion engine (ICE) vehicles and fast re-fuelling, as opposed to maximum ranges of ca. 200 miles and charging times of at least 30 minutes for battery EVs. However, the power capability and response times of fuel cells are lower than Li-ion batteries[*] [10-13]. As such, fuel cell vehicles require hybridisation with batteries or supercapacitors for acceleration, regenerative breaking and to allow fuel cell operation at more optimum efficiencies. High power batteries and supercapacitors could also be used for hybridisation with certain hybrid electric and ICE designs [12-14].

1.2.2 Grid services

There has been a clear growth in interest and necessity for power grid electrochemical energy storage over the past few years. This can be demonstrated by the worldwide map of grid energy storage facilities, created by the US department of energy, that are operational, under construction or announced by 2018 [15]. 1076 current electrochemical storage sites corresponds to a 31% increase to the number of reported projects from June 2016, the majority being Li-ion batteries followed by flow batteries, sodium based batteries and supercapacitors[†] (29 projects). In systems with large shares of variable renewable generation, maintaining a stable frequency (either 50 Hz or 60 Hz) becomes increasingly difficult with variations ranging from seconds to tens of minutes. These variations in frequency generally occur through short to long term imbalances between supply and

[*] Since fuel cells require external fuel storage, pumps, heat exchangers etc, it is difficult to compare metrics such as specific energy/power or energy/power densities with those of batteries.
[†] Also known as electrochemical capacitors and ultracapacitors.

demand. Operation outside the designated frequency can lead to electrical equipment damage, power plant disconnection and even black-outs [16]. Current power systems smooth frequency deviations through the inertia of high mass, synchronised motors inherent in gas and steam turbines. However, system inertia decreases with distributed, non-synchronised sources such as solar PV and wind, therefore requiring alternative mechanisms for maintaining stability and frequency. Energy storage provides one such option, charging when frequency and supply is higher than required and discharging when frequency is lower than required and there is an excess of demand. The timescales for these imbalances in supply and demand range from seconds to hours. Taking North America as an example, the mechanisms for rebalancing frequency falls into three time frames: primary response corresponds to power deployment over 10-60 seconds, secondary deployment over a maximum of 10 minutes and tertiary deployment over a maximum of 1 hour [17]. High power devices, such as supercapacitors, would be particularly suitable for primary and secondary response where power, efficiency and lifetime would take precedence over total energy storage capacity. High power energy storage can also be used to provide voltage and reactive power support which becomes necessary due to the variety of inductive and capacitive electrical loads [18].

Battery storage and electrochemical devices can also provide a number of other grid services, a brief summary of which is seen in Table 1.1. For example, the role of arbitrage is likely to increase with renewable penetration, which will increase the difficulty of balancing supply and demand over the course of several hours to days. It involves buying low cost energy, e.g at times of low demand and excess renewable resource, and selling at high prices when demand is high or renewable generation is low. Energy storage can also play a role in reinforcing local grid infrastructure (e.g. a transformer substation), which can become constrained due to rising populations in cities i.e. within relatively small areas. In such cases, peak demand may exceed load capacity of a local transmission and distribution grid. By effectively sharing the load during peak demand, energy storage can mitigate the need for increasing grid load capacity whilst also extending the lifetime of networks by reducing peak loads on distribution cables [17-23]. This can also improve the uptake of renewable energy sources. For example, energy storage over a 10-minute timescale can increase exported energy from wind turbines by storing energy when power output is higher than the local network capability [24].

Table 1.1. Summary of energy storage applications for electric power grids [17-23]

Application	Timeframe	Description
Frequency response and power regulation	Seconds – minutes	Dynamic variations in frequency need smoothing to maintain stable grid performance. Voltage support and real power support can be required due to capacitive and inductive loads.
Spinning, non-spinning and supplementary support	Seconds - hours	Reserve capacity is needed to counter unexpected loss of traditional generation or spikes in demand. Alternatively, where generators may be needed to reduce output due to excess production, energy storage can store this excess.
Load following and renewable integration	Minutes - weeks	Large fluctuations in voltage and power from solar PV farms can require smoothing. Balance must also be maintained between energy production and consumption throughout the day and over weeks and months.
Arbitrage	Minutes - hours	Energy storage can help exploit the difference in energy prices arising from varying energy production and consumption patterns.
Peak shaving	Minutes - hours	Reducing the peak generation capacity required by supplying energy from energy storage during periods of peak power consumption.
Transmission and distribution asset	Minutes - hours	Reducing peak loads delivered through cables and substations can extend life of infrastructure. Peak loads through distribution nodes may increase beyond capability and would traditionally require upgrades to the distribution network - this can be deferred or avoided through the implementation of load side energy storage.
Behind the meter and customer power quality	Seconds - hours	Certain businesses/institutes need to incorporate measures to maintain stable power and power quality. Uninterruptible power supplies are often used for power critical operations. End users can also utilise energy storage for increasing energy self-sufficiency or reducing peak energy costs.

Similarly, energy storage can smooth the output from a solar PV panel or array. Figure 1.1 shows the power output from a photovoltaic (PV) array in March, between 8 am and 8 pm, with the bell curve representing a possible desired power output. PV data was taken from a solar PV array at University of Southampton's Highfield campus, UK, on 27th March 2018. The application of the curve is somewhat arbitrary (the desired output could also be a straight line) but illustrative of reducing power fluctuations that would be exported on to the local grid. Parameters of the curve were set such that total energy above the curve equalled the energy below. For a battery to produce such a bell curve from the PV output, it would have to switch from charging to discharging (i.e. where the power output crosses the bell curve) 192 times, demonstrating a potential application for high power energy storage.

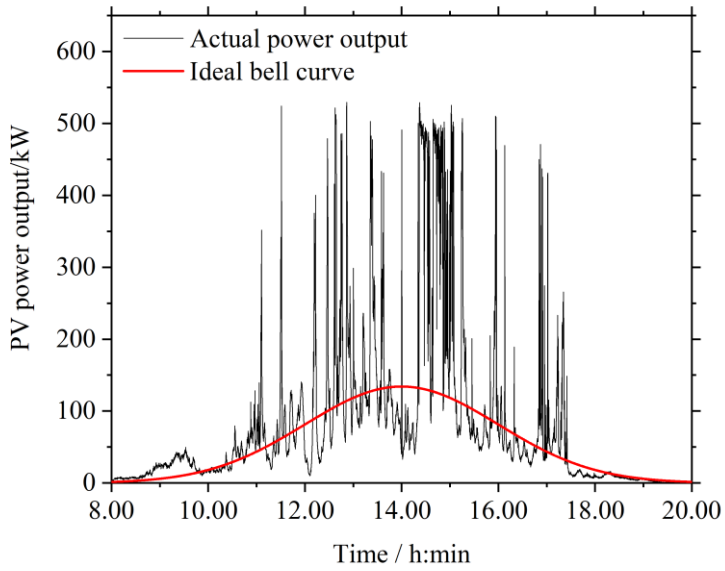

Figure 1.1. Power output from a solar PV array at the University of Southampton on 27th March 2018. The red line represents an idealised PV output which could be achieved with the use of energy storage.

1.2.3 Consumer electronics

The number of electronic devices has grown rapidly in recent years. The high energy density of some Li-ion chemistries has led to their ubiquitous use in consumer electronics. More recently, wearable electronics and clothing have been touted as potential applications, requiring flexible, safe and non-toxic energy storage [25-28]. Supercapacitors, with aqueous/PVA based gel

electrolytes, have been researched as a promising option for wearable electronics due to long operation life, high power density and potential for designing flexible devices. Low cost, safe materials and facile production methods are naturally important factors for such applications [29-32].

1.3 Motivation for aqueous Al-ion

While considerable research is focussed on improvements to energy density for EVs and consumer electronics, the previous section demonstrates that the range of applications for energy storage devices requires a range of performance characteristics. High specific power devices will remain and become important for a number of applications. Additionally, there is a drive across all technologies and electrochemical device chemistries to improve factors such as cost, safety and environmental benignity.

Supercapacitors are high power devices that have gained significant interest of late but currently have limited energy density and as such are expensive on a per unit energy basis. Like Li-ion, the majority of commercial supercapacitors also rely on flammable organic electrolytes. The linear voltage vs state-of-charge (SoC) dependence also limits their usable energy density further and can complicate system design. Devices based on pseudocapacitive and aqueous intercalation materials could allow for greater energy density over supercapacitors and bridge the performance gap between them and Li-ion batteries.

The aqueous aluminium-ion (Al-ion) cell [33] is a recent addition to the more widely investigated aqueous metal-ion chemistries which function through the reversible intercalation of cations into host electrodes [34-37]. The use of aqueous electrolytes promise improvements to safety, cost and power capability compared to Li-ion batteries that employ highly flammable organic solvents, such as mixtures of ethylene carbonate, diethyl carbonate and propylene carbonate. Using an aluminium based electrolyte would also be advantageous given its high abundance in the Earths crust. However, only three electrodes to date provide a reversible electrochemical capacity in aqueous aluminium based electrolytes, although this issue is not limited to aluminium electrolytes, with a dearth of electrode couples present for other alternative aqueous chemistries such as Na-ion. This point will be demonstrated through a review of the literature in Chapter 2, allowing a more rigorous justification for the use of TiO_2 and aqueous aluminium salt electrolytes. While a greater amount of electrodes are available for use in aqueous Li-ion batteries, the use of lithium for lower energy density batteries can be questioned, given it is the only realistic option for providing the high energy density required for EVs and portable electronics, especially in the short-term. Future

developments may provide energy density and specific energy improvements but the most promising and researched chemistries are also Li based e.g. Si anodes, high voltage cathodes, Li-air and Li-S [6]. This becomes problematic given the high unit cost of lithium and potential supply risks [38-41]. Furthermore, significant fundamental and engineering challenges exist for metal-air batteries [42-44], while Li-S is unlikely to provide significant, if any, improvements to the energy density of current Li-ion chemistries (due to the low density and volumetric expansion of sulphur), despite its potential for providing high specific energy and low costs [6, 45-48]. Alternative chemistries could therefore be important for applications where energy density is not as highly prioritised over metrics including power, cost, safety and environmental impact. It has also been demonstrated that alternative chemistries, specifically ionic liquid Al-ion, have the potential for lower environmental impact over current Li-ion chemistries [39]. This work, while not central to this thesis, was performed in order to present further evidence of the attraction of developing new battery technologies.

1.4 Research focus

This work addresses the need for the development of high power energy storage devices constructed from abundant, environmentally benign materials. There is also an aim to understand the performance characteristics and limitations of TiO_2 in aqueous Al^{3+} electrolytes.

Chapter 4 focusses on the demonstration of a proof-of-concept aqueous Al-ion battery using anatase TiO_2 and copper hexacyanoferrate (CuHCF). The electrochemical activity of both electrodes was confirmed before assembling in to full cell configuration, including a 2-cell bipolar battery. Performance was determined through extended cycling and cycling at various C-rates. The reason for cell degradation was explored and found to be a result of an unexpected performance drop from CuHCF. However, this was in turn a result of the lower coulombic efficiency of the TiO_2 negative electrode. As such, the following chapters focussed on the negative electrode.

Chapter 5 explores the use of TiO_2 as a negative electrode in aqueous Al^{3+} electrolytes. Previous studies show the potential of the material, specifically, up to 250 mA h g^{-1} could be reversibly obtained but for no more than 300 cycles. Furthermore, though not explicitly discussed, low coulombic efficiencies are generally observed along with limited cycle lives. The potential of TiO_2 as a high rate electrode, as well as its performance limitations, were investigated. Dissolved O_2 content, electrode thickness and particle size were shown to be important factors in electrode performance. Potential charge storage mechanisms and self-discharge mechanisms from the TiO_2 electrodes, in aqueous Al^{3+}-containing electrolytes, are explored through the analysis of cyclic

voltammetry scans and open circuit potentials after constant current cycling. Possible electrode degradation processes are also discussed.

Chapter 6 explores the potential of electrochemically treating TiO_2 in order to improve coulombic efficiency, especially during initial cycling, as well as capacity and rate capability. Constant current cycling and electrochemical impedance spectroscopy were the primary methods used to analyse the electrodes. X-ray photoelectron spectroscopy (XPS), X-ray diffraction (XRD) and scanning electron microscope (SEM) imaging were also employed to elucidate any differences between the treated and untreated TiO_2 electrodes.

Further potential improvements to the performance of both TiO_2 and CuHCF are discussed within Chapter 7, which presents a number of ink and electrode manufacturing conditions that affect performance in aqueous Al^{3+}-containing electrolytes. It was found that TiO_2 was sensitive to parameters including carbon black loading, binder types and ink coating method. Furthermore, considerable improvements to the rate capability of both electrodes were possible through the vacuum impregnation of electrodes with electrolyte.

1.4.1 Publications

1. A. Holland, R. D. Mckerracher, A. Cruden, R. G. A. Wills, *An aluminium battery operating with an aqueous electrolyte,* Journal of Applied Electrochemistry, 2018, **48**, p243-250

   (Some of the work presented in Chapter 4 was published in this article)

2. A. Holland, R. D. Mckerracher, A. Cruden, R. G. A. Wills, *TiO_2 nanopowder as a high rate, long cycle life electrode in aqueous aluminium electrolyte,* Materials Today Energy, 2018, **10**, p208-213

   (Some of the work presented in Chapter 5 was published in this article)

3. A. Holland, R. D. Mckerracher, A. Cruden, R. G. A. Wills, *Electrochemically treated TiO_2 for enhanced performance in aqueous aluminium-ion batteries*, Materials, 2018, **11 (11)**, 2090

   (The majority of the work presented in Chapter 6 was published in this article)

4. A. Holland, A. Zerey, R. D. Mckerracher, A. Cruden, R. G. A. Wills, *Electrochemical study of a TiO_2 electrode in aqueous $AlCl_3$ electrolyte and vacuum impregnation for superior high-rate performance,* In preparation for Materials Today Energy, 2018

   (Some of the work presented in Chapter 5 and Chapter 7 have been used)

5. Linda Ager-Wick Ellingsen, Alex Holland, Jean-Francois Drillet, Willi Peters, Martin Eckert, Carlos Concepcion, Oscar Ruiz, Jean-François Colin, Etienne Knipping, Qiaoyan Pan, Richard G. A. Wills, Guillaume Majeau-Bettez*, Environmental Screening of Electrode Materials for a Rechargeable Aluminum Battery with an AlCl3/EMIMCl Electrolyte,* Materials, 2018*,* **11(6)**, *936*

6. Mckerracher, R. D., Holland, A., Cruden, A. and Wills, R. G.A., *Comparison of carbon materials as cathodes for the aluminium-ion battery*. Carbon, **144**, 2019, p333-341

7. A. Holland, H. J. Kimpton, R. D. Mckerracher, A. Cruden, R. G. A. Wills, *CuHCF as an electrode material in an aqueous dual-ion Al^{3+}/K^{+} ion battery,* Energy Procedia, **151**, 2018, p69-73

   (Data and work for this proceedings article was taken from Chapter 4)

1.4.2 Novel contributions from this work

This work presents the first demonstration of a full aqueous cell combining TiO_2 and CuHCF and demonstrates the feasibility of a bipolar electrode for the construction of a 2-cell battery. Through characterisation of cell performance, a partially reversible 2nd plateau from CuHCF was observed, which allowed full cell operation but led to premature degradation. The work also reiterates the importance of considering full cell construction and explicitly highlights the low coulombic efficiency of TiO_2 to be a primary drawback.

TiO_2 was demonstrated to provide high rate capability, up to 10.0 A g^{-1} from as-manufactured electrodes. Cycle life was also demonstrated to be considerably higher than previously reported, i.e. ca. 5000 compared to 300. It was also shown that this improved cycle life may have been due to the more positive potential limit used upon charging the electrode. Studies also elucidated the

charge storage mechanism of TiO_2 in aqueous Al^{3+}-containing electrolytes. Potential causes of low coulombic efficiency and self-discharge were described and studied.

Improvements to the negative TiO_2 electrode were shown to be possible through both a cathodic electrochemical treatment and tailoring electrode manufacture parameters, specifically the use of a vacuum impregnation technique. Both resulted in greater stability of capacity and efficiency during initial cycling in addition to further improvements to rate capability.

Chapter 2 Literature review

2.1 History of electrochemical energy storage

A large range of battery chemistries exist and in order to give the body of this work context, Table 2.1 provides some important performance metrics of prominent rechargeable batteries. The Pb-acid battery, first demonstrated in 1859, is still ubiquitously used in vehicles to provide a current surge to starter motors due to their low cost and robustness. The higher energy density NiMH battery, developed in the 1960's, found applications in communications satellites, portable electronics and electric vehicles. However, the higher energy density Li-ion battery has diminished the use of NiMH. Commercialised by Sony in the 1990's, Li-ion batteries facilitated the functionality and widespread adoption of smartphones and laptops. The vast majority of electric vehicles (EVs) and hybrid EVs now use Li-ion chemistries too, while they are also growing in popularity for grid applications. The surge in Li-ion use for portable electronics and EVs is primarily due to its high energy density and specific energy, where cells are approaching and surpassing 200 Wh kg^{-1}. This in turn is a result of the relatively high capacities of the graphite negative electrode (ca. 250-300 A h kg^{-1}), metal oxide positive electrodes (ca. 150-200 A h kg^{-1}) and high average cell voltages (ca. 3.2 - 3.6 V) and it is these values by which alternative energy storage technologies and materials are generally benchmarked. The popularity of Li-ion for grid applications stems from high efficiency, cycle life and reasonable power density, which allows them to help with short term imbalances in supply and demand. However, for load shifting and peak shaving, lowering costs on a per kWh basis takes precedent. Development of redox flow batteries (RFBs) aims at allowing cost-effective long duration discharging (>2 hours) and with electroactive species being in the electrolyte as opposed to the electrode, scaling up storage capacity should be easier. However, problems with electrolyte corrosiveness, due to Br in the commercialised Zn/Br system, or toxicity from vanadium in the demonstrated all-vanadium system, as well as general engineering (e.g. cell designs, electrolyte leaking, corrosion resistance, auxiliary maintenance) and cost issues have so far limited the uptake of RFBs. Supercapacitors are characterised by high power density (> 1 kW kg^{-1}), fast response time and long cycle life, allowing them to be used for smoothing short duration (<1 minute) power surges and voltage variations on the grid [49]. These characteristics also makes them useful for other high power applications such as regenerative braking in automotive vehicles. However, usable specific energies are limited due to low electrode capacities and triangular voltage profiles, leading to high costs per unit energy. As a result, development of high power, higher energy electrochemical devices has led to research in pseudocapacitive electrodes, hybrid capacitor/batteries and aqueous intercalation chemistries.

Table 2.1. Comparison of high-level characteristics of commercial battery technologies*.

Chemistry	Energy density	Efficiency (DC-DC)	Cycle life	Cost	Safety remarks
Li-ion (LFP) [50, 51]	80-125Wh kg^{-1}	90%	1000+	c.a. \$250-500 kWh^{-1} [52, 53]	Electrolyte is highly flammable with high vapour pressure. Dendrite formation can cause short circuits.
Li-ion ($LiCoO_2$) [50, 51]	170-186Wh kg^{-1}	90%	500+	c.a. \$250-500 kWh^{-1} [52, 53]	Electrolyte is highly flammable with high vapour pressure. Dendrite formation can cause short circuits.
Li-titante [50, 54]	65-100Wh kg^{-1}	90%	10,000	c.a. \$1000-2000 kWh^{-1} [55, 56]	Somewhat safer than other Li-ion due to high rate capability and high potential of LTO vs Li/Li^+. Gassing can occur due to LTO reacting with electrolyte.
Valve regulated lead acid [50, 53, 57]	30-50Wh kg^{-1}	60-80%	500-1000	c.a. \$200-400 kWh^{-1}	Toxic Pb. Highly acidic electrolyte.
Zn/Br RFB [57]	-	65-75%	2000+	-	Environmental hazard from possible bromine leakage.
VRFB [57] [58]	-	60-85%	10,000+	-	Use of toxic vanadium.
$NaNiCl_2$ [57]	100-120Wh kg^{-1}	80-85%	2500+	c.a. \$100-200 kWh^{-1}	Maintenance of high temperatures required. Use of corrosive molten salts.
Supercapacitor [49] [57]	<10Wh kg^{-1} (c.a. 1kW kg^{-1})	90%	500,000	c.a. \$500-3000 kWh^{-1}	Explosion hazard. High self-discharge.

* Figures for costs especially are estimates, where different technology sub-groups (e.g. many Li-ion chemistries exist), production scenarios and system integration possibilities greatly affect cost estimations as well as the economic viability of a given technology.

The development of batteries is, within reason, either focussed on greater energy density for consumer electronics and electric vehicles or cost and safety for stationary grid applications. Similarly, supercapacitor developments aim at increasing energy density (probably decreasing cost/kW h as a consequence) without adversely affecting power density or cycle life.

2.2 Introduction to intercalation batteries

At their most basic, batteries comprise a positive electrode, negative electrode and electrolyte and function through electrochemical redox reactions, converting electrical energy into chemical energy. This process is reversible for the battery technologies described in Table 2.1. In an intercalation cell, cations present in the electrolyte migrate and insert into the structure of a negative electrode with cations being extracted from the positive with the insertion and extraction processes accompanied by redox reactions. In the majority of Li-ion cells, the negative electrode is graphite and the positive a transition metal oxide (TMO). The positive electrode material used defines the cell chemistry, with the exception being lithium-titanate, which is named after the $Li_4Ti_5O_{12}$ used as the negative electrode. The electrode materials used define the potential at which these redox reactions take place and therefore the cell potential. In addition, electrode materials are often highly sensitive to the intercalating cation. It is well considered that small, monovalent cations, i.e. Li^+, are preferable for fast diffusion through the electrode, leading to high utilisation and good rate capability of the electrode. Intercalation of multivalent cations into porous electrode structures can be problematic due to a) large size, or coordination sphere, inhibiting their diffusion through the electrode structure and/or b) high charge density, resulting in strong electrostatic interactions between cation and host electrode. However, as will be discussed later in this chapter, several electrode materials have been shown to perform reasonably as a result of the reversible intercalation of multivalent cations from aqueous electrolytes.

The capacity of an electrode is defined by the amount of electrical charge that can be reversibly stored in the material. Combining the capacities of the positive and negative electrodes, via equation (2.1), where C_{cell}, C_{-ve} and C_{+ve} are the capacities of the cell, negative electrode and positive electrode, provides the theoretical capacity of a cell in mA h g^{-1}. Multiplying the value by the potential difference between the electrodes provides the theoretical specific energy of a cell in mW h g^{-1} (although larger and commercial cells are often characterised in W h kg^{-1}).

$$C_{cell} = \frac{C_{+ve}C_{-ve}}{C_{+ve} + C_{-ve}} \tag{2.1}$$

The high energy density of Li-ion batteries has facilitated the widespread adoption of portable consumer electronics and allowed electric vehicle range, if only in a few cases, to rival that of conventional ICE vehicles. However, specific energy and energy density are only two metrics by which battery storage is evaluated. For grid and micro-grid applications, which will need increasing amounts of energy storage to offset the effect of variable renewable generation, levelised cost, power density, safety and environmental benignity can be of greater importance [59, 60]. Aqueous intercalation batteries are a promising class of technology which could feasibly improve several parameters by using aqueous electrolytes [34, 35, 61-73].

- The replacement of highly flammable organic electrolytes leads to an inherent improvement in safety.
- Cost reductions will be possible through the use of a widely available solvent, i.e. water, and through less stringent atmospheric and safety requirements during cell manufacture.
- The higher ionic conductivity, by up to 2 orders of magnitude, of aqueous electrolytes can improve power capability and efficiency at high rates.

Ionic liquid electrolytes, while non-flammable, also suffer from high cost, lower conductivity and stringent manufacture requirements as well as being highly corrosive [65, 66]. The aim of aqueous intercalation batteries is not only to provide a safer and more environmentally benign option than current Li-ion chemistries but to provide energy storage at a higher power density than Li-ion (>1 kW kg^{-1}) and a higher energy density than current supercapacitors (>15 W h kg^{-1}) or lead acid batteries (>50 W h kg^{-1}). As ever, lowering cell costs is also desired. Using low cost materials can help achieve this, where active materials including positive electrode, negative electrode, separator and electrolyte can dominate cell manufacture costs [54, 74-76]. They can account for 58% of Li-ion battery pack cost (29% from the positive electrode when NMC-622[*]) [77]. Aqueous electrolytes may also help lower costs and energy consumption during manufacturing, through lowering

[*] NMC-622 refers to $LiNi_{0.6}Mn_{0.2}Co_{0.2}O_2$.

complexity, the need for dry rooms and argon glove boxes, in addition to being cheaper than organic or ionic liquid solvents [39, 78].

However, the low potential stability window of water, 1.23 V vs SHE, limits energy density and is a central limitation of aqueous intercalation batteries. However, rate capability of aqueous batteries could be superior to those based on organic and ionic liquid solvents due to the higher conductivities of aqueous electrolytes. As the most abundant metal in the Earth's crust, use of aluminium may also be favourable from economic and sustainability viewpoints. Firstly, a summary is provided on aqueous Li-ion chemistries as well as other aqueous-ion chemistries and dual-ion systems. Section 2.4 will then discuss electrode materials reported to be suitable for aqueous Al-ion cells, highlighting pertinent research questions surrounding aqueous Al-ion electrodes. Finally, a discussion of aqueous super- and pseudo- capacitors is given in section 2.5.

2.3 Aqueous intercalation batteries and electrodes

2.3.1 Overview

The use of aqueous electrolytes can provide improvements to safety, cost and power capability compared to Li-ion batteries. Aqueous intercalation batteries were re-introduced by Dahn et al in 1994, with the working principal analogous to that of conventional organic electrolyte Li-ion cells [79]. The paper reported an aqueous Li-ion cell, using $LiMn_2O_4$ and the VO_2 polymorph VO_2(B), in 5 mol dm^{-3} $LiNO_3$ and 1 mmol dm^{-3} LiOH, with the positive and negative electrodes functioning via Reactions (2.2) and (2.3) where $0 \leq x \leq 1$ (left to right corresponds to charging of the cell). A number of electrodes have since been found to reversibly insert Li^+ from aqueous solutions.

$$LiMn_2O_4 + \rightleftharpoons Li_{1-x}Mn_2O_4 + xLi^+ + xe^- \quad (2.2)$$

$$VO_2(B) + xLi^+ + xe^- \rightleftharpoons Li_xVO_2(B) \quad (2.3)$$

The insertion or extraction of Li^+ is coupled with the addition or removal of an equal number of electrons to/from the d-orbital of the transition metal in the host electrode. Therefore, for a given

working ion, the transition metal species in the crystal structure plays an important role in defining cell potential, where higher discharge potentials are generally observed for transition metals with higher electronegativity; the greater attraction between nuclei and electrons resulting in greater energy release or consumption during electron transfer between orbitals (Fe and Mn do not follow this trend as the 6th electron in the 3d orbital of Fe is paired and therefore in a higher energy state) [67, 68]. The open circuit cell potential, $E_{cell,OC}$, is related to the change in Gibbs free energy, ΔG_{cell}, via Equation (2.4).

$$\Delta G_{cell} = -zFE_{cell,OC} \tag{2.4}$$

where *z* is the electron stoichiometry per insertion/extraction event and *F* is Faraday's constant. In order to maintain electroneutrality, intercalation electrodes must allow the transport of cations through and into lattice vacancies or interstitial sites in the crystal structure [80]. For example, $LiCoO_2$ can be described as layers of CoO_6 octahedra with Li ions occupying sites between the layers. The capacity of an electrode will be defined by the amount of working ion (and therefore charge) that can be reversibly intercalated in the crystal structure. The theoretical specific capacity, C_s, of an electrode is given by equation (2.5), where *z* is the electron stoichiometry, F = 96485 C mol^{-1} is Faraday's constant and M is the molar mass of the electrode material. The multiplication factor of 3600 s h^{-1} can be used to convert capacity from C kg^{-1} , if M is given in kg mol^{-1}, to the commonly used units of mA h g^{-1} (energy density is given by mA h cm^{-3} but is less often used in laboratory stage analysis).

$$C_s = \frac{zF}{M} \tag{2.5}$$

However, theoretical capacities of electrodes are seldom reached. For example, $LiCoO_2$ and TiO_2 have practical capacities of approximately 140 mA h g^{-1} and 160 mA h g^{-1} despite having theoretical capacities of 280 mA h g^{-1} and 320 mA h g^{-1} respectively, since only half of the Li ions can be reversibly inserted [68, 70, 71]. Reaction (2.6) describes the insertion of a Li^+ ion into TiO_2, which has a capacity of 335 mA h g^{-1} when $x = 1$, but reversible intercalation of Li^+ is generally considered to take place only up to c.a. $x = 0.5$, leading to an achievable capacity of c.a. 160 mA h g^{-1}.

$$TiO_2 + xLi^+ + xe^- \leftrightarrow Li_xTiO_2$$

(2.6)

Performance can also be limited by species diffusion and internal electrode resistances which lower power output and increases concentration polarization, resulting in lower available capacity [81]. Considering this, it is important to consider the origin of losses within a cell, where the measured cell potential can be given by Equation (2.7).

$$E_{cell} = E_{cell,OC} - \sum |I|R - \sum |\eta|$$

(2.7)

Ohmic losses originate from the ionic resistance of the electrolyte and the electronic resistance of electrodes as well contact resistances and resistance that may arise from potential solid electrolyte interphase (SEI) layers. Overpotentials, η, relate to charge transfer kinetics and concentration gradients. Concentration and charge transfer overpotentials are generally deemed to be governed by the Nernst and Butler-Volmer equations [69, 73].

2.3.2 Aqueous Li-ion

Compared to the aqueous Al-ion chemistry, a greater number of materials have been developed and explored for use in aqueous Li-ion cells. Reviews of these intercalation electrode based chemistries can be found in [82] and [83] and therefore this section will be kept brief. Since the combination of $LiMn_2O_4$ and VO_2(B), a variety of electrodes have been investigated for use in aqueous Li-ion cells [79]. $LiCoO_2$, $LiFePO_4$ and $LiMn_{0.05}Ni_{0.05}Co_{0.9}O_2$ have all been investigated as positive electrodes while reported negative electrodes include $LiTi_2(PO_4)_3$, VO_2, LiV_3O_8, V_2O_5, polypyrrole and activated carbon, which functions as a supercapacitor electrode [84-87]. Reasonable capacities have been obtained from many of these electrodes, with capacities ranging from 40 mA h g^{-1} to 150 mA h g^{-1} [5, 20]. However, many of these systems also suffered from low coulombic efficiency, poor cycle life and low rate capability.

Removal of O_2 from electrolyte has been shown to be beneficial to the performance of aqueous Li-ion systems [84, 86]. Luo et al, showed that removing dissolved O_2 from the electrolyte increased the coulombic efficiency of $LiTi_2(PO_4)_3$ as well as drastically reducing self-discharge of the electrode, evidenced by the decay of the open circuit potential (OCP), see Figure 2.1. This allowed a cell, using

$LiFePO_4$ as the positive electrode, to retain 90% of initial capacity when cycled 1000 times at a 6C rate, however, when cycled at C/8 the capacity retention was 85% after only 50 cycles. Furthering this, Sun et al were able to report an impressive 5500 cycles for a carbon coated $LiTi_2(PO_4)_3$ electrode at a specific current of 750 mA g^{-1} [88]. A 2 mol dm^{-3} Li_2SO_4 electrolyte was used along with excess mass of $LiMn_2O_4$ as the positive electrode. However, only 1200 cycles were reported at 150 mA g^{-1}, and 100 cycles at 30 mA g^{-1}. Although only limited capacity fade was measured at 30 mA g^{-1}, coulombic efficiency was lower at approximately 94% compared to >99% for the higher specific currents. The use of an excess mass of positive electrode will also affect cell performance since balanced electrode capacities will have effectively overcharged the positive electrode when cycled at 30 mA g^{-1}. This highlights the importance of cycle regime and shelf life in addition to cycle life, especially in the case of aqueous metal-ion chemistries.

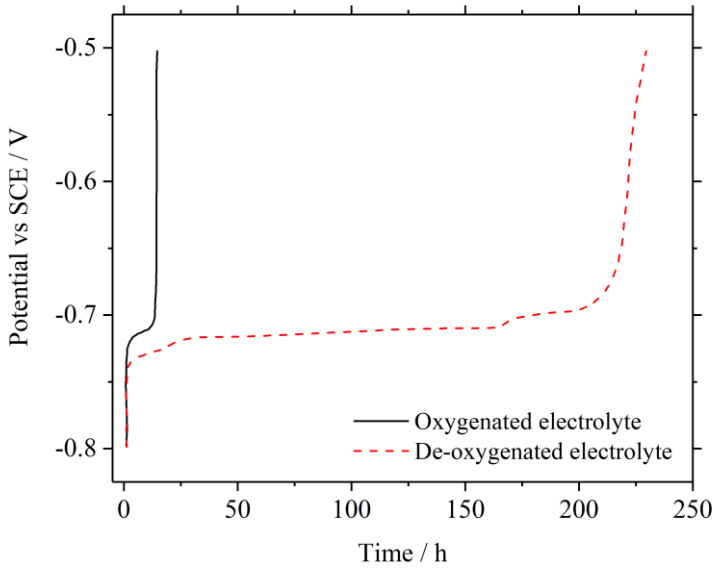

Figure 2.1. Approximate open circuit potential of a lithiated $Li_{3-x}Ti_2(PO_4)_3$ electrode in oxygenated and de-oxygenated Li_2SO_4. Figure has been adapted from [89].

A number of additional issues exist with current aqueous Li-ion chemistries, for example the co-intercalation of H^+ into layered oxide electrodes [90, 91], deterioration of crystal structure in LiV_3O_8 [92], and the dissolution of electrodes such as V_2O_5, $LiFePO_4$ and $LiMn_2O_4$ [93-96]. A number of measures have been investigated to mitigate these issues, including the optimisation of electrolyte pH [97], electrolyte concentration and the application of carbon coatings [86, 95, 98]. Use of carbon coatings on $LiFePO_4$ was shown to improve cycle life by blocking access of OH^- and dissolved O_2. TEM images were shown of electrodes cycled with and without O_2, where it can be seen that cycling in O_2 leads to the presence of floccules. However, despite improvements being made, cycle life and

coulombic efficiency remain problematic, especially at lower cycle rates (i.e. where lower charge and discharge currents are used and discharge times are therefore longer) [86, 95, 96, 98-101]. The mechanism for capacity degradation at low cycle rates is rarely discussed and clearly improvements to the longevity and cycling versatility of aqueous Li-ion cells are required. Contrary to this, Wang and Xia and Qu et al report 20,000 and 10,000 cycles for cells utilising activated carbon as the negative electrode and $LiMn_2O_4$ as the positive, although relatively high rates of 9C and 10C were again used [87, 102]. The excess mass of $LiMn_2O_4$ used was also deemed critical for limiting Mn dissolution into the electrolyte solution.

2.3.3 Aqueous Na-ion and Zn-ion

In addition to Li chemistries, there has been renewed interest in the investigation and construction of other alkali-ion cells, including Na-ion [35, 103]. However, the large ionic sizes of the cations can hinder solid-state diffusion and cause unwanted volume expansion/contraction for host electrodes that can accommodate interstitial alkali ions. Despite this, a number of promising positive and negative electrodes have been identified. For example, $Na_{0.44}MnO_2$, of interest due its crystal structure forming large tunnels, exhibits a capacity of 45 mA h g^{-1} at a cycle rate of C/8 and 20 mA h g^{-1} at 10 C [104, 105]. Furthermore, hybrid battery/supercapacitors can be constructed through the use of activated carbon as the negative electrode, leading to the report of a cell with a coulombic efficiency of >99% at a slow C/10 rate, without any measureable capacity fade over 700 cycles – an improvement over many aqueous Li-ion cells [106]. NASICON type electrodes have also been studied for aqueous Na-ion due to the reasonably high capacities that have been obtained [83]. Used as a negative electrode, $NaTi_2(PO_4)_3$ can exhibit a capacity of 120 mA h g^{-1} at 1C [107]. However, these electrodes can also suffer from electrode dissolution, loss of crystallinity and low coulombic efficiency [108-110]. On the other hand, Prussian blue analogues have reasonably low capacities (approximately 50 mA h g^{-1}) but have been shown to have high coulombic efficiency (>99%), rate capability (up to 80C) and cycle life (up to 10000) [111-113].

The performance of negative electrodes is still lacking for aqueous Na-ion and Li-ion cells. As such, the best performing Li-ion and Na-ion cells have used activated carbon as the negative electrode, therefore constituting hybrid battery/supercapacitor systems. While this has allowed high cycle life at high rates, it naturally limits the capacity of the cell. An interesting solution to the lack of suitable positive and negative electrode combinations could be through using dual-ion electrolytes, as has been demonstrated by a number of recent papers [114-118]. Separate cations could then be inserted into the negative and positive electrodes respectively, potentially allowing the advantages

of electrodes from separate metal-ion chemistries to be combined. Chen et al, demonstrated the feasibility of $LiMn_2O_4/Na_{0.22}MnO_2$ and $Na_{0.44}MnO_2/TiP_2O_7$ electrode combinations in mixed aqueous Li^+/Na^+ electrolyte [119]. The insertion of Na^+ was favoured by $Na_{0.44}MnO_2$ and Li^+ by $LiMn_2O_4$ and TiP_2O_7 resulting in cells with specific energies of 17 W h kg^{-1} and 25 W h kg^{-1}. Once again, coulombic efficiency (approximately 96%) and cycle life were poor. A hybrid Zinc/Al-ion cell has also been demonstrated using metallic Zinc as the negative electrode, graphite nanosheets as the positive and a mixed $Al_2(SO_4)_3/Zn(CHCOO)_2$ electrolyte [120]. However, a large potential drop between charge and discharge lowers energy efficiency.

2.4 Aqueous aluminium-ion electrode materials

2.4.1 Titanium dioxide

TiO_2 has long been used as a pigment in paints and sunscreens [121]. The advent of nanoscience has seen a renewed interest in TiO_2 for use in photocatalytic water splitting, photovoltaics, sensors, electrochromic and energy storage devices. It is an intrinsic semi-conductor material with advantages of good chemical stability and low cost, toxicity and environmental impact [122-124].

This has led to studies of its use in Li-ion [125] and Na-ion [126] batteries using organic electrolytes as well as supercapacitors, where its generally cycled between 0 V – 0.8 V vs an Ag/AgCl reference during cyclic voltammetry (CV) in aqueous electrolytes [127-129]. However, the insertion of multivalent cations is generally considered problematic due to high charge density and large solvation spheres inhibiting diffusion through many host electrodes. The use of an aqueous electrolyte can help shield this high charge density through water complexation of the metal cation but further complicates the mechanism of insertion [130]. The Al^{3+} ion will form a six co-ordinated complex and undergo the following equilibrium reaction to form an acidic solution such that co-intercalation of H^+ may be possible, as has previously been described with certain Li-ion electrodes [35, 82, 131].

$$Al(H_2O)_6{}^{3+} \rightleftharpoons Al(OH)(H_2O)_5{}^{2+} + H^+ \tag{2.8}$$

Indeed, high charge density is the likely reason only three electrode materials have been found to reversibly intercalate Al^{3+} from an aqueous electrolyte, with 4 of 6 publications describing the use of nanostructured TiO_2. TiO_2 exists as three common polymorphs: anatase, rutile and brookite, with

the synthetic bronze phase, TiO_2 (B), recently gaining interest as a Li-ion intercalation electrode. However, only anatase TiO_2 has been reported for use in an aqueous Al-ion cell. These TiO_2 polymorphs can be described by the arrangement and distortions of TiO_6 octahedra which leads to open channels through which cations can diffuse [132].

Given that the insertion of Li^+ into TiO_2 follows reaction (2.9), the aluminium insertion process has been expressed via reaction (2.10).

$$TiO_2 + xLi^+ + xe^- \rightleftharpoons Li_xTiO_2 \quad (2.9)$$

$$TiO_2 + xAl^{3+} + 3xe^- \rightleftharpoons Al_xTiO_2 \quad (2.10)$$

A number of studies have been presented on the use of anatase TiO_2 in aqueous Al^{3+} containing electrolytes. The electrodes, electrolytes, capacities, cycle lives, efficiencies and potential ranges are compared in Table 2.2. The first report of an electrode suitable for use in aqueous Al^{3+} electrolyte came from S. Liu et al, in 2012 [133]. TiO_2 nanotube arrays were prepared through anodization of Ti foil, in a NH_4F/water/ethylene glycol electrolyte, at 60 V for 30 min at room temperature using a graphite counter electrode. CV of the as-prepared nanotube array (NTA) in 1 mol dm^{-3} $AlCl_3$ produced clear redox peaks at scan rates between 20 mV s^{-1} to 100 mV s^{-1}. Cathodic peaks shifted from approximately -1.25 V vs SCE at 20 mV s^{-1} to -1.35 V vs SCE at 100 mV s^{-1} with anodic peaks shifting from approximately -0.84 V to -0.76 V vs SCE. Linearity of the peak currents with respect to the square of the scan rate suggests a diffusion limited process and was attributed to the solid-state diffusion of Al^{3+} through the electrode. The potential profile from constant-current cycling at 4 mA cm^{-2} (geometric area) is shown in Figure 2.2. The profile shows a discharge capacity of 75 mA h g^{-1} after a charge input of ≈85 mA h g^{-1} with cycling performed in a region between -0.2 V and -1.2 V vs SCE (nanotubes were ultrasonically separated from the foil to estimate the weight of TiO_2). Despite being a vital performance characteristic, the reason for the low coulombic efficiency is not explored. Indeed, the low coulombic efficiency of TiO_2 is not explored within the literature at all, despite being observed for the majority of TiO_2 materials tested. X-ray photoelectron spectroscopy (XPS) spectra for an aluminium inserted electrode shows that both Ti^{3+} and Ti^{2+} were present, after the electrode was charged, although Ti^{4+} was still the dominant species. While the low coulombic efficiency was not explicitly mentioned, the electrochemical irreversibility of the Ti^{4+}/Ti^{2+} reaction may have been responsible. SEM was used to give the morphology and

dimensions of the nanotubes while X-ray diffraction (XRD) produced a pattern that correlated well with anatase TiO_2. While a reasonable capacity was obtained from the nanotube array, no cycling data was provided for the electrode.

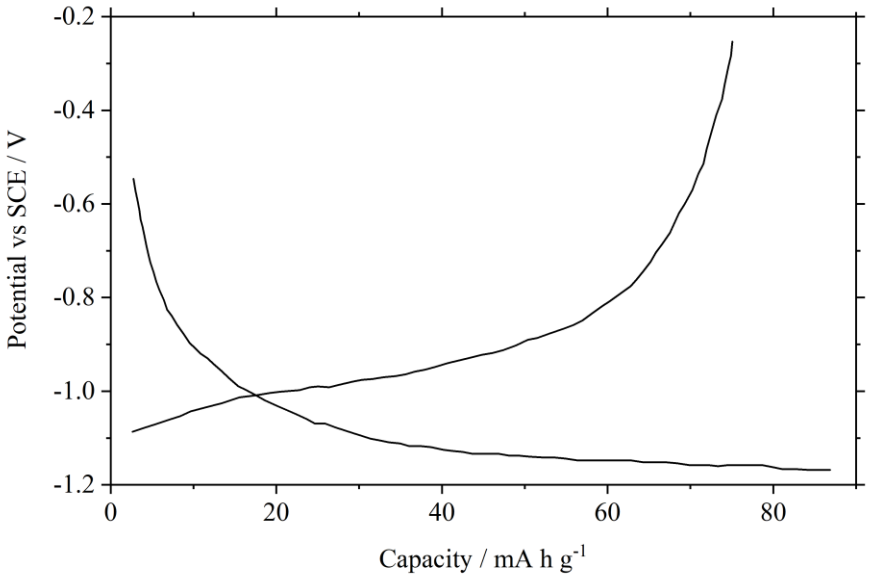

Figure 2.2. Charge/discharge curve of a TiO_2 NTA electrode in 1 mol dm^{-3} $AlCl_3$ cycled at a current density of 4 mA cm^{-2}. Graph has been modified from [133].

Furthering this work, Y. Liu et al, attempted to elucidate the mechanism of Al^{3+} insertion into a TiO_2 nanotube array [134]. The array was prepared through a similar anodisation process in [133] and a number of CV and electrochemical impedance spectroscopy (EIS) experiments were then performed on the electrode with electrolytes varying in Na^+, Al^{3+} and Cl^- content. Again, in the presence of Al^{3+}, a linear relationship was found between the peak current density, during CV, and the square root of scan rate. The peak currents measured were also found to increase as NaCl was added to an $Al_2(SO_4)_3$ solution. XPS analysis again found the presence of Ti^{3+} after polarisation of the NTA in $AlCl_3$, though care must be taken that the de-convolution of peaks is performed logically and accurately. Furthering this, EIS measurements were taken in electrolytes with varied ratios of Al^{3+}/Cl^-. There was a clear reduction in the characteristic semi-circle radius which is generally assigned to a reduction in the charge transfer or polarisation resistance. The measurements were modelled using an equivalent circuit where a resistive element, used to describe surface functionality, ion accessibility or polarisation resistance, was found to decrease with increasing Cl^- content. However, a clear explanation of how Cl^- assists the insertion of Al^{3+} was not given and a simple increase in solution conductivity cannot be ruled out as a reason for the improved electrochemical response.

Doped TiO_2, in the form of black anatase nanoleaves, was also investigated by Y. He et al for use as a negative electrode, with the nanoleaves prepared via a solution plasma process [135]. XPS was used to determine the extent of Ti^{4+} reduction and also found the presence of N and H. The chemical composition according to the XPS analysis was determined to be $TiO_{1.976}(NH)_{0.0024}$ with Fourier transform infrared analysis (FTIR) analysis used to further confirm the presence of Ti-N-H bonds. Electrochemical testing gave rise to impressive electrode performance characteristics using a 1 mol dm^{-3} $Al(NO_3)_3$ electrolyte, in contrast to other Al-ion TiO_2 studies which used 1 mol dm^{-3} $AlCl_3$. A high capacity of 260 mA h g^{-1} at 100 mA g^{-1} was reported and a capacity of 141 mA h g^{-1} was retained at the high specific current of 2000 mA g^{-1}, although only 300 cycles were reported with an 8.3% capacity loss at this point. Charge/discharge cycles were performed against aluminium foil and gave rise to flat plateaus at around -0.95 V vs SCE when cycled at 50 mA g^{-1}. While the high specific surface area of the electrode may suggest a capacitive or pseudocapacitive charge storage mechanism the flat voltage plateau suggests a redox reaction via intercalation. In-situ XRD showed an increase in the lattice parameter, a, during Al^{3+} insertion (1st discharge) in not only the black nanoleaves but also in a "commercial" white anatase. This presents evidence for the insertion of Al^{3+} into anatase TiO_2. However, since no morphological data was given on the commercial white anatase, separating the effects of nano structuring (i.e. nanoleaves) and oxygen deficiencies (i.e. black 'coloration') on electrochemical performance was not possible.

TiO_2 nano-spheres were synthesised by Kazazi et al, through the hydrothermal treatment of a prepared sol-gel [136]. Composite TiO_2, acetylene black and PVDF electrodes performed well in 1 mol dm^{-3} $AlCl_3$ electrolyte providing a good discharge capacity of 105 mA h g^{-1} at a 0.15 C cycle rate, while a capacity of 180 mA h g^{-1} was obtained at 6C (10 minute charge). However, coulombic efficiency was low at approximately 90% and only 30 cycles were performed with a 6% capacity fade measured. A comparison was also made using commercially available P25 TiO_2 nanopowder which exhibited lower capacities. Most recently, the introduction of graphene was shown to improve the storage capacity of TiO_2 nanoparticle electrodes. Discharge capacity was measured at approximately 20 mA h g^{-1} at 6.25 A g^{-1}, however, the discrepancy between charge and discharge capacity was severe, resulting in a coulombic efficiency of approximately 50% (as estimated from the graphical data) [137]. The publication also shows CV scans with almost non-existent redox peaks, questioning the quality of the materials and experimental procedures employed. Certainly, charge storage from the bulk insertion of Al^{3+} into the structure of TiO_2, enhanced by the use of graphene additives, is a claim that requires further evidence.

Table 2.2. Summary of all aqueous Al-ion electrodes reported.

Paper	Electrode and Electrolyte	Specific Capacity	Cyclability	Columbic Efficiency*	Voltage range/ profile
Lahan et al, ***J. Phys. Chem. C 121***, 2017 [137]	**Half-cell –** graphene-TiO_2. $AlCl_3$	25-10 mA h g^{-1}	ca. 50% fade over 125 cycles	ca. 50%	-0.5 V - -1.05 V vs Ag/AgCl
Kazazi et al, ***Solid state Ionics 300***, 2017[136]	**Half-cell –** TiO_2 nano-spheres. 1M $AlCl_3$	180 mA h g^{-1} at 50.25 mA g^{-1}. 105 mA h g^{-1} at 2010 mA g^{-1}.	ca. 6% fade over 30 cycles	ca. 90% from 50.25 mA g^{-1} 2010 mA g^{-1}.	-0.3V - -1.2V vs Ag/AgCl. Discharge plateau at -0.95V - -0.9V.
Gonzalez et al, ***RSC Advances 6,*** 2015 [138]	**Half-cell -** V_2O_5 aerogel. 1M $AlCl_3$	120 mA h g^{-1} at 60 mA g^{-1}. ~15 mA h g^{-1} at 200 mA g^{-1}	ca. 40% fade at 60 mA g^{-1} and ca. 25% fade at 200 mA g^{-1} over 13 cycles	ca. 85%	-0.4V – 0.15V vs MSE. Discharge plateau at -0.15V.
Liu et al, ***J. Mater. Chem. 3***, 2015 [139]	**Half-cell –** CuHCF. 0.5M $Al_2(SO_4)_3$	41 mAh g^{-1} at 400 mA g^{-1}	45% fade over 1000 cycles	ca. 100%	1-0.2V. No plateau.
He et al, ***J. Mater. Chem. 2***, 2014 [135]	**Half-cell –** TiO_2 nano-leaves. 1M $Al(NO_3)_3$.	271 mA h g^{-1} at 50 mA g^{-1}. 141 mA h g^{-1} at 2A g^{-1}	8.4% fade after 300 cycles at 50 mA/g	ca. 100%	1.35-0.45V. Discharge plateau at ~0.97V.†
Y. Liu et al, ***Electro. Acta 143***, 2014[134]	**Half-cell –** TiO_2 nano-wire array film. Various inc. 0.5M $Al_2(SO_4)_3$	75 mA h g^{-1} at 4mA cm^{-2}	-	ca. 85%	1.1-0.9V/ Discharge plateau just below 1V
S. Liu et al, ***Energy and Environ. Science 5***, 2012 [133]	**Half-cell**. TiO_2 nano-tube array film. 1M $AlCl_3$	75 mA h g^{-1} at 4mA cm^{-2}	-	ca. 90%	1.1-0.4V/ Discharge plateau between 1.1 - ca. 0.8V

* Coulombic efficiencies had to be estimated from charge/discharge voltage profiles.
† From a charge-discharge cycle, of a TiO_2/Al cell, presented in the papers supplementary material.

2.4.2 Titanium dioxide for aqueous supercapacitors

In addition to the use of nanotubes as electrodes themselves, in aqueous Al^{3+} electrolyte, they have also been studied for use in an aqueous supercapacitor [140]. Zhong et al, describe the use of TiO_2 NTA, prepared through Ti foil anodization, as substrates for pseudocapacitive MnO_2 to be used in Na_2SO_4 electrolyte. The NTA was polarised in 1M $AlCl_3$ in an attempt to increase the conductivity of the NTA, thereby describing a similar process to that seen in an insertion electrode. A 0.2 mA cm^{-2} current was applied to the NTA for times ranging between 25 s to 250 s, in a 1 mol dm^{-3} $AlCl_3$ electrolyte, against a Pt-foil counter and SCE reference electrode. XPS analysis shows a shift of the Ti $2P_{1/2}$ peak to a lower energy of 463 eV, indicating the presence of Ti^{3+} [141]. The reduction of Ti^{4+} was accompanied by the insertion of a charge compensation cation. In addition to this evidence of Ti^{3+} states at the surface of the NTA, the conductivity of the nanotubes was also seen to increase, with increasing Ti^{3+} and Al^{3+} content. While normally achieved through hydrothermal processes, it is possible that the electrochemical reduction of Ti^{4+} results in oxygen vacancies in the NTA, resulting in n-type doping and the donation of electrons to the system [142].

TiO_2 has also been studied as a potential capacitive electrode in aqueous electrolytes of KOH or Na_2SO_4 [127, 128, 143, 144]. With the incorporation of graphene, Li et al measured capacitances as high as 235.6 F g^{-1} at 0.5 A g^{-1}, while maintaining a capacitance of 200 F g^{-1} at 2.0 A g^{-1}. However, the voltage range of 0 V – 0.5 V vs Ag/AgCl would make construction of a high voltage full cell problematic. This is demonstrated by their asymmetric supercapacitor using TiO_2 as the negative and activated carbon as the positive electrode, which was cycled at a low voltage range between 0 V – 0.5 V. As a negative electrode, the storage mechanism for TiO_2 stems from the creation of a double layer with H^+, K^+, Na^+ or some other cation. A faradaic reaction, due to the accumulation of charge within the conduction band may also be present, with Ramadoss et al proposing a pseudocapacitive mechanism involving surface TiO_2 atoms and some cation, C^+, see equation (2.11) [143, 145].

$$TiO_2 + C^+ + e^- \rightleftharpoons TiOOC \tag{2.11}$$

2.4.3 Copper-hexacyanoferrate and vanadium pentoxide

In addition to TiO_2, only copper hexacyanoferrate (CuHCF) and V_2O_5 have shown electrochemical activity in aqueous Al^{3+} electrolytes. Hexacyanoferrates and Prussian blue analogues are of interest

as electrode materials due to their open framework structure. CuHCF takes on the general chemical formula of $KCu_2[Fe(CN)_6].yH_2O$ and can be synthesised through the mixing of potassium ferricyanide and copper salt solutions. The resulting precipitate can then be filtered, washed and dried, either in vacuum, at room temperature or in air at approximately 80°C. CuHCF has been shown to reversibly insert a number of metal cations from aqueous electrolyte and while the measured capacity is mediocre at approximately 50 mA h g^{-1}, very high cycle life (10000) and rate capability (80C) have been measured at high efficiency (>99% coulombic efficiency) [146]. The electrochemical charge (extraction of K^+) and discharge (insertion of K^+) of the electrode follows (2.12).

$$\mathrm{KCuFe^{III}(CN)_6 + xK^+ + xe^- \rightleftharpoons K_{1+x}Cu[Fe^{II}(CN)_6]_x[Fe^{III}(CN)_6]_{1-x}} \quad (2.12)$$

The material has also been tested in a 0.5 mol dm^{-3} $Al_2(SO_4)_3$ solution [139]. A CV showed redox activity was present but exhibited itself as very broad peaks with multiple shoulders present. Galvanostatic cycling also resulted in sloping charge/discharge curves as opposed to the desired plateau, with a 45% capacity fade over 1000 cycles. The cause of this capacity fade was not discussed. Insertion of Al^{3+} into CuHCF is therefore sub-optimal when compared to the insertion of other metal cations.

A V_2O_5 xerogel has also been investigated as a host electrode in 1 mol dm^{-3} $AlCl_3$ [138]. A 10 mV s^{-1} CV scan gave rise to redox peaks at -0.25 V and 0.0 V vs MSE, however, performance under galvanostatic cycling was poor. Cycling at 200 mA g^{-1}, gave an initial capacity of approximately 120 mA h g^{-1} which reduced to 75 mA h g^{-1} after 13 cycles. Coulombic efficiency was both above and below 100% at several cycles. Cycling at 60 mA g^{-1} produced a more stable response, however, the measured capacity was ca. 20 mA h g^{-1} and reduced to <10 mA h g^{-1} after 13 cycles. Indeed the use of V_2O_5 may be problematic due to the potential for dissolution [35, 147]. Table 2.2 provides a summary of electrode materials used to date in the aqueous Al-ion system.

2.5 Electrochemical capacitors

2.5.1 Overview

Due to some conflicting performance characteristics present for the aqueous Al-ion battery described in later chapters, an overview of capacitive storage mechanisms, specifically in aqueous supercapacitors, becomes necessary. In contrast to batteries, charge storage in electrochemical capacitors occurs through the separation of electric charge from the adsorption of ions, from an electrolyte, onto high surface area electrode materials. Double layer capacitance is defined by equation (2.13), where ε_r and ε_0 are the electrolyte and vacuum dielectric constants, A electrode surface area and d the effective charge separation distance. Given that d is on the order of ionic radii and the high values of A (ca. 1000 m^2 g^{-1}) from electrode roughness and porosity, supercapacitors achieve considerably higher capacitances than parallel plate or electrolytic capacitors.

Capacitive behaviour from electrodes arise in the form of a near rectangular CV response and a linear voltage dependence during constant current cycling. Figure 2.3 (a) shows the near rectangular response from a 10F supercapacitor during CV scans at 33.33 mV s^{-1} and 66.66 mV s^{-1} between 0 V – 1 V. The supercapacitors voltage during a constant current cycle at 167 mA between 0 – 1 V is illustrated by Figure 2.3 (b). The linearly increasing profile is understood by the continuous work required to accumulate additional charge on a surface and is formally described by equation (2.14), where U = energy stored or Gibbs free energy, q = accumulated charge over an area, V = voltage and C = capacitance [148]. This contrasts to the comparatively constant potentials of batteries, which are defined by the potential of the redox reactions taking place at negative and positive electrodes. The lack of electron transfer, phase change or chemical reaction from capacitive electrodes allow for high specific current (>1 A g^{-1}) and cycle life (100,000 – 1,000,000) but since storage occurs on electrode surfaces rather than within the bulk material, specific energy (<10 W h kg^{-1}) and energy density are sacrificed compared to batteries [149].

$$C = \frac{\varepsilon_r \varepsilon_0 A}{d} \tag{2.13}$$

$$U = \frac{qV}{2} = \frac{CV^2}{2}$$

(2.14)

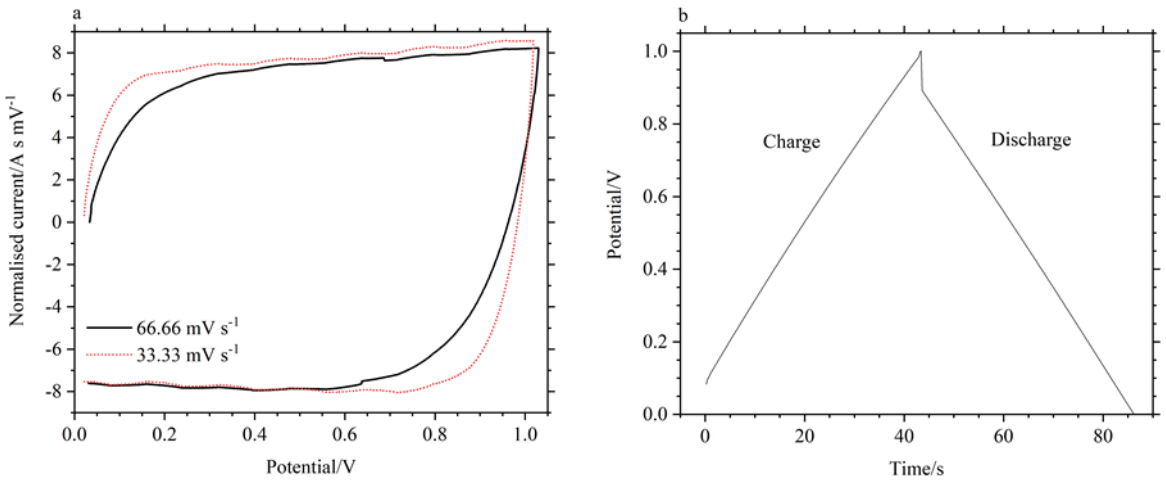

Figure 2.3. a) CV scans of a commercial 10 F, 2.7 V cylindrical supercapacitor at 33.33 and 66.66 mV s^{-1}. b) Constant current cycle of the same supercapacitor at 167 mA.

Pseudocapacitive materials have also gained interest, exhibiting properties of both capacitive and faradaic electrodes. The term pseudocapacitance refers to materials that exhibit capacitive responses to electrochemical tests, i.e. rectangular CVs and triangular voltage profiles during galvanostatic cycling, but where charge storage is a result of electron transfer [150-152]. This charge transfer can be due to the adsorption of ions on the surfaces of an electrode or through the intercalation of ions without crystallographic phase change. However, there is some debate and confusion over the description of certain materials as pseudocapacitive presenting difficulty in distinguishing between pseudocapacitive electrodes and battery electrodes [153]. As such, pseudocapacitive materials are often defined by their response to a suite of electrochemical techniques, including CV, galvanostatic cycling and EIS. Varying the scan rate of CV scans can allow distinction between capacitive and diffusion processes through (2.15) where $i(V)$ = current at a given potential, ν = scan rate and k_1 and k_2 = solvable constant. The contribution from diffusion and capacitive currents are given by $k_1\nu^{1/2}$ and $k_2\nu$ respectively [150, 153].

$$i(V) = k_1\nu^{1/2} + k_2\nu$$

(2.15)

Typical CV responses from pseudocapacitive materials can include a rectangular plot with small peaks but can also exhibit broad electrochemical peaks with small peak voltage separation. Galvanostatic cycling should give rise to a triangular potential vs time profile, while EIS gives rise to a straight line at mid-low frequencies with a phase angle <-45° and approaching -90° (as would be the case from a purely capacitive element) [150]. A semi-circle associated with a charge transfer resistance can also be present. As an example, representative CV scans of $RuO_2.nH_2O$ and $H_2Ti_3O_7$ are given in Figure 2.4 [154, 155].

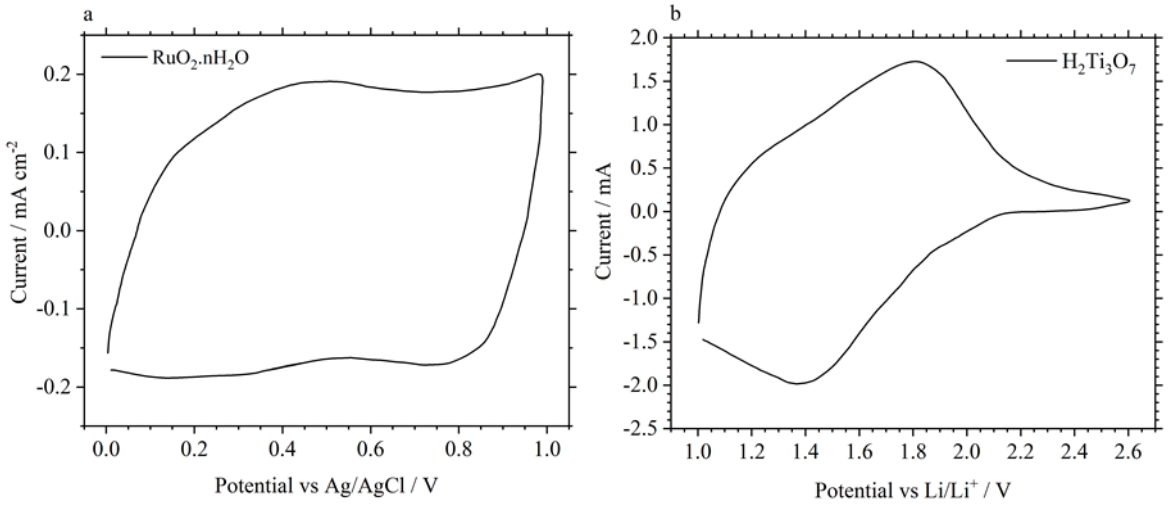

Figure 2.4. (a) CV scan of $RuO_2.nH_2O$ showing a predominantly rectangular shape. (b) CV scan of $H_2Ti_3O_7$ presenting broad but distinct peaks centred around 1.6 V vs Li/Li^+. Data and figures have been modified from [154, 155].

Development of pseudocapacitive materials is driven by a desire to improve the energy density of supercapacitors while maintaining high rate capability. However, materials such as RuO_2 are prohibitively expensive while some rate capability and stability over cycling can be lost. Some difficulty can also arise from the manufacture of scalable transition metal oxide electrodes electrodes such as MnO_2, due to the poor electronic conductivity of MnO_2. This makes it difficult to recreate the high capacitances measured from thin films when film thickness and size are increased [153].

2.5.2 Aqueous supercapacitors

In addition to battery chemistries, aqueous supercapacitors are also being explored. They present many of the same advantages and disadvantages as aqueous batteries do to Li-ion e.g. improved

cost, safety and power capability at the expense of specific energy. A number of electrode materials are being used that fall into the category of either capacitive or pseudocapacitive. Hybrid cells have also been explored using an intercalation/faradaic electrode coupled to a capacitive one. There is also a large range of electrolytes being used, the pH and working ion of which, is highly dependent on the electrode materials being used. Important factors include supporting a suitable potential window corresponding with the working potential of both electrodes, conductivity and viscosity, pH, and wettability of electrodes with electrolyte. Na_2SO_4 is an often-used electrolyte but acidic, neutral and alkaline electrolytes of Li^+, K^+ and Na^+ salts, or some combination of, are also employed. A Ragone plot of aqueous capacitors including symmetric, asymmetric and capacitor-battery hybrids communicated since 2014 is shown in Figure 2.5, while Table 2.3 gives a performance overview of the same aqueous capacitors. In Figure 2.5, a given shape and coloured point represents a single cell chemistry with dashed lines between them connecting the reported capacities, from that cell, at the highest and lowest reported power.

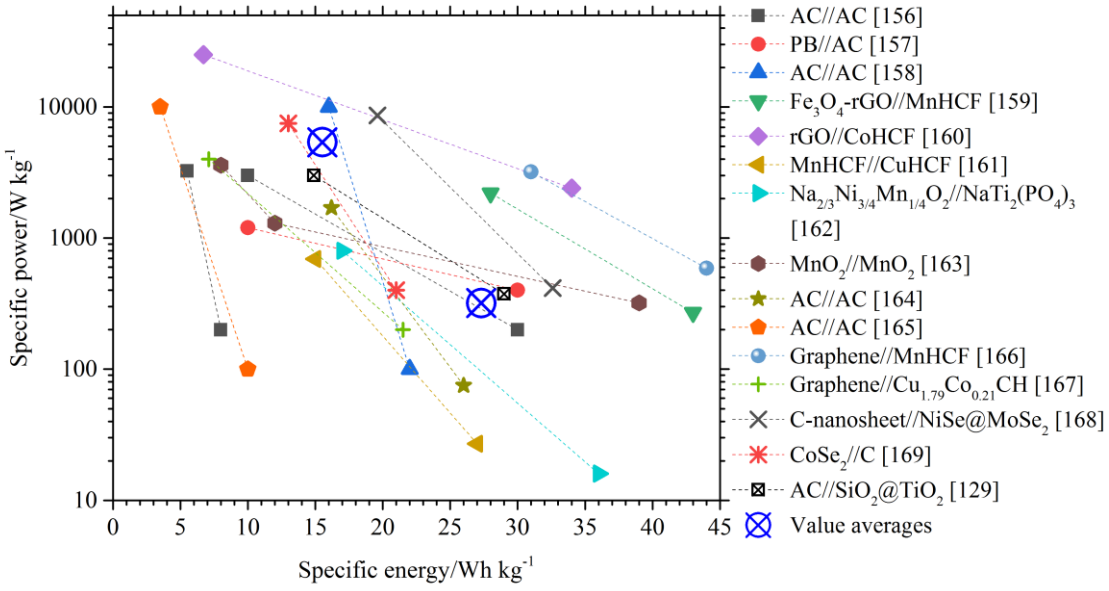

Figure 2.5. Ragone plot of selected high power aqueous devices, using a combination of capacitive, pseudocapacitive and battery electrodes, reported in the literature since 2014 [129, 156-169].

The plot is a useful guide to determining the power and energy capabilities of an electrochemical device. However, it does not provide a complete picture of performance characteristics. Table 2.3 provides further comparison of the materials presented in the Ragone plot. For example, power output from a capacitive device will decrease steadily due to the triangular galvanostatic voltage

profile, decreasing the usable energy from the device and increasing difficulty of their integration into systems [170]. On the other hand, batteries provide power at a more constant level due to the defined potentials of redox couples. Referring to the Ragone plot, some of the constructed cells do present impressive energy and power capability. For example, the reduced graphene oxide (rGO), cobalt-hexacyanoferrate (CoHCF) cell presented by Zhao et al produced a capacity of 34 W h kg^{-1} at 2.4 kW kg^{-1} and 6.7 W h kg^{-1} at the very high power of 25 kW kg^{-1}. However, on inspection of the voltage profiles presented, the efficiency can be estimated to be lower than 50% at 10 A g^{-1} – this corresponded to the minimum recorded power of 2.4 kW kg^{-1}.

For reference, commercial supercapacitors are often rated at the power possible whilst maintaining 95% energy efficiency and the matched impedance power where energy efficiency equals 50%, assuming 100% coulombic efficiency. A separate issue relates to the potentially low masses and mass loadings of electrodes used. Pazhamalai et al constructed a cell using a 1.4 mg graphene negative electrode and 1.0 mg MnHCF positive electrode (both over only a 1 cm^2 current collector), producing some of the highest values of 44 W h kg^{-1} at 0.59 kW kg^{-1} and 31 W h kg^{-1} at 3.2 kW kg^{-1}. These numbers are likely to decrease with higher masses and mass loadings, especially at higher currents and powers. The use of materials such as molybdenum and cobalt could also prove problematic from a cost perspective [161]. The Ragone plot also illustrates the desirable high rate properties of activated carbon, as shown by the high gradient of the lines connecting low power and high power capacities. Figure 2.5 shows that while symmetric AC cells have specific energies toward the lower end of the scale, the proportional decrease in capacity at higher powers is considerably lower than cells constructed using a non-carbon based material at either the negative or positive electrode.

Table 2.3. Material and performance overview of selected high power aqueous devices using a combination of capacitive, pseudocapacitive and battery electrodes reported in the literature since 2014. The same data are presented in Figure 2.5 [129, 156-169, 171].

Paper	Electrode materials (negative//positive)	Electrolyte	Voltage range	Energy at max power	Energy at min power
Menzel et al, ***Prog. Nat. Sci.*, 25,** 2015 [156]	AC//AC	KI/$Mg(NO_3)_2$ pH9	0 V – 1.8 V (linear)	10 Wh kg^{-1} at 3 kW kg^{-1}	30 Wh kg^{-1} at 0.2 kW kg^{-1}
Zhou et al, ***RSC Adv, 6*,** 2016 [157]	AC//PB	Na_2SO_4	0 V – 1.8 V (linear to 1V with sharp increase after)	10 Wh kg^{-1} at 0.4 kW kg^{-1}	10 Wh kg^{-1} at 1.2 kW kg^{-1}
Fic et al, ***Electro. Acta, 206*,** 2016 [158]	AC//AC	$LiNO_3$/KOH	-	15 Wh kg^{-1} at 10 kW kg^{-1}	20 Wh kg^{-1} at 0.1 kW kg^{-1}
Lu et al, ***J. Mater. Chem. A*, *3*,** 2015 [159]	Fe_3O_4-rGO//MnHCF	0.5 M Na_2SO_4	0 V – 1.8 V (approx. linear)	28 Wh kg^{-1} at 2.2 kW kg^{-1}	43 Wh kg^{-1} at 0.27 kW kg^{-1}
Zhao et al, ***ACS AMI, 6*,** 2014 [160]	rGO//CoHCF	0.5 M Na_2SO_4	0 V – 2 V (curved without distinct plateau*)	6.7 Wh kg^{-1} at 25 kW kg^{-1}	34 Wh kg^{-1} at 2.4 kW kg^{-1}
Pasta et al, ***Nat. Comms, 5*,** 2014 [161]	MnHCF//CuHCF	10M $NaClO_4$	0.5 V – 1.3 V (faradaic S-curve)	15 Wh kg^{-1} at 0.693 kW kg^{-1}	27 Wh kg^{-1} at 0.027 kW kg^{-1}
Yu et al, ***Ceramic. Int, 43*,** 2017 [162]	$NaTi_2(PO_4)_3$// $Na_{2/3}Ni_{1/4}Mn_{3/4}O_2$	1M Na_2SO_4/1M Li_2SO_4	0.6 V – 1.7 V (plateaus present)	16.5 Wh kg^{-1} at 0.798 kW kg^{-1}	36 Wh kg^{-1} at 0.016 W kg^{-1}
Kumar et al, ***Electro. Acta, 220*,** 2016 [163]	MnO_2//MnO_2	1M Na_2SO_4	0 V – 1 V (linear discharge)	8 Wh kg^{-1} at 3.6 kW kg^{-1}	39 Wh kg^{-1} at 0.32 kW kg^{-1}

* Examination of voltage profile shows efficiency can be estimated to be lower than 50% at 10 A g^{-1} due to voltage hysteresis. 50 A g^{-1} was used for a max power output of 25 kW kg^{-1}.

…continued

Paper	Electrode materials (negative//positive)	Electrolyte	Voltage range	Energy at max power	Energy at min power
Abbas et al, ***JPS*, 326,** 2016 [164]	AC//AC	KI/Li_2SO_4	-	16.2 Wh kg^{-1} at 1.7 kW kg^{-1}	26 Wh kg^{-1} at 0.075 kW kg^{-1}
Mostazo-Lopez et al, ***Int. J. Hydrogen En, 41*,** 2016 [165]	Doped-C//doped-C	1M H_2SO_4	0V – 1.2 V (linear)	3.5 Wh kg^{-1} at 10 kW kg^{-1}	10 Wh kg^{-1} at 0.1 kW kg^{-1}
Pazhamalai et al, ***J. Ind. Eng. Chem, 64*,** 2018 [166]	Graphene//MnHCF*	$LiNO_3$/KOH	0 V – 2 V (approx. linear)	31 Wh kg^{-1} at 3.2 kW kg^{-1}	44 Wh kg^{-1} at 0.59 kW kg^{-1}
Liu et al, ***Electro. Acta, 188*,** 2016 [167]	Graphene-Ni//$Cu_{1.79}Co_{0.21}CH$	6M KOH	0 V – 1.6 V (curve on charge)	7.1 Wh kg^{-1} at 4 kW kg^{-1}	21.5 Wh kg^{-1} 0.2 kW kg^{-1}
Peng at al, ***ACS Sust. Chem. Eng, 5*,** 2017 [168]	Doped-C//NiSe-$MoSe_2$	2M KOH	0 V – 1.6 V (curved)	19.6 Wh kg^{-1} at 8.6 kW kg^{-1}	32.6 Wh kg^{-1} at 0.415 kW kg^{-1-}
Peng et al, ***JPS, 297*,** 2015 [169]	$Co_{0.85}Se$//doped-C	2M KOH	0 V – 1.6 V (slight curve)	13.2 Wh kg^{-1} at 7.5 kW kg^{-1}	21.1 Wh kg^{-1} at 0.4 kW kg^{-1}
Zhang et al, ***ACS AMI, 9*,** 2017 [129]	AC//SiO_2@TiO_2	1M KOH	0 V – 1.5 V (triangular with curve)	14.9 Wh kg^{-1} at 3 kW kg^{-1}	29 Wh kg^{-1} at 0.375 kW kg^{-1}
Hanna et al, ***JPS, 354*,** 2017 [171]	AC//$LiMn_2O_4$	2M Li_2SO_4	0.5 V – 1.8 V (approx.. linear)	-	14 Wh kg^{-1}

* Electrodes were 1.4 and 1.0 mg respectively over 1 cm^2.

While the data used for Figure 2.5 and Table 2.3 are not exhaustive, it should be representative of recently published aqueous supercapacitors and provides a good range of performance characteristics. Therefore, despite the limitations of using only specific energy and power values, the data presented in Figure 2.5 and Table 2.3 was used to provide an average of the specific energies at the reported highest and lowest power values – these averages are represented by the two crossed-circles and can be used to provide an approximate performance benchmark. The average high power value of 5.38 kW kg^{-1} produced an average specific energy of 15.5 W h kg^{-1}, while the average low power value of 0.319 kW kg^{-1} produced an energy of 27.2 W h kg^{-1}. These specific energy figures are higher than those reported for commercial supercapacitors which are generally <10 W h kg^{-1} at powers around 1 kW kg^{-1}. For a high-rate battery or device to be compared alongside these devices, individual electrode capacities and specific current ranges should be noted alongside an electrode couple voltage range. Then, using equation (2.1)

and assuming equal electrode mass and capacity for convenience, along with a representative potential of 1.5 V, capacities of 36.2 mA h g^{-1} and 20.7 mA h g^{-1} per electrode would be required at specific currents of 0.42 A g^{-1} and 7.17 A g^{-1}, respectively, for above average performance.

H_2SO_4 electrolytes are used in commercial aqueous AC//AC capacitors due to high conductivity and solubility. However, the acidity can limit the use of certain low cost metal current collectors. KOH and Na_2SO_4 electrolytes also seem to be popular electrolyte choices in recent studies. Again, both have reasonable conductivities and solubilities. The choice of working ion, such as H^+, Li^+, K^+, Na^+, is dependent on the electrode material used, where performance or psuedocapacitance in a material can be enhanced by the use of a certain cation. This has shown to be the case for AC [172]. In the case of AC, the strong solvation of Li^+ with H_2O, due to its small size, was deemed to be partially responsible by allowing an increased potential range before water decomposition. From a similar perspective, the high charge density and small size of Al^{3+} could be beneficial. It was also posited that the slower diffusion of Li^+ in the electrolyte, compared to K^+ or Na^+ actually improved performance. This slow diffusion was said to allow Li^+ to stay close to the electrode surface during discharge as opposed to propagating into the bulk electrolyte. These conclusions were obtained through the use of CVs, galvanostatic cycling and EIS. All three show the highest capacitance value from AC with the use of Li_2SO_4 [172]. In contrast, Barzegar et al found improved electrochemical performance from AC electrodes using 6 mol dm^{-3} KOH over 6 mol dm^{-3} LiCl and 1 mol dm^{-3} Na_2SO_4 [173]. Additionally, using CV, Li et al showed similar capacitance values from AC in 1 mol dm^{-3} Li_2SO_4, Na_2SO_4 and K_2SO_4 at various scan rates, with an approximate 18% increase at the lowest scan rate of 1 mV s^{-1} and no discernible difference above 10 mV s^{-1}. Though CV scans showed no redox peaks, the pseudocapacitive nature of MnO_2 makes it possible that the increase at slower scan rates was due to the intercalation of Li^+ [174]. Using 0.5 mol dm^{-3} K_2SO_4, instead of 1 mol dm^{-3} Li_2SO_4 or

Na_2SO_4, resulted in an approximately 20% decrease in capacity at 833 mA g^{-1}. Alternatively, Misnon et al measured the specific capacitance of δ-MnO_2 to increase depending on the electrolyte in the order 1 mol dm^{-3} NaOH > LiOH > KOH. It was suggested that this was due to the pore sizes present in the MnO_2 electrode being optimal for Na^+ ions. Indeed, optimising pore size to that of electrolyte cations and anions is considered to be a critical factor in supercapacitor design.

The role of the electrolyte in aqueous supercapacitors and pseudocapacitors is complex. Performance is dependent on a variety of factors, including ionic conductivity, solvation energies, ionic size and charge density, pH, electrolyte concentration and electrode pore sizes.

2.6 Summary and conclusions

The justification for aqueous electrolyte batteries have been presented. The energy density and specific energy of aqueous electrolyte batteries will likely be limited due to the lower potential stability window of water compared to organic and ionic liquid electrolytes. While this is less important for applications in grid scale energy storage, it increases cost per unit energy, requiring higher cycle lives and lower cost materials, such as TiO_2 or MnO_2, to offset this. However, aqueous electrolytes have the advantage of higher ionic conductivity and easier handling. The development of aqueous electrolyte batteries is justified by the possibility of high rate capability (>1 A g^{-1} or >1 W g^{-1}), intrinsic safety, low toxicity and potentially low cost storage devices. For example, the cost of ionic salts used in conventional organic electrolyte supercapacitors have been quoted as costing between $50-$100/kg with acetonitrile and propylene carbonate solvents costing around $5-$10/L [175]. For comparison, 5 kg of $AlCl_3.6H_2O$ from Alfa Aesar currently costs £118 or £23.60/kg (≈ $31/kg), which is likely to be considerably more expensive than the cost of wholesale quantities that will provide further cost reductions compared to acetonitrile or propylene carbonate. The stringent environmental controls required in the use of organic and ionic liquids (e.g. dry rooms, argon glove boxes) could also be reduced, helping to lower operational costs and energy usage. Interest in the use of an aluminium electrolyte stems from the high abundance and low cost of aluminium. The high charge density of Al^{3+} may also minimise the decomposition of aqueous electrolytes, helping to widen the practical potential of the electrolyte. It is also possible that if a double layer is formed, Al^{3+} could allow for a higher charge accumulation on the surface of TiO_2. However, its trivalency presents difficulty in finding new electrodes capable of Al^{3+} insertion, though reports of TiO_2 electrodes with good capacity and reasonable rate capability in aqueous aluminium electrolytes presents rationale for its use.

The nanostructuring of electrode materials decreases diffusion lengths and increases electrolyte/electrode contact, allowing higher rate cycling [176]. For TiO_2, in aqueous Al^{3+} electrolyte, this may be necessary to offset the high charge density of Al^{3+} which would otherwise result in slow diffusion through bulk TiO_2. In summary, there is reasonable evidence that the insertion of Al^{3+} into nanostructured anatase TiO_2 (nanotube arrays, nanoleaves, nanospheres) can take place. CVs show pronounced redox peaks for nanotube arrays and nanoleaves, XPS evidenced the presence of Ti^{3+} in nanotube arrays that had been polarized by constant currents in 1 mol dm^{-3} $AlCl_3$, while X-ray diffraction (XRD) analysis showed an increase in lattice volume during the 1st discharge of TiO_2 vs Al-foil. However, a number of issues remain. All forms of white anatase exhibit a low coulombic efficiency as evidenced by the typical charge/discharge curves presented in [136, 177, 178] and shown in Figure 2.2. There are three readily available explanations for this low coulombic efficiency:

- The insertion of Al^{3+} into white anatase may lead to partial reduction of Ti^{4+} to Ti^{2+} which is electrochemically irreversible, although only S. Liu et al found Ti^{2+} to be present after Al^{3+} insertion [133].
- Dissolved O_2 in the electrolyte results in the oxidation of Ti^{3+} back to Ti^{4+} (Ti^{3+} is known to be oxidised by atmospheric O_2) [142].
- H_2 evolution can take place at approximately -0.2 V vs SHE in pH 3 solution, although this will be hindered by kinetics and the strong solvation of ions. Indeed, CVs show H_2 evolution at a reduced potential, lower than peaks attributed to Al^{3+} insertion.

Any combination of the above would naturally lead to a decrease in coulombic efficiency. The first option highlights the possibility for further investigation of the ratio of Ti^{2+} to Ti^{3+} at different SoC and its possible sensitivity to charging current. However, neither Zhong et al nor Y. Liu et al found evidence for Ti^{2+} under XPS [140, 178]. The 2nd option is certainly feasible as Ti^{3+} can be easily reduced when exposed to air and corresponds to a self-discharge process. Since no purging of electrolyte has been described, the oxidation of electrochemically reduced Ti^{3+} from dissolved O_2 cannot yet be ruled out and warrants further testing in controlled electrolytes and atmospheric environments. Aqueous Li-ion batteries have shown marked improvements when cycled in O_2-free electrolytes [89]. In addition, while evidence for Al^{3+} insertion into CuHCF and V_2O_5 exists, electrochemical performance is relatively poor.

The review was extended to include a brief discussion of the aqueous Li-ion chemistry. A number of positive and negative electrodes have been investigated with capacities ranging from 40-150 mA h g^{-1}. However, while reasonable capacities and rate capabilities (up to 50C) have been demonstrated, cycle lives (generally less than 200) under low rate cycling (<2C) is a central problem and has yet to be overcome. The importance of realistic cycling regimes is therefore highlighted, while a better understanding of the low coulombic efficiency and capacity fade for intercalation electrodes in aqueous solution electrolyte will be required. Recently, the possibility of dual-ion cells has been reported and presents an interesting avenue for the improvement of aqueous intercalation batteries.

Given the potential high rate capability of aqueous intercalation cells, a review of aqueous supercapacitors was also presented. In supercapacitors, negative electrodes are also dominated by carbon based materials e.g. AC, graphene and graphene oxide. MnHCF and MnO_2 could provide low cost options. However, the MnHCF//CuHCF cell described by Pasta et al was only tested to the relatively low power of 0.69 kW kg^{-1} and had a low average voltage of around 0.9 V – 1.0 V, despite having other desirable features such as a stable voltage plateau. The symmetric MnO_2 cell described by Kumar et al suffers from an even lower average voltage around 0.5 V, which would require several cells in parallel to obtain a usable voltage, further decreasing realistic specific energy and power. The low number of negative electrodes suitable for aqueous ion batteries and supercapacitors presents further rationale for the use of TiO_2 in an aqueous aluminium salt electrolyte. The relatively low redox potential of Ti^{4+}/Ti^{3+} in acidic electrolytes such as $AlCl_3$ would allow for the construction of a comparatively high voltage cell, whilst also being a low cost, safe and environmentally benign material, factors that are becoming increasingly important.

Chapter 3 Experimental methods

3.1 Electrochemical measurements

3.1.1 Electrochemical set-up

Proof-of concept two-electrode experiments were performed in the cell design shown in Figure 3.1 (a). Electrodes covered an area of 10 cm^2 with approximately 3 mm between positive and negative electrodes being filled with electrolyte using a syringe. The cell design allows tests to be performed on larger format electrodes than in the glass cell and allowed the construction of a battery using bipolar electrodes, Figure 3.1 (b). Cell components, i.e. end plates, gasket, current collector, electrodes and electrolyte cavity, were screwed together. This created electrical contact and ensured there was no leakage of electrolyte.

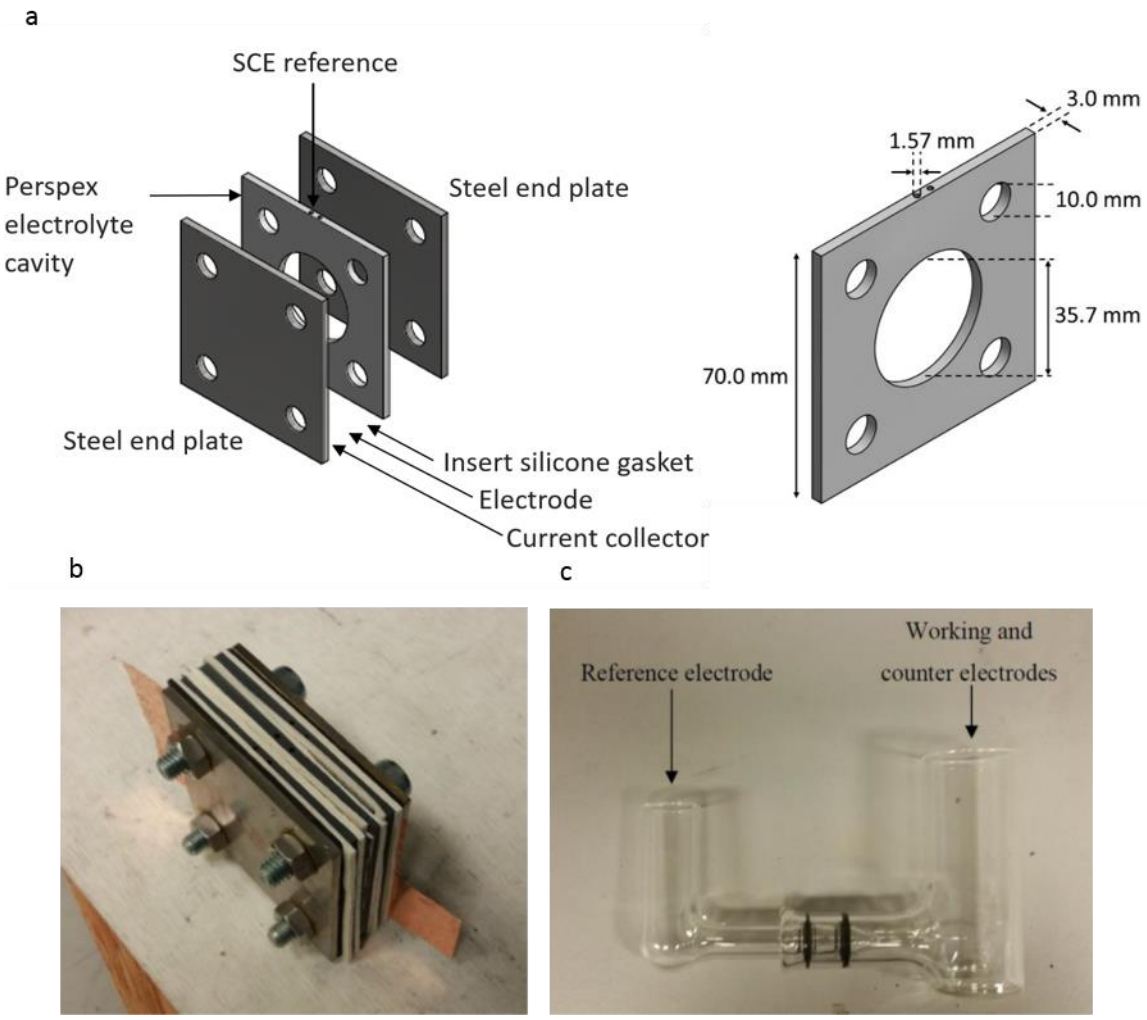

Figure 3.1. (a) Schematic diagram of the larger format cell design. (b) Photograph of a constructed multi-cell battery. (c) Photo of a glass cell used for 3-electrode characterisation.

All 3-electrode electrochemical tests were performed in glass cells, such as the one shown in Figure 3.1 (c). A standard calomel electrode (SCE) was used as the reference electrode throughout.

3.1.2 Cyclic voltammetry

Cyclic voltammetry is often the first electrochemical technique employed to characterise electrode materials and electrolytes, providing a fast method to obtain qualitative information. A current response is recorded as the potential, against a defined reference, across an electrode is swept between two values. As discussed in section 2.5, the resulting shape of the voltammogram gives an initial understanding of the charge storage processes from an electrode. For all CV experiments, a saturated calomel electrode (SCE) was used as the reference electrode. Either platinum wire or carbon-polymer was used as the counter electrode.

3.1.3 Galvanostatic (constant current) cycling

Galvanostatic cycling involves the application of a constant current to an electrode or cell with the corresponding potential measured. This more closely resembles how electrochemical cells and batteries are used in real world applications. As with CV scans, an SCE was used as reference. Pt wire was used as the counter electrode during CV experiments. However, extended 3-electrode galvanostatic experiments used a CuHCF as a reversible counter electrode. The mass of CuHCF counter electrodes were manufactured to be far in excess, at least 10× the mass of the working electrode, of the working electrode in order to minimise the water decomposition that would take place at a Pt-wire or carbon polymer counter. While 3-electrode testing is important for isolating the performance characteristics of individual positive or negative electrodes, 2-electrode cells are necessary in order to determine realistic performance of a full cell. Here, it is the cell potential that is measured, though insertion of an SCE reference allowed individual electrode potentials to be measured in full cell configuration, by using a NI data-acquisition-module (DAQ).

Throughout, charge and discharge have been defined as the change in potential that would take place if charging or discharging a full cell. Therefore, for the negative TiO_2 electrodes, a decrease in potential to more negative potentials is defined as “charging” the electrode while an increase in potential to more positive potentials is defined as “discharging” the negative electrode. Conversely, an increase in potential of the positive (hexacyanoferrate) electrodes to more positive potentials is defined as “charging” the electrode and vice versa.

3.1.4 Electrochemical impedance spectroscopy

For battery electrode systems, electrochemical impedance spectroscopy commonly involves the application of an AC voltage perturbation to an underlying DC voltage. It is important that the potential of the electrode is stable and does not drift over periods shorter than the time-frame of the measurements. Perturbations typically have amplitudes of the order of 10 mV. The resulting phase shifted AC current is measured as the frequency of the perturbation is changed (often between 10 kHz – 0.1 Hz). It is then possible to solve for impedance which can be expressed as a complex number, as given by equation (3.1), where Z' and Z'' are the real and imaginary parts of impedance, ESR = equivalent series resistance, f = applied frequency and C= capacitance.

$$Z = Z' + iZ'' = ESR - \frac{i}{2\pi f C} \tag{3.1}$$

Plotting the real and imaginary parts on the x and y-axes, respectively, gives the commonly seen Nyquist plot, which can provide information on electrolyte resistance, charge transfer and ionic diffusion. Further analysis fits the data to an equivalent RC circuit, although care must be taken that resistive, capacitive and inductive elements in the equivalent circuit correspond to meaningful processes in the electrode (and electrolyte). The electrochemical surface area of an electrode can be determined by keeping the electrode in a potential region where no faradaic reactions are expected to take place. In a suitably high concentration electrolyte, capacitive impedance can then be attributed to double layer capacitance.

3.2 Electrode preparation

3.2.1 Hexacyanoferrate synthesis

Copper-hexacyanoferrate (CuHCF) was prepared through a co-precipitation method previously described in the literature [111]. Here, a 0.2 mol dm^{-3} solution of $Cu(NO_3)_2$ was added to 0.1 mol dm^{-3} solution of $K_3[Fe(CN)_6]$ and stirred for a minimum of 2 hours at room temperature. The precipitate was centrifuged and washed five times before drying in air at 80°C and grinding to form CuHCF powder. Cobalt-hexacyanoferrate and Nickel-hexacyanoferrate were prepared through the

same method using $Co(NO_3)_2$ and $Ni(NO_3)_2$ in place of $Cu(NO_3)_2$. An XRD pattern from the synthesised CuHCF is given in Figure 3.2, confirming the face centred cubic crystal structure of other hexacyanoferrates and Prussian blue analogues.

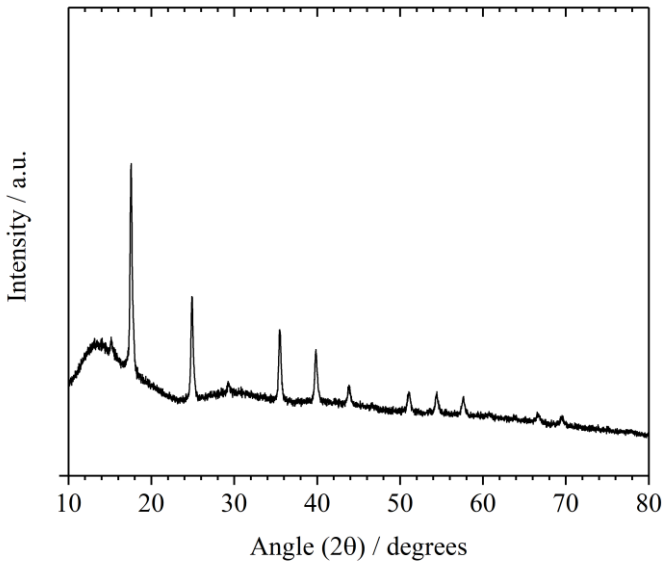

Figure 3.2. XRD pattern of CuHCF synthesised as described above.

3.2.2 Electrode manufacture

Electrodes were manufactured through shear mixing of CuHCF (or CoHCF/NiHCF) or TiO_2, carbon black (10 wt% for CuHCF and 5 wt% for TiO_2) Nafion binder (7.5 wt%) and propanol at 5000 rpm for 30 minutes using a Silverson shear mixer. Approximately 2.5 g of additional propanol was added per gram of dry powder (TiO_2 + carbon) before shear mixing. Inks were then sonicated in an ultrasonic bath for a further 20 minutes before thin coatings were applied to carbon polymer current collectors from Sigracell and allowed to dry in ambient conditions. Higher mass loadings were achieved through the application of additional thin coatings on to previous coatings that had been allowed to dry. Electrodes used in half-cell experiments were typically 6 cm^2 – 8 cm^2. Figure 3.3 gives a photo of two CuHCF electrodes with the active material coated onto a carbon polymer substrate. The importance of proper ink dispersion and mixing is demonstrated in Figure 3.4, which shows the 1st CV scan of a shear mixed and a magnetically stirred TiO_2 electrode. The electrode constructed from the shear mixed ink shows a much higher specific current, suggesting better adhesion and more even distribution of constituent materials.

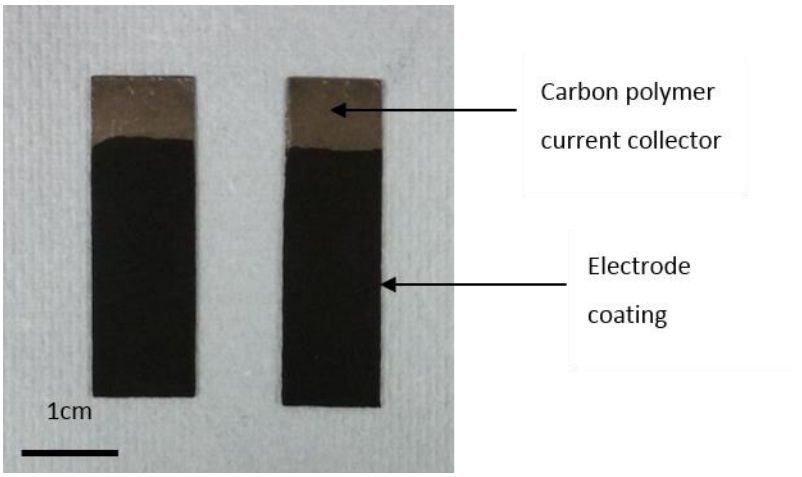

Figure 3.3. Photographic image of two CuHCF electrodes. Electrode inks are coated onto carbon polymer current collectors and allowed to dry.

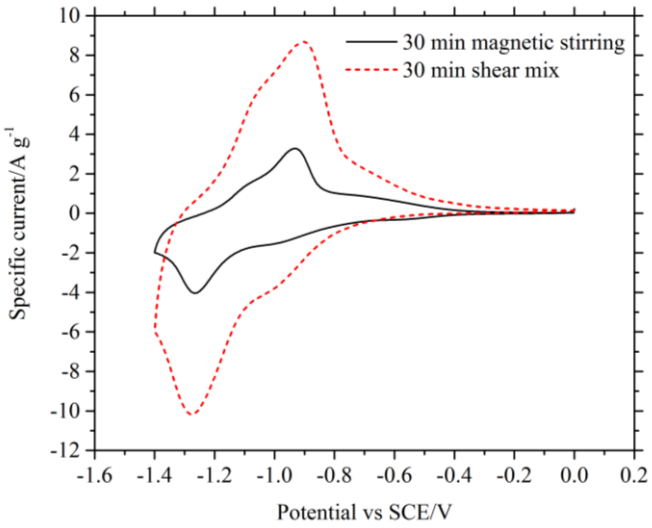

Figure 3.4. 1st CV scan of <25 nm TiO_2 magnetically stirred for 30 minutes (black) and shear mixed for 30 minutes at 5000 rpm (dashed red) at 20 mV s^{-1} in 1 mol dm^{-3} $AlCl_3$ vs SCE reference and Pt wire counter electrode.

Nafion binder was used instead of PVDF due to its need for the volatile, toxic and expensive NMP solvent [179]. The use of PTFE was also avoided due to its requirement of being treated above 100 °C, where the decomposition of HCFs can take place and result in the formation hydrogen cyanide. Carbon polymer was chosen as the current collector in order to avoid potential reactions with metallic foils. The polymer is an expanded graphite and will likely be cheaper than metal foils such as platinum and titanium.

3.3 Physical characterisation

3.3.1 X-ray diffraction

X-ray diffraction (XRD) is a commonly used method for determination of crystal structures and polymorphs. The physical basis for XRD is the elastic scattering of X-rays due to the atomic spacing in a crystal according to Bragg's law. This produces a series of peaks of varying intensity at given angles of X-ray incidence. Patterns can be indexed to assign peaks to the correct miller indices, allowing Reitvfeld refinement to give unit cell parameters. Numerous studies have used XRD to demonstrate lattice expansion/contraction due to the intercalation of cations during cycling. Additionally, XRD can be used to measure phase changes that can occur beyond certain intercalation ratios. XRD measurements were performed using a Bruker D2 Phaser.

3.3.2 Scanning electron microscopy

Scanning electron microscopy (SEM) is an imaging technique capable of x100 000 magnification resulting in image resolutions of several nanometres. SEM accelerates an electron beam, from a filament, to voltages up to 30 kV. Detection of back scattered electrons then allows examination of particles size morphology and distribution. Samples need to be conductive to avoid charge build-up at insulating or semi-conductor surfaces. This is important for battery electrodes, such as TiO_2, which are intrinsic semi-conductors. All SEM images presented were taken using a JEOL 6500 FEG-SEM.

3.3.3 X-ray photoelectron spectroscopy

During X-ray photoelectron spectroscopy (XPS), X-rays incident on the material of interest result in the emission of a spectrum of electrons. The energies and intensities of the emitted electrons can allow the identification of elemental composition, chemical states and electronic states. However, XPS generally measures emitted electrons from the top 1-10 nm of material. It therefore constitutes a surface analysis technique and cannot elucidate information on the bulk material.

3.3.4 UV-vis spectroscopy

UV-vis spectroscopy measures the attenuation of UV or visible light after absorption by a solution. Analysis of solid materials can also be carried out, though this is less common. A spectra-showing absorbance as a function of light wavelength can allow for the identification of chemical compounds in the solution. Quantification of solution concentrations can also be obtained since absorbance is related to concentration of the absorbing species through the Beer-Lambert law.

Chapter 4 A proof-of-concept aqueous Al-ion battery

4.1 Confirmation of the electrochemical activity of TiO_2

The negative electrodes in this section were manufactured using a commercial anatase TiO_2 powder with a nominal particle size of <25 nm.

To date, no operational data exists on the performance of an aqueous Al-ion cell or battery, mainly due to the low number of suitable electrode materials. Namely, only TiO_2, V_2O_5 and copper-hexacyanoferrate (CuHCF) have shown electrochemical activity in Al^{3+}-containing electrolyte. While CuHCF has been used as a positive electrode, cycle life was considerably lower than has shown to be possible in K^+ or Na^+ aqueous electrolytes. In 0.5 mol dm^{-3} $Al_2(SO_4)_3$, CuHCF showed a sloping voltage profile between 0.3 V and 1.0 V vs SCE compared to the relatively flat profile centred around 1.0 V vs SHE in 1 mol dm^{-3} KNO_3, measured by Wessells et al [111]. The sloping profile is likely due to the slow diffusion of Al^{3+} through the interstitial sites in CuHCF, while low cycle life could also be due to repeated stress on the crystal structure due to the high charge density of Al^{3+}. As such, a full cell could perform better with the use of a mixed Al^{3+}/K^+ electrolyte.

First, the electrochemical activity of TiO_2 and CuHCF in aqueous electrolytes were confirmed. A CV scan was obtained from a TiO_2 electrode (cell negative electrode) in aqueous 1 mol dm^{-3} $AlCl_3$. Separate electrolytes of 1 mol dm^{-3} KCl and 1 mol dm^{-3} KCl/10 mmol dm^{-3} HCl were also used in order to consider any charge storage from H^+ or K^+. The potential was swept from 0 V to -1.5 V vs. SCE. A constant sweep rate of 10 mV s^{-1} was maintained throughout.

Figure 4.1 presents the voltammogram with overlaying photographic images of the electrode surface at key potentials. Towards negative potentials, a reduction wave associated with Al^{3+} interacting with the TiO_2 electrode commences at ca. -0.8 V with an associated peak at ca. -1.31 V. The current peaks at -9.7 A g^{-1}. On the reverse sweep, an oxidation wave is observed, with a peak of 7.2 A g^{-1}, at -0.85 V. Both reduction and oxidation waves have secondary peaks, at ca. 0.98 V and ca. -1.05 V respectively, indicating more than one reaction process associated with the TiO_2/Al^{3+} interaction. In 1 mol dm^{-3} $AlCl_3$, electrolyte stability at the electrode is good, with the onset of H_2 evolution not yet visible at -1.5 V. An electrolyte containing 1 mol dm^{-3} KCl gave rise to no discernible redox activity, however, demonstrating that the redox phenomena are linked to the presence of Al^{3+} in the electrolyte solution. With the addition of HCl, small reduction and oxidation peaks, of approximately 1.0 A g^{-1}, became apparent at roughly -0.9 V and -0.8 V respectively. This suggests an inherent response from anatase TiO_2 in acidic aqueous electrolyte, which is an order of magnitude smaller in capacity than the response obtained in the presence of Al^{3+}.

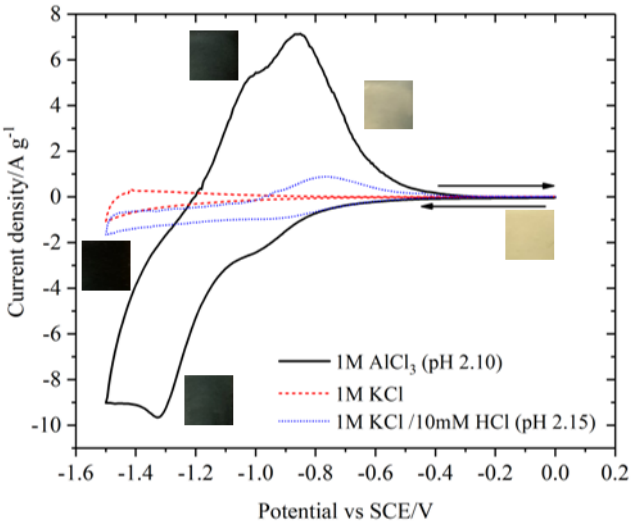

Figure 4.1. 10th cyclic voltammetry scans of TiO_2 electrodes in 1 mol dm^{-3} $AlCl_3$ as well as 'blank' electrolytes consisting of 1 mol dm^{-3} KCl and 1 mol dm^{-3} KCl with 10 mmol dm^{-3} HCl. A scan rate of 10 mV s^{-1} was used. Photographic images of a TiO_2 electrode, without carbon black, are overlaid at the potentials where colour changes were observed.

Photographic images were periodically taken, during a scan of a TiO_2-only electrode (i.e. an electrode without carbon black), and have been overlaid at the appropriate potentials in Figure 4.1. These images visually show the charge/discharge process at the negative electrode. In the charged state, the electrode is dark blue-grey, while in the discharged state the electrode almost returns to the original white colour associated with TiO_2. These changes are attributed to the reduction of Ti^{4+} to Ti^{3+} due to four possible processes: Al^{3+} surface adsorption, Al^{3+} intercalation, H^+ surface adsorption and/or H^+ intercalation.

The CV in Figure 4.1 demonstrates the higher electrochemical activity of TiO_2 in aqueous electrolyte consisting of an aluminium salt, compared to potassium salt. The requirement of aluminium in the aqueous electrolyte was further demonstrated through galvanostatic cycling. A selection of mono- and multi-valent ions, in aqueous electrolyte, were assessed for their effect on TiO_2 electrode capacity. TiO_2 electrodes were immersed in 1 mol dm^{-3} KCl, NaCl, $MgCl_2$ and $AlCl_3$ and charged to a minimum of -1.10 V vs SCE at a specific current of 945 mA g^{-1}. The resulting capacities, compared to ion charge, can be seen in Table 4.1. With 1 mol dm^{-3} $AlCl_3$, a capacity of 15.6 mA h g^{-1} was achieved. 1 mol dm^{-3} $MgCl_2$ produced the second highest capacity but was only 2.97 mA h g^{-1} with a small linear increase in capacity in the order $Mg^{2+} > Na^+ > K^+$. These results demonstrate that an appreciable charge storage machanism is reliant on the presence of $AlCl_3$.

Table 4.1. Discharge capacity of TiO_2 immersed in chloride salt electrolytes containing cations with differing ionic radii and charges: K^+, Na^+, Mg^{2+}, Al^{3+}. The presence of Al^{3+} in the electrolyte was the only scenario where an appreciable storage capacity.

Ion	Charge (e)	Non-hydrated ionic radius (pm)	Discharge capacity (mA h g^{-1})
K^+	+1	152	1.57
Na^+	+1	116	1.76
Mg^{2+}	+2	86	2.97
Al^{3+}	+3	67.5	15.6

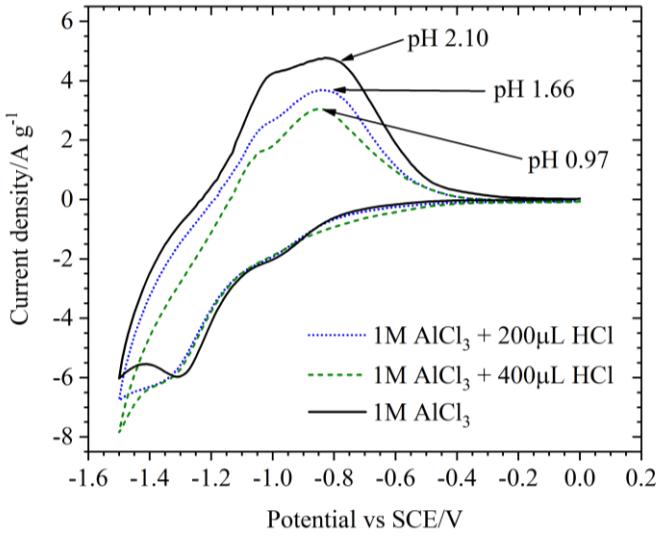

Figure 4.2. CV scans of a TiO_2 electrode in 1 mol dm^{-3} $AlCl_3$ electrolytes of increasing acidity through the addition of 200 and 400 µl HCl to 100 ml of 1 mol dm^{-3} $AlCl_3$. A scan rate of 10 mV s^{-1} was used.

In order to determine the effect of pH, CV scans were taken of a TiO_2 electrode in 1 mol dm^{-3} $AlCl_3$ and in electrolytes where either 200 and 400 µl were added to 100 ml of 1 mol dm^{-3} $AlCl_3$. Electrolyte pH was 2.10 without HCl, 1.66 with the addition of 200 µl HCl (ca. 23.6 mmol dm^{-3} HCl in 1 mol dm^{-3} $AlCl_3$) and 0.97 with 400 µl HCl added. The effect of 1 mol dm^{-3} $AlCl_3$ electrolyte acidity on CV scans of TiO_2, at 10 mV s^{-1}, is shown in Figure 4.2. Anodic peak currents were seen to decrease with

increasing acidity, while the prominence of cathodic peaks decreased, due to the dominance of H_2 evolution. This provides additional evidence that redox activity from TiO_2 was not caused by H^+ ions and that increasing acidity would be detrimental to cell performance.

Given the use of K^+ containing electrolytes in previous studies of CuHCF as a battery electrode, and in section 4.2, a TiO_2 electrode was cycled in 1 mol dm^{-3} $AlCl_3$/1 mol dm^{-3} KCl (i.e. an equal volume of 2 mol dm^{-3} $AlCl_3$ was added to 2 mol dm^{-3} KCl). Maximum and minimum potential limits of +0.4 V and -1.1 V vs SCE were used. Figure 4.3 shows the potential profiles obtained at 0.2, 0.5, and 2.0 A g^{-1}. During the charge phase, the potential decreases sharply from +0.1 V to ca. -0.6 V where potential begins to stabilise. Upon discharging the electrode, a relatively linear potential is obtained between -1.1 V and ca. -0.5 V with minimal initial voltage drop. At 0.5 A g^{-1}, a sharp increase in potential is seen to begin at approximately -0.55 V. At 2.0 A g^{-1}, a steeper voltage plateau increase is observed between -1.1 V and approximately -0.5 V where the potential increases sharply to +0.4 V.

Figure 4.4 gives the discharge capacity and coulombic efficiency at 0.1, 0.2, 0.5, 1.0 and 2.0 A g^{-1}. Discharge capacity can be seen to decrease steadily from 19.33 mA h g^{-1} at 0.10 A g^{-1} to 14.06 mA h g^{-1} at 2.0 A g^{-1}. However, the coulombic efficiency increases with specific current, from 77.3% at 0.1 A g^{-1}, to 87.5% at 0.2 A g^{-1}, 92.2% at 0.5 A g^{-1} and 98.1% at 2.0 A g^{-1}. This lower coulombic efficiency at lower specific currents is not well understood but is likely a result of a self-discharge process. This will be further analysed and discussed in section 5.3.3.

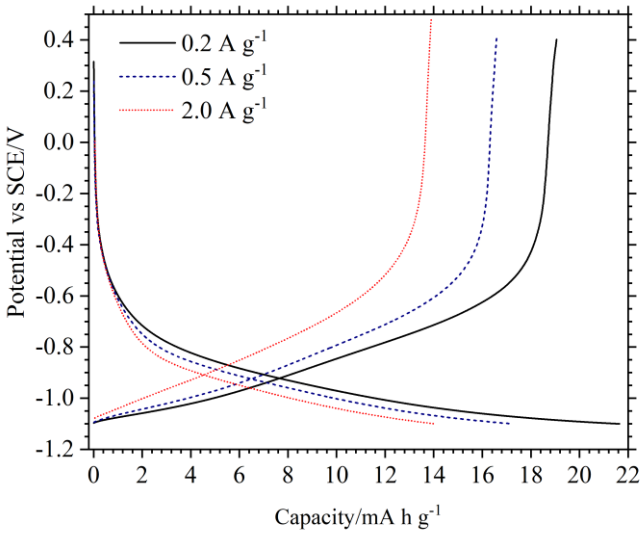

Figure 4.3. Potential profile of a TiO_2 electrode cycled at 0.2, 0.5 and 2.0 A g^{-1} in 1 mol dm^{-3} $AlCl_3$/1 mol dm^{-3} KCl. Potential limits were set between +0.4 to -1.1 V vs SCE.

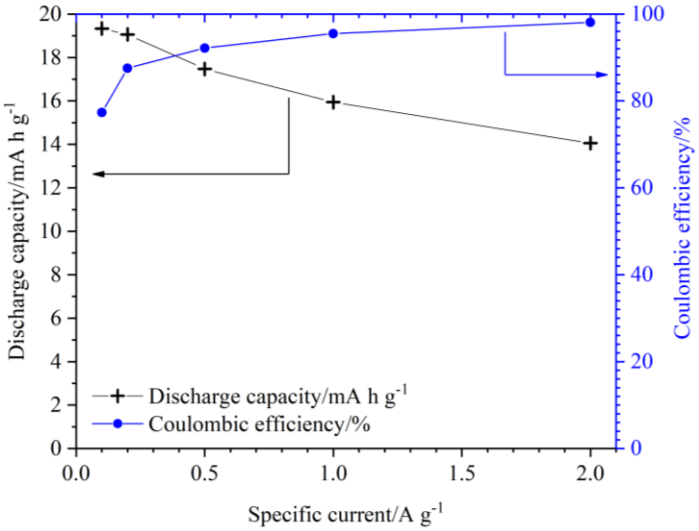

Figure 4.4. Discharge capacity and coulombic efficiency of TiO_2 as a function of specific current. The electrode was cycled in 1 mol dm^{-3} $AlCl_3$/1 mol dm^{-3} KCl between +0.4 to -1.1 V vs SCE.

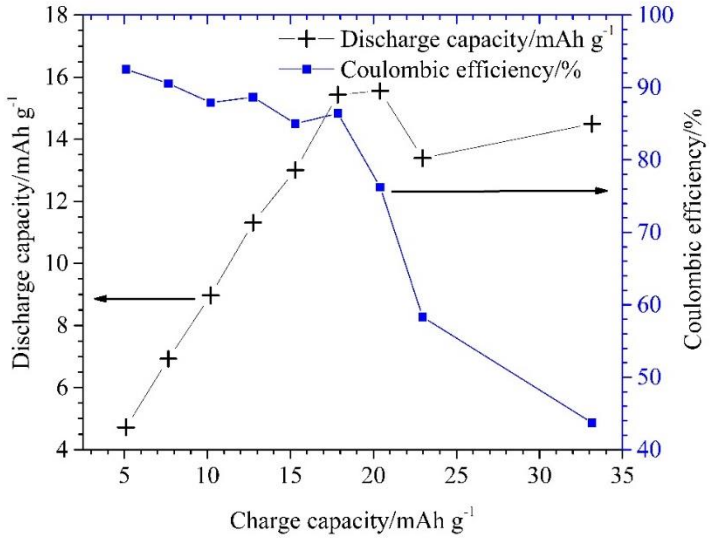

Figure 4.5. Discharge capacity and coulombic efficiency, of a TiO_2 electrode, as a function of charge input during galvanostatic cycling at 333 mA g^{-1} in 1 mol dm^{-3} $AlCl_3$/1 mol dm^{-3} KCl.

Given the decreasing coulombic efficiency at lower specific current, the discharge capacity of TiO_2 as a function of charge capacity input was explored. An electrode was charged at 333 mA g^{-1} for various time periods, corresponding to charge inputs ranging from 5 mA h g^{-1} to 33 mA h g^{-1}. Figure

4.5 gives the discharge capacity and coulombic efficiency as a function of charge input. As expected, discharge capacity increases with charge capacity between 5 mA h g^{-1} and 17 mA h g^{-1}, though coulombic efficiency decreases slightly from 91.6% to 88.8%. Above a charge capacity of 17 mA h g^{-1}, there is a limited increase in discharge capacity while coulombic efficiency decreases dramatically, falling to 76% after a charge input of 21 mA h g^{-1} at 333 mA g^{-1}. This graph points toward a maximum capacity limit for TiO_2, which may be necessary in addition to the potential limits used in Figure 4.3.

4.2 Using copper hexacyanoferrate vs TiO_2 in an aqueous Al-ion cell

Cyclic voltammetry scans were performed on copper (CuHCF), cobalt (CoHCF) and nickel (NiHCF) hexacyanoferrates in 1 mol dm^{-3} $AlCl_3$. Figure 4.6 shows the 10th cycle from these electrodes using a scan rate of 10 mV s^{-1}. CuHCF shows broad reduction and oxidation peaks centred around 0.4 V and 0.6 V respectively with peak heights of 2.3 A g^{-1} and -2.5 A g^{-1}. Secondary shoulders are also observed during the anodic and cathodic sweeps, centred on 0.80 V and 0.85 V respectively. Figure 4.6 shows there is no O_2 evolution visible at 1.0 V vs SCE at the CuHCF electrode. CoHCF gives rise to oxidation and reduction peaks at 0.45V and 0.42 V vs SCE with heights of 1.30 and -1.40 A g^{-1}. Secondary shoulders are again present, though at less negative potentials of around 0.25 V and 0.10 V. NiHCF gives rise to broad redox activity with oxidation and reduction peaks occurring around 0.45 V and 0.25 V with magnitude of the heights being 0.75 A g^{-1}. In 1 mol dm^{-3} KCl, the redox peaks from all three electrodes are clearly more prominent and symmetrical. During a 10 mV s^{-1} scan between 0.20 V and 1.00 V, CuHCF gives rise to an oxidation wave starting at ca. 0.55 V, where current beings to rise rapidly, giving rise to an 8.2 A g^{-1} peak at 0.70 V. This current then drops to effectively zero at 1.00 V. On the reverse scan, current drops at ca. 0.80 V with a clear reduction peak of -8.3 A g^{-1} at 0.58 V. This current decays back to zero by 0.20 V. CoHCF and NiHCF produce similarly shaped peaks but with measured peak currents being lower than CuHCF and lowest for NiHCF. Redox peaks also occur at less negative potentials from CuHCF to CoHCF to NiHCF, where oxidation and reduction peaks occur at 0.48 V and 0.35 V respectively. A comparison between Figure 4.6 (a) and (b) clearly suggests improved electrochemical activity in the presence of K^+. The broad redox activity of CuHCF in $AlCl_3$ suggests slow diffusion of Al^{3+} through interstitial sites with the cubic framework. Presence of secondary shoulders and peaks also suggests the possibility of separate or multistage redox processes. Further investigating the insertion species may be possible through the use of an electrochemical quartz microbalance. Active material can be applied to the quartz substrate to be used as a working electrode in a 3-electrode set-up. Combining electrochemical and quartz microbalance measurements is then achieved through overlapping a

DC voltage with a high frequency AC voltage. Mass changes due to intercalating/de-intercalating species during charge and discharge change the resonant frequency of the quartz and can therefore help elucidate intercalating species as well as states-of-charge [180].

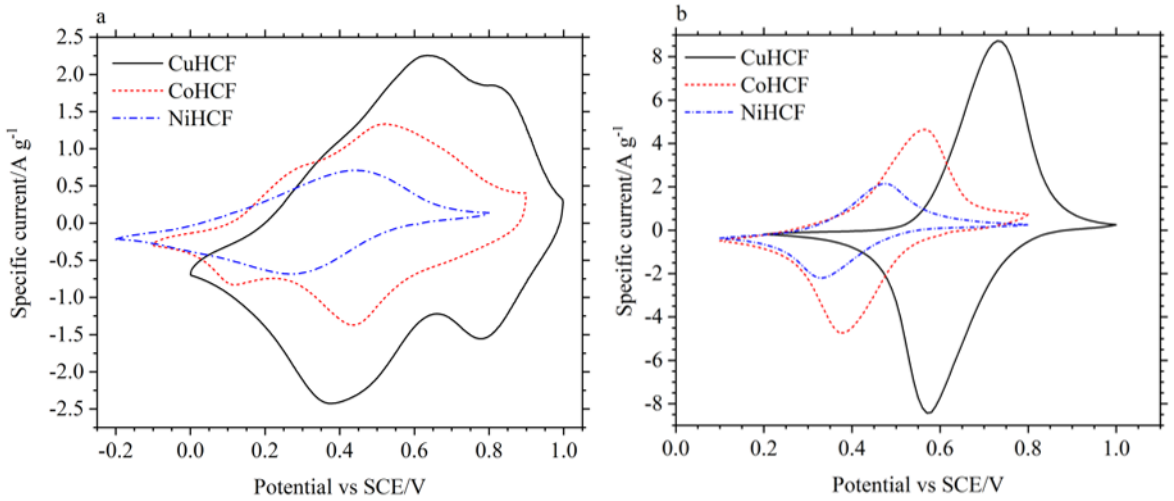

Figure 4.6. CV scans of CuHCF (black), CoHCF (red dotted) and NiHCF (blue dash-dot) at 10 mV s^{-1} in (a) 1 mol dm^{-3} $AlCl_3$ and (b) 1 mol dm^{-3} KCl. An SCE reference electrode was used.

After 10 initial cycles at 1.0 A g^{-1}, CuHCF was then galvanostatically cycled at 0.2, 0.5 and 2.0 A g^{-1}. Figure 4.7 (a) gives the potential profile in 1 mol dm^{-3} $AlCl_3$, showing a sloping profile between 0.20 V and 1.05 V. Capacity decreases from 41.1 mA h g^{-1} at 0.2 A g^{-1} to 34.1 mA h g^{-1} at 2.0 A g^{-1}. Figure 4.7 (b) was obtained from cycling in 1 mol dm^{-3} $AlCl_3$/1 mol dm^{-3} KCl and shows a considerably flatter plateau centred at ca. 0.70 V vs SCE. Upon charge at 0.2 A g^{-1}, the potential increases quickly from 0.42 V to 0.65 V where a flat potential is measured up to ca. 42 mA h g^{-1} where a potential of ca. 0.90 V increases sharply to 1.0 V. A similar profile is seen in reverse during electrode discharge. Capacity decreases from 42.5 mA h g^{-1} at 0.2 A g^{-1} to 38.9 mA h g^{-1} at 2.0 A g^{-1} with minimal changes in the potential profiles apart from a small increase in the potential hysteresis. At 0.2 A g^{-1} there is a 78 mV and 12 mV potential hysteresis in the $AlCl_3$ and $AlCl_3$/KCl electrolytes, respectively. At 2.0 A g^{-1}, they increase to 130 mV in $AlCl_3$ and 77 mV in $AlCl_3$/KCl. Clearly, CuHCF performance is improved in the presence of K^+.

The use of CuHCF in 0.5 mol dm^{-3} $Al_2(SO_4)_3$ was reported by Liu et al [181], but only 1000 cycles were possible before capacity had decreased by 45%. This is considerably lower than the 30000+ cycle life reported for CuHCF in 1 mol dm^{-3} KNO_3 [111]. Therefore, CuHCF was cycled in $AlCl_3$ in order to determine whether the comparatively low reported cycle life was a result of the reaction

mechanism/insertion with Al^{3+}, or a result of electrode manufacture. Figure 4.8 shows the capacity and coulombic efficiency of CuHCF over 28000 cycles, between 0.2 – 1.05 V vs SCE, in 1 mol dm^{-3} $AlCl_3$. Cycling at 1.0 A g^{-1} between cycle 0 – 4200 resulted in an 8.9% drop in capacity from 35.4 mA h g^{-1} to 32.5 mA h g^{-1}. Between cycles 4201 – 18000, various specific currents were used between 0.5 A g^{-1} and 6.0 A g^{-1}, with cycling performed at 2.0 A g^{-1} from cycle 18000 onwards. From the 4001st cycle (at 2.0 A g^{-1}) to the 28000th cycle (at 2.0 A g^{-1}), there was a further 19 % drop in capacity from 30.0 mA h g^{-1} to 25.2 mA h g^{-1}. This is a considerable improvement over the cycle life reported by Liu et al [139] and suggests the reported cycle life of 1000 was not a result of structural degradation due the insertion/extraction of Al^{3+}. Instead, it likely highlights the importance of the electrode manufacture process. The rigorous, high speed shear mixing performed for this work as well the careful application of ink to the current collector may well be responsible for the improved performance. This suggests high speed shear mixing and drip coating inks to be an improvement over the electrode manufacture method described by Liu et al, where powders are mixed with PTFE, dried at 50 °C and pressed into a Ti mesh at 30 MPa.

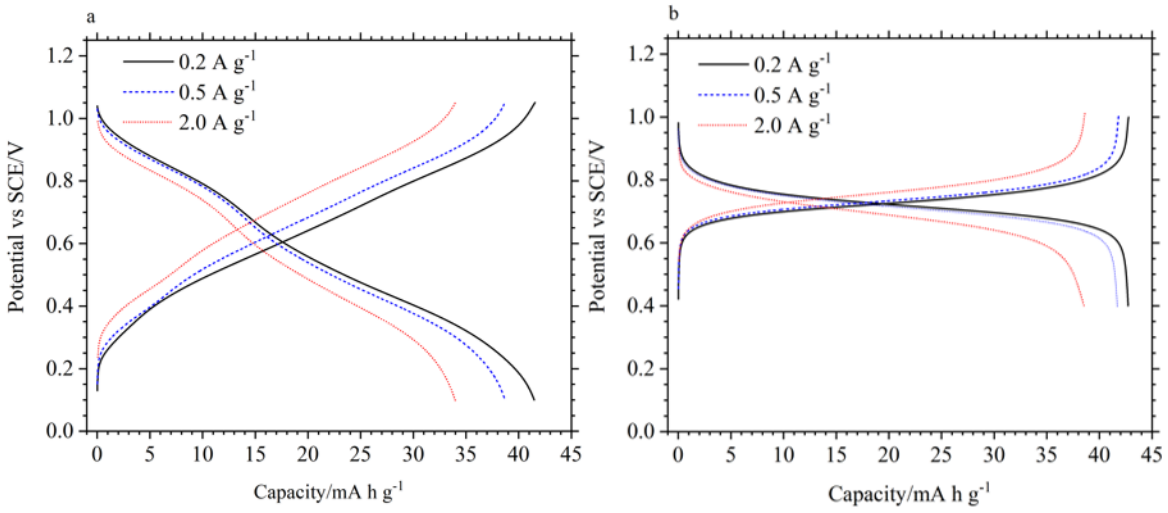

Figure 4.7. Potential profiles of CuHCF vs an SCE reference at 0.2, 0.5 and 2.0 A g^{-1} in 1 mol dm^{-3} $AlCl_3$ (a) and 1 mol dm^{-3} $AlCl_3$/1 mol dm^{-3} KCl (b).

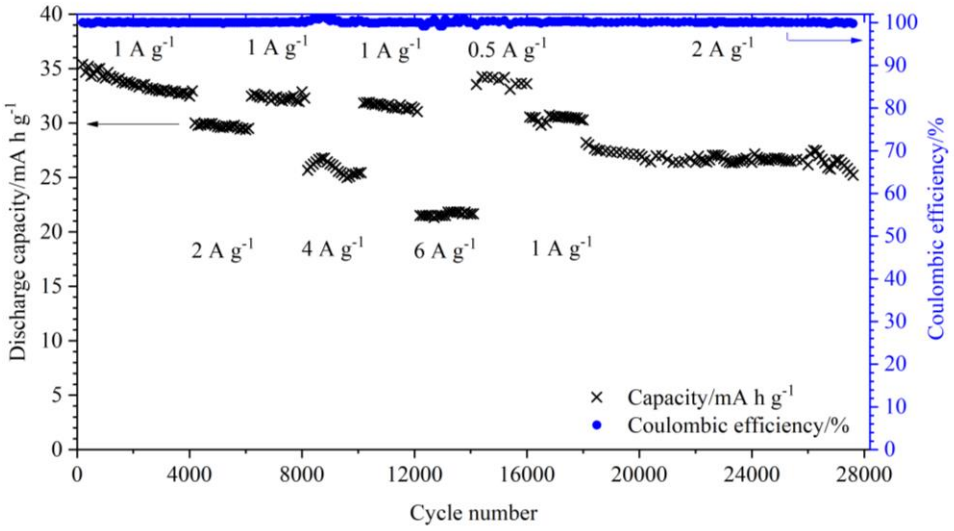

Figure 4.8. Evolution of capacity and coulombic efficiency during extended cycling of CuHCF in 1 mol dm^{-3} $AlCl_3$ between 0.20 V and 1.05 V vs SCE at specific currents from 0.5 A g^{-1} to 6.0 A g^{-1}.

4.2.1 Tailoring the state-of-charge of CuHCF

While CuHCF can be extensively cycled in a 3-electrode set-up, as-synthesised CuHCF gives rise to an electrode in a partially charged state. This would be problematic for a full cell, where the voltage limit would be reached prematurely i.e. before the full capacity of the negative electrode can be utilised. Otherwise, O_2 evolution would be expected to occur at the positive CuHCF electrode. To demonstrate the initial state-of-charge (SoC) of CuHCF, the open circuit potential (OCP) of an as-synthesised electrode was measured in 1 mol dm^{-3} $AlCl_3$/ 1mol dm^{-3} KCl, followed by galvanostatic cycles at 1.0 A g^{-1} between 0.4 V to 1.0 V vs SCE. Figure 4.9 (a) shows the initial OCP of CuHCF over 300 seconds, in 1 mol dm^{-3} $AlCl_3$/1 mol dm^{-3} KCl, along with the 1st charge/discharge cycle at 1.0 A g^{-1}. The OCP is seen to be stable at 0.79 V vs SCE. During the initial charge phase, the electrode potential rises quickly before reaching 1.00 V after only 40 s of charging. During the subsequent discharge, potential drops to ca. 0.78 V where a sloping plateau is visible between ca. 0.75 V to 0.62 V. The potentials drops to 0.40 V after a 250 s discharge. Figure 4.9 (b) shows the potential profile of this 1st cycle against capacity, along with the profiles from the 2nd and 3rd cycles. The initial 40 s charge leads to an initial charge capacity of only 4 mA h g^{-1} before reaching the upper potential limit of 1.00 V, with the subsequent 1st cycle discharge capacity of 35 mA h g^{-1}. During the subsequent two cycles, the more pronounced plateaus seen in Figure 4.7 (b) are observed with a stable capacity of approximately 43 mA h g^{-1}.

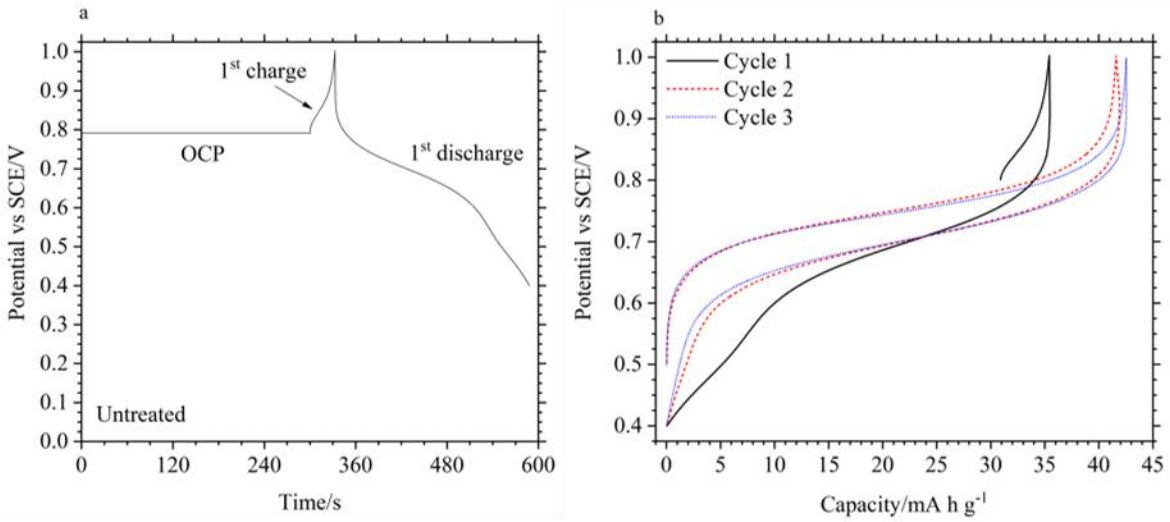

Figure 4.9. (a) Initial OCP of CuHCF followed by the first charge/discharge cycle at 1.0 A g^{-1} in 1 mol dm^{-3} $AlCl_3$/1 mol dm^{-3} KCl with potentials limits set between 0.4 V and 1.0 V vs SCE. (b) Charge/discharge capacities during the first three cycles at 1.0 A g^{-1}.

To control the initial SoC, it is possible it is possible to chemically reduce CuHCF through the addition of sodium thiosulphate ($Na_2S_2O_3$) to the precursor solution of potassium ferricyanide and copper nitrate, as mentioned by Pasta et al [182]. In this work, manufactured electrodes were soaked in 10 mmol dm^{-3} $Na_2S_2O_3$ for 0 – 40 mintues. The OCP of CuHCF, in 1 mol dm^{-3} $AlCl_3$/1 mol dm^{-3} KCl, after different soaking times in 10 mmol dm^{-3} $Na_2S_2O_3$ is shown in Figure 4.10 (A). Without chemical reduction, the OCP of CuHCF is 0.79 V vs SCE, as shown in Figure 4.9 (a). After 1 minute in $Na_2S_2O_3$, the OCP drops to 0.75 V vs SCE, which then decreases steadily with increasing soaking times, up to 30 minutes, where the OCP was measured at 0.65 V. From 30 minutes to 40 minutes, the potential drops off more rapidly to an OCP of 0.45 V. The graph of OCP, in $AlCl_3$KCl, vs soaking time, roughly follows the potential profile during galvanostatic cycling. It is likely then that the chemical reduction treatment results in the nsertion of Na^+, in the absence of K^+, with concomitant reduction of CuHCF and the OCP. It is suggested that the chemical reduction of CuHCF in $Na_2S_2O_3$ follows reaction (4.1).

$$\mathrm{KCuFe^{III}(CN)_6 + xNa^+ + xe^- \rightleftharpoons KNa_xCu[Fe^{II}(CN)_6]_x[Fe^{III}(CN)_6]_{1-x}} \quad (4.1)$$

Figure 4.10 (a) also shows how increasing the soaking time decreases the effective SoC of the electrode. After 30 minutes in 10 mmol dm^{-3} $Na_2S_2O_3$, a CuHCF electrode is effectively ina 0% SoC. This can be seen in Figure 4.10 (b), which show the first three cycles at 1.0 A g^{-1} after being chemically reduced for 30 minutes. A first full cycle charge capacity of 39.7 mA h g^{-1} is reached at

1.0 A g^{-1}, and is reversible upon discharge with 99.5% coulombic efficiency. Chemical reduction for time periods longer than 30 minutes results in a SoC of charge lower than 0%, resulting in some irreversible charge capacity during the 1st cycle. Figure 4.11 (a) shows the first three cycles and the 1000th cycle after a 40 minute reduction in $Na_2S_2O_3$. An initial charge capacity of 43.4 mA h g^{-1} is followed by the subsequent discharge capacity of 40.5 mA h g^{-1}. Second and third cycle capacities stabilise at ca. 40.4 mA h g^{-1} with CE >99.5%. After 1000 cycles, a capacity of 40.1 mA h g^{-1} is measured. It therefore assumed that this chemical reduction process has no detrimental effect on the cycling stability of the electrodes even with excessive reduction, i.e. to an OCP <0.65 V vs SCE in 1 mol dm^{-3} $AlCl_3$/1 mol dm^{-3} KCl. As a natural extension of this, chemical oxidation was also shown to be feasible in order to increase the initial SoC of CuHCF. Figure 4.11 (b) shows the first three cycles of an electrode after a 60 minute chemical oxidation in 100 mmol dm^{-3} $KMnO_4$. The OCP was measured at 0.87 V vs SCE resulting in an initial discharge capacity of 42.5 mA h g^{-1} and subsequent charge capacity of 40.0 mA h g^{-1}. Second and third cycle capacities then stabilise back at around 42.0 mA h g^{-1}

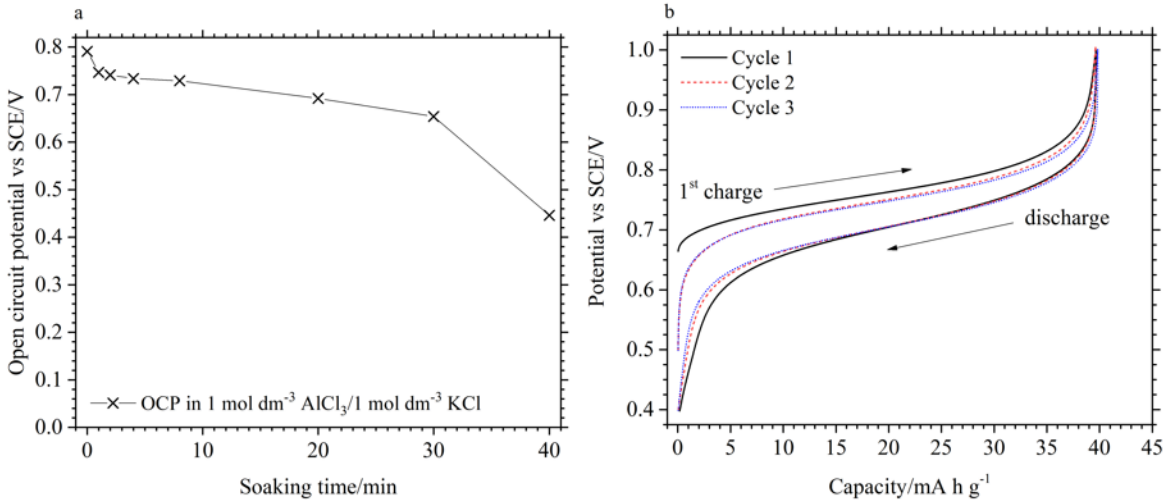

Figure 4.10. (a) OCP of CuHCF electrodes vs SCE, in 1 mol dm^{-3} $AlCl_3$/1 mol dm^{-3} KCl, after soaking in 10 mmol dm^{-3} $Na_2S_2O_3$ for 0 – 40 minutes. (b) First three cycles, at 1.0 A g^{-1}, of an electrode soaked in $Na_2S_2O_3$ for 30 minutes.

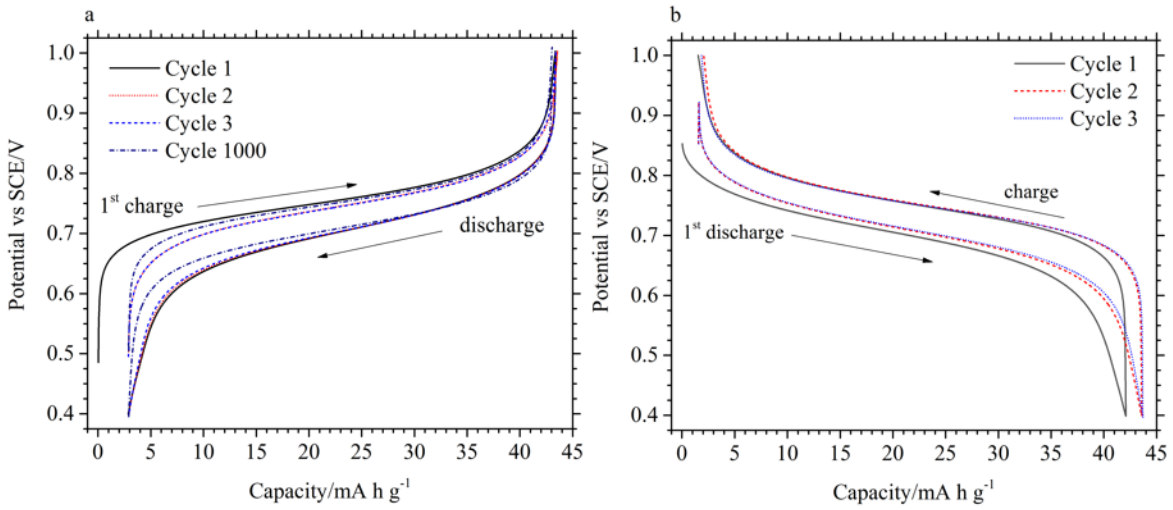

Figure 4.11. Initial cycles of CuHCF electrodes in a 3-electrode cell with an electrolyte of 1 mol dm^{-3} $AlCl_3$/1 mol dm^{-3} KCl and using a specific current of 1.0 A g^{-1}. (a) after soaking in 10 mmol dm^{-3} $Na_2S_2O_3$ for 40 minutes. (b) after soaking in 100 mmol dm^{-3} $KMnO_4$ for 60 minutes.

The chemical reduction treatment is important in order to construct a full cell where both electrodes are in their desired redox states i.e. with a TiO_2 electrode in a fully oxidised state, the positive CuHCF electrode should be in a fully reduced state. The chemical oxidation of CuHCF has not been previously reported and while not applicable to its use opposite TiO_2, demonstrates the feasibility of chemical oxidation in $KMnO_4$. This could be applicable to aqueous, rechargeable Zn-ion batteries as Zn metal will be in a fully charged state, which undergoes dissolution upon the first discharge, allowing Zn^{2+} cations to migrate and insert into the positive electrode.

4.3 Characterising full aqueous Al^{3+}/K^{+} cells

4.3.1 Electrochemical performance

The carbon polymer itself shows no electrochemical activity, as shown by a CV of the bare current collector in 1 mol dm^{-3} $AlCl_3$ at 20 mV s^{-1} given in Figure 4.12. The CV also demonstrates the relatively wide potential stability window of the electrolyte of > 2 V. H_2 evolution at the carbon polymer current collector becomes apparent between -1.2 V and -1.3 V vs SCE, while O_2 evolution begins to occur at approximately +1.2 V vs SCE. Based on the main redox peaks, a cell combining TiO_2 and CuHCF should have charge and discharge potentials of ca. 2.3 V and 1.7 V respectively, though these

will obviously be affected by factors including cycling rates, electrode thickness and size and the conductivity of the current collector.

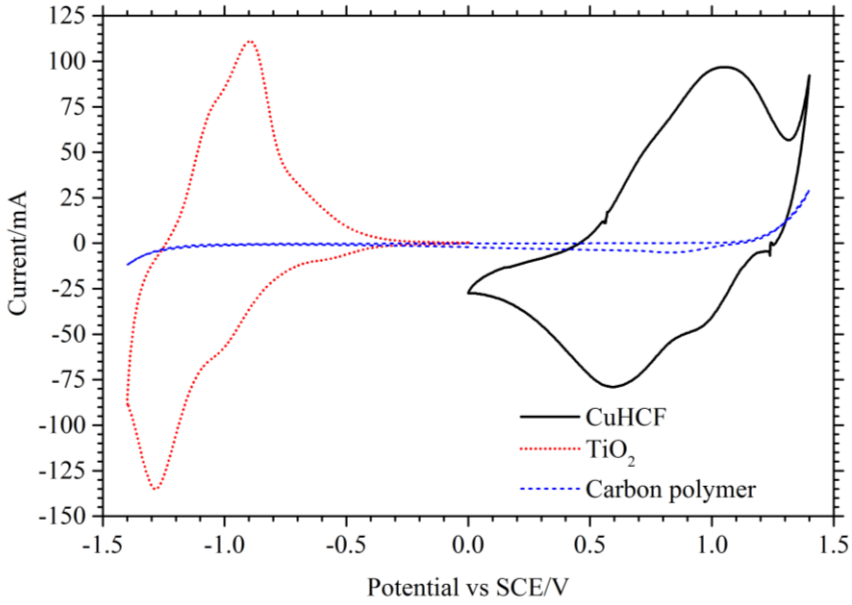

Figure 4.12. CV scan of CuHCF (black line), <25 nm TiO_2 (red dot) and carbon polymer (blue dash) at 20 mV s^{-1} in 1 mol dm^{-3} $AlCl_3$. Approximately 7 cm^{-2} of each electrode were submerged in the electrolyte.

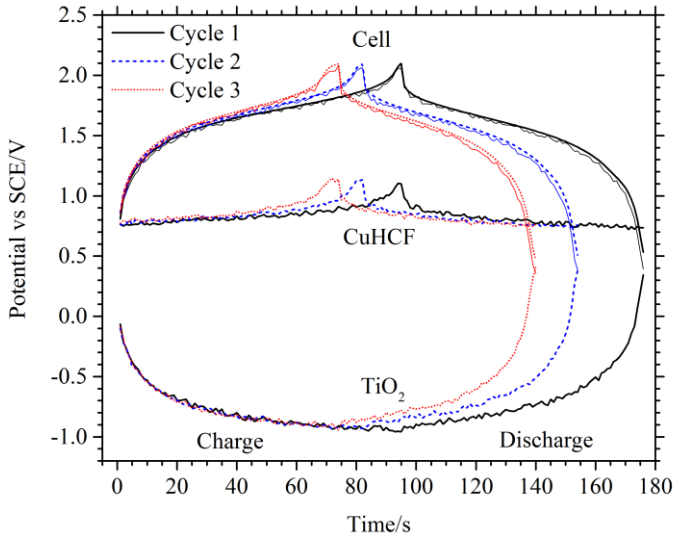

Figure 4.13. Cell voltage profile during 2-electrode cycling in 1 mol dm^{-3} $AlCl_3$/1 mol dm^{-3} KCl between 0.5 V and 2.1 V. CuHCF and TiO_2 potentials vs SCE are also shown with the specific current being 1.5 A g^{-1}_{CuHCF}. Individual electrodes were measured through connection to an external NI DAQ with the cell controlled via the galvanostat.

A full cell was constructed using CuHCF as the positive electrode, TiO_2 as the negative and 1 mol dm^{-3} $AlCl_3$/1mol dm^{-3} KCl as the electrolyte. The cell was cycled at a specific current of 1.5 A g^{-1}, based on the mass of CuHCF, while cell voltage was limited between 0.50 V and 2.10 V. Individual electrode potentials were measured against an SCE reference, placed between the positive and negative electrodes, connected to an external National Instruments data-acquisition module (DAQ). Figure 4.13 shows how the cell, TiO_2 and CuHCF voltages vary vs time during the first three cycles. The individual electrode potentials are shown along with the measured cell potential. Additionally, the cell potential, E_{cell}, as calculated via equation (4.2) is shown by the thin solid lines. E_{+ve}, is the measured potential of the CuHCF electrode and $-ve$ is the measured potential of the TiO_2 electrode. There is negligible difference between the measured and calculated cell potentials, demonstrating the low resistance contributed by the electrolyte.

$$E_{cell} = E_{+ve} - E_{-ve} \tag{4.2}$$

Figure 4.13 shows that during the first cycle, the cell voltage limit is reached after 95 s (i.e. 40 mA h g^{-1}_{CuHCF} as calculated by the mass of the CuHCF electrode), but decreases to 82 s during the second cycle and 74 s during the third. The CuHCF potential can be seen to start at 0.75 V and remains stable up to ca. 85 s where its potential rises above 1.0 V and the cell voltage limit is reached. Concurrently, the TiO_2 negative electrode potential becomes more negative from -0.1 V to -0.7 V vs SCE after 10-15 s, where the profile curves off, reaching approximately -1.0 V after 95 s. During the first discharge, the potential of CuHCF again remains stable. After an initial IR-drop, the potential decreases from ca. 0.8 V to ca. 0.7 V at the end of cell discharge, without any significant decrease in potential that would signify the SoC of CuHCF approaching zero. This is due to the lower coulombic efficiency of TiO_2, compared to CuHCF, where its potential can be seen to rise back to ca. +0.4 V vs SCE, after 170 s or 75 s into the 1st discharge. This is before the positive CuHCF electrode has fully discharged. This results in the CuHCF electrode starting the next cycle at a partially charged state and reaching full SoC after progressively lower charging times. This results in a lower available charge capacity before the 2.1 V limit is reached.

As such, it was decided to cycle a full cell without a voltage limit. Instead, a full cell was charged to a specified capacity of 16.5 mA h g^{-1} based on the mass of TiO_2 with the CuHCF electrode sized to allow for a capacity of ca. 35 mA h g^{-1}. Some O_2 evolution will be present at the positive electrode, especially during initial cycles, but with an excess of electrolyte, reversible cycling of a full cell would be possible. A full cell was constructed using TiO_2 and CuHCF in a mass ratio of 1: 0.45 (85 mg TiO_2:38 mg CuHCF) and cycled at a 20 C rate, where 20 C = 333 mA g^{-1}_{TiO2} or 745 mA g^{-1}_{CuHCF}. Charge input

was therefore 16.5 mA h g^{-1} based on the mass of TiO_2, which according to Figure 4.5 would result in a discharge capacity around 14 mA h g^{-1} at approximately 85-90% coulombic efficiency.

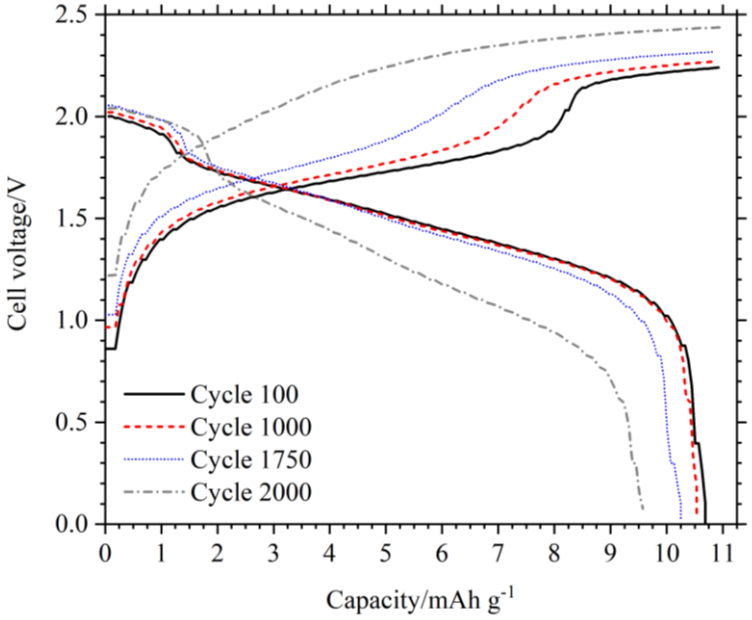

Figure 4.14. Voltage profile of a cell consisting of TiO_2 (85 mg) as negative electrode, CuHCF (38 mg) as positive and 1 mol dm^{-3} $AlCl_3$/1 mol dm^{-3} KCl as electrolyte. Cycling was performed at 20C corresponding to a specific current of 333 mA g^{-1} based on the mass of TiO_2.

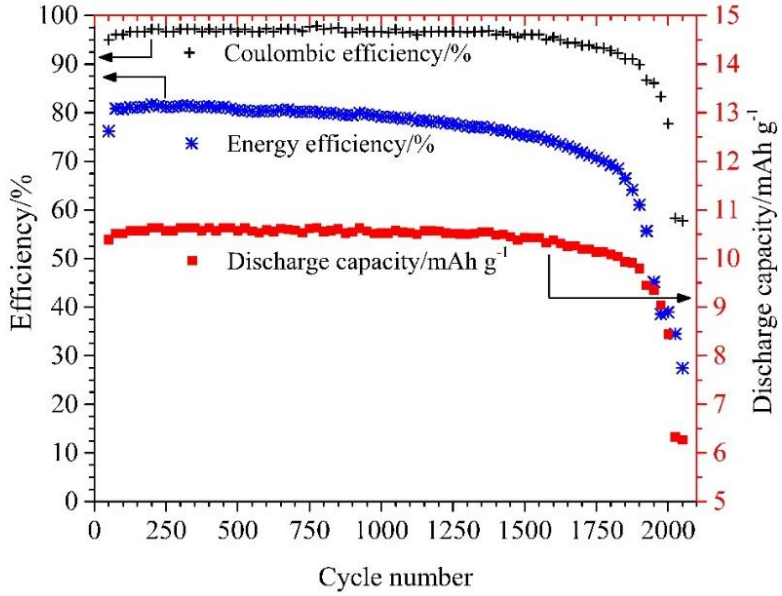

Figure 4.15. Coulombic efficiency, energy efficiency and discharge capacity of a full cell during cycling at a 20 C rate in 1 mol dm^{-3} $AlCl_3$/1 mol dm^{-3} KCl.

Figure 4.14 shows the evolution of the voltage profile from cycle 100 to 2000. The 100th cycle profile begins as expected with a plateau between 1.50 V – 1.85 V. However, between 8.0 to 9.0 mA h g^{-1} (based on the combined electrode masses), voltage rises from 1.85 V to 2.15 V where an unexpected, and previously unreported second plateau arises. Upon discharge, a similar two-plateau profile is observed. An initial voltage around 2.00 V drops to 1.80 V after 1.5 mA h g^{-1} before voltage decreases steadily to 1.15 V after approximately 10 mA h g^{-1} before dropping to 0.0 V between 10.0 mA h g^{-1} to 10.7 mA h g^{-1}. Therefore, the mechanism for this second plateau, which has not previously been reported, is at least partially reversible. As such, O_2 evolution cannot be the sole reaction after the 'full' CuHCF SoC is reached. By cycle 1000, the second plateau upon charge occurs around 7.8 mA h g^{-1} and at around 6.8 mA h g^{-1} during cycle 1750. During cycling, there is also a small increase in the 1st and 2nd plateau voltages. By cycle 2000, the CuHCF electrodes has degraded with distinct plateaus no longer visible. A cell voltage of 2.40 V is reached by the end of the charge phase with discharge capacity decreasing to 9.5 mA h g^{-1}. Figure 4.15 shows the discharge capacity along with coulombic and energy efficiencies during this cycling regime. A maximum capacity, calculated from the combined mass of electrodes, of ca. 10.6 mA h g^{-1} remained above 10 mA h g^{-1} until cycle 1814. An average discharge voltage which ranged between 1.49 V at cycle 100 and 1.46 V at cycle 1750, gives the cell an energy density of ca. 15 mW h g^{-1}. An initial coulombic efficiency of 96% was still above 90% by cycle 1900; energy efficiency decreased from >80% to 70% at cycle number 1778.

Figure 4.16 gives the typical profile of CuHCF in a separate cell cycled at 10 C, confirming that the second plateau does arise from CuHCF rather than TiO_2. The use of 1 mol dm^{-3} $AlCl_3$/1 mol dm^{-3} KCl as electrolyte means that the constructed cell could be classified as a dual-ion Al^{3+}/K^+ cell with charge storage at TiO_2 requiring the presence of Al^{3+} while K^+ is preferentially intercalated within CuHCF. However, a full cell using only 2 mol dm^{-3} $AlCl_3$ electrolyte should be feasible. Figure 4.17 presents the individual electrode potentials cycled in a cell, at a 20 C rate, using either 2 mol dm^{-3} $AlCl_3$ or 1 mol dm^{-3}/1 mol dm^{-3} KCl as electrolyte. The voltage of the full cell without KCl is also given. The voltage profiles show both cells function with the effect of the electrolyte primarily seen on the CuHCF electrode. Using 2 mol dm^{-3} $AlCl_3$, the discharge potential ranges from 1.2 V to 0.4 V, in comparison to 1.2 V to 0.7 V in 1 mol dm^{-3} $AlCl_3$/1 mol dm^{-3} KCl. Energy efficiency increased from 66.2 % in 2 mol dm^{-3} $AlCl_3$ to 73.3% in 1 mol dm^{-3} $AlCl_3$/1 mol dm^{-3} KCl

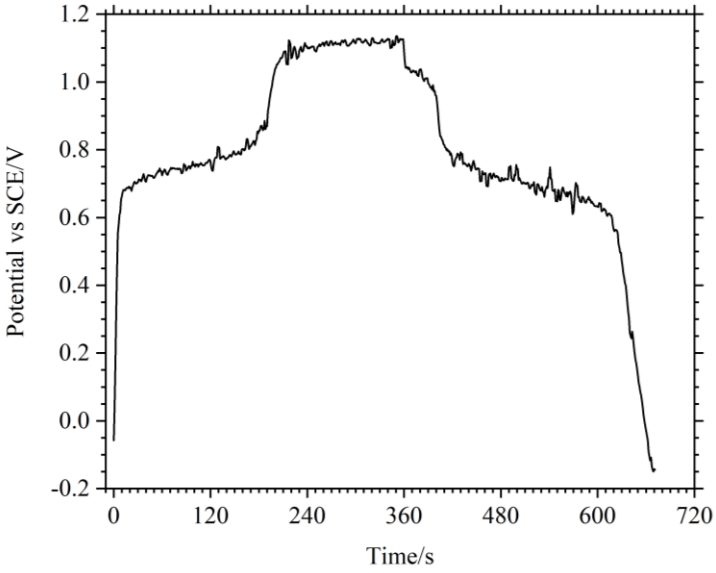

Figure 4.16. Typical profile of a CuHCF electrode in a full cell cycled at a 10C rate, using a TiO_2 negative electrode and 1 mol dm^{-3} $AlCl_3$/1 mol dm^{-3} KCl aqueous electrolyte.

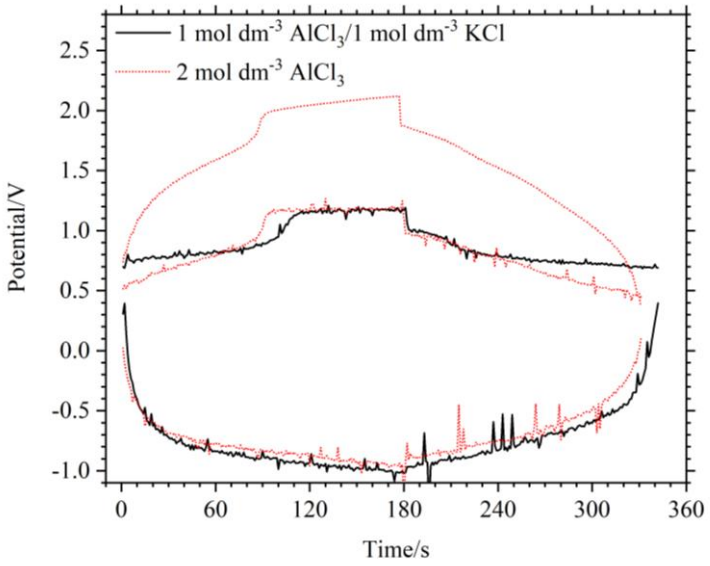

Figure 4.17. Individual electrode potentials vs SCE, during a cycle in a full cell at a 20 C rate using 1 mol dm^{-3} $AlCl_3$/1 mol dm^{-3} KCl (black) and 2 mol dm^{-3} $AlCl_3$ (red-dot). Cell voltage using 2 mol dm^{-3} $AlCl_3$ is also shown (red-dot).

A full cell was also cycled at various specific currents. Figure 4.18 presents a Ragone plot from a full aqueous cell cycled between 0.114 A g^{-1} – 1.14 A g^{-1}. The specific current and capacity take into account the mass of both electrodes while the specific power and energy also make use of the

average discharge voltage. The plot shows both specific energy and energy efficiency decreasing with increasing power. As expected from previous results, coulombic efficiency increases with power and current. A specific energy of 14.7 mW h g^{-1} is possible at the maximum power of 2.6 W g^{-1} (2.6 kW kg^{-1}). At 0.3 W g^{-1}, a specific energy of 16.3 mW h g^{-1} is obtained.

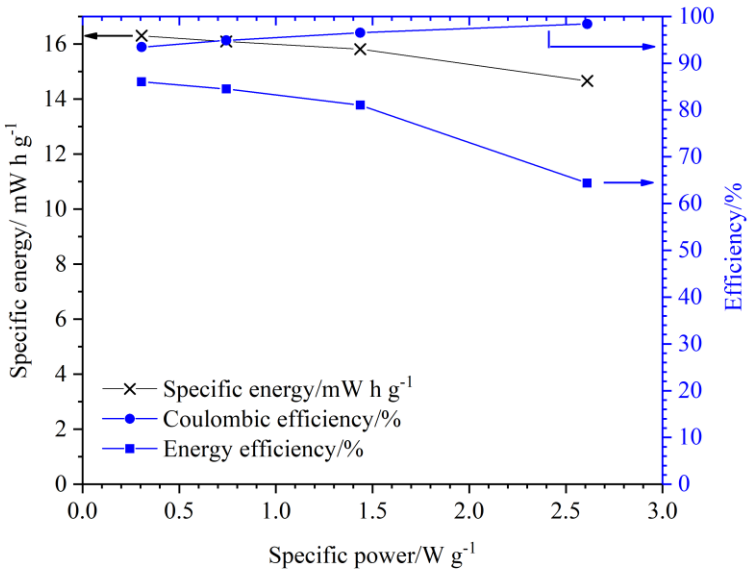

Figure 4.18. A Ragone plot of a full cell, giving the specific discharge energy and efficiencies as a function of specific power. Specific energy and power were calculated using the average discharge voltage and combined electrode mass.

A 2-cell aqueous Al-ion battery is also demonstrated using a bipolar electrode. The voltage vs. time profile is compared to a single cell in Figure 4.19. The charge and voltage efficiencies are comparable. The small discrepancy between the onsets of the second plateau can be accounted for by the lower mass ratio of CuHCF:TiO_2 in the 2-cell battery. Cycling at a 10 C rate, the charge voltage increases steadily from ca. 2.0 V to 3.5 V, at which point there is a more rapid increase in voltage to 4.1 V before a further steady increase to 4.5 V at the end of charge. During discharge, the voltage decreases steadily from 4.0 V to 3.7 V, at which point there is a rapid drop-off to 3.4 V followed by a more steady decline to 2.0 V at the end of discharge. The two voltage stages are associated with the CuHCF positive electrode. An average discharge voltage of 2.9 V was achieved, giving the battery an energy density of 14.8 mW h g^{-1} according to total mass of active material in both electrodes. The data from Figure 4.19 along with that from Figure 4.15 and Figure 4.14 used 10 cm^2 electrodes and the cell design shown in Figure 3.1 (a) with TiO_2 and CuHCF mass loadings of 7-8 mg cm^{-2} and 3-4 mg cm^{-2}, respectively. The size of these electrodes are considerably higher than have been

reported with regards to aqueous Al-ion electrodes and in general, other aqueous intercalation or supercapacitor electrodes. This suggests scale up of these electrodes is feasible.

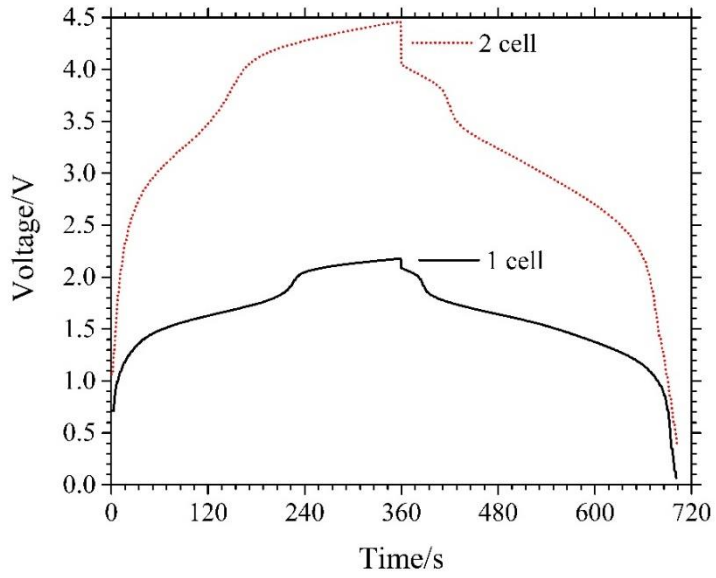

Figure 4.19. Typical profile of a 1-cell and 2-cell Al-ion battery cycled at a 10C charge/discharge rate in 1 mol dm^{-3} $AlCl_3$/1 mol dm^{-3} KCl electrolyte.

4.3.2 Degradation of CuHCF

The partial reversibility of the second plateau observed from CuHCF allowed full cells to be constructed, despite the lower coulombic efficiency of TiO_2. However, this clearly led to the premature degradation of CuHCF. Aside from the degradation in electrochemical performance, the electrolyte was also seen to turn a pale yellow colour. Under charging the CuHCF electrode, the first plateau and primary storage mechanism derives from the extraction of K^+ and the oxidation of Fe^{2+}, as shown in reaction (2.12) [112]. It is posited that the deep oxidation of CuHCF, during the charge phase, leads to the presence of the 2nd plateau. Considering that a solution of $FeCl_3$, and other aqueous solutions containing Fe^{3+}, take on a yellow-brown colour, it is possible that the onset of the second plateau leads to some dissolution of Fe^{3+} into solution. UV-vis spectroscopy was performed on an unused electrolyte as well as an electrolyte used within a full cell. To confirm the presence of Fe^{3+}, spectroscopy was also performed on a solution of $AlCl_3$/KCl/$FeCl_3$, i.e. new electrolyte with added $FeCl_3.6H_2O$. Figure 4.20 shows the spectra of the solutions between 220 and 650 nm. The new electrolyte shows an initial absorbance that falls to nearly zero by 250 nm, which is expected given the clarity of the electrolyte in the visible wavelength range. This spectra was then used as a background and subtracted from those taken from the used electrolyte and

$AlCl_3$/KCl/$FeCl_3$ solution. Both the used electrolyte and $AlCl_3$/KCl/$FeCl_3$ solution follow the same spectra. A relatively sharp absorbance peak is centred about 235 nm with a second broader peak at ca. 335 nm. At longer wavelengths, absorbance decays toward zero at ca. 470 nm. Given the highly similar spectra between the electrolyte used in a full cell and $AlCl_3$/KCl/$FeCl_3$, it can be confirmed that Fe^{3+} is present in the used electrolyte. This can only be due to the CuHCF electrode. No iron is present in the current collector while it was ensured that stainless steel crocodile clips were both well covered with parafilm and not immersed in the electrolyte. Furthermore, the 2nd plateau must be responsible for the presence of Fe^{3+}, since no colour change in the electrolyte was observed when CuHCF was cycled in a 3-electrode cell, between 0.2 to 1.05 V vs SCE, over 28000 cycles, Figure 4.8. However, the electrochemical reaction behind the 2nd plateau and the cause of Fe^{3+} dissolution is still unknown.

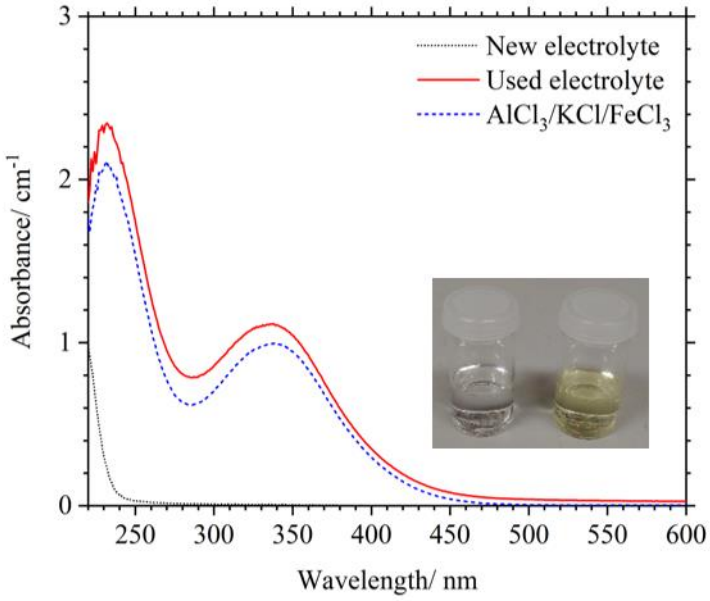

Figure 4.20. UV-vis spectra of unused 1 mol dm^{-3} $AlCl_3$/1 mol dm^{-3} KCl electrolyte (black dot), electrolyte used in a full cell over 1500 cycles and a solution of $AlCl_3$/KCl/$FeCl_3$. Inset is an image of new and used (pale-yellow) electrolytes.

4.4 Conclusions

This chapter describes the construction and characterisation of a full aqueous Al-ion cell for the first time, consisting of TiO_2 as the negative electrode, CuHCF as the positive and an Al^{3+} containing aqueous electrolyte. However, while a full cell functioned in 2 mol dm^{-3} $AlCl_3$, performance improved in a mixed 1 mol dm^{-3} $AlCl_3$/1 mol dm^{-3} KCl electrolyte due to the more facile intercalation of K^+ into CuHCF. Specific capacity and energy remained comparable in both electrolytes but energy

efficiency increased in the mixed electrolyte. The optimum cell therefore constitutes a dual-ion chemistry with Al^{3+} required for charge storage at the TiO_2 electrode and K^+ preferentially intercalated within CuHCF. The 1 mol dm^{-3} $AlCl_3$/1 mol dm^{-3} KCl electrolyte resulted in an average cell voltage of ca. 1.5 V, roughly in line with the potentials recorded via CV and a relatively high value for an aqueous system. A full cell was capable of over 1750 cycles, higher than previously reported for TiO_2 half-cells, before severe degradation of initial capacity and efficiencies. Throughout cycling at a 20 C cycle rate, coulombic efficiency remained above 90% and energy efficiency above 70%, remaining above 75% for over 1500 cycles. A full cell showed reasonable performance, producing a specific energy >16 W h kg^{-1} at 0.3 kW kg^{-1} and maintained >14.5 W h kg^{-1} at 2.6 kW kg^{-1}. The cells were demonstrated using electrodes of a considerably larger scale than previously described. Additionally, a 2-cell battery was shown to be feasible using a bipolar electrode with performance scaling as expected.

Within a 3-electrode set-up, nearly 28000 cycles were possible from CuHCF in 1 mol dm^{-3} $AlCl_3$. This in itself highlights the importance of electrode manufacture, with the only previous study of CuHCF as an electrode in Al^{3+} aqueous electrolyte being capable of only 1000 cycles. However, performance degradation of the full cell was found to be a result of the CuHCF electrode. This was due to the <100% coulombic efficiency of the TiO_2 electrode used, which resulted in the consistent overcharging (under discharging) of CuHCF. As a result, a second potential plateau was observed during galvanostatic cycling. The electrochemical mechanism for this plateau was electrochemically reversible, and therefore unlikely to be due to O_2 evolution only, though it became considerably less stable over repeated cycling. During full cell cycling, the electrolyte was also observed to turn a pale yellow colour. UV-vis spectroscopy showed that this was due to the presence of Fe^{3+} in solution and may point toward the degradation mechanism when CuHCF is overcharged. The colour change was not observed when CuHCF was cycled in the 3-electrode cell.

Highlighted should be the importance of full cell characterisation where, despite the very high cycle life of CuHCF in a 3-electrode cell, the relatively low coulombic efficiency of TiO_2 results in overcharging of CuHCF and its premature degradation when employed in a full cell. The limiting factor for an aqueous Al^{3+}/K^+ cell is shown to be the <100% coulombic efficiency of TiO_2. This issue had not been explicitly discussed or mentioned, despite data in the literature (i.e. voltage profiles) showing the issue to be present. The following chapters therefore focus on the electrochemical performance of TiO_2, including its non-ideal coulombic efficiency.

Chapter 5 Characterising the performance of TiO_2 in aqueous $AlCl_3$ electrolyte

For aqueous batteries, the performance characteristics of rate capability and cycle life are arguably more important than energy density, though increasing specific energy will naturally play a role in reducing costs (assuming similar material costs). This is especially true given the difficulty of surpassing the reversible energy density of Li-ion batteries with novel, non-lithium based chemistries in non-aqueous electrolytes. However, limited focus has been given to rate capability and cycle life in the literature on aqueous Al-ion electrodes. The aim of this chapter is to characterise the performance of TiO_2 nanopowders, in aqueous aluminium salt electrolytes, with this in mind. The use of commercially available powders provides advantages in terms of cost and simplicity of scale-up towards a new battery system. It also guarantees availability of material and negates potential issues around quality control and reliability that may arise from the synthesis of novel nanostructures. Compared to the literature describing TiO_2 in aqueous Al^{3+}-containing electrolyte, TiO_2 electrodes here are shown to have considerably higher cycle lives and rate capability. Equally important, the limitations of performance, and their implications, are highlighted and studied.

5.1 Performance of TiO_2 electrodes

5.1.1 Powder size comparison

Reducing particle sizes can help increase capacity and reduce polarisation at higher rates, due to shorter diffusion pathways for Al^{3+} and the shorter lengths for current flow before contact with conductive additive. In addition, smaller particle size can lead to higher surface areas, which could improve capacity if a surface charge storage mechanism is present. This may be the case given the relatively low capacity measured from TiO_2 in the previous section.

A number of commercial powders were purchased from US-nano (5 nm, 15 nm, 18 nm, 40 nm) and Sigma-Aldrich (25 nm) and used to manufacture electrodes as described in section 3.2.2. Electrodes were then cycled in 1 mol dm^{-3} $AlCl_3$/1 mol dm^{-3} KCl at 1.0 A g^{-1}. Capacities were measured between voltage limits of -1.0 V to +0.4 V and -1.1 V to +0.4 V vs SCE and are shown in Table 5.1. The particle sizes and specific surface areas (determined by N_2 adsorption BET analysis) as advertised by the manufacturers are given. However, further analysis, such as XRD, SEM and N_2 adsorption should be

performed to confirm particle and powder properties. The table shows that there is no linear correlation between measured capacity and particle size, in the range of 5 nm – 40 nm. However, important factors such as surface area and pore size were not measured, though the advertised surface areas are quoted. Confirming the lack of correlation between capacity and particle size would require testing of TiO_2 powders with particles sizes between 5 nm – 15 nm whilst controlling for factors such as surface area, pore size, pore size distribution and crystallinity. Cycled to -1.0 V, the 5 nm powder presents a discharge capacity of 22.5 mA h g^{-1} at 97.3% coulombic efficiency. All other powders produced lower capacities between 8.8 to 9.7 mA h g^{-1} with coulombic efficiency ranging from 96.3% to 99.1%. With a cut-off potential of -1.1 V, the 5 nm powder again exhibits the highest capacity. A discharge capacity of 34.6 mA h g^{-1} was measured at 1.0 A g^{-1}, though coulombic efficiency was also considerably lower at 63.3%. Again, the remaining powders exhibited similar capacities, between 15.7 to 17.9 mA h g^{-1}. However, the 25 nm powder produced a considerably higher coulombic efficiency of 98.3% compared to the next highest obtained from the 15 nm powder, when cycled to -1.1 V.

Table 5.1. Comparison of capacities measured from TiO_2 electrodes, manufactured from powders with different particle sizes, in 1 mol dm^{-3} $AlCl_3$/1 mol dm^{-3} KCl.

	1 A g^{-1} to -1.0 V vs SCE		**1 A g^{-1} to -1.1 V vs SCE**	
Particle size (BET surface area)	**Discharge capacity/mA h g^{-1}**	**Coulombic efficiency/%**	**Discharge capacity/mA h g^{-1}**	**Coulombic efficiency/%**
5 nm (289 m^2 g^{-1})	22.5	97.3	34.6	63.3
15 nm (60 m^2 g^{-1})	8.8	97.2	16.1	90.3
18 nm (200-240 m^2 g^{-1})	9.7	96.6	17.9	89.1
25 nm (45-55 m^2 g^{-1})	8.8	99.0	15.7	98.3
40 nm (35 m^2 g^{-1})	8.8	96.3	16.2	88.9

The potential profiles of the 5 nm and 25 nm powder TiO_2 electrodes cycled at a specific current of 1.0 A g^{-1} to a minimum potential of -1.0 V vs SCE are shown in Figure 5.1. Both show similar profile shapes, though during discharge, 5 nm TiO_2 gives rise to a sharper potential increase at ca. -0.55 V, corresponding to the end of discharge. The potential increase at the end of the discharge of 25 nm TiO_2 is a more gradual curve around -0.5 V.

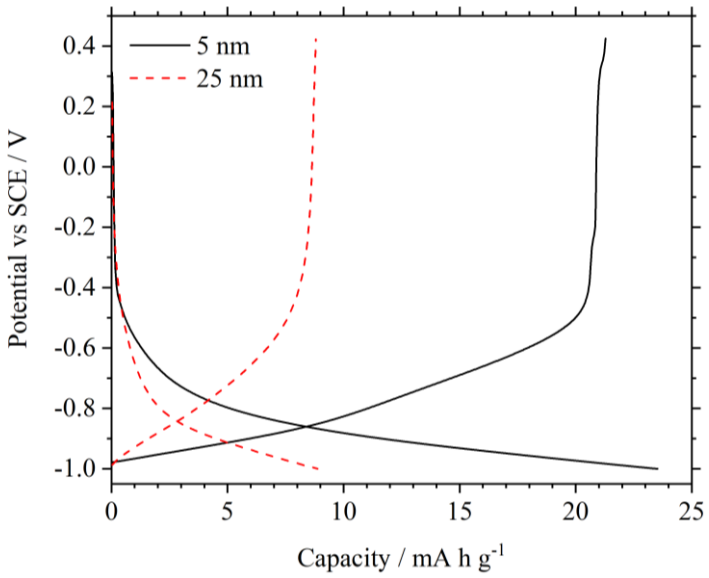

Figure 5.1. Comparison of typical voltage profiles obtained from 5 nm and 25 nm TiO_2 cycled at 1.0 A g^{-1} to -1.0 V vs SCE in 1 mol dm^{-3} $AlCl_3$/1 mol dm^{-3} KCl.

5.1.2 Potential limits and high rate capability

The rate capability of 25 nm and 5 nm TiO_2 was then investigated. 25 nm TiO_2 was cycled to -1.1 V vs SCE and 5 nm TiO_2 cycled to -1.0 V vs SCE. Figure 5.2 (a) shows the potential profile of the 25 nm-TiO_2 electrode being cycled to -1.0 V and -1.1 V vs SCE at 1.0 A g^{-1}. Discharge capacity increases from 8.8 mA h g^{-1} to 15.7 mA h g^{-1}, when the potential limit is lowered to -1.1 V vs SCE. Coulombic efficiency remains similar; decreasing only slightly, from 99.1% to 98.3%, suggesting a reversible charge storage mechanism is maintained at the more negative potential. The reason for the 5 nm electrode being cycled to -1.0 V vs SCE can be seen in Figure 5.2 (b), where an electrode was cycled at 1.0 A g^{-1} to both -1.0 V and -1.1 V vs SCE. It shows that while discharge capacity increases to 34.6 mA h g^{-1} when cycled to -1.1 V, compared to 21.3 mA h g^{-1} when limited to -1.0 V, coulombic efficiency also decreases considerably, dropping from 90.2% to 61.3% at the more negative potential limit.

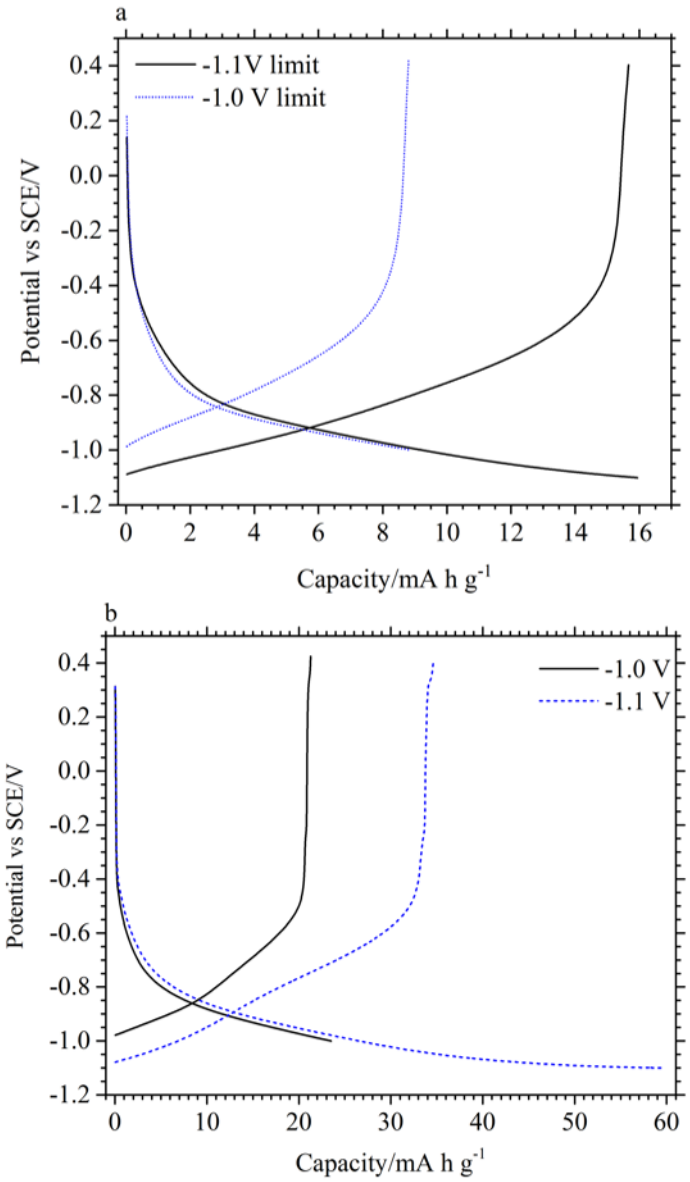

Figure 5.2. Typical voltage profiles of a 25 nm TiO_2 electrode (a) and a 5 nm TiO_2 electrode (b) in 1 mol dm^{-3} $AlCl_3$/1 mol dm^{-3} KCl during cycles at 1.0 A g^{-1} to minimum potentials of -1.0 V and -1.1 V vs SCE.

The measured capacity and coulombic efficiency of a 25 nm TiO_2 electrode at specific currents from 0.2 to 2.0 A g^{-1} are given in Figure 5.3 (a) with the corresponding potential profiles shown in Figure 5.3 (b). The data presented corresponds to the 10^{th} cycle at a given specific current. At 0.1 A g^{-1}, a discharge capacity of 18.8 mA h g^{-1} is measured at 78.1% coulombic efficiency. This actually increases to 19.1 mA h g^{-1} at 88.1% coulombic efficiency when cycled at 0.2 A g^{-1}. Above 0.2 A g^{-1}, discharge capacity decreases with a corresponding increase in coulombic efficiency observed. From 0.5 A g^{-1} to 2.0 A g^{-1}, discharge capacity decreases from 17.9 mA h g^{-1} to 13.9 mA h g^{-1} with coulombic

efficiency increasing from 95.2% to 98.8%. The potential profiles follow similar curves at these specific currents with a relative plateau between -1.1 V and ca. -0.6 V.

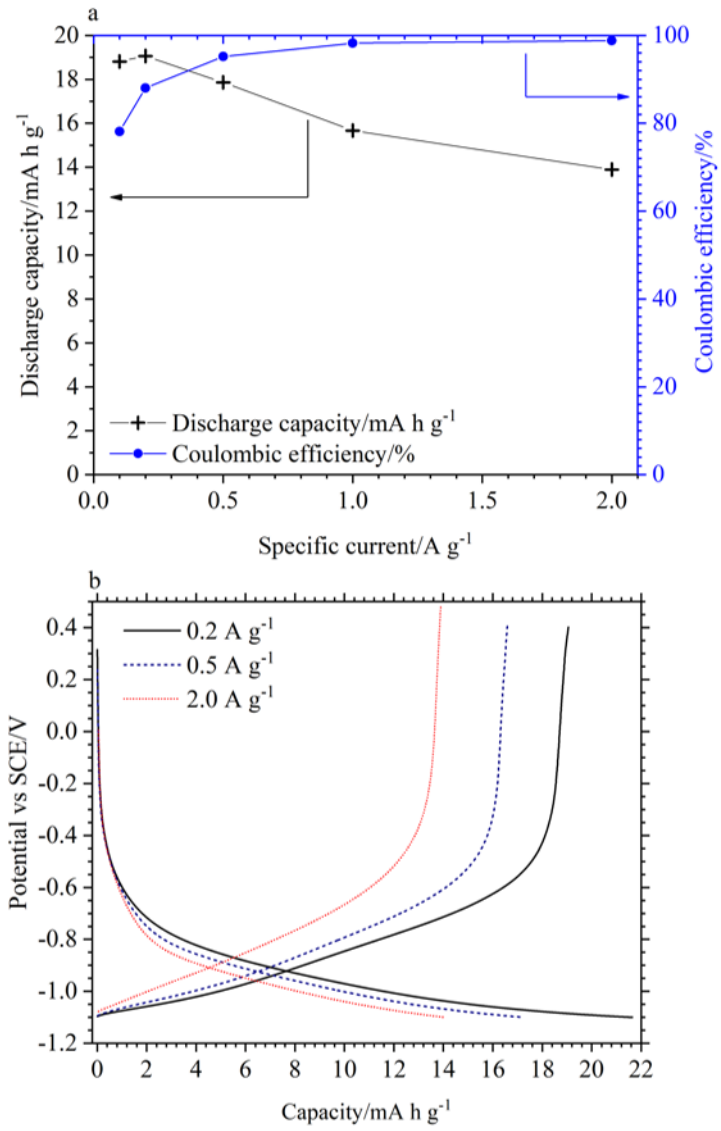

Figure 5.3. (a) Specific discharge capacity and coulombic efficiency of 25 nm TiO_2, in 1 mol dm^{-3} $AlCl_3$/1 mol dm^{-3} KCl, measured at specific currents between 0.2 to 2.0 A g^{-1}. (b) Potential profiles of TiO_2 at 0.2, 0.5 and 2.0 A g^{-1}.

Cycling was also performed to a given charge input capacity. A charge input of 16 mA h g^{-1} was chosen for electrodes using 25 nm TiO_2, with a C-rate of 10 C corresponding to a current of 158.3 mA g^{-1}, see Figure 5.4. Performance remains similar between the cycling regimes that use a potential limit (i.e. -1.1 V) or a capacity limit (i.e. 16 mA h g^{-1} input). From 10 C to 20 C, discharge capacity and coulombic efficiency increase from 14.4 mA h g^{-1} to 15.1 mA h g^{-1} and 90.8% to 95.1%.

Between 20 C and 180 C, discharge capacity and coulombic efficiency increase more steadily to 15.8 mA h g^{-1} and 99.4%. Figure 5.4 (b) shows the minimum potential reached upon charge decreasing from -1.01 V to -1.10 V. Given the more negative potentials reached during cycling at higher C-rates, a higher rate of H_2 evolution could be expected. However, coulombic efficiency increases despite the more negative potentials reached at higher C-rates, suggesting that H_2 evolution is not the primary cause of self-discharge at lower specific currents.

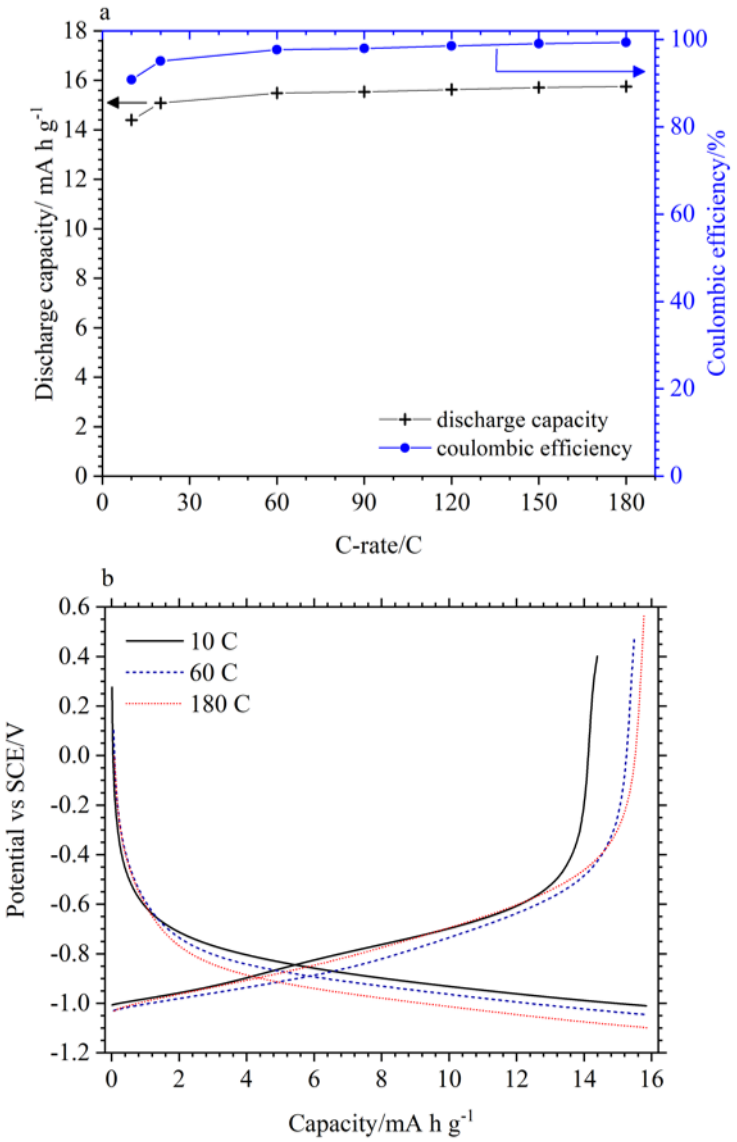

Figure 5.4. (a) Specific discharge capacity of 25 nm TiO_2 cycled at C-rates between 10 C and 180 C with corresponding potential profiles given in (b). 10 C = 158.3 mA g^{-1} in order to charge electrodes to 16 mA h g^{-1} in 360 s.

Similar tests regimes were performed on 5 nm TiO_2 electrodes. Figure 5.5 shows its response to cycling at various specific currents, with Figure 5.6 giving its response to cycling at various C-rates with a 20.0 mA h g^{-1} capacity input. Figure 5.5 (a) shows the specific discharge capacity and coulombic efficiency of 5 nm TiO_2 cycled at specific currents between 0.2 and 10.0 A g^{-1} with Figure 5.5 (b) giving the corresponding cycle profiles at 0.2, 1.0 and 8.0 A g^{-1}. As previously seen, 5 nm TiO_2 produces a slightly larger capacity cycled to -1.0 V vs SCE than 25 nm TiO_2 cycled to -1.1 V vs SCE. A maximum discharge capacity of 21.4 mA h g^{-1} is measured at 0.2 and 0.5 A g^{-1} though coulombic efficiency is 90.3% at 0.5 A g^{-1} compared to 80.7% at 0.2 A g^{-1}. Discharge capacity decreases almost linearly with increasing specific current, being 19.8 mA h g^{-1} at 2.0 A g^{-1}, 14.7 mA h g^{-1} at 8 A g^{-1} and 12.5 mA h g^{-1} at the highest specific current of 10.0 A g^{-1}.

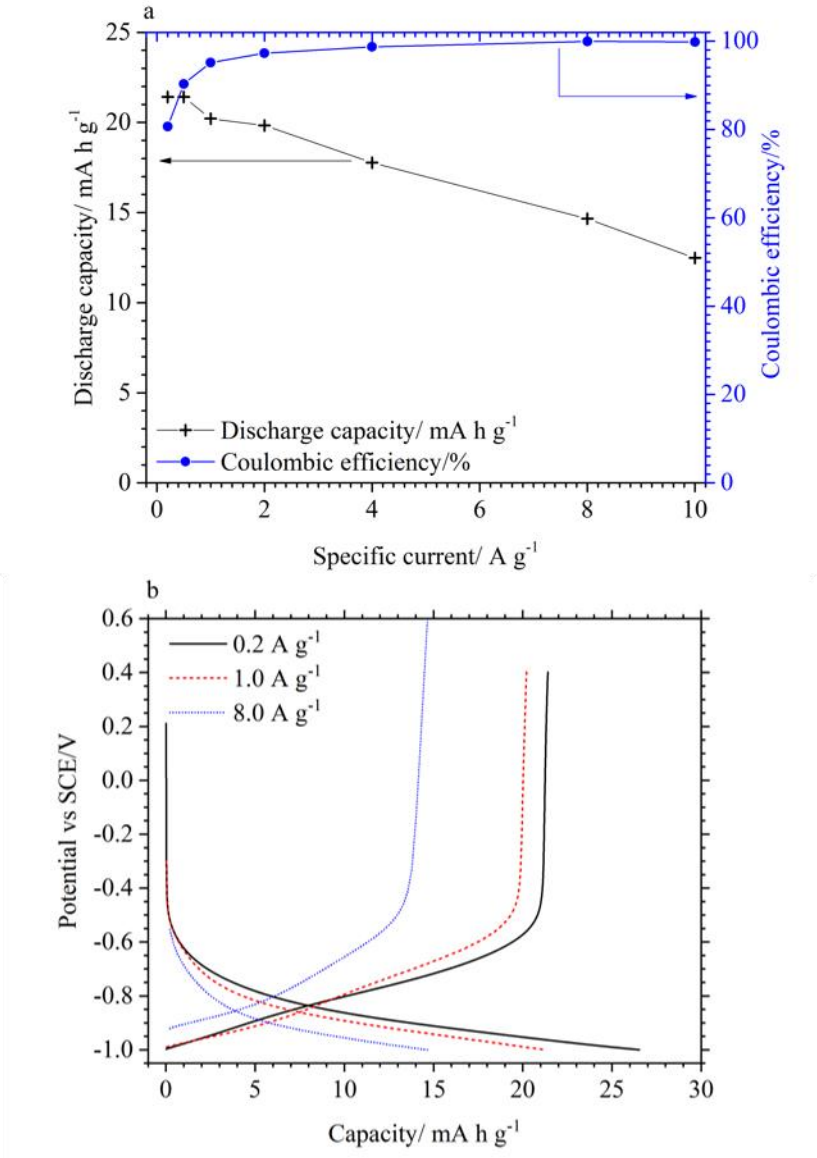

Figure 5.5. (a) Specific discharge capacity and coulombic efficiency of 5 nm TiO_2, in 1 mol dm^{-3} $AlCl_3$/1 mol dm^{-3} KCl, measured at specific currents between 0.2 to 10.0 A g^{-1}. (b) Potential profiles of TiO_2 at 0.2, 1.0 and 8.0 A g^{-1}.

As with 25 nm TiO_2, using a capacity limit over a voltage limit results in broadly similar performance. Here, a 20.0 mA h g^{-1} input was used with a 10 C C-rate equivalent to a current of 0.2 A g^{-1} for 360 s during charge. Discharge capacities and coulombic efficiencies measured at C rates between 5 C and 360 C are given in Figure 5.6. A coulombic efficiency and discharge capacity of 78.9% and 15.7 mA h g^{-1} are achieved at 5C, increasing to 96.7% and 19.3 mA h g^{-1} at 60 C. At 360 C, which corresponds to a specific current of 7.2 A g^{-1}, coulombic efficiency and discharge capacity are 99.0% and 19.8 mA h g^{-1} respectively.

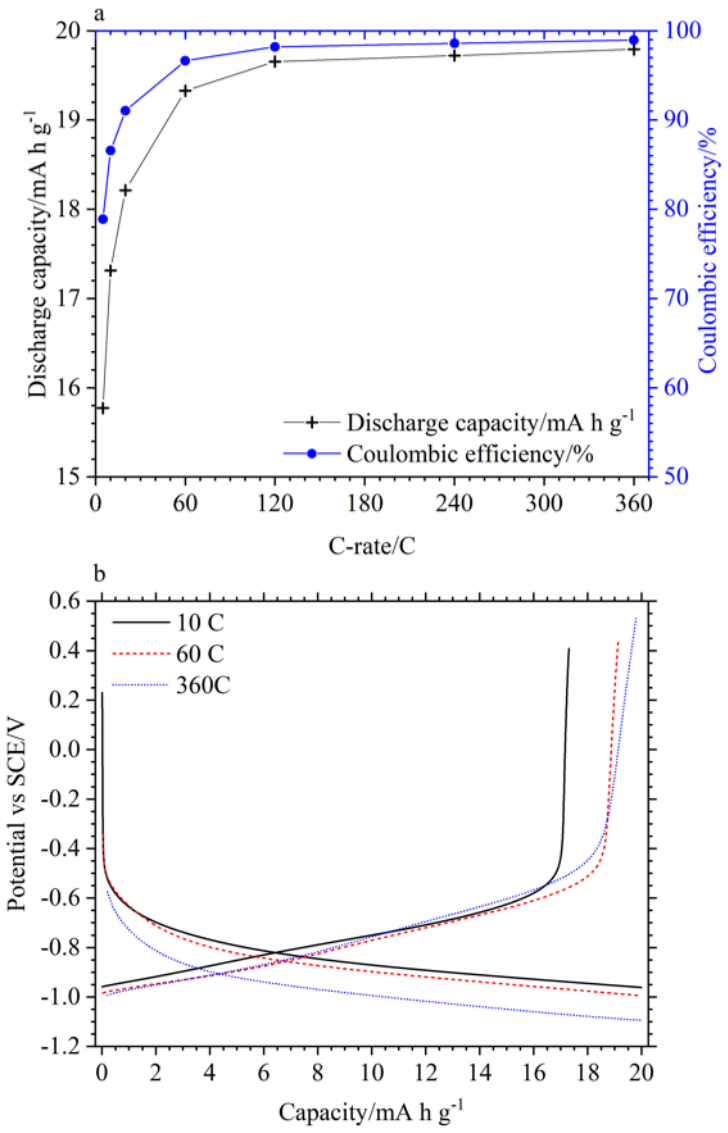

Figure 5.6. (a) Specific discharge capacity of 5 nm TiO_2 cycled at C-rates between 5 C and 360 C with corresponding potential profiles given in (b). 10 C = 0.20 A g^{-1} in order to charge electrodes to 20 mA h g^{-1} in 360 s.

Overall, 5 nm TiO_2 powder demonstrated higher capacities and rate capability than electrode manufactured using 25 nm TiO_2 powder, maintaining a discharge capacity of 14.7 mA h g^{-1} with

>99.9% coulombic efficiency at the high specific current of 8 A g^{-1}. A 19.8 mA h g^{-1} discharge capacity was measured when cycled at 360 C, resulting in a minimum potential of -1.09 V, though coulombic efficiency was marginally lower at 99.0%. However, both 5 nm and 25 nm TiO_2 electrodes showed considerably lower coulombic efficiencies at lower specific currents and C-rates. The origins of this low coulombic efficiency at low currents will be explored in section 5.3.

However, despite capacity- and potential-limited cycling giving broadly similar performance, plotting coulombic efficiency against discharge time shows the sensitivity of TiO_2 to charge input (and therefore potential) at lower specific currents. Figure 5.7 shows the coulombic efficiency of the 5 nm TiO_2 electrode as a function of discharge time, when cycled using both C-rates and specific currents to a minimum potential of -1.0 V. That is, the electrode was either charged to -1.0 V at various specific currents, before being discharged, or was charged at specified C-rates to variable minimum potentials with a charge input of 20 mA h g^{-1}. At 10 C, coulombic efficiency is 86.6% resulting in a discharge time of 311.8 s. At the same specific current of 0.2 A g^{-1} but with a potential limit of -1.0 V, a discharge capacity of 21.4 mA h g^{-1}, over 385.4 s, is obtained with a lower coulombic efficiency of 80.7%. However, cycling at 5 C results in a coulombic efficiency of 78.9% despite a discharge time of 568.1 s. This suggests how a voltage limit may not be sufficient and that a capacity limit may be required at lower specific currents in order to maximise coulombic efficiency.

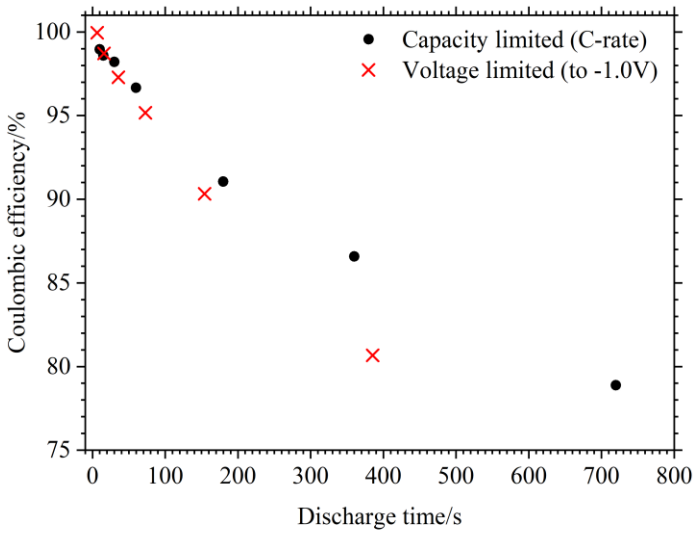

Figure 5.7. Comparison of coulombic efficiency of a TiO_2 electrode cycled using two methods. Firstly, with a 20 mA h g^{-1} charge input at various C-rates where the minimum potential varies and secondly, at various specific currents to a minimum of -1.0 V vs SCE where the charge input varies.

The capacities quoted in this section are generally lower than those reported in the literature, though the rate capabilities measured where capacities range from 15 mA h g^{-1} to 250 mA h g^{-1} [133, 135-137]. However, the rate capabilities measured are higher with Lahan et al reporting the next highest of 6 A g^{-1} [137] . In addition, the electrodes described in this section are larger with higher mass loadings than reported. The use of commercially available powders also has implications for easier electrode manufacture scale-up at low cost. In addition to this, a comparison of TiO_2 powders with different sizes and specific surface areas resulted in relatively minor differences to capacity and efficiency, demonstrating that improving performance will not simply be a case of reducing particle size or increasing surface area. Furthermore, the explicit presentation of coulombic efficiency allows the conclusion that coulombic efficiency decreases with decreasing specific currents and cycle rates, an important omission in previous reports on TiO_2 [133, 135-137]. Further study of this property will be presented in section 5.3, while methods to further improve rate capability as well as capacity and coulombic efficiency will be explored in Chapter 6 and Chapter 7.

5.1.3 Extended cycling and degradation

Extended cycling was also performed on both 25 nm and 5nm TiO_2 using both C-rates and capacity limits as well as specific currents with a potential cut-off during charge. Figure 5.8 shows 25 nm TiO_2 to have an initial discharge capacity and coulombic efficiency of 15.7 mA h g^{-1} and 99.4% that remains stable up to 4000 cycles, when cycled at 120 C, where discharge capacity and coulombic efficiency are measured at 15.3 mA h g^{-1} and 96.6%. Electrolyte replacement after 2000 cycles marginally improves performance. This is likely due to exposure to air or O_2 evolution from the CuHCF counter electrode and will be discussed in section 5.3.1. Between cycles 4000 and 5000, a decrease in coulombic efficiency and discharge capacity is observed.

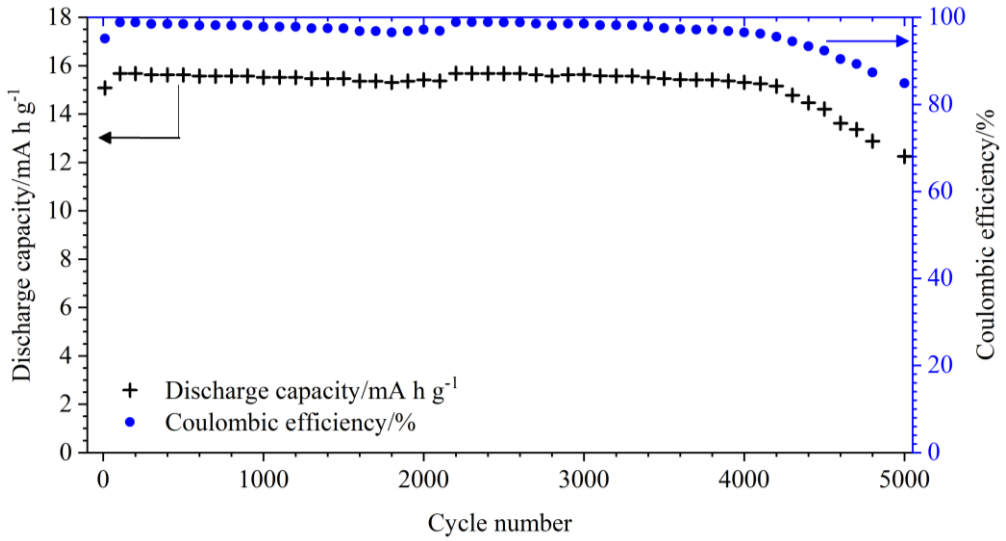

Figure 5.8. Extended cycling of a 25 nm TiO_2 electrode at 120 C (1.9 A g^{-1} charge for 30 s) in 1 mol dm^{-3} $AlCl_3$/1 mol dm^{-3} KCl.

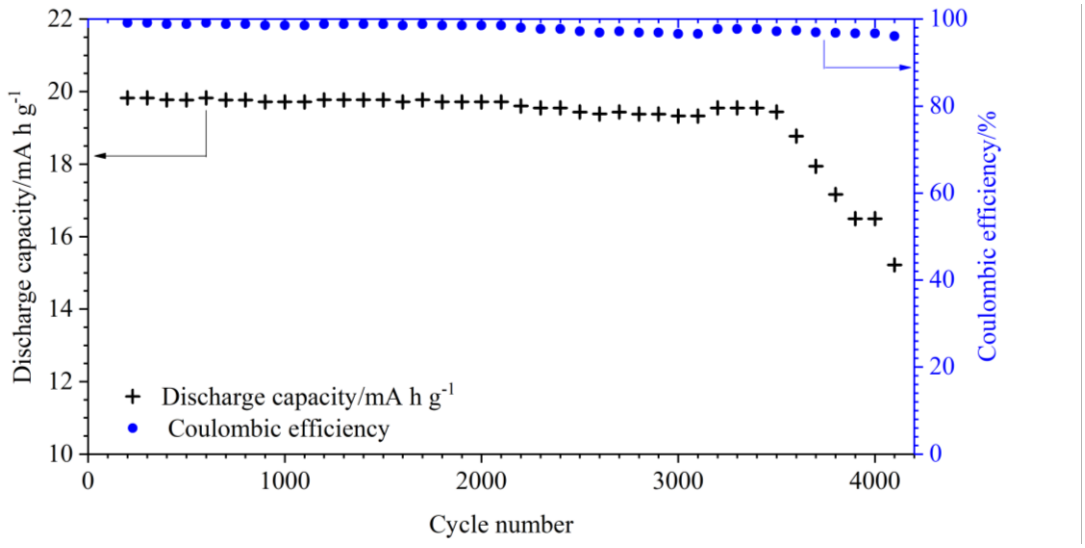

Figure 5.9. Extended cycling of TiO_2, manufactured from 5 nm powder, at 120 C (0.2 A g^{-1} charge for 30 s) in 1 mol dm^{-3} $AlCl_3$/1 mol dm^{-3} KCl.

Figure 5.9 shows the cycling of 5 nm TiO_2 at 100 C (2.0 A g^{-1}) in 1 mol dm^{-3} $AlCl_3$/1 mol dm^{-3} KCl. With charge capacity set at 20.0 mA h g^{-1}, coulombic efficiency decreased from 99.1% at cycle 100 to 98.6% at cycle 2200. By cycle 3500, discharge capacity was 19.4 mA h g^{-1}, giving a coulombic efficiency of 97.2%. At ca. cycle 3500, discharge capacity begins to decrease due to reaching a set potential limit of -1.05 V vs SCE, dropping to 15.8 mA h g^{-1} at cycle 4100 with a coulombic efficiency of 96.1%.

Furthering this, a separate 5 nm electrode was cycled to -1.0 V. Voltage limits of +0.4 V to -1.0 V vs SCE and cycling at 2.0 A g^{-1} resulted in a discharge capacity of 21.1 mA h g^{-1} and coulombic efficiency of 98.8% during the 100th cycle (the initial 100 cycles were performed at various specific currents). Capacity dropped to 18.2 mA h g^{-1} by the 1000th cycle with coulombic efficiency being 99.6%. Discharge capacity continued to degrade with cycling, falling to 12.7 mA h g^{-1} by the 6000th cycle. Coulombic efficiency remained between 99.0 and 99.6% from the 300th cycle onwards. Allowing approximately 5000 cycles, TiO_2 shows reasonable cycle life. Certainly, the cycle life is considerably greater than previously reported in the literature for TiO_2 in aqueous Al^{3+}-containing electrolyte. The second highest cycle life was reported by He et al [135] with their black TiO_2 nanoleaves showing an 8.4% capacity fade after 300 cycles. Indeed, the higher capacities reported for other TiO_2 may have been the result of extended potential windows, which will increase capacity but may have been detrimental to stability and cycle life. This possibility is briefly explored in Chapter 6. Nevertheless, while a cycle life of ca. 5000 is reasonable, the relatively low capacities would require an order of magnitude increase to the cycle life to be useful for high rate applications e.g. supercapacitors can generally be cycled over 100,000× and even lower cost, high energy Li-ion chemistries can have cycle lives above 1000.

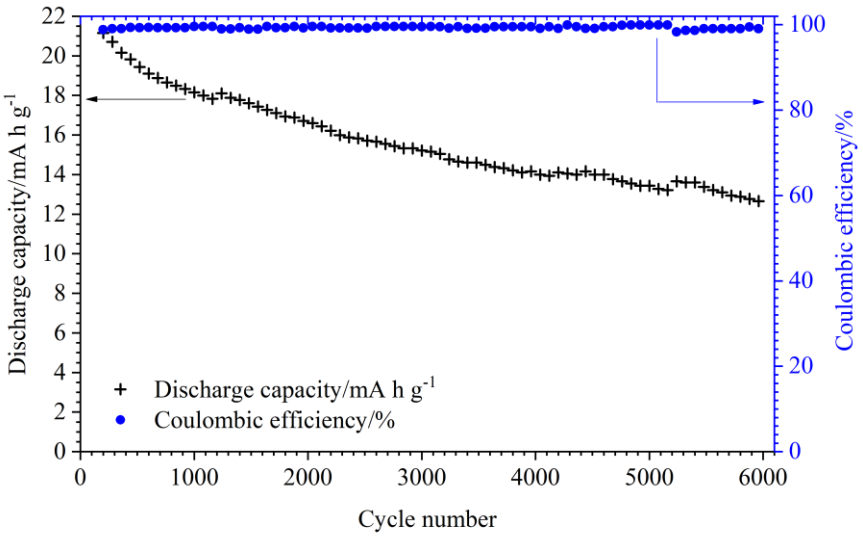

Figure 5.10. Extended cycling of 5 nm TiO_2 at 2.0 A g^{-1} between +0.4 to -1.0 V vs SCE in 1 mol dm^{-3} $AlCl_3$/1 mol dm^{-3} KCl. The initial 200 cycles were performed at various specific currents between 0.2 A g^{-1} to 10.0 A g^{-1}.

Potential causes of degradation were probed through ex-situ XRD analysis and SEM imaging. Figure 5.11 (a) and (b) present SEM images of the surface of a pristine electrode (prior to charge/discharge cycling) and (c) and (d) show SEM images after the 5000 cycles presented in Figure 5.8. Figure 5.11

(a) shows the electrode to have a relatively even coating and particle distribution. 50000x magnification in Figure 5.11 (b) allows individual particles to be revealed to have diameters of approximately 20-30 nm. A range of particle and particle agglomerations are observed up to approximately 100 nm, though it is not possible to distinguish between TiO_2 and carbon black. Figure 5.11 (c) shows the appearance of cracks after extensive cycling. This could be due to H_2 evolution at the current collector, creating bubbles and pushing off active electrode material. H_2 evolution within the active electrode can also not be ruled out. Cracking may also be due to repeated expansion/contraction of TiO_2 due to possible Al^{3+} insertion/extraction, however, post-mortem XRD analysis suggests this may not be the case. Additionally, the low specific capacity and high rate capability point toward a surface limited mechanism as opposed to a bulk process. Figure 5.11 (d) also shows signs of flocculation after cycling, while the border definition of particles becomes less clear. This may indicate dissolution of the electrode into the electrolyte upon repeated cycling.

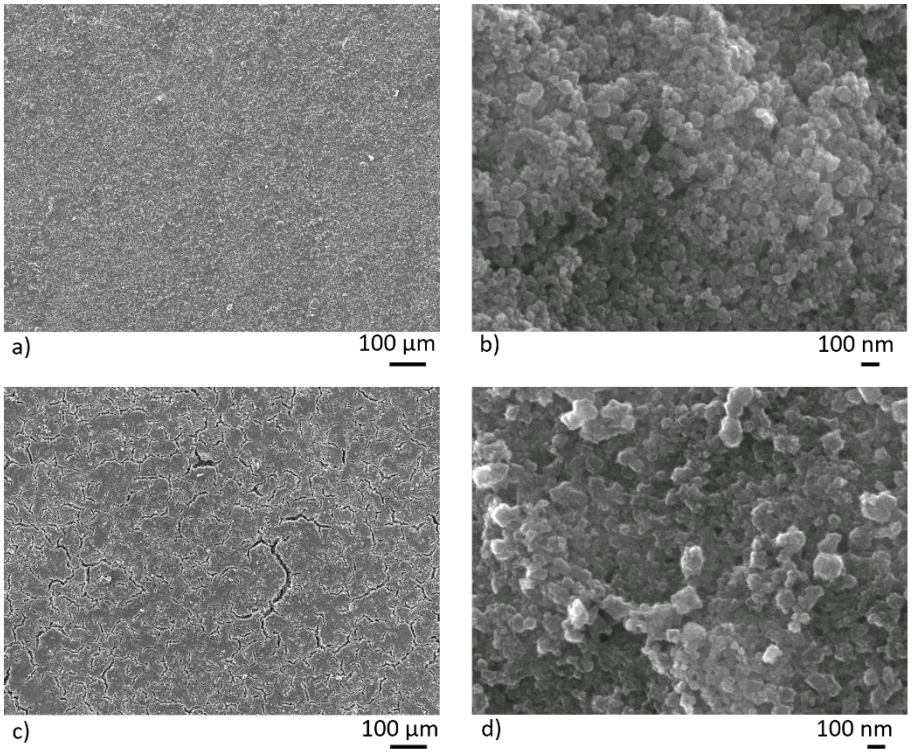

Figure 5.11. SEM images of two 25 nm TiO_2 electrodes. (a) and (b) are of a pristine electrode with (c) and (d) taken from an electrode that had undergone 5000 cycles (presented in Figure 5.8). Top and bottom images are at 100× and 75000× magnification respectively.

XRD patterns between 2θ = 20° to 2θ = 80° from the same two electrodes are presented in Figure 5.12. The Miller indices (004) and (200) were used to calculate the crystal lattice parameters of the tetragonal anatase TiO_2 powders via equation (5.1). Well-defined peaks correspond well with anatase TiO_2. Since these peaks are effectively unchanged after 5000 cycles, the bulk crystallinity of TiO_2 is determined to be unaffected throughout extended cycling. Crystal lattice parameters a and c were calculated to be 3.787 nm and 9.513 nm for the pristine electrode powder and 3.789 nm and 9.512 nm for the cycled electrode powder. Differences of 0.001 nm and 0.002 nm are unlikely to be experimentally significant and coupled with the pattern above indicates a lack of phase or lattice parameter change during extended cycling. While this does not explicitly rule out the intercalation of Al^{3+} within the interstitial sites of anatase TiO_2, it presents further evidence of a surface charge storage mechanism.

$$\frac{1}{{d_{hkl}}^2} = \frac{h^2 + k^2}{a^2} + \frac{l^2}{c^2} \tag{5.1}$$

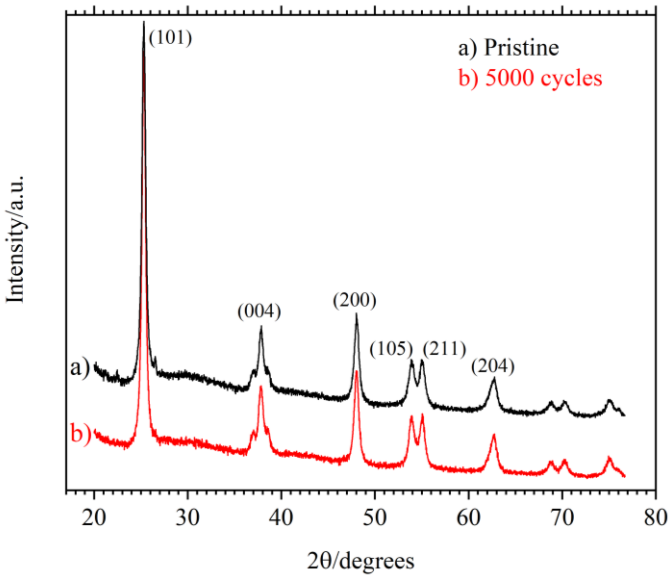

Figure 5.12. XRD patterns of two 25 nm TiO_2 electrodes: pristine (a) and after 5000 cycles (b) at 2.0 A g^{-1} in 1 mol dm^{-3} $AlCl_3$/1 mol dm^{-3} KCl.

5.2 Charge storage mechanisms

Initial cyclic voltammetry (CV) scans of TiO_2 (Figure 3.4 and Figure 4.1), in $AlCl_3$, gave rise to profiles with prominent peaks associated with redox reactions. Logically, the peaks have previously been attributed to a change in the Ti^{4+}/Ti^{3+} redox state along with the concomitant insertion/extraction of Al^{3+} [133, 134, 183, 184]. However, reversible intercalation of Al^{3+} into the crystal structure of

anatase TiO_2 should be difficult due to the high charge density of Al^{3+} while evidence for intercalation of Al^{3+} is still relatively sparse. CV scans in the literature have also shown cathodic peaks to occur at potentials more negative than the minimum cut-off potential used during constant current cycling. Furthermore, the relatively low capacities measured in this work, along with the high specific currents and taking into account the small particle sizes used, a capacitive or surface storage mechanism cannot be ruled out. To probe this further, voltamogramms were taken at various scan rates, ranging from 2 to 16 mV s^{-1}, in 1 mol dm^{-3} $AlCl_3$, between the potentials of 0.0 V to -1.3 V vs SCE.

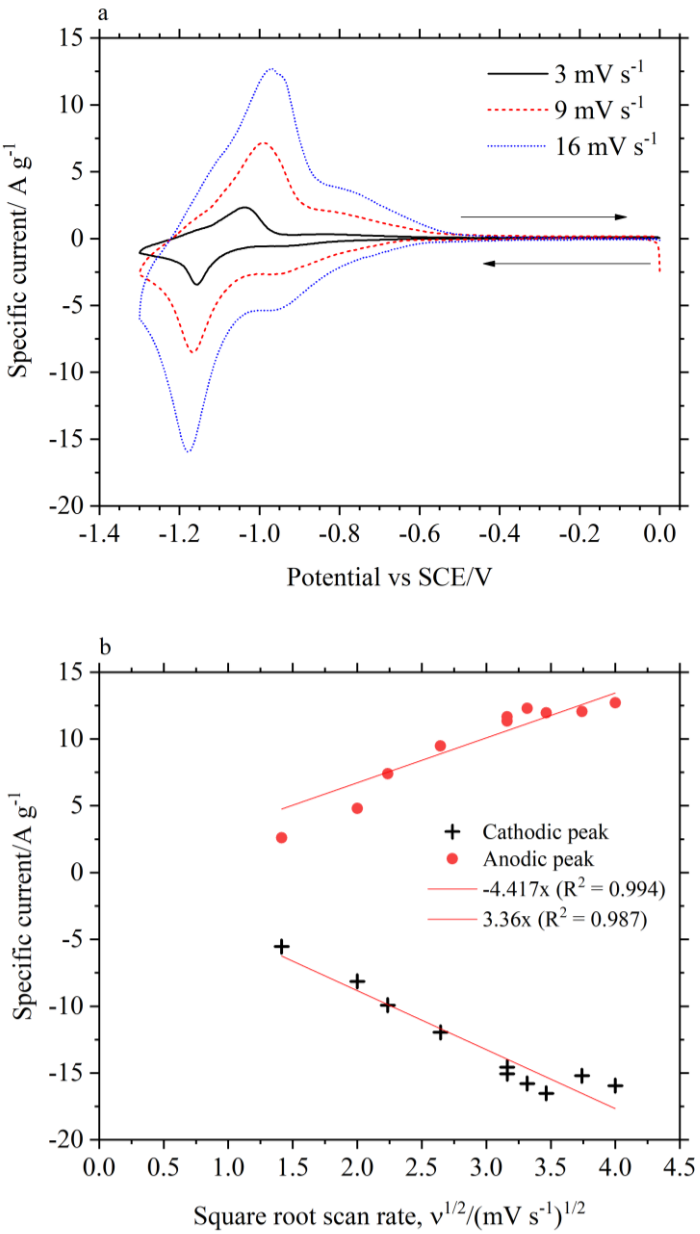

Figure 5.13. (a) CV scans of 5 nm TiO_2 in 1 mol dm^{-3} $AlCl_3$ at 3, 9 and 16 mV s^{-1} against an SCE reference. (b) Plot of the peak currents at scan rates between 2 to 16 mV s^{-1} against the square root of the scan rates.

Figure 5.13 (a) shows the CV scans at 3, 9 and 16 mV s^{-1}. The profile shapes at these three scan rates closely resemble each other. Between 0 V to -0.5 V, effectively no current was measured. During the cathodic sweep, current curves down between -0.55 V to -0.95 V where there is a brief plateau till ca. -1.1 V, where current curves down to a prominent peak between -1.15 V and -1.20 V vs SCE. At 3 mV s^{-1}, the reverse sweep gives rise to a prominent peak at -1.05 V. The position of this peak becomes more positive with increasing scan rate with peak position being approximately -0.95 V at 16 mV s^{-1}. As with the cathodic sweep, the anodic sweep gives rise to a slight shoulder and plateau – between ca. -0.9 V and -0.75 V, when current drops steadily to zero at approximately -0.5 V. Figure 5.13 (b) gives the peak currents against the square root of the scan rates. A linear fit, with an x-y intercept set to zero, shows there is an approximately linear relationship between the measured current and square root of the scan rate for both cathodic and anodic sweeps. A linear relationship suggests a diffusion-limited process, and is often seen in intercalation electrodes, with the measured current limited by the solid-state diffusion (intercalation) of the cation through the electrode. This may be the case for TiO_2 and Al^{3+}, given the use of a relatively high concentration electrolyte, which should negate the possibility of a reaction being limited by the diffusion of Al^{3+} through the electrolyte to the electrode surface. It is also possible to use the data in Figure 5.13 to estimate the diffusion co-efficient of Al^{3+} within the electrode, via the Randles-Sevcik equation, given by equation (5.2), where $I_p =$ peak current (A g^{-1}), $v =$ scan rate (V s^{-1}), $z =$ electrons transferred per redox event, $A =$ surface area (cm^2 g^{-1}), $c =$ concentration (mol cm^{-3}).

$$\frac{I_p}{v^{1/2}} \approx 2.7 \times 10^5 z^{3/2} A c D^{1/2} \tag{5.2}$$

A calculation of the diffusion co-efficient here requires assumptions/estimations to be made for the values of z, A, and c. Given the tri-valency of Al^{3+}, n is assumed to be 3, A is estimated as 2.5×10^6 cm^2 g^{-1} as given by the manufacturers calculation of surface area via N_2 adsorption and c is estimated to be 1.3×10^{-2} mol cm^{-3} by assuming a maximum concentration of one Al^{3+} per unit cell of anatase TiO_2, which has a volume of approximately 1.37×10^{-22} cm^3. Using these values along with an estimation of $I_p/v^{1/2}$ of 30 A g^{-1} $V^{-0.5}$ $s^{0.5}$, from the positive gradient in Figure 5.13 (b), gives a diffusion co-efficient of approximately 4.3×10^{-19} cm^2 s^{-1}. This is lower than the ~10^{-12} and 10^{-13} cm^2 s^{-1} calculated by Kazazi et al for their TiO_2 nanospheres and P25 respectively using 1 mol dm^{-3} $AlCl_3$ electrolyte [136]. However, their small electrode geometry of < 1 cm^2, compared to ca. 7 cm^2 in this work, will increase D, while their estimations of z, A, and c were not detailed. Comparing to

the diffusion of Li^+, the estimates for the diffusion co-efficient through TiO_2 range from 10^{-9} to 10^{-16} $cm^2\ s^{-1}$ [185-188], though the solid-state diffusion of Li^+ would be expected to be faster and Al^{3+} slower, due to its high charge density and large solvation sphere (the range in magnitude of co-efficients result from the range of techniques used e.g. CV, chronoamperometry, EIS, in-situ NMR as well as variations in electrolyte, electrode materials, state-of-charge and diffusion direction and therefore highlights the difficulty of comparing diffusion co-efficients between studies). Nevertheless, the comparatively slow co-efficient of $\sim 10^{-19}$ contradicts the high rate capability demonstrated earlier in Section 5.1 and suggests that either bulk intercalation is not the dominant charge storage mechanism or that the assumed/estimated values of z, A, and c are inaccurate. For example, the electrochemically active surface area of the manufactured TiO_2 electrodes is likely to be considerably lower than the specific surface area advertised by the 5 nm-TiO_2 powder manufacturer which was used. Decreasing A to 2.5×10^5 $cm^2\ g^{-1}$ gives a more reasonable diffusion co-efficient of 4.3×10^{-17}.

Further investigation of the charge storage mechanism was performed by limiting the potential range of the CV scans. This was especially important given the cathodic peaks in the CV scans shown in Figure 5.13 are observed to be at more negative potentials than reached during the constant current cycling seen in previous sections, as was also seen in the literature. Figure 5.2 (b) in section 5.1 showed how coulombic efficiency began to decrease dramatically, from 90.2% to 61.3%, once cycled to -1.1 V at 1 A g^{-1} rather than -1.0 V vs SCE. Cycling to -1.2 V resulted in failure of the electrode. Scans were therefore taken in the potential range of 0 V to -1.0 V in order to more closely align with the potential ranges used for constant current cycling. Scans were performed on an electrode, in 1 mol dm^{-3} $AlCl_3$, at scan rates between 2 and 100 mV s^{-1}. Figure 5.14 (a) shows the profiles measured at 2, 5, 10, 20, 40 and 100 mV s^{-1}. As expected, there are no discernible redox peaks. For capacitive electrodes, measurements taken at different scan rates should fall onto a single profile once the CVs are normalised by scan rate. During the cathodic sweep, all scan rates give rise to the beginnings of a broad reduction wave, with current increasing at around -0.60 V vs SCE. However, at 10 mV s^{-1} the reverse anodic sweep gives rise to a small peak between -0.95 V and -0.90 V, while a second shoulder is observed at around 0.65 V. These details become less prominent with increasing scan rate. At 100 mV s^{-1}, the anodic sweep gives rise to a very broad, almost rectangular oxidation profile. Figure 5.14 (a) shows that current, at 100 mV s^{-1}, reaches a maximum of 10.6 A g^{-1} at -0.77 V before curving down to 7.5 A g^{-1} at -0.52 V, where current drops more quickly to nearly 0 A g^{-1} at -0.4 V vs SCE. Figure 5.14 (b) shows scans at a number of rates divided by the given scan rate used. It can be seen that the CVs do not fall onto a single profile, while there are variations in the shape of the CVs obtained. This suggests that the electrode is not entirely capacitive, though surface charge storage may still be present.

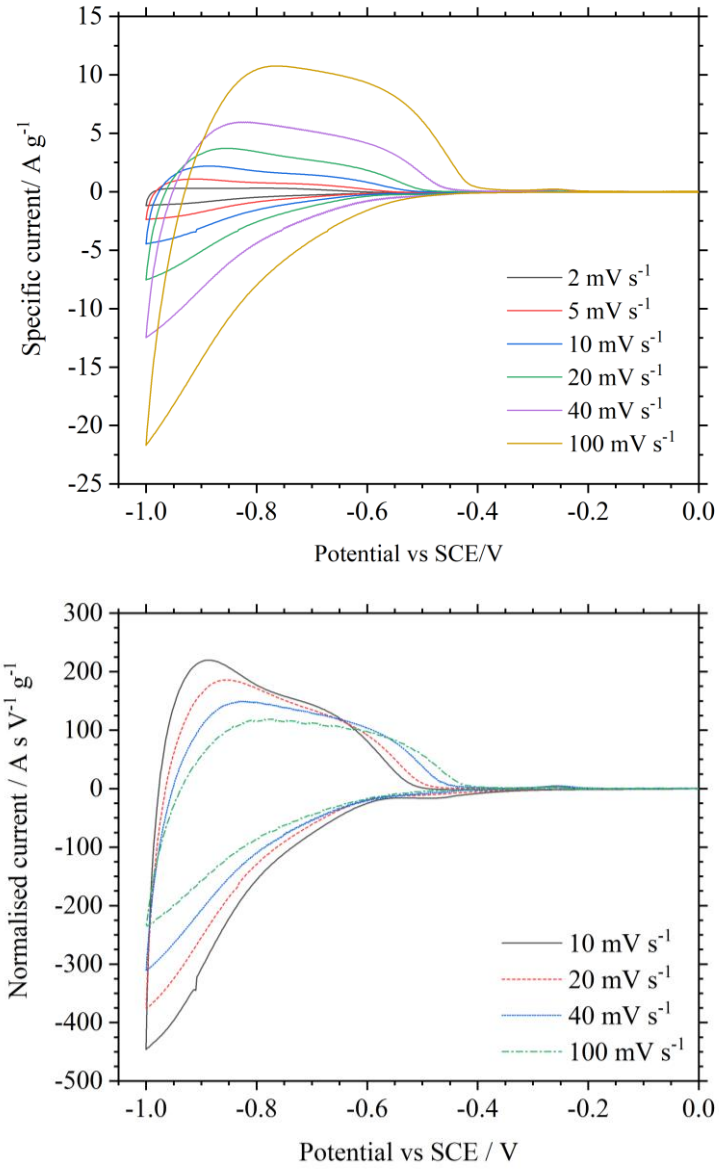

Figure 5.14. (a) CV scans of 5 nm TiO_2, in 1 mol dm^{-3} $AlCl_3$, between potentials of 0 V to -1.0 V vs SCE at scan rates ranging from 2 mV s^{-1} to 100 mV s^{-1}. (b) shows the same data with profiles normalised by scan rate.

In addition, electrode stability is considerably enhanced in this narrower potential range, i.e. greater degradation of the scan profile is observed when the potential range is widened to -1.3 V. Figure 5.15 (a) shows the profile from TiO_2 during the 10^{th}, 30^{th} and 80^{th} scan at 10 mV s^{-1} between 0.0 V to -1.0 V vs SCE. The profiles can be seen to be nearly identical irrespective of scan number. The data shown in Figure 5.14 was taken between the 10^{th} and 30^{th} scan. Figure 5.15 (b) presents the profiles measured from TiO_2 at the 10^{th}, 18^{th} and 25^{th} cycles when swept between the extended potential range of 0.0 V to -1.3 V vs SCE. Between the 10^{th} and 18^{th} cycle there is a small reduction

in the cathodic peak, from -13.0 A g^{-1} to -11.8 A g^{-1}, while the anodic peak potential shifts from -1.03 V, during the 10th scan, to -0.97 V vs SCE during the 18th. Data shown in Figure 5.13 was taken between the 10th and 18th scan. Clearly, greater stability over scan number is achieved by limiting the potential range, though further work could be done to investigate the relationship and optimum operational voltage range for capacity and cycle life.

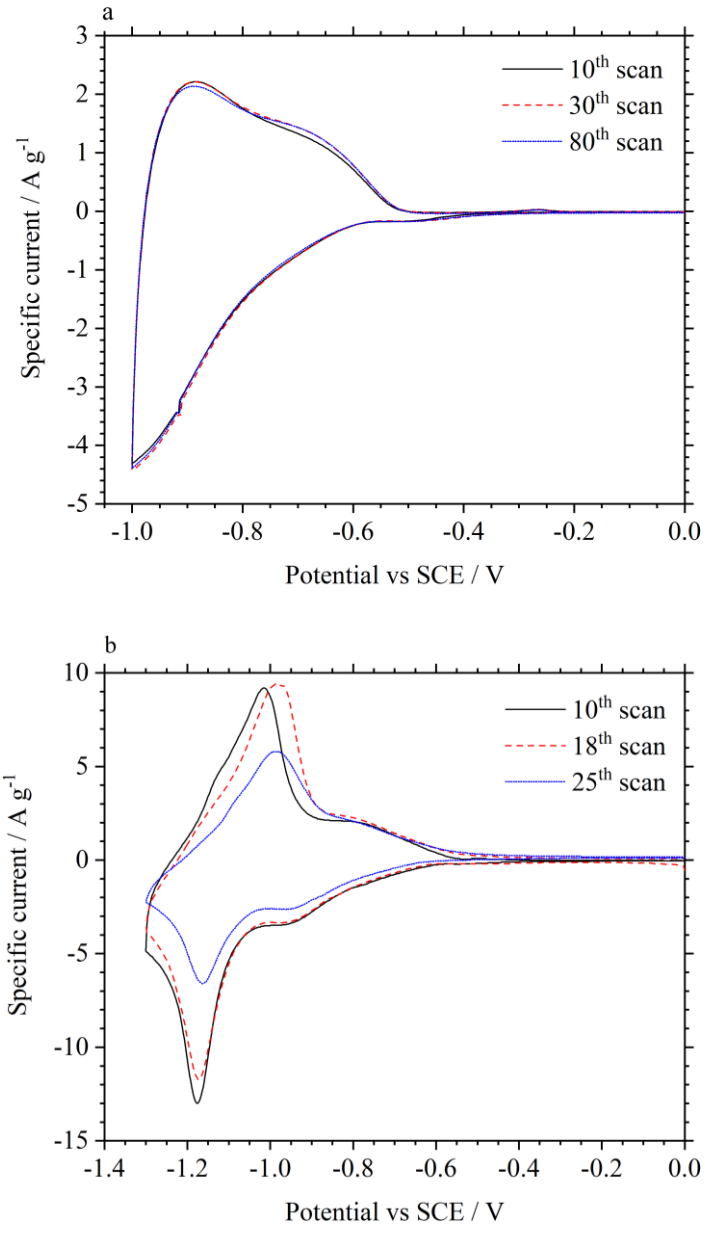

Figure 5.15. Stability of TiO_2 CV profiles with scan number measured in 1 mol dm^{-3} $AlCl_3$ at 10 mV s^{-1} between 0 V to -1.0 V vs SCE (a) and 0 V to -1.3 V vs SCE (b).

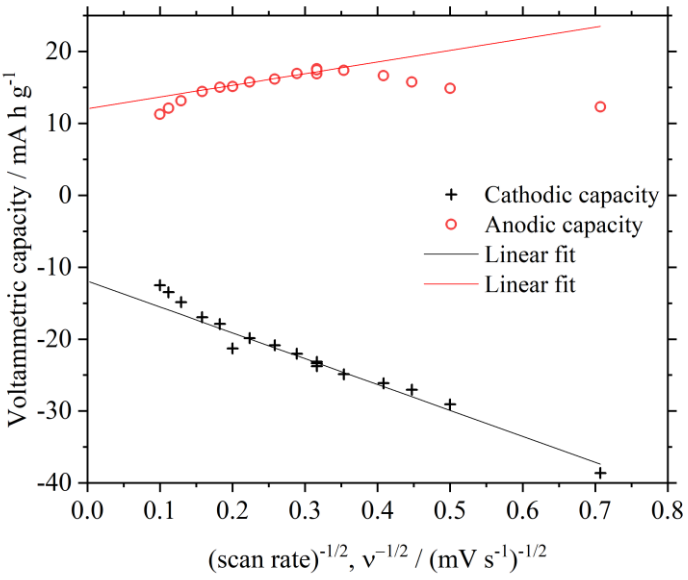

Figure 5.16. Capacity, calculated from CV scans in 1 mol dm^{-3} $AlCl_3$ between 0 V to -1.0 V vs SCE, plotted against the inverse of the square root of the scan rate, $\upsilon^{-1/2}$. Scan rates ranged between 2 mV s^{-1} to 100 mV s^{-1}.

Further analysis of the CV profiles can be performed by calculating the capacity of the electrodes at different scan rates and plotting against the inverse of the square root of the scan rate. This technique has previously been used in the literature with pseudocapacitive metal oxides, such as Nb_2O_5 or $NiCo_2O_4$, as well as conductive polymers [153, 189, 190]. It can provide an indication of charge storage arising from bulk vs surface mechanisms and to determine capacitive contributions from electrodes at a given scan rate and therefore time scales. The capacity of a purely capacitive or surface storage process should remain constant with scan rate, while a linear dependence of capacity against the inverse of the square root of the scan rate, $\upsilon^{-1/2}$, indicates a semi-infinite diffusion limited process. However, since surface storage mechanisms should still be present at high scan rates, extrapolation of the linear fit to 0 $(mV\ s^{-1})^{-1/2}$ gives a value of the capacity that would be present at an infinite scan rate and therefore the contribution of surface processes to the total measured capacity.

Figure 5.16 presents the integrated capacities measured from CV scans, between 2 mV s^{-1} to 100 mV s^{-1}, plotted against $\upsilon^{-1/2}$. For the cathodic charge input, the volumetric capacity is linearly proportional to $\nu^{-1/2}$ at scan rates up to 30 mV s^{-1}, 0.182 $mV^{-1/2}\ s^{1/2}$. Extrapolation of the linear fit to 0 $(mV\ s^{-1})^{-1/2}$ suggests a capacitive charge storage contribution of approximately 12 mA h g^{-1}. Therefore, at a scan rate of 10 mV s^{-1} for example, the capacitive contribution to capacity would be approximately 50%. The remaining charge could then be the result of a bulk process such as

intercalation. Alternatively, it could suggest that there are areas of the electrode, such as narrow pores, that are difficult to access. At scan rates above 30 mV s^{-1} (0.182 $mV^{-1/2}$ $s^{1/2}$), the charge vs $\upsilon^{-1/2}$ deviates from linearity, suggesting a change in the rate-limiting charge storage process or that charge storage is almost entirely dominated by a semi-infinite diffusion. At lower scan rates, between 2 to 30 mV s^{-1}, the extrapolation of the linear dependence of cathodic capacity vs $v^{-1/2}$, to approximately 12 mA h g^{-1}, suggests that there is mixed diffusion and surface limited charge storage. Given the low capacities, it is still unlikely that this diffusion limitation is a result of Al^{3+} intercalation through the crystal structure of anatase-TiO_2 but may instead be due to the limited diffusion of electrolyte and Al^{3+} through the pores of the electrode.

A similar trend is observed for anodic capacities with a linear dependence between 10 mV s^{-1} (0.316 $mV^{-1/2}$ $s^{1/2}$) to 30 mV s^{-1} giving rise to an infinite scan rate capacity of approximately 11.3 mA h g^{-1}. Measured capacity again deviates from this linear extrapolation at 40 mV s^{-1}. However, unlike during cathodic scans, the measured capacity begins to decrease at scan rates below 8 mV s^{-1}, suggesting a decrease in coulombic efficiency over longer time scales. This will be explored in section 5.3.

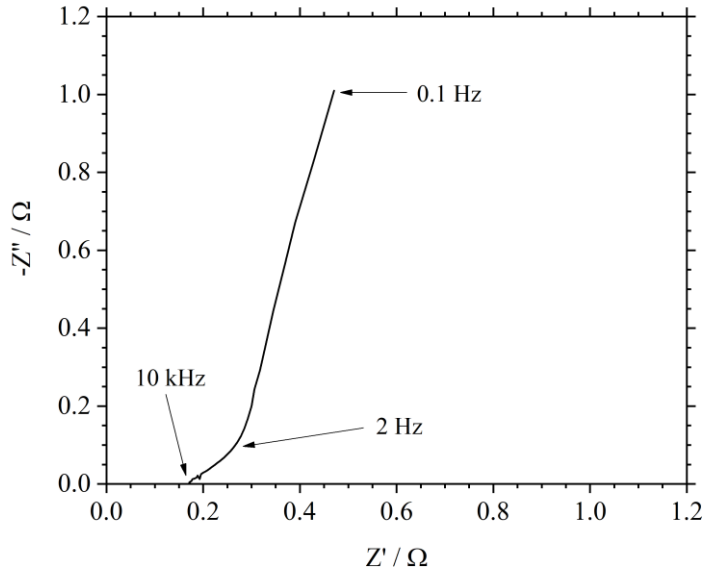

Figure 5.17. Nyquist plot of a TiO_2, in 1 mol dm^{-3} $AlCl_3$, electrode at OCP after being charged to -0.8 V, vs SCE, at 0.1 A g^{-1} and a 60 s potentiostatic hold at -0.8 V. A frequency range of 0.1 Hz to 10 kHz was used with an AC perturbation of 20 mV.

Evidence for possible capacitive or surface charge storage contributions can also be obtained through electrochemical impedance spectroscopy (EIS) with typical intercalation redox electrodes

and capacitive electrodes often providing distinct Nyquist plots. EIS was performed on a TiO_2 electrode with a 20 mV perturbation in 1 mol dm^{-3} $AlCl_3$. Measurements were performed on the electrode in a partially charged state in order to gain information on the charge storage mechanism at the relevant potential. The electrode was therefore charged to -0.8 V vs SCE at 100 mA g^{-1} before a potentiostatic hold at -0.8 V to ensure a stable electrode potential. EIS measurements were then taken at OCP between 0.1 Hz to 10 kHz. The potential decay due to self-discharge was assumed to be slow enough that EIS measurements were performed around a stable potential of approximately -0.8 V vs SCE. Figure 5.17 presents the resulting Nyquist plot. The equivalent series resistance is measured at 0.17 Ω, as represented by the intersection of the profile with the x-axis (real impedance). The plot shows an approximate 45° line, till ca. 0.275 Ω on the x-axis, recorded at ca. 2 Hz. This 45° line can be associated with a diffusion-limited process. Here, at frequencies lower than 2 Hz, the gradient increases to another straight line with a gradient >45°. A semi-circle between high-mid frequencies is often present in intercalation electrodes and associated with a charge transfer resistance. The lack of an obvious semi-circle here suggests either rapid charge transfer or a capacitive charge storage mechanism, which would be consistent with the relatively high rate capability observed so far. At low frequencies, the >45° line can be associated with a semi-infinite diffusion process and is often indicative of capacitive or surface controlled behaviour.

The galvanostatic, voltammetric and impedance spectroscopy data presents several options for the charge storage mechanisms of these TiO_2 electrodes in aqueous Al^{3+} electrolytes. The clear peaks at ca. -1.2 and -1.0 V during CV scans provide evidence of redox reactions. However, galvanostatic cycling was stable only up to -1.1 V vs SCE with no obvious end of state-of-charge. While a relative plateau is observed, between ca. -0.5 to -1.0 V (when cycled to -1.0 V), capacity remained considerably lower than is theoretically possible from an intercalation process, suggesting the possibility of a surface or capacitive charge storage mechanism within this potential range. Further CV scans were therefore performed in a limited potential range in order to discern whether a capacitive storage region exists. Previous studies have studied capacitance from anatase-TiO_2 in acidic aqueous electrolytes at negative potentials vs SCE. By limiting the swept potential between 0 and -1.0 v vs SCE, profiles were considerably more stable over the number of cycles. However, CV scans did not fall onto a single profile when plotting the normalised current response ($i/v^{-1/2}$) against scan rate, as would be expected from a purely capacitive electrode. Nevertheless, by calculating the voltammetric capacity and plotting against $v^{-1/2}$, a surface controlled contribution to charge storage was implied, indicating a mixture of surface and diffusion controlled charge storage. Again, given the relatively low capacity, it seems unlikely that this is the result of intercalation and might instead be attributed to the slow diffusion of electrolyte and Al^{3+} through the electrode structure.

5.3 Probing the low coulombic efficiency of TiO_2 at low currents

5.3.1 The effect of dissolved O_2 in the electrolyte

Previous publications on TiO_2 in aqueous electrolyte have shown low coulombic efficiencies without a discussion of potential causes. The charge/discharge voltage curves in the reports [133, 134, 136] demonstrate this. Figure 4.4 and Figure 4.5 in the previous chapter further demonstrate this in addition to showing that coulombic efficiency decreases at lower specific currents. There are a number of readily available explanations for this low coulombic efficiency.

- Dissolved O_2 in the electrolyte can result in the oxidation of Ti^{3+} back to Ti^{4+} resulting in a self-discharge process.
- H_2 evolution can take place at approximately -0.2 V vs SHE in pH 3 solution, though this will be hindered by kinetics and the strong solvation of water to Al^{3+}. Indeed, CVs show H_2 evolution at a more negative potential, lower than that of Al^{3+} insertion.
- The insertion of Al^{3+} into anatase TiO_2 may lead to the partial reduction of Ti^{4+} to Ti^{2+} which is electrochemically irreversible, though only Liu et al found Ti^{2+} to be present (via XPS) after cycling in Al^{3+} electrolyte.

Previous studies on $LiTiPO_4$, in an aqueous Li-ion cell using 1 mol dm^{-3} $LiSO_4$, have shown a marked improvement in stability with the removal of O_2 from electrolyte with poor stability attributed to the reoxidation of Ti^{3+} by dissolved O_2 [84]. To quantify the effect of dissolved oxygen on the coulombic efficiency of TiO_2, separate electrodes were cycled 1 mol dm^{-3} $AlCl_3$/1 mol dm^{-3} KCl* in the presence and absence of dissolved O_2 in the electrolyte. Dissolved O_2 was removed through the bubbling of dry N_2 (>99.95%), through a porous frit, into the electrolyte under vigorous stirring for at least 30 minutes. Figure 5.18 presents the capacity vs. electrode potential for separate electrodes cycled in de-oxygenated and aerated electrolytes. During the charge phase, the capacity vs voltage profile, from the two electrodes in de-oxygenated or aerated electrolytes are broadly similar. The potential starts at ca. 0.35 V vs. SCE at zero state of charge (SoC) and rapidly becomes more negative towards -0.6 V vs. SCE at ca. 1 mA h g^{-1} before the gradient flattens and steadily approaches -0.98

* While it was shown that electrochemical activity at TiO_2 was reliant on Al^{3+}, a mixed electrolyte was used as standard due to the improved performance of CuHCF in the presence of K^+.

V vs. SCE at 16 mA h g^{-1}. During the discharge process, however, there is a marked diffence between the aerated and de-oxygenated electrolytes. In the aerated electrolyte, the voltage is ca. 20 mV lower at the start of discharge compared to the de-oxygenated electrolyte. This difference widens to 100 mV after 10 mA h g^{-1} discharge, after which the voltage rapidly decays. The coulombic efficiency therefore increases from 77.2% to 95.1% at 20 C in aerated to de-oxygenated 1 mol dm^{-3} $AlCl_3$ containing electrolyte.

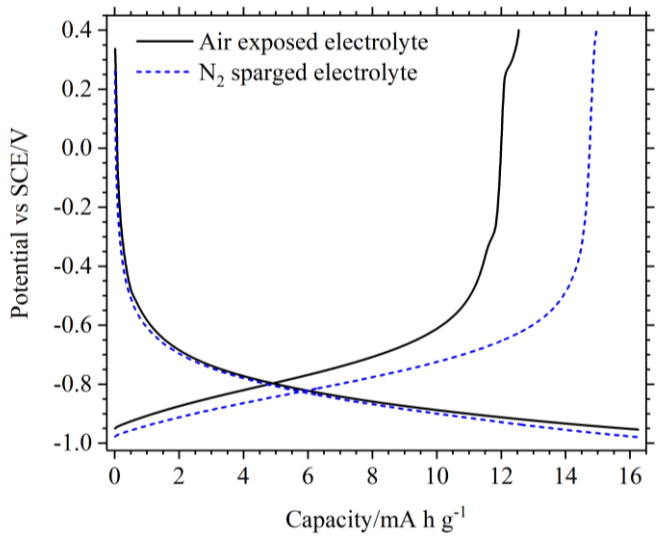

Figure 5.18. Typical charge/discharge profile of a TiO_2 electrode cycled at a 10 C rate in aerated (black) and de-oxygenated 1 mol dm^{-3} $AlCl_3$/1 mol dm^{-3} KCl electrolyte (blue-dash).

Clearly, reducing the dissolved O_2 content within the electrolyte results in a stark improvement in the coulombic efficiency of TiO_2. Therefore, it can be concluded that Ti^{3+} oxidation takes place and could be responsible for the low coulombic efficiency of TiO_2, in Al-ion cells, reported in the literature. However, while a coulombic efficiency increase was observed in N_2 purged electrolyte, it remains at <100%. Therefore, other self-discharge mechanisms must also be present and is explored further in section 5.3.3.

5.3.2 The effect of mass loadings

Increasing the mass loadings of electrode coatings is an important factor for scalable devices. Augustyn et al, in their review of pseudocapacitive oxide materials, quote a value of >1 mg cm^{-2} being used in order to demonstrate potential scalability of an electrode, with a value of 8 mg cm^{-2}

considered a high mass loading [153]. Throughout this section, electrode loadings were typically 2-3 mg cm^{-2}, however, some discrepancies in performance were observed as a result of varying mass loadings. Therefore, a number of 25 nm-powder electrodes were prepared with mass loadings of 1.3, 2.0, 3.6, 5.0 and 6.7 mg cm^{-2} and imaged in a scanning electron microscope (SEM) at 500x and 50000x magnification.

Figure 5.19 shows SEM images of electrodes with 3.6 and 6.7 mg cm^{-2} of active material. At 3.6 mg cm^{-2}, see figure 3a and 3b, an even particle distribution can be seen across the surface of the electrode while only very minimal cracking can be seen. At 6.7 mg cm^{-2}, see figure 3c and 3d, both a less even distribution and a greater level of cracking are evident. As such it was difficult to produce electrodes with higher mass loadings and further work would need to be performed on ink compositions and electrode preparation techniques, see Chapter 7.

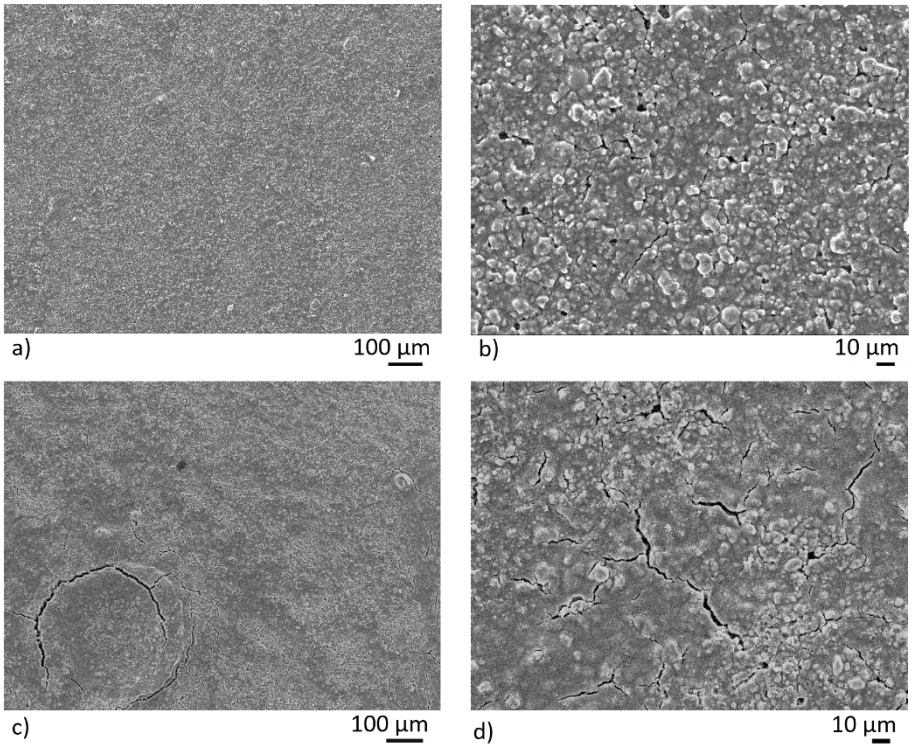

Figure 5.19. SEM images of an as-prepared 25nm-TiO_2 electrodes. Images a) and b) are of an electrode with a 3.6 mg cm^{-2} mass loading with c) and d) from a 6.7 mg cm^{-2} electrode.

Electrodes of various mass loadings were then cycled at C-rates between 10 C and 180 C. Figure 5.20 (a) gives the coulombic effiiency of the five electrodes as a function of C-rate. At 10 C, efficiency increases from 65.0% to 90.5% between the two electrodes with mass loadings of 1.3 mg cm^{-2} and 5 mg cm^{-2}, respectively. Coulombic efficiency then decreases to 86.8% at an electrode mass loading

of 6.7 mg cm^{-2}. At 60 C, coulombic efficiency increases from 89.0% to 97.6% between 1.3 mg cm^{-2} and 5.0 mg cm^{-2}, decreasing to 93.9% at at 6.7 mg cm^{-2}. At all C-rates, a general trend of increasing coulombic efficiency with increasing mass loadings up to 5.0 mg cm^{-2} can be observed. The improvements are most drastic at lower C-rates. Figure 5.20 (b) shows the potential profiles obtained from the 1.3 mg cm^{-2} and 5.0 mg cm^{-2} electrodes at a C-rate of 60 C. The obtained profiles are roughly similar between the two mass loadings with the 5.0 mg cm^{-2} electrode capable of a 15.5 mA h g^{-1} discharge, in contrast to the 14.2 mA h g^{-1} discharge capacity measured from the 1.3 mg cm^{-2} electrode.

The reason for improved performance up to 5.0 mg cm^{-2} is still unclear. However, given the time dependance of the improved performance (i.e improvements from higher mass loadings are greatest during the longer charge-discharge times), it may be possible that H^+ diffusion to the current collector is lowered in thicker electrodes, thus reducing H_2 evolution. It could also be possible that increasing the mass loading, up to a point, helps improve adhesion of electrode constituents to each other and the current collector. This would improve the conductivity of the electrode and may account for the improved performance at higher mass loadings. Another possibility could be linked to the sensitivity of electrode performance to O_2 content in the electrolyte, as shown in section 5.3.1. Since O_2 is likely to result in the reduction of Ti^{3+}, the top layers of thicker electrodes may consume any O_2 present, protecting the bulk of the electrode from further oxidation.

Of the mass loadings tested, an optimum of 5.0 mg cm^{-2} has been identified, though peak perfomance may be between 5.0 and 6.7 mg cm^{-2}. Clearly, further work is required to elucidate the nature of the <100% coulombic efficiency of anatase TiO_2 in 1 mol dm^{-3} $AlCl_3$/1 mol dm^{-3} KCl. However, the good performance of these electrodes at these mass loadings suggest the scale-up of these electrodes into a practical device to be possible. It should also be noted that changing the ink composition could allow for higher mass loadings, that is, a higher percentage of carbon black changes ink properties such that higher mass loadings can be achieved without electrode cracks. Additional binder or even addition of a second binder, such as PTFE, could also have a similar effect.

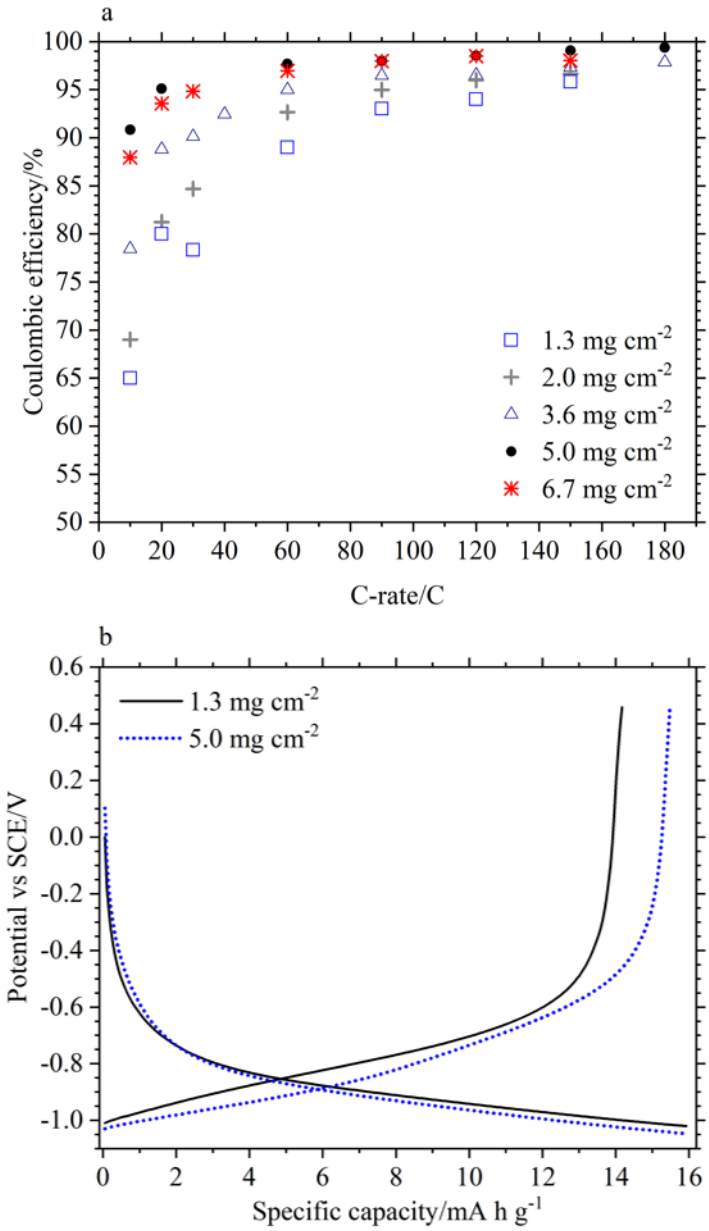

Figure 5.20. (a) Coulombic efficiency as a function of C-rate of five electrodes, cycled at 60 C in 1 mol dm^{-3} $AlCl_3$/1 mol dm^{-3} KCl, with mass loadings of 1.3, 2.0, 3.6, 5.0 and 6.7 mg cm^{-2}. (b) Typical potential profiles of the 1.3 and 5.0 mg cm^{-2} electrodes at the 60 C C-rate.

5.3.3 Self-discharge mechanisms

5.3.3.1 Diffusion vs activation controlled self-discharge

Figure 5.18 shows the detrimental effect of electrolyte O_2 content on discharge capacity, illustrating that coulombic efficiency remained below 100% even in N_2 sparged electrolyte. Therefore, further analysis of the potential causes of this low coulombic efficiency and self-discharge were explored through the analysis of OCP between charge and discharge. Firstly, a similar experiment that

produced Figure 5.18 was repeated, with an electrode being cycled at 10 C in aerated and de-oxygenated electrolytes, but with a 30 minute open circuit period between charge and discharge. Figure 5.21 shows the resulting potential profiles in the two electrolytes. Similar profiles are seen up to the 6th minute, though the potential in aerated electrolyte only reaches –0.94 V vs SCE compared to -0.97 V in the de-oxygenated electrolyte. This itself may be evidence of Ti^{3+} oxidation during the charge phase. A 30 minute rest period between charge and discharge gives to rise to a significant difference in the OCP profile. In de-oxygenated electrolyte, the potential decays steadily from -0.97 V to -0.86 V, allowing a 3 minute 44 second discharge, which corresponds to a coulombic efficiency of 62.2%. However, in aerated electrolyte, potential decay is considerably more severe, following an elongated S-shaped curve. The potential initially decays from 0.940 V to ca. – 0.70 V between the 6th and 20th minute. Here, the potential curves upward to ca. -0.40 V at the 25th minute before tailing off to a steadier increase in potential between the 25th and 36th minute. The final OCP after the 30 minute rest period was -0.230 V, which allowed only a very brief 10 second discharge corresponding to a coulombic efficiency of only 2.8%.

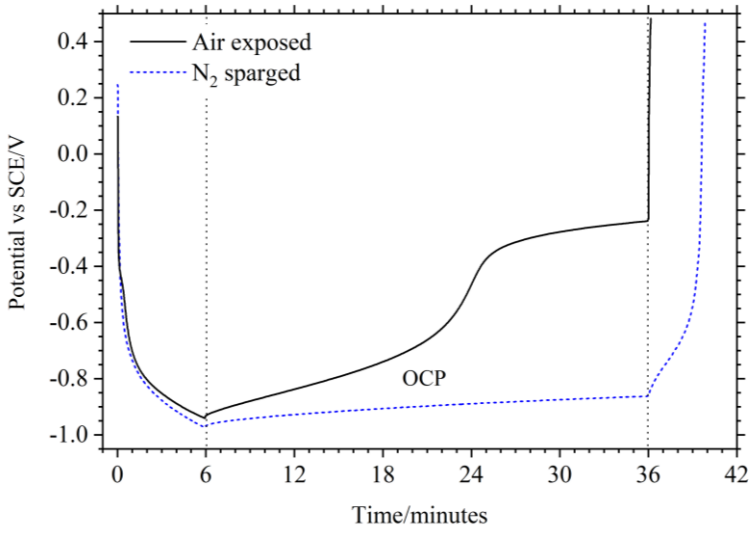

Figure 5.21. Typical charge/discharge profiles of a TiO_2 electrode cycled at a 10 C rate in aerated (black) and de-oxygenated 1 mol dm^{-3} $AlCl_3$/1 mol dm^{-3} KCl electrolyte (blue-dash). The electrode was left at OCP, between the 6th – 36th minute, after the charge input of 16 mA h g^{-1}.

From the results seen so far, the low coulombic efficiency is likely the result of a time-dependent self-discharge process. Evidence for this comes from the lower coulombic efficiency at lower specific currents i.e. longer charge-discharge times. For Faradaic self-discharge, reactions can either be diffusion-controlled or activation-controlled mechanisms. Diffusion controlled mechanisms

exhibit a linear drop in potential with $t^{1/2}$. For activation controlled mechanisms, a plot of potential vs log(t) should give rise to a plateau followed by a linear drop.

Further analysis of the OCP profile can help elude to the self-discharge mechanism. Given the relatively low capacities and high charge-discharge rates, it may be helpful to draw on the potential self-discharge mechanisms present in supercapacitors, where self-discharge rates can also be significant, especially with aqueous supercapacitors [191-193]. Generally, self-discharge is considered to be a result of either an ohmic leakage, parasitic Faradaic reaction or charge redistribution. For a TiO_2 negative electrode at ca. -1.0 V vs SCE, Faradaic reactions, such as H_2 evolution are a possibility. Charge redistribution may also be feasible due to inhomogeneities of electrolyte and Al^{3+} in various pores. While an ohmic leakage caused by some short circuit should not be possible, it is prudent to evaluate this possibility first. In relation to porous carbon electrodes, an ohmic self-discharge was modelled to have a linear relation between time and the natural log of the potential. That is, if some short-circuit exists, a plot of t vs ln(OCP), after charging the electrode, will give rise to a linear plot [192]. Therefore, an electrode was charged to -1.0 V vs SCE, at a specific current of 0.5 A g^{-1} before being left at open circuit potential (OCP) for 30 minutes. The electrode had previously undergone 120 charge-discharge cycles at a variety of specific currents to ensure a stable and representative response. This graph of the time vs ln(-V) is shown in Figure 5.22. A non-linear profile can be seen, further demonstrated by the non-conformity of the attempted linear fit. As such, it can be concluded that an ohmic leak is not responsible for the self-discharge or low coulombic efficiency observed from TiO_2.

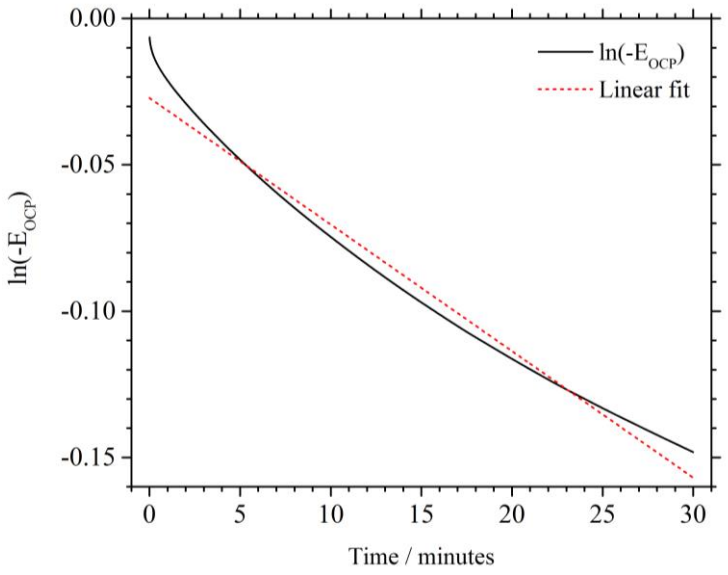

Figure 5.22. Natural logarithm of the open circuit potential of a TiO_2 electrode, over 30 minutes, after being charged to -1.0 V vs SCE at 0.5 A g^{-1} in 1 mol dm^{-3} $AlCl_3$/1 mol dm^{-3} KCl. The 3-electrode cell was cycled in air.

A plot of the TiO_2 potential against $t^{1/2}$, during the OCP shown in Figure 5.21, is shown in Figure 5.23. The plot is linear between 225 s and 1800 s (15 $s^{1/2}$ to 42.4 $s^{1/2}$), signifying a self-discharge process that is diffusion controlled. Possibilities include the de-adsorption and diffusion of Al^{3+} away from the electrode due to local concentration gradients or the diffusion of O_2 toward the negative electrode causing oxidation of Ti^{3+} and its own reduction into H_2O. The diffusion of O_2 to the electrode, resulting in Ti^{3+} oxidation could be also be responsible – though this should be minimised with N_2 sparged electrolytes. However, this diffusion controlled self-discharge can also be caused by charge redistribution, which can exhibit both diffusion and activation-controlled behaviour.

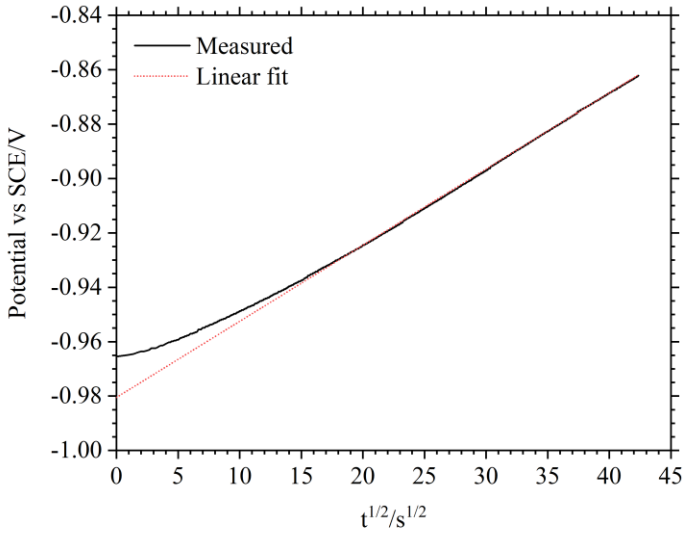

Figure 5.23. Potential of TiO_2 against $t^{1/2}$ after being charged at a 10 C rate to 16.0 mA h g^{-1} in 1 mol dm^{-3} $AlCl_3$/1 mol dm^{-3} KCl.

Furthering this work could be achieved through chronoamperometric experiments, where a measurement of the current decay with respect to time, at a given defined potential, would have allowed use of the Cottrell equation to determine the diffusion co-efficient, which could be used to elucidate the species causing the current and potential decay. The Cottrell equation is given by equation (5.3), where $i =$ current, $n =$ electron stoichiometry, $F =$ Faraday's constant, $A =$ geometric surface area, $D =$ diffusion co-efficient and $t =$ time.

$$i = \frac{nFA\sqrt{D}}{\sqrt{\pi t}} \tag{5.3}$$

5.3.3.2 H_2 evolution and pH dependence

Initial cyclic voltammetry of TiO_2 electrodes gave rise to profiles that showed H_2 evolution occurring at potentials more negative than the dominant redox peaks. Furthermore, when cycled using C-rates to a given capacity, higher C-rates result in more negative potentials being reached upon charging. Despite this, higher C-rates resulted in higher coulombic efficiency, suggesting that H_2 evolution is not the dominant process as the rate of the H_2 evolution reaction should increase at lower potentials. However, H_2 evolution can still be expected given the negative working potential of TiO_2 being outside the thermodynamic potential stability window of water.

Given 1 mol dm^{-3} $AlCl_3$/1 mol dm^{-3} KCl has a pH of 1.62, H_2 evolution would be expected to occur via reaction (5.4) at -0.096 V vs SHE, according to the Nernst equation at standard conditions. The loss of electrons from TiO_2 would result in its self-discharge through the oxidation of Ti^{3+} to Ti^{4+}.

$$2\mathrm{H}^+ + 2\mathrm{e}^- \rightleftharpoons \mathrm{H}_2 \tag{5.4}$$

H_2 evolution as a cause of self-discharge was investigated by cycling a number of TiO_2 electrodes in electrolytes of varying pH. 84.4 and 422.9 µl of HCl were added to 100 ml of 1 mol dm^{-3} $AlCl_3$/1mol dm^{-3} KCl to produce concentrations of 10 and 50 mmol dm^{-3} HCl. Electrolytes in this section will herein be referred to by their HCl concentration. In addition to charge/discharge cycles, electrodes were left at OCP for 30 minutes between charge and discharge. Furthermore, an electrode was cycled in an electrolyte that had been sparged with H_2 as opposed to N_2. If H_2 evolution is a cause of self-discharge, the input of dissolved H_2 into the electrolyte should lower the rate of H_2 evolution [194]. This can be understood via the Nernst equation given by equation (5.5), where E is the half-cell potential, E^0 the potential under standard conditions, k_B is Boltzmann's constant N_A is Avogadro's constant, T is temperature, n the number of electrons transferred per reaction, F is Faraday's constant and Q the reaction quotient which can be approximated by the ratio of the activities of the reduced and oxidised species. For reaction (5.4), the reaction quotient can be approximated by equation (5.6). Therefore, by increasing the concentration of H_2 dissolved in the electrolyte, the potential for H_2 evolution should shift to more negative potentials, decreasing the rate of self-discharge.

$$E = E^0 - \frac{k_B N_A T}{nF} \ln(Q) \tag{5.5}$$

$$Q = \frac{[H^+]^2}{[H_2]} \tag{5.6}$$

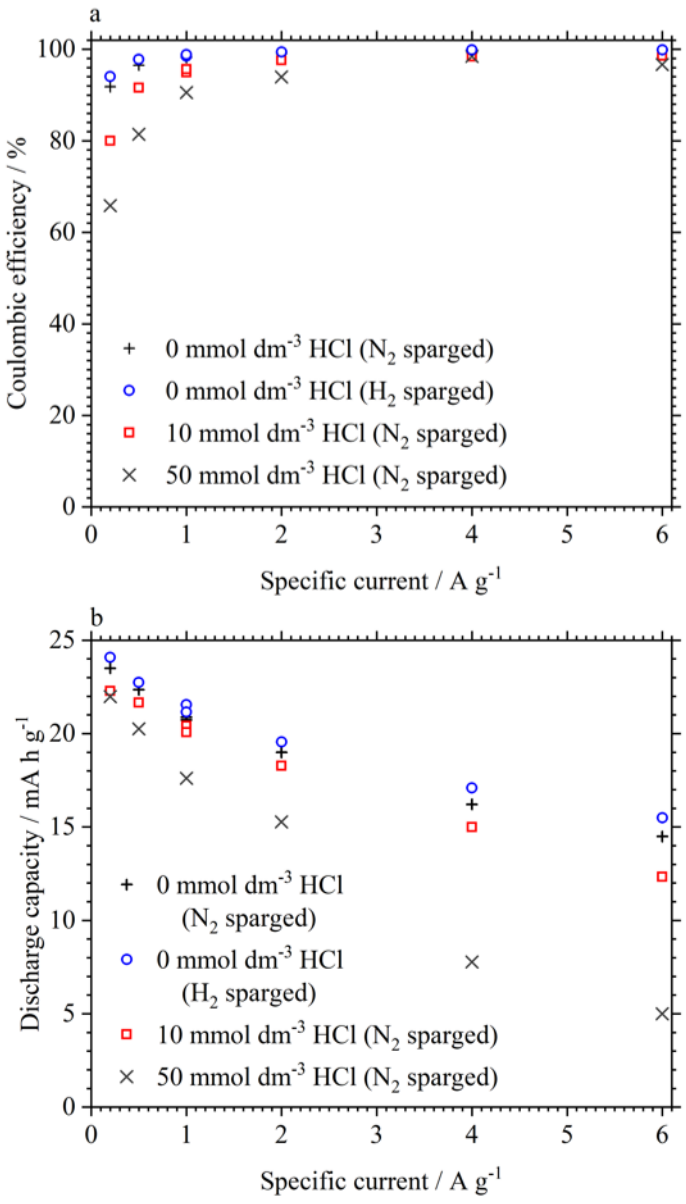

Figure 5.24. The effect of H_2 vs N_2 sparging and HCl content, added to 1 mol dm^{-3} $AlCl_3$/1 mol dm^{-3} KCl, on the coulombic efficiency (a) and discharge capacity (b) of a TiO_2 electrode cycled at specific current between 0.2 A g^{-1} to 6.0 A g^{-1}.

Figure 5.24 shows the dependence of coulombic efficiency and discharge capacity at different specific currents in 1 mol dm^{-3} $AlCl_3$/1 mol dm^{-3} KCl with the addition of HCl to form electrolyte HCl concentrations of 0 mmol dm^{-3}, 10 mmol dm^{-3} and 50 mmol dm^{-3}. Electrolytes with added HCl were purged with >99.95% dry N_2. The pH of these electrolytes were measured as 1.62, 1.28 and 0.50 respectively, using a Jenway 3510 pH meter. An additional electrode was cycled in 1 mol dm^{-3} $AlCl_3$/1 mol dm^{-3} KCl purged with H_2 and the data taken also shown in Figure 5.24. As previously seen, coulombic efficiency increases with specific current with discharge capacity decreasing, though at 6.0 A g^{-1}, coulombic efficiency begins to decrease in electrolytes with added HCl. There is also a small improvement in the H_2-sparged, compared to the N_2-sparged, 1 mol dm^{-3} $AlCl_3$/1 mol dm^{-3} KCl electrolyte. At 0.2 A g^{-1} a coulombic efficiency of 91.8% is measured in 0 mmol dm^{-3} HCl, 80.0% in 10 mmol dm^{-3} HCl and 65.9% in 50 mmol dm^{-3}. In H_2-sparged 0 mmol dm^{-3} HCl electrolyte, coulombic efficiency was 94.03%.

By 1.0 A g^{-1}, the differences in coulombic efficiency had decreased somewhat, with TiO_2 producing a coulombic efficiency of 98.4% in 0 mmol dm^{-3} HCl, 95.0% in 10 mmol dm^{-3} HCl, 86.8% in 50 mmol dm^{-3} HCl and 98.5% in H_2 sparged electrolyte. At the specific current of 4.0 A g^{-1}, coulombic efficiencies are roughly similar though still lower in electrolytes with added HCl. TiO_2 in 10 mmol dm^{-3} and 50 mmol dm^{-3} HCl produced a coulombic efficiency of 98.4% and 98.5% respectively, while N_2-sparged and H_2-sparged electrolytes without added HCl produced coulombic efficiencies of 99.2% and 99.9%. Both these 0 mmol dm^{-3} HCl electrolytes produced a coulombic efficiency of 99.9% at 6.0 A g^{-1}, while TiO_2 in 10 mmol dm^{-3} HCl gave rise to a coulombic efficiency of 98.6%. In 50 mmol dm^{-3} HCl, coulombic efficiency decreased from 98.5% at 4.0 A g^{-1} to 96.7% at 6 A g^{-1}. In contrast to coulombic efficiency, the difference between discharge capacities in the three electrolytes tended to increase with increasing specific current with discharge capacity being highest in the electrolyte without the added HCl. At 0.2 A g^{-1}, discharge capacity was 23.5 mA h g^{-1} in N_2-sparged electrolyte and 24.1 mA h g^{-1} in H_2-sparged electrolyte. This was approximately 2 mA h g^{-1} lower in 10 and 50 mmol dm^{-3} HCl electrolytes. At 6.0 A g^{-1}, discharge capacities of 14.5 mA h g^{-1} and 15.5 mA h g^{-1} were measured from the N_2- and H_2-sparged electrolytes and 12.3 mA h g^{-1} in 10 mmol dm^{-3} HCl, while TiO_2 in 50 mmol dm^{-3} HCl gave rise to a discharge capacity of only 5.0 mA h g^{-1}.

The addition of further HCl to 1 mol dm^{-3} $AlCl_3$/1 mol dm^{-3} KCl electrolyte is clearly detrimental to electrode performance with both coulombic efficiency and discharge capacity decreasing at higher HCl concentrations in 1 mol dm^{-3} $AlCl_3$/1 mol dm^{-3} KCl. This would be expected from a higher rate of H_2 evolution. Similarly, a small improvement in coulombic efficiency and discharge capacity was observed in H_2-sparged (compared to N_2-sparged) electrolyte as H_2 evolution should decrease as a consequence of increasing the concentration of dissolved H_2 in the electrolyte.

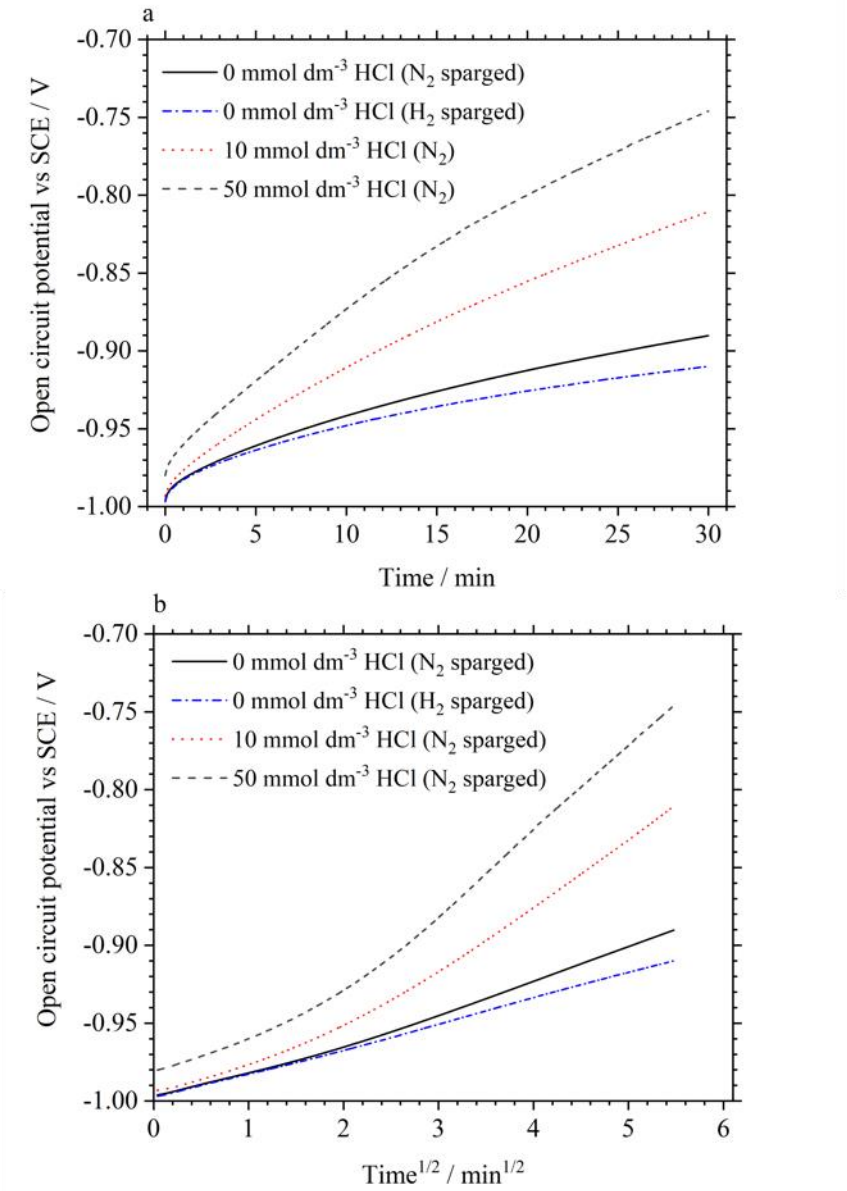

Figure 5.25. (a) OCP of TiO_2 after being charged to -1.0 V vs SCE at 0.5 A g^{-1}. Measurements are of four separate electrodes in N_2-sparged 1 mol dm^{-3} $AlCl_3$/1 mol dm^{-3} KCl with HCl added to produce concentrations of 0, 10 and 50 mmol dm^{-3} HCl as well as 1 mol dm^{-3} $AlCl_3$/1 mol dm^{-3} KCl sparged with H_2. (b) OCP plotted against $t^{1/2}$.

To further study the effect of pH and possible H_2 evolution as a cause of self-discharge, the potentials of the TiO_2 electrodes were also measured at open circuit for 30 minutes after being charged to -1.0 V vs SCE at 0.5 A g^{-1}. This was performed after an initial 120 cycles, the data from which was used in Figure 5.24. Figure 5.25 (a) shows the OCP of the three electrodes in 1 mol dm^{-3} $AlCl_3$/1 mol dm^{-3} KCl electrolytes with 0, 10 and 50 mmol dm^{-3} HCl concentrations. From the 4th

minute, the OCP in all electrolytes shows a linear dependence with $t^{1/2}$, as shown in Figure 5.25 (b), again pointing toward a diffusion controlled self-discharge process. After 30 minutes at open circuit with no added HCl, the potential of TiO_2 reaches -0.89 V vs SCE in N_2-sparged electrolyte and -0.91 V in H_2-sparged electrolyte. In 10 and 50 mmol dm^{-3} HCl electrolytes, potentials of -0.81 V and 0.75 V were reached at the end of the rest period. These results lead to the conclusion that H_2 evolution occurs at the TiO_2 electrode, at open circuit potential, after being charged.

Previous evidence had pointed toward H_2 evolution not being the dominant process responsible for self-discharge or low coulombic efficiencies. Cyclic voltammetry showed that H_2 evolution became dominant at potentials more negative than ca. -1.3 V vs SCE. While this is outside the potential stability window of water, it is possible this was extended due to the high charge density of Al^{3+} giving rise to a strong solvation shell. Furthermore, as was previously stated, higher C-rates where electrodes were charged to given capacity input, resulted in more negative charging potentials which should increase the rate of H_2 evolution. Despite this, coulombic efficiency continued to increase with increasing C-rate. However, Figure 5.24 and Figure 5.25 clearly show an increase in the rate of decay of the electrode potential (i.e. TiO_2 potential increases to more positive potentials more quickly) with decreasing pH. This results in lower coulombic efficiencies and therefore suggests a higher rate of self-discharge. Furthermore, while relatively small, there was both an increase in coulombic efficiency and discharge capacity as well as a decrease in the rate of self-discharge when electrolytes were sparged with H_2 rather than N_2. The decrease in self-discharge would be expected from the Nernst equation and an increase in the amount of dissolved H_2 in the electrolyte. This indicates that H_2 evolution is occurring, resulting in the self-discharge of TiO_2, which itself would be oxidised if hydrogen is being evolved. The $t^{1/2}$ dependence of the open circuit potential points toward a diffusion controlled process, which could be the diffusion of H^+ to the electrode or alternatively, through the bulk of the electrode. Given that pH of 1 mol dm^{-3} $AlCl_3$/1 mol dm^{-3} KCl was measured at 1.62, the concentration of H^+ should be 24.0 mmol dm^{-3}. This may be low enough that self-discharge is controlled by the diffusion of H^+ in the electrolyte to the electrode surface. The typical cell in this section consisted of 50 ml of electrolyte and a 25 mg TiO_2 electrode, such that the amount of H^+ ions in the electrolyte would be approximately 1.2 mmol (24 mmol dm^{-3} x 0.05 dm^{-3}). This is in comparison to only 0.3125 mmol of TiO_2 (0.025 g x 79.86 g mol^{-1}). It is therefore possible that a 25 mg TiO_2 electrode in 50 ml of 1 mol dm^{-3} $AlCl_3$ can be fully discharged via H_2 evolution at the electrode, equation (5.4).

Certainly, further work on the effect of H^+ on the self-discharge of TiO_2 should be carried out. A rotating disk TiO_2 electrode experiment can be envisaged, where rotation of the electrode should increase the rate of self-discharge. However, entirely ruling out the effect of O_2 oxidising Ti^{3+} would be difficult to confirm without performing experiments in glove boxes. It was shown that the rate

of self-discharge could be reduced through the addition of dissolved H_2 into the electrolyte while it may also be possible to reduce the amount of electrolyte to the point where the moles of H^+ are lower than the moles of TiO_2 and thus decrease self-discharge. However, H_2 will continue to be a primary issue for an aqueous Al-ion cell cycled at low specific currents.

5.3.3.3 Charge redistribution

In porous capacitive electrodes, self-discharge can also occur through charge redistribution. This often occurs as the result of the outer surfaces of an electrode charging more rapidly, to a given potential, than the bulk. When an electrode is then left at OCP, some form of charge propagation will occur to equalize the differences in potential within the electrode. Depending on the behaviour of the potential relaxation, charge redistribution can, as with faradaic self-discharge, be described as either a diffusion or activation controlled process. Activation controlled Faradaic self-discharge exhibit slopes that are independent of charging potential while activation controlled charge redistribution exhibit a dependence [192]. Given the high rates of cycling performed on TiO_2 so far, where 1 A g^{-1} constitutes a charging time of ca. 60-70 s, charge redistribution may be a possible cause of self-discharge. Despite this, it is unlikely that charge redistribution plays a significant role in the self-discharge of the TiO_2 electrodes, given that higher coulombic efficiency is measured at higher specific currents, when inhomogeneity in electrode charging should be greater.

Nevertheless, charge redistribution in TiO_2 was explored by changing the rate of charge i.e. changing the specific current used to cycle the electrode. If charge redistribution exists, then decreasing the charging current should result in a lower amount of self-discharge, since longer charging times should result in more even charging of the electrode. Therefore, an electrode was charged at specific currents of 0.5, 1.0, 2.0, 4.0 and 8.0 A g^{-1} to -1.0 V vs SCE before measuring its OCP for 30 minutes, then discharging the electrode at the same current used for charging. Table 5.2 presents the associated discharge capacity and coulombic efficiency.

Table 5.2. Discharge capacity and coulombic efficiency of 5 nm powder TiO_2 electrodes when cycled in 1 mol dm^{-3} $AlCl_3$/1 mol dm^{-3} KCl to a minimum potential of -1.0 V vs SCE at given specific currents including a 30 minute OCP period between charge and discharge.

Specific current/ A g^{-1}	**Discharge capacity / mA h g^{-1}**	**Coulombic efficiency**
0.2	18.80	77.35
0.5	17.24	72.77
1.0	17.91	81.35
2.0	16.89	81.75
4.0	13.46	74.6
6.0	12.32	75.44

Figure 5.26 (a) presents the graph of open circuit potential of TiO_2 against time under these different cycling conditions. The shapes of the OCP profiles can be seen in Figure 5.26 (b). The profiles are roughly similar and independent of the specific current used to charge the electrode. However, the average potential at OCP becomes more positive with increasing specific current. The potential after the 30 minute rest period is -0.91 V after charging at 0.2 A g^{-1} but -0.84 V after charging at 6.0 A g^{-1}, though this is almost entirely accounted for by the initial drop in potential. This is expected from the greater polarisation of the electrode at higher specific currents, meaning a lower amount of charge capacity can be input before reaching the cut-off potential. As such, a comparison between these profiles required a plot of potential vs $t^{1/2}$. At all specific currents, self-discharge seems to be diffusion controlled as shown by the linear trends of OCP vs $t^{1/2}$. However, there appears to be two self-discharge processes after charging at 2.0, 4.0 and 6.0 A g^{-1} – the two self-discharge segments being most pronounced at 6.0 A g^{-1} and least pronounced at 2.0 A g^{-1}. Plotting this initial 3 seconds (0.224 $min^{1/2}$) of OCP against $t^{1/2}$ is as shown in the top-left inset of Figure 5.26 (b). This plot again shows a clear linear dependency. Therefore, it is reasonable to conclude that at high specific currents (above 2.0 A g^{-1} in this case), there is a small amount of self-discharge caused by diffusion-controlled charge redistribution in the TiO_2 electrode, but that a second self-discharge process dominates past an initial period of ca. 3 seconds. This is likely to be either H_2 evolution or reduction of TiO_2 by O_2.

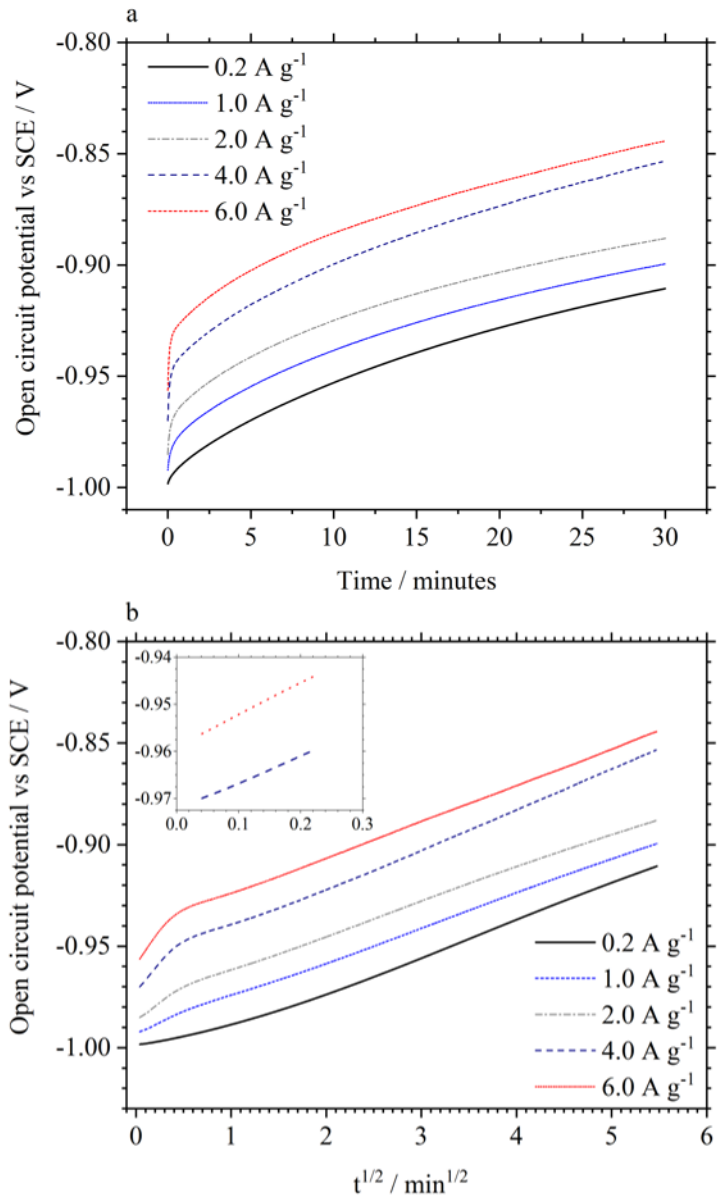

Figure 5.26. (a) Open circuit potential of a TiO_2 electrode, in 1 mol dm^{-3} $AlCl_3$/1 mol dm^{-3} KCl after being charged at various specific current to -1.0 V vs SCE. (b) Plots of the OCPs against $t^{1/2}$. Inset is the OCP during the first 0.224 $min^{1/2}$ (3 seconds) at OCP after charging at 4.0 and 6.0 A g^{-1}.

Upon first glance, there is no clear trend in the coulombic efficiency, with the highest coulombic efficiency measurements, of 81.35% and 81.75%, made at 1.0 and 2.0 A g^{-1}. However, without an OCP period between charge and discharge, higher specific currents would normally lead to higher coulombic efficiency in this system. Therefore, the fact that coulombic efficiency at 6.0 and 4.0 A g^{-1} is lower when an OCP period is used, further supports the conclusion that there is a small amount of charge redistribution present at high specific currents.

5.3.4 Self-discharge conclusions

This section presented, for the first time, results on the coulombic efficiency of TiO_2 in aqueous Al^{3+}-containing electrolytes. It was explicitly shown that coulombic efficiency decreases at lower currents and that a self-discharge process exists, important factors ignored in the literature on aqueous Al-ion electrodes. The section has attempted to shed some light on the cause for the low coulombic efficiency of TiO_2, in aqueous Al^{3+} electrolyte, at low specific current and C-rates. It wass shown that the low coulombic efficiency at low currents is due to a self-discharge process which has a $t^{1/2}$ dependance, that is, when the OCP of a charged electrode is plotted against $t^{1/2}$, a linear profile arises. Self-discharge can therefore be concluded to be a result of a diffusion controlled process. It was first shown that removing O_2 from the electrolyte could drastically improve coulombic efficiency. In the presence of O_2, Ti^{3+} would be oxidised, resulting in the self-discharge of TiO_2. However, some self-discharge remained even after rigorously bubbling dry N_2 (99.95%) through the electrolyte for more than 30 minutes. A small amount of O_2 cannot be ruled out and self-discharge could well be the due to the diffusion of O_2 to the electrode. Given the negative potentials, ca. -0.5 V to -1.0 V vs SCE, H_2 evolution could be expected. Increasing electrolyte pH through the addition of HCl resulted in lower coulombic efficiencies. The OCP of a charged electrode also increased at faster rate with increased acidity, suggesting that H_2 evolution is present and partially responsible for self-discharge. However, clearly distinguishing between H_2 evolution and Ti^{3+} oxidation by O_2 was not possible, though given that electrolytes were thoroughly sparged with N_2, H_2 evolution seems the most likely cause of self-discharge, since the majority of dissolved O_2 should have been removed from the electrolyte. Therefore, while the negative working potential of TiO_2 in aqueous Al^{3+} electrolytes is desirable for increasing cell voltages, the consequential H_2 evolution would become highly problematic for cells cycled at low specific currents. In addition to self-discharge via H_2 evolution, it was also found that a short period, ca. 3 seconds, of diffusion-controlled charge redistribution occurs within TiO_2 electrodes after being charged at high specific currents. This likely accounts for the more positive open circuit potentials measured from electrodes charged at higher specific currents, and accounts for the lower coulombic efficiencies

when cycled at higher specific currents when a 30 minute rest period is included between charge and discharge. Some of the analyses on self-discharge has previously been used for understanding self-discharge of carbonaceous supercapacitor electrodes. However, the basic principles along with the similarity and consistency of the voltage profiles when performing this experimental analysis (between TiO_2 and carbon) suggests the conclusions to be valid [194].

5.4 Conclusions

Composite TiO_2 nanopowder electrodes with high mass loadings (up to 6.7 mg cm^{-2}) have superior high-rate performance to TiO_2 electrodes recently reported for use in the aqueous Al-ion chemistry. Small particle size and a large electrolyte-electrode interface can allow for fast Al^{3+} diffusion and many surface sites for potential capacitive contributions. The flat voltage profile under galvanostatic cycling along with cyclic voltammetry profiles (both previously reported and for these specific electrodes) suggest an insertion redox process. However, a capacity of 20 mA h g^{-1} coupled with a high rate capability of 7.2 A g^{-1} and lack of crystal structure changes during extended cycling complicates the matter and suggests a surface storage mechanism. Cyclic voltammetry performed at different scan rates, and potential windows, further suggested the possibility of a surface controlled charge storage mechanism. Furthermore, there was no discernible semi-circle from the Nyquist plot of TiO_2, which implies a lack of charge transfer, a characteristic often seen with capacitive electrodes. Clearly, further work is required to understand this. In-situ XRD could allow measurements of unit cell parameter changes during charge and discharge, though the precision of XRD analysis may be insufficient to measure small changes. Exploring any relationship between capacity and specific surface area, pore size and pore size distribution would also be useful in clarifying charge storage mechanisms.

This chapter also reports the decrease in coulombic efficiency with decreasing specific current i.e. increasing charge-discharge times. It was concluded that Ti^{3+} was oxidised by dissolved O_2 present in the electrolyte. This constituted a significant cause of self-discharge and was therefore partially responsible for the decrease in coulombic efficiency with decreasing specific current. By purging electrolytes with N_2, self-discharge could be limited, e.g. 63% of capacity was retained after a 30 minute OCP rest period in N_2 purged electrolyte compared to effectively 0% in aerated electrolyte. It was also found that by increasing the acidity of electrolytes, through the addition of HCl, coulombic efficiency decreased at any given specific current, while there was a greater decay of the OCP of charged TiO_2 electrodes. Nonetheless, the described electrodes demonstrated the possibility of 5000 cycles, >99% coulombic efficiency and high specific current of up to 7.2 A g^{-1} and

as such represent a higher cycle life and rate capability than has previously been reported in the literature regarding TiO_2 in aqueous Al^{3+} electrolytes.

Chapter 6 Electrochemically treated TiO_2

6.1 Introduction

Doped TiO_2 could provide a method to incorporate Ti^{3+} to improve electrode conductivity and potentially improve insertion kinetics of Al^{3+}. However, only He et al have described the potential of doped TiO_2 via their synthesis of black nanoleaves [184]. Their method of solution plasma processing is not yet well understood and may not be feasible for producing large quantities of material. As such, alternative methods of doping are important to help verify the effect of doping on TiO_2 electrodes and its application in aqueous batteries [195, 196].

Other methods of TiO_2 doping have been widely explored for use in other applications such as photocatalytic hydrogen production, environmental pollutant removal or supercapacitor electrodes [197]. It is with alternative applications in mind that various methods of doping have been proposed. Doped TiO_2 nanostructures have been prepared via high temperature, >500 ºC, treatments in H_2, Ar and N_2 atmospheres [128, 198-200]. The electrochemical reduction method used has been previously reported as a safe and facile method of producing self-doped TiO_2. Electrochemically doped TiO_2-NTA has shown improved electrochemical performance as aqueous supercapacitor current collectors, while self-doped TiO_2 nano structures have demonstrated improved photocatalytic activity for water splitting [201, 202].

This chapter describes electrochemically treated TiO_2 electrodes for use in aqueous Al-ion batteries. The treatment consists of a safe and repeatable electrochemical reduction method used in an attempt to introduce Ti^{3+} and oxygen vacancies, though the introduction of Ti^{3+} could not be directly verified. The reduction process manipulated electrode open circuit potential (OCP), which remained stable throughout cycling, and improved capacity, rate capability, coulombic efficiency and stability when galvanostatically cycled in 1 mol dm^{-3} $AlCl_3$/1 mol dm^{-3} KCl. Electrochemical impedance spectroscopy (EIS), X-ray diffraction (XRD), scanning electron microscope (SEM) imaging and X-ray photoelectron spectroscopy (XPS) were also employed to elucidate the origin of this improved performance.

6.2 Electrochemical reduction treatment

Electrochemical experiments were carried out in 3-electrode cells using a saturated calomel reference electrode and copper-hexacyanoferrate as a reversible counter electrode. Electrodes

were manufactured as explained in section 3.2 with all electrolytes degassed with dry nitrogen. Electrochemical performance was determined in an electrolyte of 1 mol dm^{-3} $AlCl_3$/1 mol dm^{-3} KCl with the electrochemical reduction being performed in 1 mol dm^{-3} KOH. The reduction process consisted of holding electrodes at -1.4 V vs SCE in 1 mol dm^{-3} KOH for 15 minutes which was repeated ten times with a 3 minute OCP between repeats. Figure 6.1 shows the current response of a composite TiO_2 electrode held at -1.40 V vs SCE in 1 mol dm^{-3} KOH. A current of ca. -2.50 A g^{-1} decreases rapidly to ca. -0.10 A g^{-1} after 3 s and to around -0.05 A g^{-1} after 7.8 s. Between minutes 6 and 8, the measured current is less than -0.04 A g^{-1} as shown by the inset of Figure 6.1. Despite this negative potential, there were no obvious signs of H_2 evolution or bubbling at the TiO_2 electrode. Treated electrodes were washed with de-ionised water before being characterised.

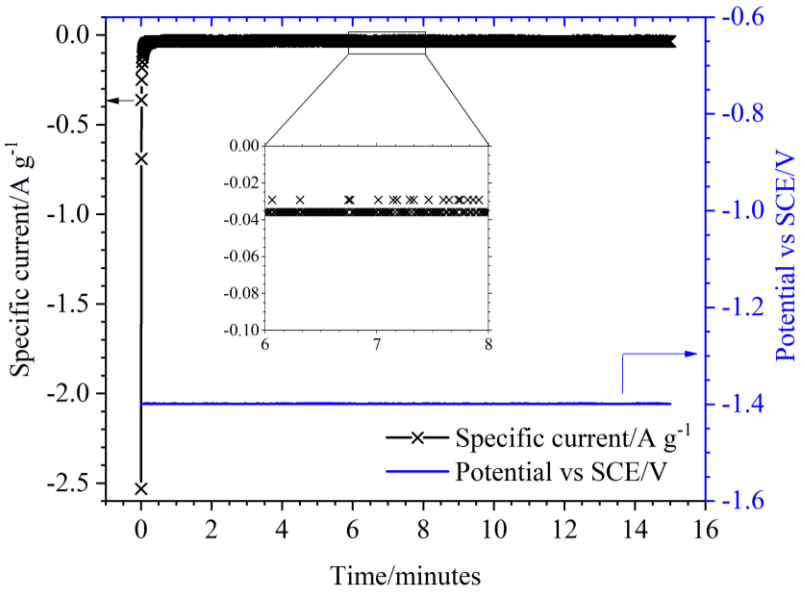

Figure 6.1. The current measured from a TiO_2 electrode in response to a potentiostatic hold at -1.4 V vs SCE, in 1 mol dm^{-3} KOH.

6.3 Electrode characterisation

Figure 6.2 (a) shows photographic images of an as-manufactured (left) and electrochemically treated-TiO_2 (right) electrode following the cathodic electrochemical treatment. Carbon black was omitted from these electrodes in order to observe any colour change. The white colour of TiO_2 can be seen to shift to a pale yellow after the treatment. This would be consistent with a change in its band gap energy. Despite previous self-doped TiO_2 nanotube arrays developing a blue colour [203], a yellow colour has also been shown to occur when TiO_2 has undergone hydrogenation [204, 205], hydrothermal treatment [206] or N_2 doping [207]. Figure 6.2 (b) gives the XRD patterns from a TiO_2

and treated-TiO_2 electrode. Both show the characteristic anatase pattern with no difference between the two, suggesting a lack of bulk crystallographic change to the TiO_2 electrodes.

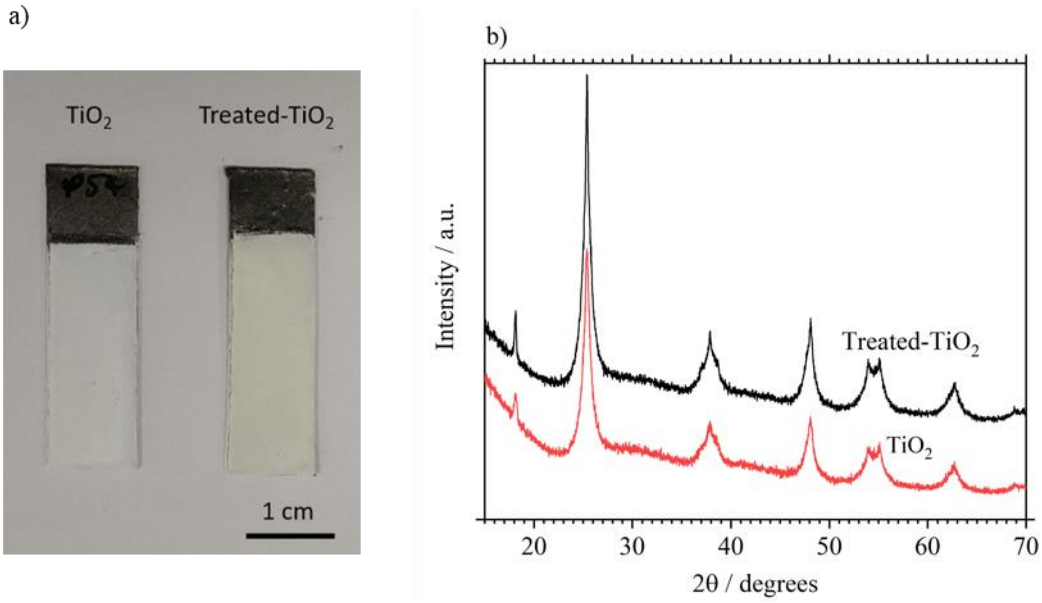

Figure 6.2. (a) Photo of a TiO_2 (left) and an electrochemically reduced-TiO_2 (right) electrode. Carbon black was excluded from the electrodes photographed. (b) XRD patterns from a TiO_2 (bottom) and treated-TiO_2 electrode (top).

Figure 6.3 (a) and (b) show SEM images of an as-manufactured TiO_2 electrode, at 1000× and 40000× magnification, with Figure 6.3 (c) and (d) giving images from treated-TiO_2. At 1000× magnification, both electrodes show an even coating of active material, though larger agglomerations can also be seen. At 40000× magnification, individual particle agglomerations can be observed, though resolution of individual particles cannot be seen due to the small TiO_2 particle size of ca. 5 nm. No significant change can be observed in the structure of the electrodes. This suggests that any change in electrode performance was not due to particle flocculation or minor electrode cracking, which could have increased surface area or improved electrode wettability.

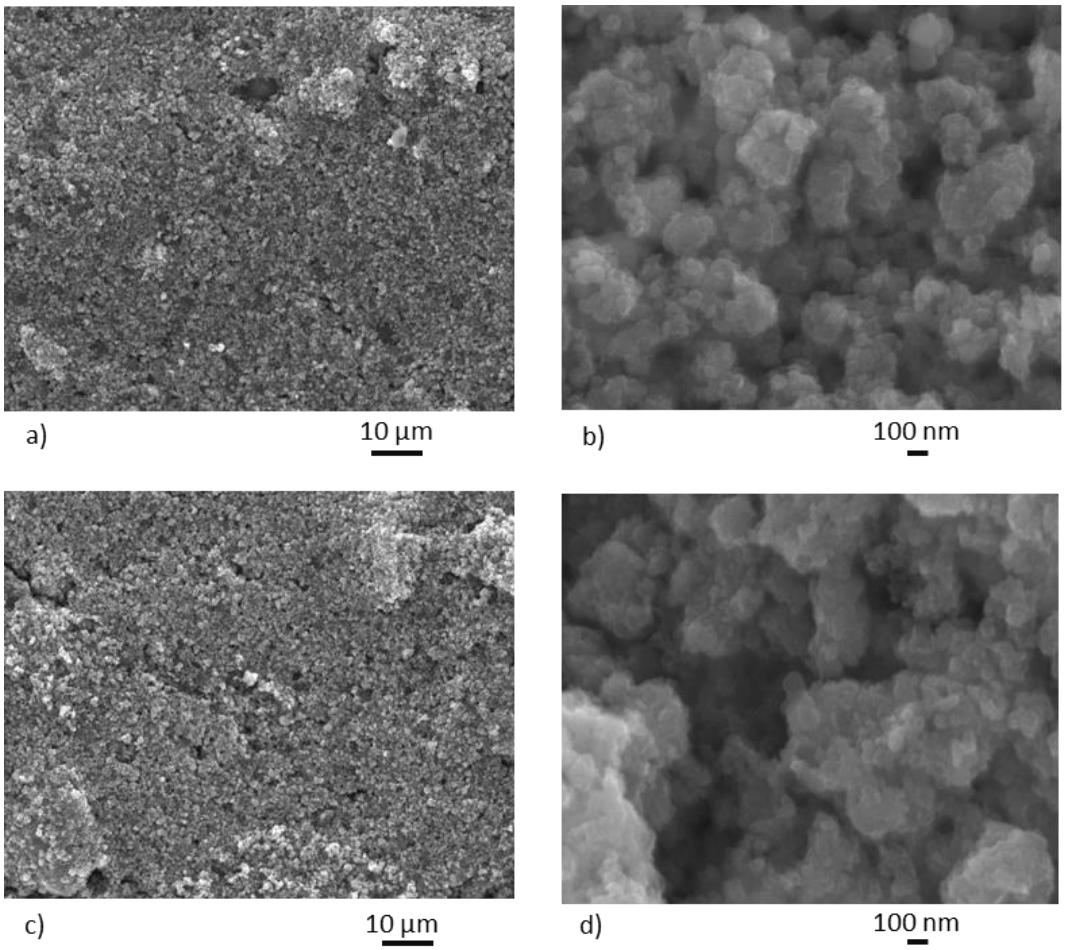

Figure 6.3. a) and b) present SEM images of a TiO_2 electrode at 1000× and 40000× magnification. c) and d) show images from a treated-TiO_2 electrode at the same magnifications.

X-ray photoelectron spectroscopy was performed on the samples shown in Figure 6.1 (b) to investigate the surface states of untreated and doped-TiO_2 electrodes*. Figure 6.4 gives the Ti 2p spectra of TiO_2 (a) and reduced-TiO_2 (b) electrodes. No detectable difference can be observed between the samples. This could indicate that Ti^{3+} states exist within the bulk rather than the surface. However, given that measurements were performed ex-situ, it is more likely that any Ti^{3+} formation is followed by re-oxidation in air. Ti $2p_{3/2}$ peaks are located at 459.40 eV and 458.71 eV for TiO_2 and reduced-TiO_2 respectively, while Ti $2p_{1/2}$ peaks are located at 465.15 eV and 464.46 eV. Unexpectedly, the presence of inorganic Ti-oxyfluoride, <1%, was detected in both samples, which may arise during ink preparation but could alternatively arise from low level X-ray degradation.

* Measurements were performed externally by Lucideon UK ltd.

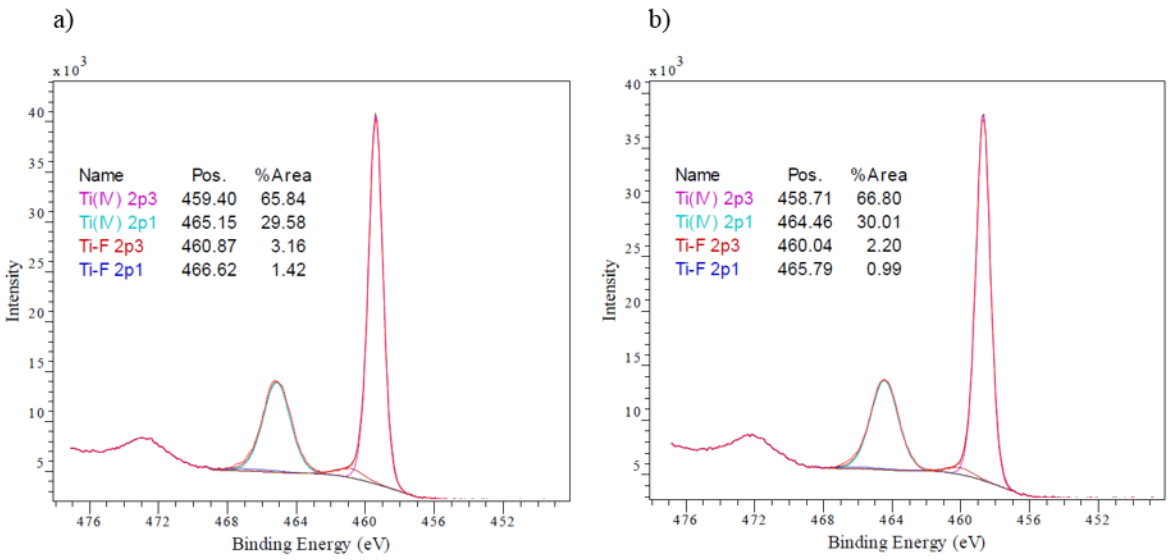

Figure 6.4. High resolution Ti 2p spectra of TiO_2 (a) and treated-TiO_2 (b). Original measurements given in red with brown denoting the sum of the fitted curves.

In order to determine whether the electrochemical treatment resulted in the introduction of Ti^{3+} and oxygen vacancies, Mott-Schottky plots were produced, which can provide information on semi-conductor type, flat band potential and majority charge carrier densities. The typical plot graphs the inverse of capacitance squared, measured at a single frequency, against the applied DC potential [208, 209]. For Mott-Schottky analysis, full EIS spectra were obtained using a 10 mV perturbation between 10 kHz to 10 Hz at DC bias potentials between +0.40 V to -0.70 V vs SCE. Figure 6.5 shows Mott-Schottky plots produced from EIS measurements performed at DC bias potentials between 0.40 V to -0.70 V vs SCE, in 1 mol dm^{-3} $AlCl_3$/1 mol dm^{-3} KCl. Figure 6.5 (a) compares a TiO_2 and treated-TiO_2 electrode at a frequency of 5 kHz. Capacitance values were calculated via equation (6.1), where C = capacitance, f = frequency and Z'' = imaginary impedance part. The positive and linear gradient produced by the as-manufactured TiO_2 electrode, between ca. -0.45 V to -0.30 V vs SCE, is indicative of an n-type semi-conductor and has an approximate gradient of 0.0748. The decrease in C^{-2} from the treated-TiO_2 electrode suggests an increase in the number of donors (i.e. electrons) according to equation (6.2), where C = capacitance, A = area, N_d = number of donors, e = electronic charge, V = applied potential, V_{FB} = flat band potential, k = Boltzmann's constant and T = absolute temperature [208].

$$C = -\frac{i}{2\pi f Z''} \tag{6.1}$$

$$\frac{1}{C^2} = \frac{2}{\varepsilon\varepsilon_0 A^2 e N_d}(V - V_{FB} - \frac{kT}{e}) \quad (6.2)$$

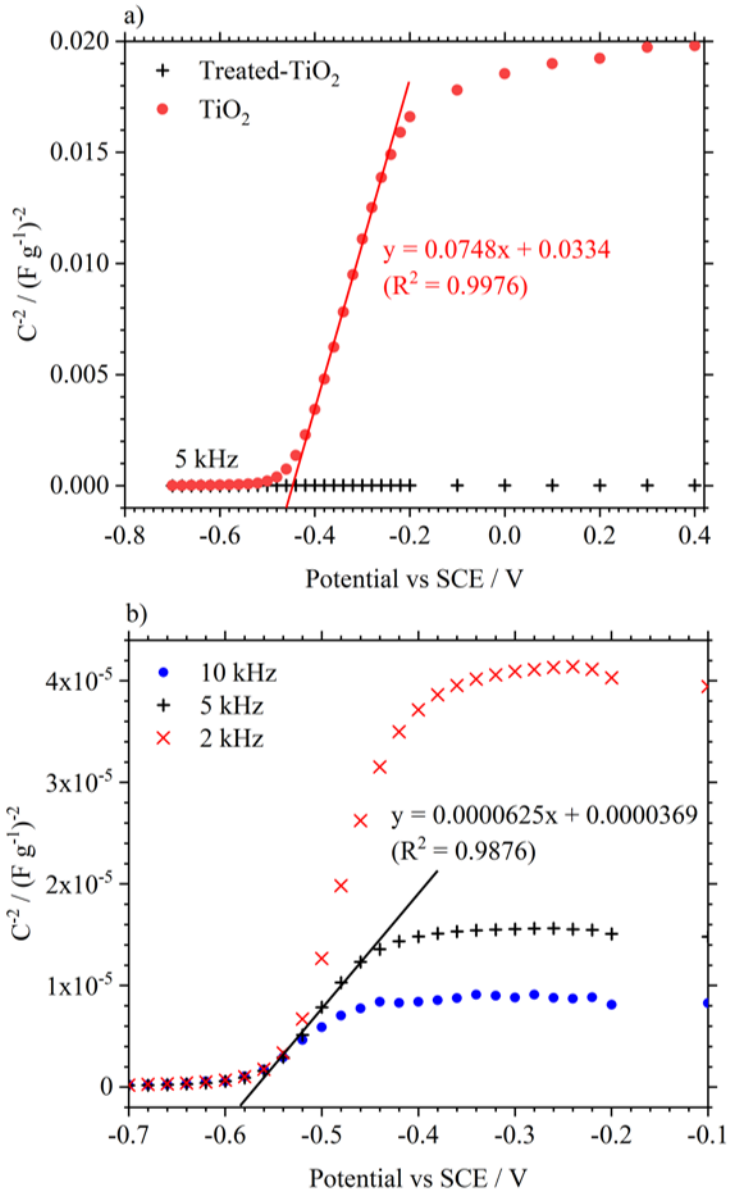

Figure 6.5. a) Mott-Schottky plots of treated-TiO_2 and TiO_2 at 5 kHz in 1 mol dm^{-3} $AlCl_3$/1 mol dm^{-3} KCl. b) Mott Schottky plots of the treated TiO_2 electrode at 2, 5 and 10 kHz.

Figure 6.5 (b) shows an expanded view of the response from treated-TiO_2 and also shows the response at frequencies of 2 kHz and 10 kHz. The Mott-Schottky plot is again indicative of an n-type semi-conductor. The gradient of the linear portion of the plot, between -0.46 and -0.56 V vs SCE, is

approximately 6.25×10^{-5}. This is 3 orders of magnitude lower than the approximate gradient found from the as-manufactured TiO_2 electrode at the same frequency, providing clearer evidence that the electrochemical treatment resulted in an increase in the electron donor level. The number of donors, N_d, was not estimated since the electrochemically active surface area was not known. Nevertheless, the cathodic electrochemical treatment resulted in an increase in the number of donors (electrons) and a shift of the V_{FB} to a more negative potential. Both these criteria would be expected from an introduction of Ti^{3+} or oxygen vacancies into TiO_2, as expected from the cathodic treatment at -1.4 V vs SCE in 1 mol dm^{-3} KOH.

Ideally, further characterisation of treated electrodes would have been performed using UV-vis spectroscopy or electro paramagnetic resonance (EPR) spectroscopy. Given the observed colour change after electrochemical treatment, UV-vis spectroscopy could have provided a direct measurement of the band gap of as-manufactured and treated-TiO_2, which would have provided evidence for the introduction of Ti^{3+}. Additionally, EPR could have provided direct evidence for the presence of Ti^{3+} because Ti^{3+} provides a paramagnetic response where Ti^{4+} does not.

6.4 Electrochemical performance

To determine variations in electrode performance, 10 galvanostatic cycles were performed at each of the specific currents of 0.2, 0.5, 1.0, 2.0, 4.0, 6.0 and 8.0 A g^{-1}. Treated-TiO_2 was then also cycled at 10.0 A g^{-1}. Figure 6.6 (a) and (b) show the discharge capacity and coulombic efficiency against cycle number at the given specific currents. Figure 6.7 (a) and (b) compare the discharge capacity and coulombic efficiency from the two electrodes, as a function of specific current. During the initial 10 cycles, the discharge capacity of both electrodes increases before stabilising during subsequent cycling, while the improved performance from treated-TiO_2 becomes most obvious at higher specific currents. Figure 6.6 (b) shows how the coulombic efficiency requires a greater number of cycles before stabilising. After 30 cycles, coulombic efficiency is relatively stable at a given specific current for both electrodes.

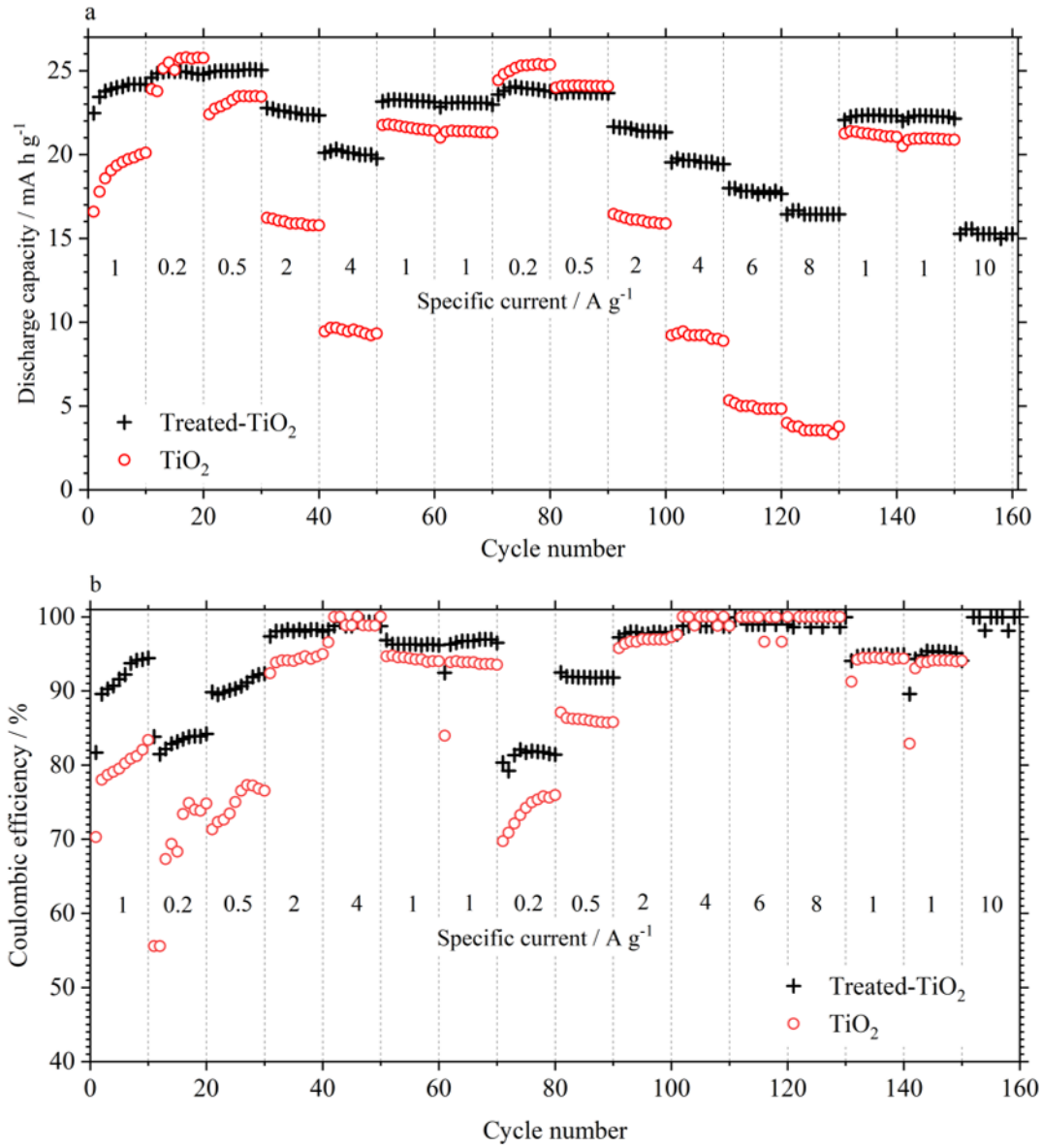

Figure 6.6. Discharge capacity (a) and coulombic efficiency (b), vs cycle number, from a treated-TiO_2 (black cross) and TiO_2 electrode (red circle). Electrodes were cycled in 1 mol dm^{-3} $AlCl_3$/1 mol dm^{-3} KCl between -1.0 V and +0.4 V vs SCE.

To better show differences in performance, Figure 6.7 (a) and (b) show the discharge capacity and coulombic efficiency of the two electrodes as a function of specific current. The data points for these figures were taken between cycle 60 and 160, shown in Figure 6.6, using the 10th cycle from each specific current to ensure a stable response had been reached. Figure 6.7 (a) shows the discharge capacity of TiO_2, at 0.2 A g^{-1}, to be 25.3 mA h g^{-1}, which is actually marginally higher than the 23.8 mA h g^{-1} measured from the treated-TiO_2. However, the improved performance of treated-TiO_2 becomes obvious at higher specific currents. At 2.0 A g^{-1}, the discharge capacities of TiO_2 and treated-TiO_2 are 15.9 mA h g^{-1} and 21.3 mA h g^{-1} respectively. At 8.0 A g^{-1}, the TiO_2 electrode can

produce a capacity of only 3.2 mA h g^{-1} while a capacity of 15.3 mA h g^{-1} was measured from treated-TiO_2 at the higher specific current of 10.0 A g^{-1}, clearly showing superior rate capability. The coulombic efficiency of treated-TiO_2 was measured to be 81.4% and 91.8% at 0.2 A g^{-1} and 0.5 A g^{-1}, respectively, Figure 6.7 (b). This is higher than the coulombic efficiencies of 75.9% and 85.0% for the TiO_2 electrode. Above specific currents of 1.0 A g^{-1}, the coulombic efficiency of both electrodes are roughly similar, increasing from approximately 98% to >99.9% at 8.0 A g^{-1} (and >99.9% at 10.0 A g^{-1} for the treated-TiO_2). A discharge capacity of 15.3 mA h g^{-1} at 10.0 A g^{-1} is the highest specific current recorded from TiO_2 in aqueous Al^{3+} electrolytes [133, 135-137] and a higher specific current than recorded from $NaTi_2(PO_4)_3$ or $Li_4Ti_5O_{12}$ in aqueous Na-ion cells [117, 210].

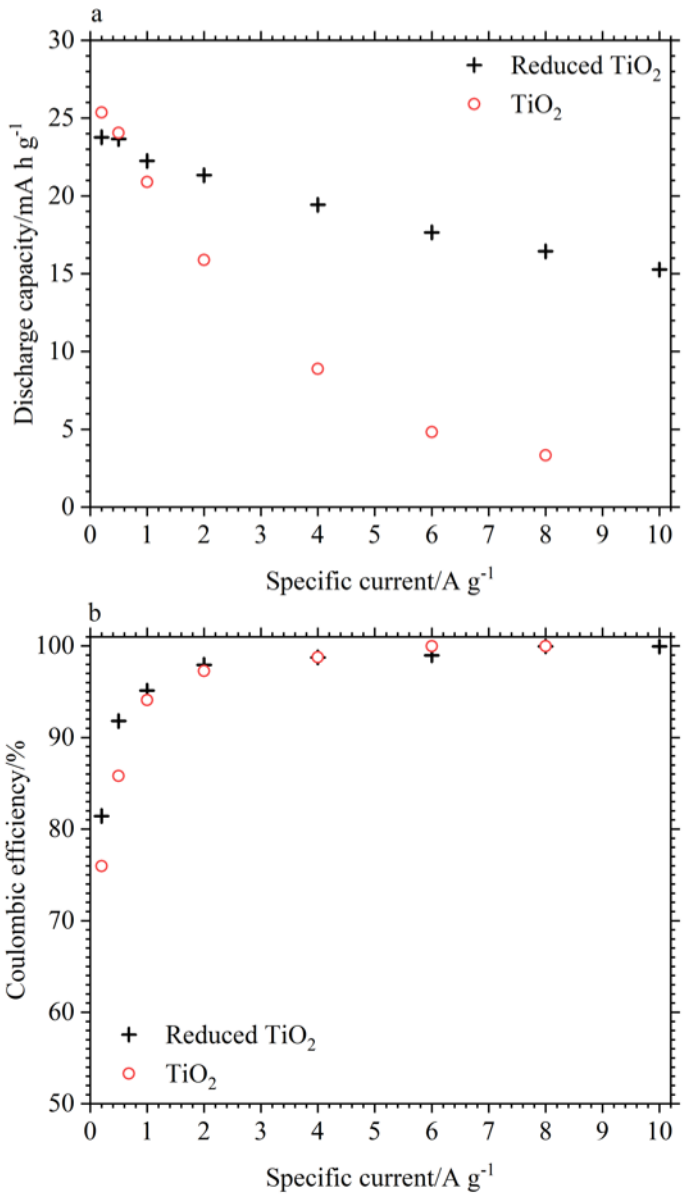

Figure 6.7. Comparison of the discharge capacity (a) and coulombic efficiency (b) from a reduced-TiO_2 (black cross) and TiO_2 electrode (red circle) cycled in 1 mol dm^{-3} $AlCl_3$/1 mol dm^{-3} KCl vs an SCE reference between -1.0 V and +0.4 V.

Figure 6.8 gives the voltage profiles of the same reduced-TiO_2 (a) and TiO_2 (b) electrodes during the 1st, 10th and 60th cycle. For reduced-TiO_2, a 1st cycle discharge capacity of 22.5 mA h g^{-1} was measured, corresponding to a coulombic efficiency of 81.7%. This increased to 24.2 mA h g^{-1} at a coulombic efficiency of 94.4% by the 10th cycle with a discharge capacity and coulombic efficiency of 23.1 mA h g^{-1} and 96.2% measured during the 60th cycle. For the untreated TiO_2 electrode, an initial discharge capacity of 16.6 mA h g^{-1} was measured with a coulombic efficiency of 70.3%. Discharge capacity and coulombic efficiency were measured as 20.1 mA h g^{-1} and 83.4% during the 10th cycle and 21.4 mA h g^{-1} and 94.0% by the 60th cycle. The increased discharge capacity and coulombic efficiency from the reduced-TiO_2 electrode during initial cycling would be a particularly important consideration for full cell construction.

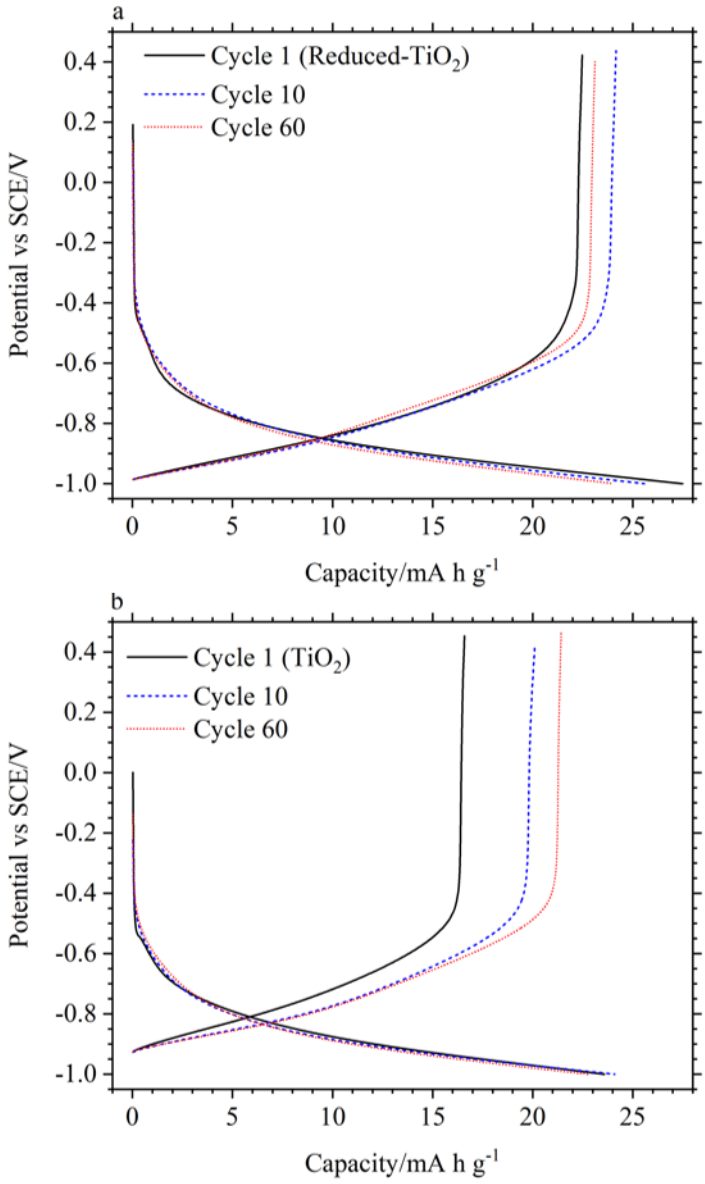

Figure 6.8. Voltage profile of TiO_2 electrodes vs SCE during cycling at 1.0 A g^{-1} in 1 mol dm^{-3} $AlCl_3$/1 mol dm^{-3} KCl at cycles 1, 10 and 60. The response from reduced-TiO_2 is given by (a) and as-manufactured TiO_2 by (b).

The IR-drop, between charge and discharge (measured as the total change in potential between charge and discharge), as a function of specific current is shown in Figure 6.9. It can be seen that the IR-drop for the reduced-TiO_2 electrode is lower throughout the cycling regime, resulting in a lower equivalent series resistance (ESR) compared to the TiO_2 electrode not electrochemically reduced. Both electrodes follow a linear increase in IR-drop with increasing specific current as represented by the linear fits with x and y intercepts of 0. The difference between the reduced-TiO_2 and TiO_2 electrodes is 11.7 mV at 0.2 A g^{-1}, increasing linearly to 116.5 mV at 2.0 A g^{-1}. At 10.0 A g^{-1}, the IR-drop from reduced-TiO_2 is 135.2 mV, while the IR-drop from TiO_2 at 8.0 A g^{-1} is 539.3 mV. The gradient of the linear fits were used to determine an ESR of 0.562 Ω for reduced-TiO_2 and 2.843 Ω for untreated TiO_2. This suggests a significant improvement in the conductivity of TiO_2, a reasonable conclusion from the introduction of Ti^{3+} expected from the electrochemical reduction process. Electrodes were both 24 mg for the treated and pristine electrodes respectively, both covering an area of approximately 7 cm^2 such that differences in electrode impedance arising from differences in mass loading and electrode thickness can be reasonably neglected.

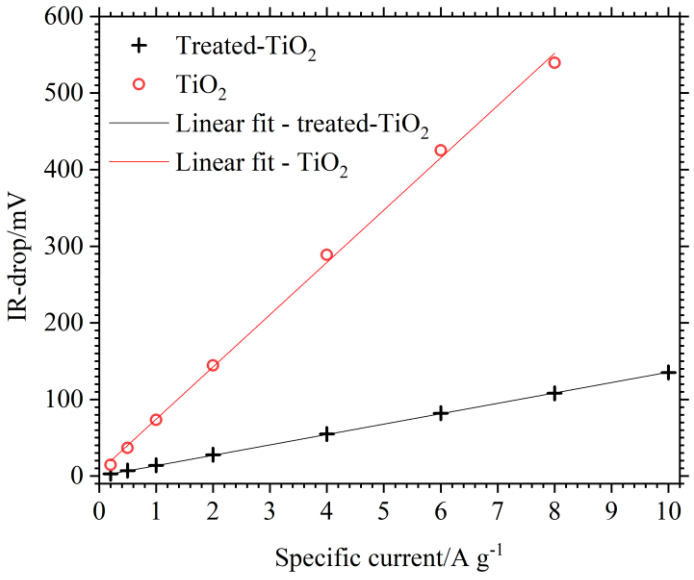

Figure 6.9. Comparison of IR-drop, between charge and discharge, for reduced-TiO_2 (red dots) and TiO_2 (black cross) cycled in 1 mol dm^{-3} $AlCl_3$/1 mol dm^{-3} KCl, vs an SCE reference, as a function of specific current.

The effect of the treatment was further characterised with the use of electrochemical impedance spectroscopy (EIS). TiO_2 and reduced-TiO_2 electrodes were left at OCP before being subject to a

number of EIS protocols. Measurements were performed between 0.1 Hz – 10 kHz with a 20 mV perturbation. Electrodes were analysed in partially charged states by applying a 100 mA g^{-1} charge current to -0.8 V and -0.9 V, holding the electrodes at these potentials for 120 s then performing measurements at OCP.

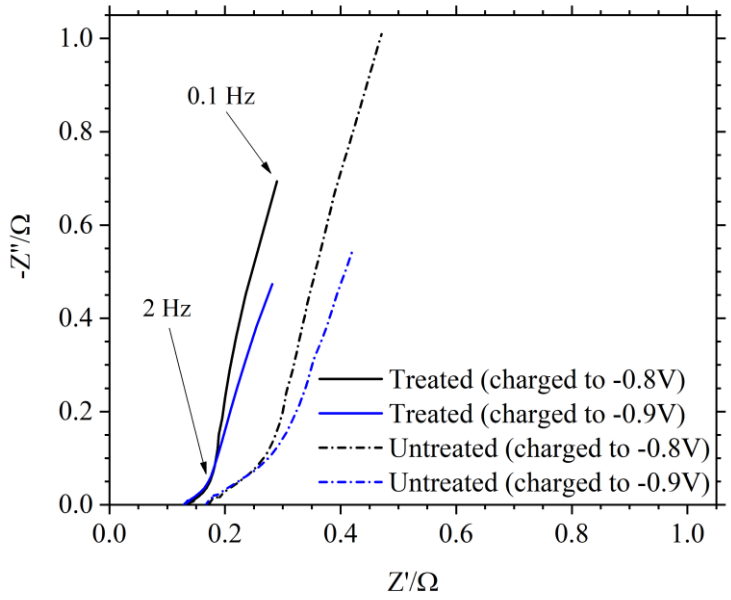

Figure 6.10. Nyquist plot of TiO_2 (dash-dot line) and reduced-TiO_2 (solid line) electrodes. Measurements were taken at OCP, in 1 mol dm^{-3} $AlCl_3$/1 mol dm^{-3} KCl, after being charged to -0.8 V (black) and -0.9 V (blue) vs SCE.

Figure 6.10 gives the Nyquist plot of a pristine and electrochemically treated TiO_2 electrode at OCP after charging to -0.8 V or -0.9 V. For both electrodes, the Nyquist plots follow a ca. 45º impedance line at high to mid frequencies before curving up to a >45º line. This occurs at ca. 2 Hz for the treated electrode and at approximately 1 Hz for the pristine electrode. The characteristic semi-circle present for many insertion battery electrodes is not immediately obvious, suggesting either rapid charge-transfer or a lack of charge-transfer resistance. The >45º slope present at mid to low frequencies further suggest the possibility of capacitive behaviour from the electrodes [202]. However, the plateau observed during galvanostatic cycling, such as in Figure 6.8, indicates a faradaic mechanism being responsible for charge capacity. The lower length of the segment in the high to mid frequency region, of reduced-TiO_2 compared to untreated TiO_2, suggests a lower impedance. This could be assigned to a lower charge transfer resistance if the high frequency region is represented by a depressed semi-circle with a smaller radius. Alternatively, the ca. 45º line may represent a Warburg impedance which can describe the transport of ions through electrode pores [211].

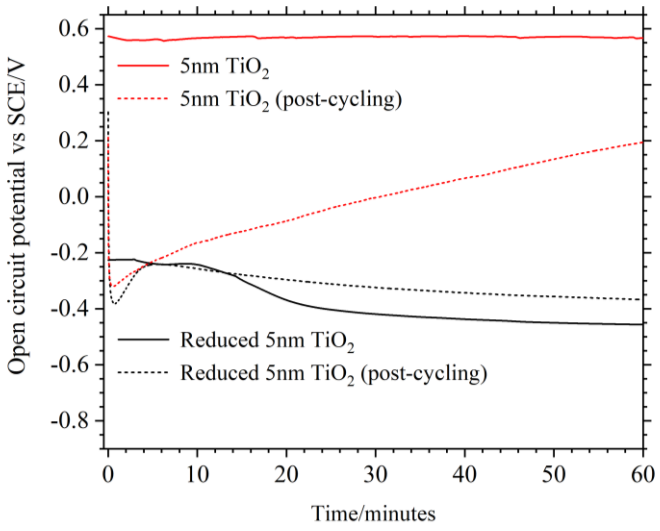

Figure 6.11. 1 hour OCP measurements of TiO_2 (red) and reduced-TiO_2 (black) taken before cycling (dashed-line) and after the cycling regime presented in Figure 6.6 (solid-line).

The potential of TiO_2 and reduced-TiO_2 was measured for 1 hour, in 1 mol dm^{-3} $AlCl_3$/ 1 mol dm^{-3} electrolyte, at open circuit both before and after the cycling regimes seen in Figure 6.7 and Figure 6.8. Figure 6.11 shows the open circuit potential (OCP) of these electrodes before and after cycling. The OCP of TiO_2 (red) before cycling remains stable at around 0.56 V vs SCE. In contrast, reduced-TiO_2 has an initial OCP of -0.23 V, which slowly becomes more negative to a value of -0.26 V after 12 minutes. Between minutes 12 and 22, potential decreases more quickly to -0.40 V where it begins to stabilise, reaching a value of -0.46 V vs SCE after a total of 1 hour at open circuit. During the first 30 seconds at open circuit after cycling (dashed line), the potential of the TiO_2 electrode quickly drops from 0.21 V to -0.32 V. Its potential then curves toward a more positive value, increasing steadily to 0.20 V vs SCE after 1 hour at open circuit. If left for longer at OCP, the electrode would likely have continued toward its initial pre cycling potential of 0.56 V. Similarly, the reduced-TiO_2 electrode drops rapidly during the first 40 seconds at OCP post cycling, from 0.25 V to -0.38 V, before increasing to -0.24 V after approximately 5 minutes. However, at around minute 6, the potential of reduced-TiO_2 post cycling begins to drop again, reaching a value of -0.37 V vs SCE after 1 hour at OCP.

The altered OCP of reduced-TiO_2 could suggest a change in the band gap and charge carrier density of TiO_2. This is further supported by the observed colour change from white to pale-yellow after electrochemical reduction and the presented Mott-Schottky plots. Figure 6.11 also shows that this

change in OCP remains stable in electrolyte and during cycling. The behaviour of both electrodes potentials becoming more negative, after their final discharge, before increasing again is unexpected. Furthering the discussion on charge redistribution in section 5.3.3.3, a similar potential recovery, after a full discharge, has been previously observed in electrochemical capacitors [212]. The phenomenon was explained through charge re-distribution in the porous capacitive electrodes and could be modelled through an equivalent circuit consisting of a series of RC circuits with varying time constants. This is a viable explanation for the potential recovery seen from TiO_2, given the high rate capability as well as evidence for capacitive contribution to charge storage and evidence for charge re-distribution shown in section 5.3.3.3. Nonetheless, the behaviour of reduced-TiO_2 having two inflection points, i.e. the gradient of potential over time changing sign twice, is certainly odd.

A treated-TiO_2 electrode was also cycled to -1.1 V after an initial 50 cycles to -1.0 V. The discharge capacity and coulombic efficiency over these 100 cycles are given in Figure 6.12 (a). At any given specific current, cycling to -1.1 V naturally resulted in an increase in discharge capacity, as also shown in Figure 5.2. However, during extended cycling at 2.0 A g^{-1}, capacity degradation is still accelerated, as shown in Figure 6.12 (b). A capacity of 32.9 mA h g^{-1} during the 100th cycle falls to just 17.1 mA h g^{-1} by cycle 1100. Coulombic efficiency is also marginally lower throughout, falling between 98.0 to 98.8%. The first 100 cycles from the electrode shown in Figure 6.12 (b) were presented in Figure 6.12 (a). The treated-TiO_2 electrode was then compared to an untreated electrode being cycled to -1.1 V vs SCE. Figure 6.13 shows the voltage profile of TiO_2 and treated-TiO_2 cycled at 1.0 A g^{-1} to -1.1 V vs SCE. An increase in discharge capacity is measured from both electrodes: 34.6 mA h g^{-1} and 37.2 mA h g^{-1} for TiO_2 and treated-TiO_2 respectively. However, there is a considerable decrease in coulombic efficiency from as-manufactured TiO_2, measured at only 58.0% compared to 85.0% when cycled to -1.0 V at 1.0 A g^{-1}. In contrast, coulombic efficiency is only marginally lower for treated-TiO_2 at 90.3% compared to 90.9%. This further demonstrates the drastic improvement provided by the electrochemical reduction treatment.

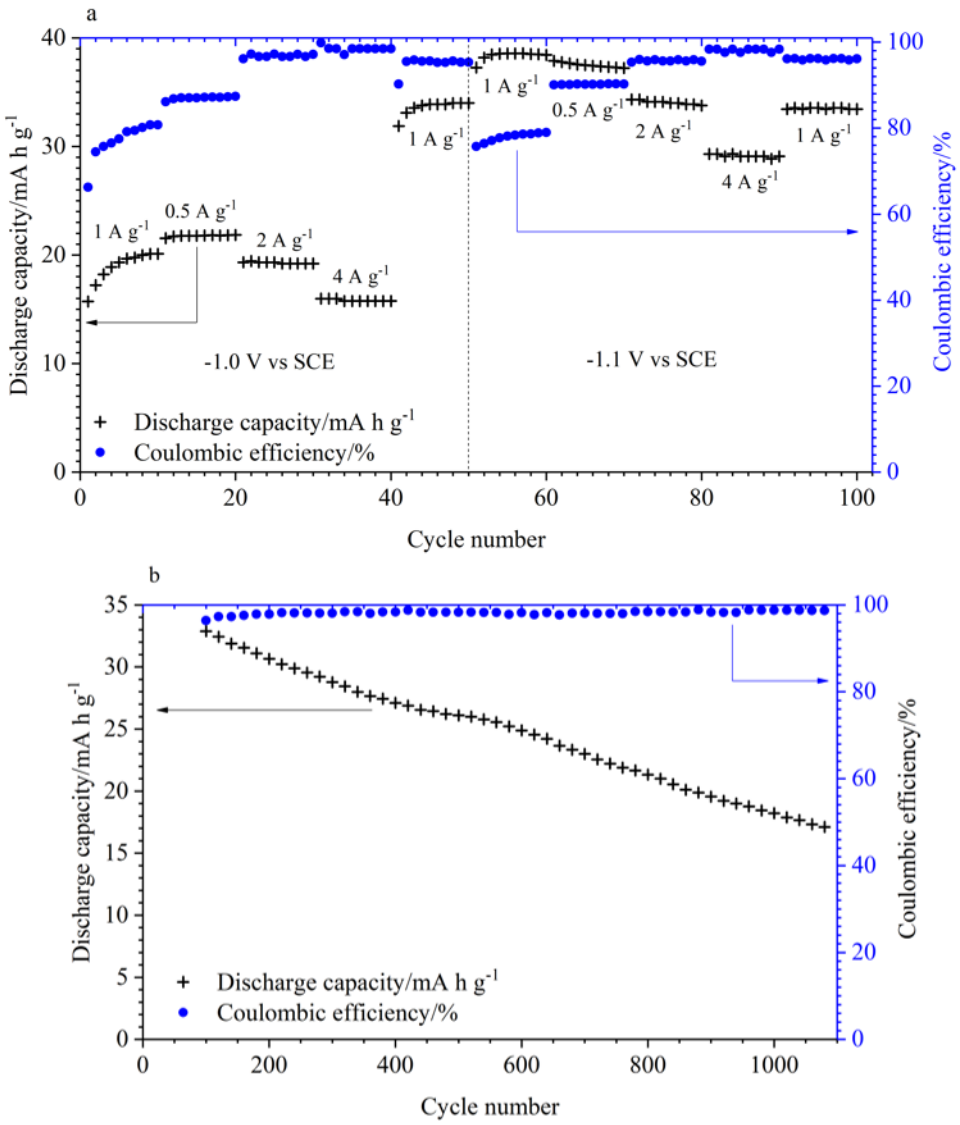

Figure 6.12. Cycling of a treated-TiO_2 electrode in 1 mol dm^{-3} $AlCl_3$/1 mol dm^{-3} KCl. (a) discharge capacity and coulombic efficiency of the first 100 cycles of a treated-TiO_2 electrode at the specified currents between +0.4 to -1.0 V for the first 50 cycles and +0.4 to -1.1 V for cycles 51 – 100. (b) cycling of the same electrode at 2.0 A g^{-1}.

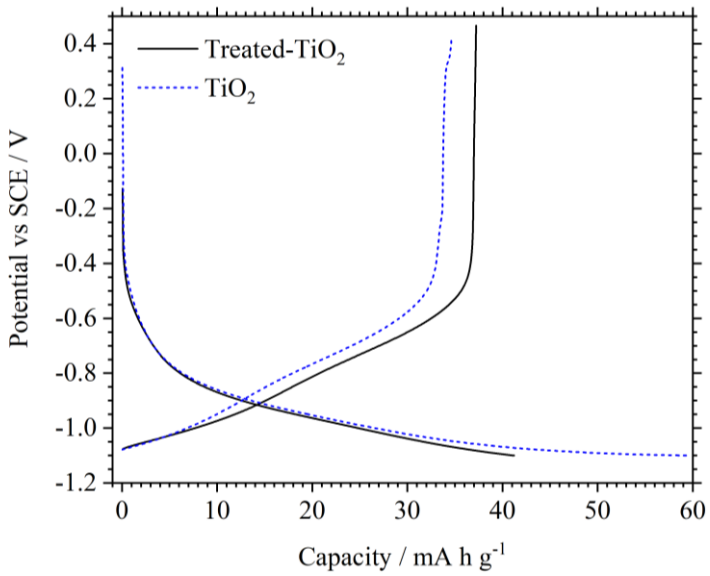

Figure 6.13. Voltage profiles of TiO_2 (blue-dash) and treated-TiO_2 (black) cycled to -1.1 V vs SCE at 1.0 A g^{-1} in 1 mol dm^{-3} $AlCl_3$/1 mol dm^{-3} KCl.

6.4.1 Treatment reliability

Despite attempts at keeping the ink and electrode manufacture process consistent, it needs to be noted that there was some variation in the electrode manufacture process, which lead to variations in electrode performance. For example, the as-manufactured electrode described in the previous section (section 6.4) had a discharge capacity of <5 mA h g^{-1} at 6.0 A g^{-1} where previously (throughout Chapter 5) a capacity of nearly 15 mA h g^{-1} could be maintained at 8.0 A g^{-1}. Variations in ink viscosity, mixing time and mass loading could be responsible for these discrepancies in performance. Direct comparisons within all chapters have been made between electrodes manufactured within the same batch. However, to ensure the effect of the treatment is reliable and to differentiate between performance discrepancies arising from electrode manufacture, the treatment was repeated on both 5 nm and 25 nm electrodes and their performance characterised via constant-current cycling. In addition, the treatment was also applied to a 5 nm electrode using 7.5 wt% polyvinylidene fluoride (PVDF) and 2.5 wt% polytetrafluoroethylene (PTFE) as binders (the effect of ink composition and application techniques are discussed in Chapter 7). Figure 6.14 shows the initial 60 cycles from additional treated-TiO_2 and as-manufactured TiO_2 electrodes (manufactured using 5 nm TiO_2 powder) cycled between +0.4 V to -1.0 V vs SCE, between 0.2 A g^{-1} to 4.0 A g^{-1} in 1 mol dm^{-3} $AlCl_3$/1 mol dm^{-3} KCl. Treated-TiO_2 shows improved discharge capacity and coulombic efficiency throughout while performance from the as-manufactured electrode is similar to the 5 nm electrodes presented in section 5.1.2. Discharge capacity from as-manufactured TiO_2

was approximately 17 mA h g^{-1} at 4.0 A g^{-1} and above 20 mA h g^{-1} from treated-TiO_2, while coulombic efficiency was also higher throughout from the treated-TiO_2 electrode.

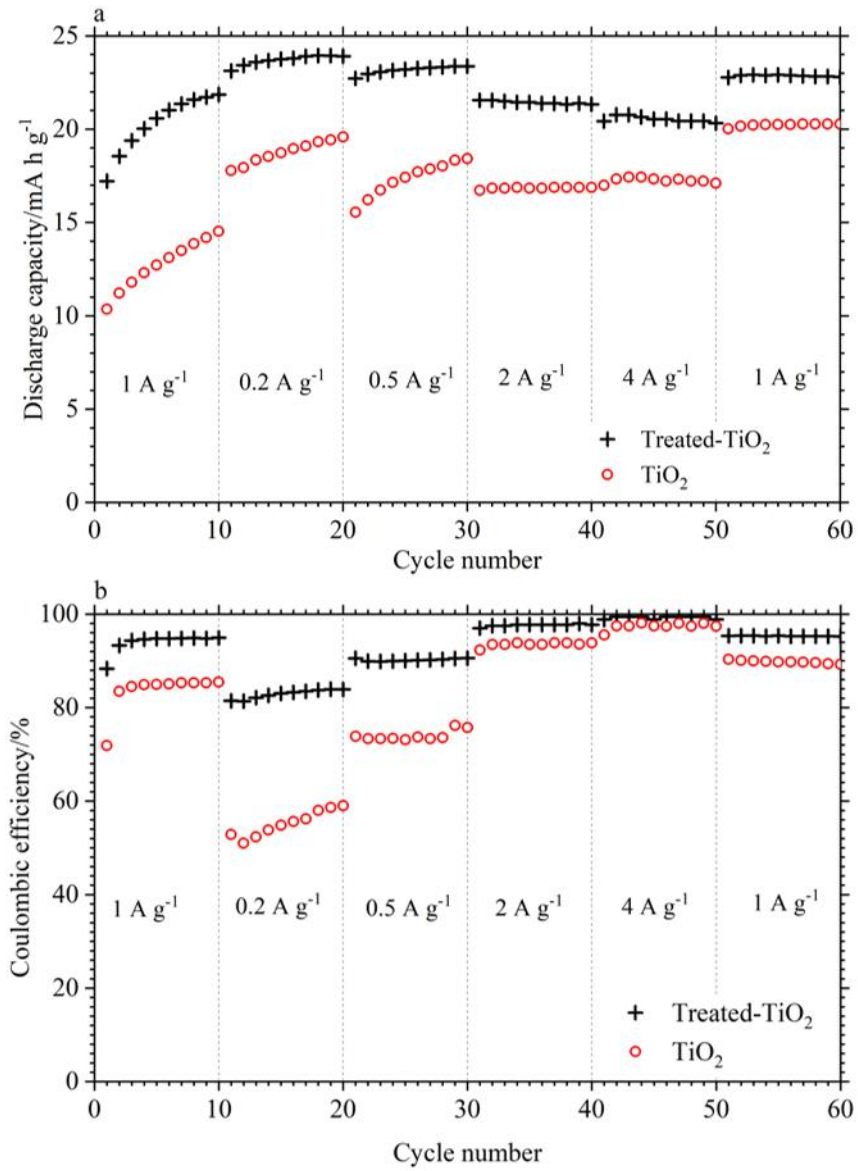

Figure 6.14. Discharge capacity (a) and coulombic efficiency (b), vs cycle number, from a treated-TiO_2 (black cross) and TiO_2 electrode (red circle). Electrodes used 5nm TiO_2 powder, 7.5 wt% Nafion and were cycled in 1 mol dm^{-3} $AlCl_3$/1 mol dm^{-3} KCl.

Figure 6.15 shows the initial 60 cycles from treated and as-manufactured TiO_2 electrodes using 7.5 wt% PVDF and 2.5 wt% PTFE as binders. Carbon black percentage was kept at 5 wt%. During the first 10 cycles at 1.0 A g^{-1} the treated PVDF electrode has a discharge capacity of approximately 30.5 mA h g^{-1} and a coulombic efficiency which increases from 87.2% to 94.5%. The as-manufactured PVDF electrode has a discharge capacity approximately 3 mA h g^{-1} lower, while coulombic efficiency increases from 82.86% to 93.54%. Cycling at 0.2 A g^{-1} and 0.5 A g^{-1}, between the 11th to 30th cycle,

discharge capacity from the treated electrode remains approximately 3 mA h g^{-1} higher at approximately 30.5 mA h g^{-1}. Coulombic efficiency from the treated PVDF increases from 85.88% to 86.1%, from the 11th to 20th cycles at 0.2 A g^{-1}, and increases from 90.3% to 92.4% from the 21st to 30th cycles at 0.5 A g^{-1}. Coulombic efficiency of the as-manufactured PVDF electrode increases from 78.1% to 84.6% from the 11th to 20th cycles at 0.2 A g^{-1} and remains at approximately 89.6% between the 21st to 30th cycles at 0.5 A g^{-1}. At 4.0 A g^{-1}, discharge capacity from treated-TiO_2 is approximately 4.5 mA h g^{-1} higher while the coulombic efficiency of both electrodes are approximately 99%. During the final 10 cycles at 1.0 A g^{-1}, coulombic efficiency from the two electrodes are approximately equal at 96.6%, while discharge capacity from the treated electrode remains approximately 2.7 mA h g^{-1} higher.

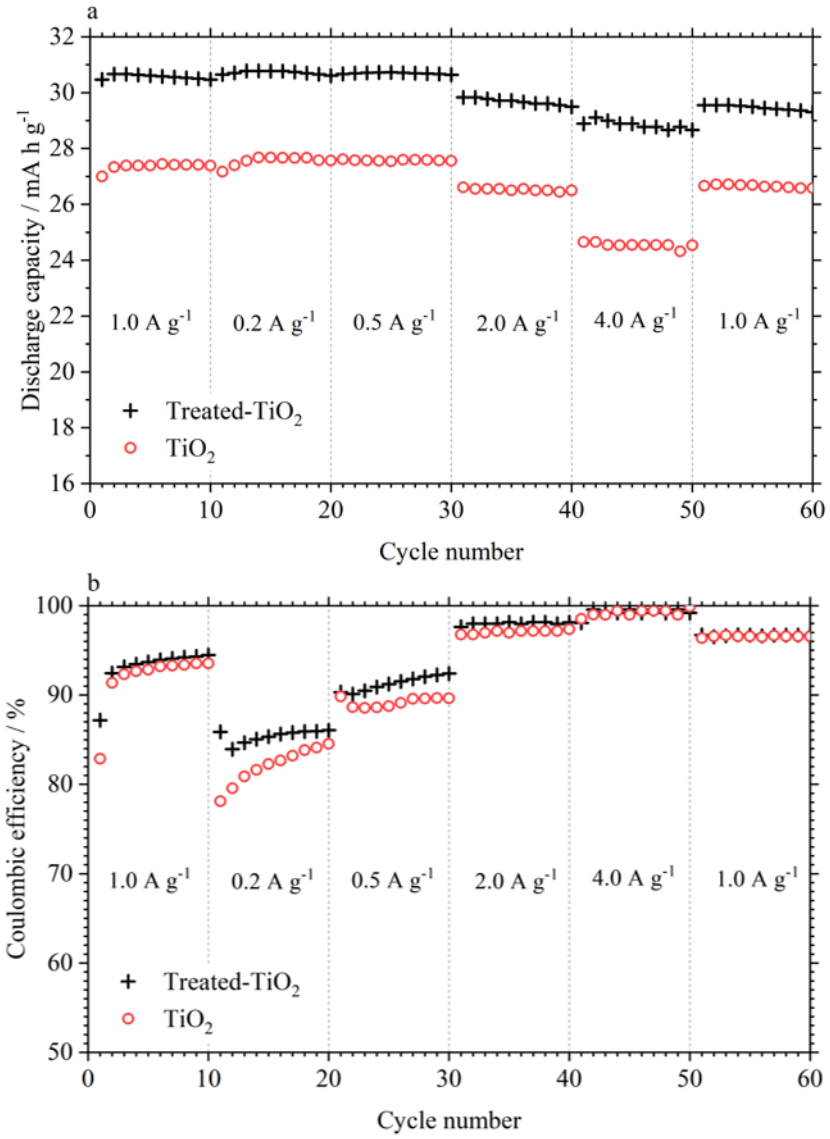

Figure 6.15. Discharge capacity (a) and coulombic efficiency (b), vs cycle number, from a treated-TiO_2 (black cross) and TiO_2 electrode (red circle). Electrodes used 7.5 wt% PVDF and 5 wt% PTFE as binders and 5 nm TiO_2 powder. They were cycled in 1 mol dm^{-3} $AlCl_3$/ 1 mol dm^{-3} KCl.

Similarly, Figure 6.16 gives the discharge capacity and coulombic efficiency from treated and as-manufactured electrode that make use of 25 nm TiO_2 powder as opposed to 5 nm TiO_2 powder. Similar patterns can be seen to previous comparisons of treated and as-manufactured electrodes, where both discharge capacity and coulombic efficiency improved as a result of the cathodic electrochemical treatment in 1 mol dm^{-3} KOH.

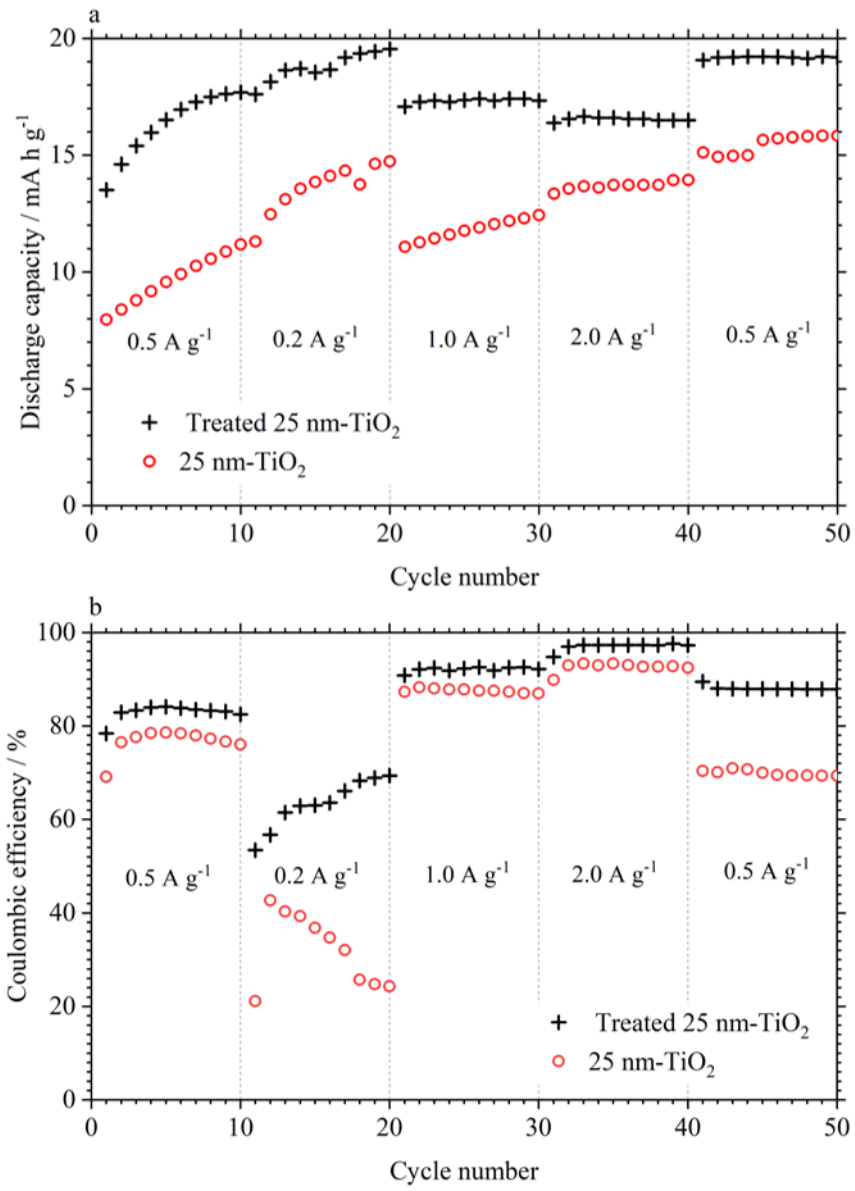

Figure 6.16. Discharge capacity (a) and coulombic efficiency (b), vs cycle number, from a treated-TiO_2 (black cross) and TiO_2 electrode (red circle). Electrodes used a 25 nm TiO_2 powder and 7.5 wt% Nafion as binder and were cycled in 1 mol dm^{-3} $AlCl_3$/1 mol dm^{-3} KCl.

This section has demonstrated the repeatability of the electrochemical treatment, where separate electrodes all demonstrate improved performance during constant-current cycling. However,

further work would be necessary to determine optimum cathodic treatment time and potential, whilst treatment in electrolytes other than 1 mol dm^{-3} KOH may also affect electrode performance and characteristics. The use of PVDF binder in place of Nafion also resulted in higher initial discharge capacities. Approximately 27 mA h g^{-1} and 30.5 mA h g^{-1} were measured from the as-manufactured and treated electrodes, when cycled at 1.0 A g^{-1}, with coulombic efficiencies remaining above 90%. The reason for this improved capacity is unclear though factors such as improved or more uniform adhesion could be a factor. The effect of binder choice, carbon black loading and ink application techniques are discussed further in Chapter 7.

6.5 Conclusions

Electrochemically treated TiO_2 electrodes were prepared through a potentiostatic hold at -1.4 V vs SCE, in 1 mol dm^{-3} KOH. The electrochemical reduction protocol was shown to be repeatable and improved capacity, coulombic efficiency and stability during initial cycling. Conductivity also improved, observed via EIS and analysis of the IR-drop between charge and discharge cycles. It is demonstrated that the electrochemical treatment described can improve the performance of composite TiO_2 electrodes for use in aqueous Al-ion batteries, while it may also be feasible to apply the technique to titanium oxide electrodes in other metal-ion batteries. A discharge capacity of 15.3 mA h g^{-1} was possible from treated-TiO_2 at 10.0 A g^{-1} – the highest specific current recorded from TiO_2 in aqueous Al^{3+} electrolyte and a higher specific current than recorded from $NaTi_2(PO_4)_3$ or $Li_4Ti_5O_{12}$ in aqueous Na-ion cells [117, 210]. Furthermore, a capacity of 28.5 mA h g^{-1} was measured at 4.0 A g^{-1} from a treated electrode using PVDF as the primary binder. This is compared to approximately 24.5 mA h g^{-1} from an un-treated electrode with the same constituent make-up. The observed improvements to coulombic efficiency and stability during the first 10 cycles are particularly important for use in full cells but still requires further improvements and understanding. Cycling a separate treated-TiO_2 electrode at 1.0 A g^{-1} allowed a capacity of 37.2 mA h g^{-1} at 90.3% coulombic efficiency, where an as-manufactured TiO_2 electrode produced 34.6 mA h g^{-1} at a much lower coulombic efficiency of 58.0%, further demonstrating the improved stability from the electrochemically treated TiO_2 electrodes.

It cannot be ruled out that the electrochemical reduction process improves performance through factors such as improved electrode wetting or enhanced surface area. However, neither SEM imaging nor XRD analysis showed any structural or bulk crystallographic change from treated-TiO_2. XPS showed no measureable change in the surface oxidation state of treated-TiO_2, though this could have been due to re-oxidation of Ti^{3+} in air, given the ex-situ manner of the analysis. However,

the observed colour change and different OCP values of the electrodes suggest a change in the band gap, which would be consistent with the introduction of Ti^{3+}. This change in OCP also remains stable in the electrolyte and during cycling. Furthermore, a Mott-Schottky plot implied treated-TiO_2 to have a greater electron charge carrier number, which would be the expected result from the introduction of Ti^{3+} or oxygen vacancies. Further careful analysis of the Mott-Schottky plots could also be performed and would allow estimations of electron density and the flat band potential. Given the improved performance from treated-TiO_2 and the likely reduction of Ti^{4+} to Ti^{3+} during the treatment, the work in this chapter also highlights the importance of TiO_2 doping for improved electrode performance in high-rate, aqueous electrolyte batteries.

Chapter 7 Electrode manufacture and composition

7.1 Vacuum impregnation for improved performance

The data presented in Chapter 5 suggested a likelihood that charge storage in TiO_2 is partially a result of a capacitive or surface storage mechanism. Evidence for this came from the relatively low capacities and high specific currents as well as the electrochemical impedance spectroscopy (EIS) responses seen in Figure 6.10 and the cyclic voltammetry (CV) responses at different scan rates. Increasing the amount of surface available for capacitive storage is possible by ensuring that electrolyte/electrode contact is maximised, since electrolyte penetration through the pores of the electrodes may be hindered by the surface tension of the electrolyte at macro-, meso- and micro-pore openings. Figure 7.1 (a) shows the N_2 adsorption and desorption isotherms of 5 nm TiO_2, at -196°C, obtained using a Gemini 2375 analyser. The profile bears similarity to a type IV isotherm, according to the IUPAC classification, demonstrating mesoporous structure (2-50 nm). The Brunauer-Emmett-Teller (BET) surface area was calculated to be 260.4 $m^2\ g^{-1}$ and is in relatively good agreement with the advertised surface area of 289 $m^2\ g^{-1}$. Figure 7.1 (b) gives the pore size distribution, where a dominant peak can be seen at approximately 50 Å. The distribution of pore sizes is observed to be predominantly between 25 Å and approximately 100 Å, which could arise from pores within and between individual nanoparticles as well as between nanoparticle agglomerates. As such, improved performance could be obtained by increasing electrode/electrolyte contact. Previous constant-current cycling data has also shown that some initial cycling (ca. 20 cycles) is necessary before stable capacities and efficiencies are reached, which could be due to gradual electrode wetting during those initial cycles. To improve electrode wetting and electrolyte impregnation, electrodes were subjected to a vacuum impregnation technique, which removes air from the porous electrode, replacing it with electrolyte. The experimental set-up used is shown in Figure 7.2 with a proposed schematic of how electrolyte is forced into electrode pores being presented in Figure 7.3. The technique had previously been reported by Yong et al for the impregnation of textile supercapacitor electrodes with gel electrolytes [213].

In contrast to previous chapters, the TiO_2 electrodes here made use of a slightly altered ink composition. Electrodes consisted of 85 wt% TiO_2, 5 wt% carbon black and 6 wt% Nafion/4 wt% polytetrafluoroethylene (PTFE). The addition of PTFE allowed for electrodes with higher mass loadings with the effect of different binder types discussed in section 7.2. Forced electrode wetting was performed using a vacuum pump connected Buchi tube, where a TiO_2 electrode was submerged in the electrolyte of 1 mol dm^{-3} $AlCl_3$/1 mol dm^{-3} KCl. A Fischerbrand vacuum filtration pump was used to create a vacuum of 20 mbar with the electrode left for ca. 10 minutes. The air

vent was then opened, letting air in, before the process was repeated a further three times by which point air bubbles were no longer visible at the electrode surface. The electrode was then transferred to a 3-electrode cell and its electrochemical performance tested.

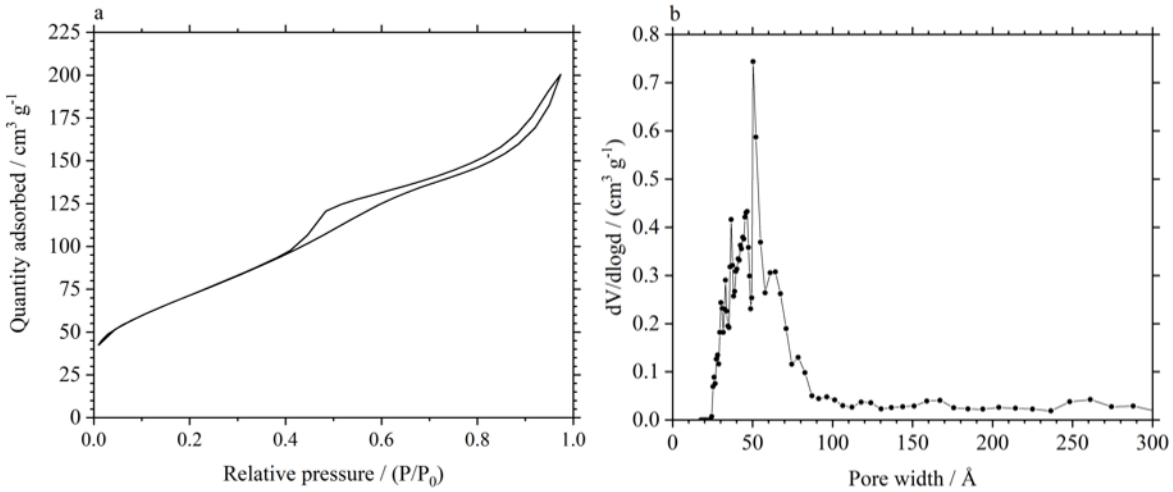

Figure 7.1. (a) Nitrogen adsorption and desorption isotherms and (b) pore size distribution of 5 nm TiO_2 powder, at -196°C.

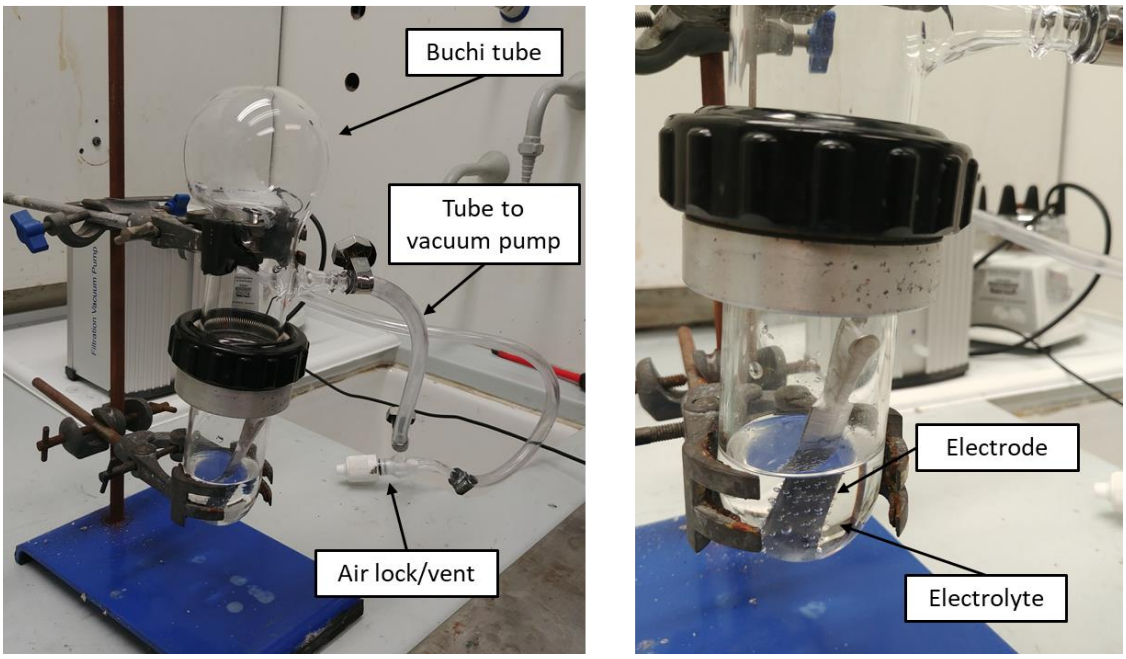

Figure 7.2. Experimental set-up for vacuum impregnation and removal of air pockets from composite electrodes.

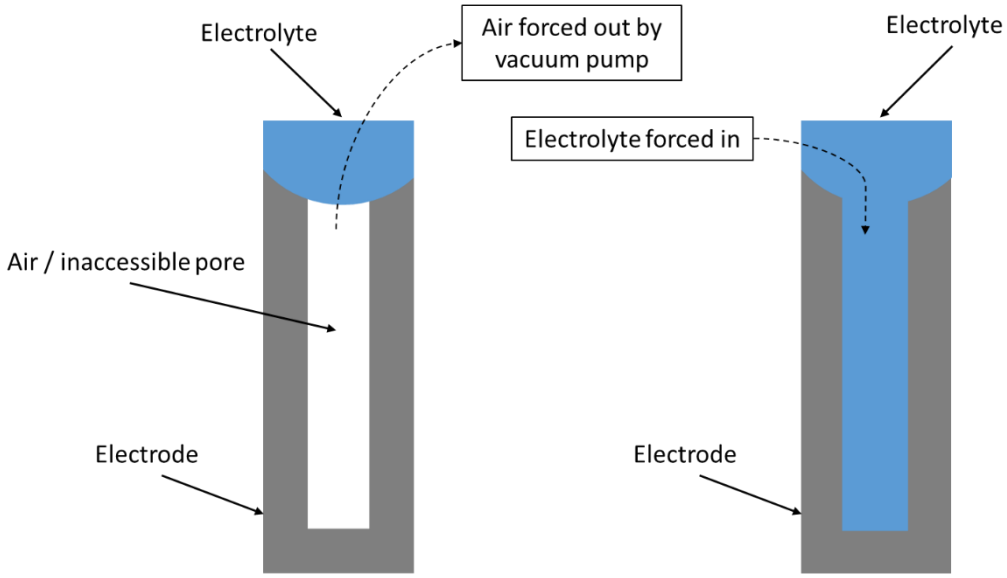

Figure 7.3. Schematic of the proposed process by which air is removed from electrode pores, forcing electrolyte in.

7.1.1 Vacuum impregnation of TiO_2

An as-manufactured and a vacuum impregnated electrode were tested via constant current cycling in 1 mol dm^{-3} $AlCl_3$/1 mol dm^{-3} KCl between +0.4 V to -1.0 V vs SCE. The as-manufactured electrode was cycled at specific currents between 0.2 A g^{-1} to 6.0 A g^{-1} with the vacuum impregnated electrode cycled between 0.2 A g^{-1} to a maximum specific current of 40.0 A g^{-1}. Figure 7.4 gives the discharge capacity (a) and coulombic efficiency (b) of the two electrodes against cycle number. Discharge capacity of the as-manufactured electrode can be seen to increase steadily during the 1st 10 cycles, from 13.7 mA h g^{-1} to 18.9 mA h g^{-1}. Discharge capacity increases more slowly during the next 10 cycles at 0.5 A g^{-1}, increasing from 19.9 mA h g^{-1} to 21.2 mA h g^{-1}. The discharge capacity measured from the vacuum impregnated electrode is more stable over these 1st 20 cycles, increasing from 18.8 mA h g^{-1} to 20.2 mA h g^{-1}, from the 1st to the 10th cycle at 1.0 A g^{-1}. Discharge capacity then increases from 20.8 mA h g^{-1} to 21.6 mA h g^{-1} between the 11th and 20th cycles at 0.5 A g^{-1}. For both electrodes, discharge capacity remained relatively stable during cycling thereafter. The discharge capacity of as-manufactured TiO_2 was around 19.1 mA h g^{-1} at 2.0 A g^{-1} between cycle 21-30, 16.5 mA h g^{-1} between cycle 31-40 at 4.0 A g^{-1} and 14.4 mA h g^{-1} between cycle 41-50 at 6.0 A g^{-1}. In contrast, vacuum impregnated TiO_2 shows a lower drop in discharge capacity with increasing specific current. Discharge capacity was approximately 19.9 mA h g^{-1} at 2.0 A g^{-1} between cycle 21-30 but at 6.0 A g^{-1}, between cycle 41-50, discharge capacity remained at approximately 19.0 mA h g^{-1}. Specific current was then incrementally increased past the 70th cycle, where the discharge

capacity of the vacuum-impregnated electrode remained above 15.0 mA h g^{-1} at the very high specific current of 40.0 A g^{-1}.

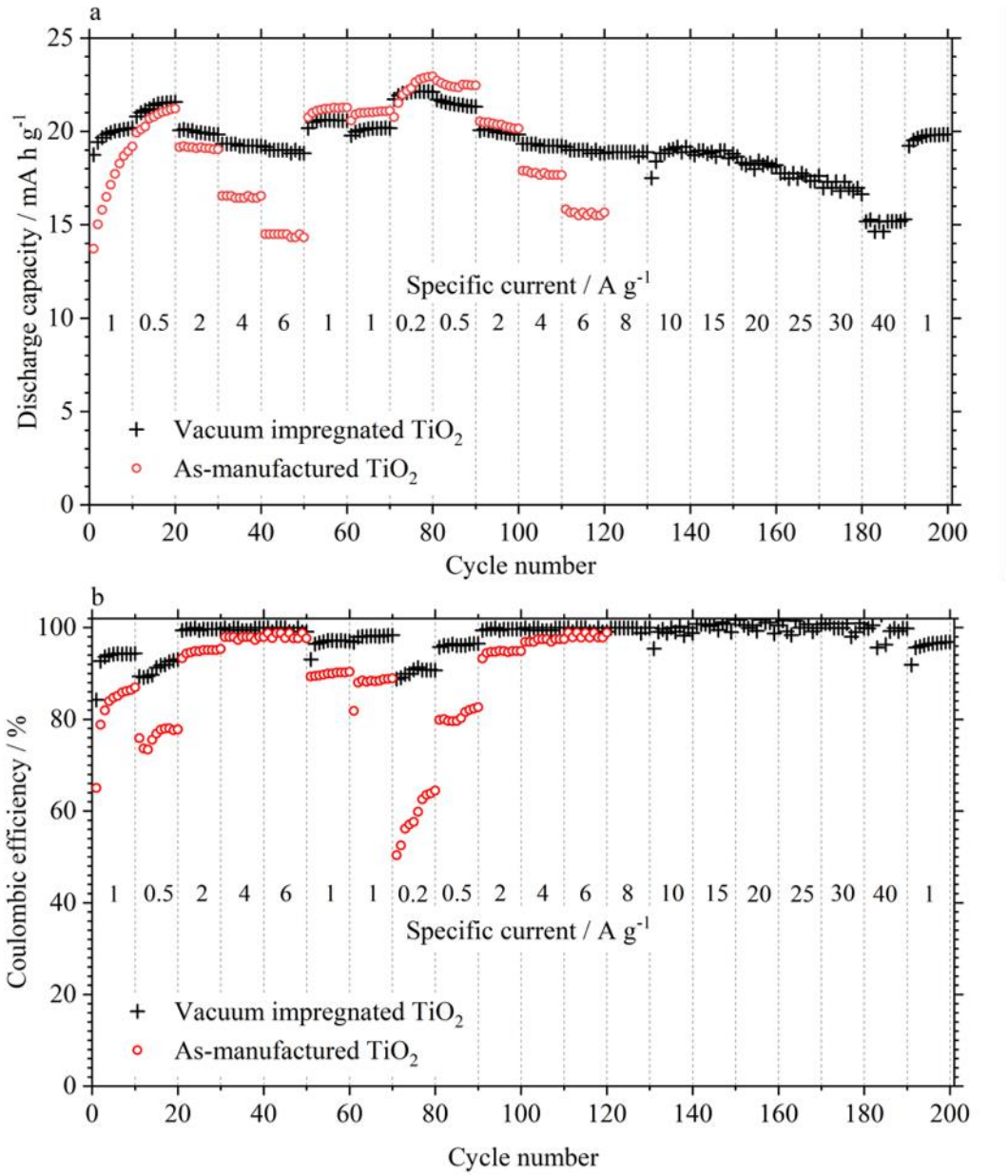

Figure 7.4. (a) Discharge capacity and (b) coulombic efficiency vs cycle number of an as-manufactured and vacuum impregnated TiO_2 electrode. Cycles were performed in 1 mol dm^{-3} $AlCl_3$/1 mol dm^{-3} KCl between +0.4 V to -1.0 V vs SCE.

Coulombic efficiency was also improved throughout cycling because of the impregnation process. During the 1st 10 cycles at 1.0 A g^{-1}, coulombic efficiency increased from 65.1% to 87.0%. During the next 10 cycles at 0.5 A g^{-1}, coulombic efficiency increased from around 75.0% to 77.8%. The vacuum impregnated electrode had an initial coulombic efficiency of 84.2%, which increased to 92.7% during the 2nd cycle and 94.38% by the 10th. From cycle 11-20 at 0.5 A g^{-1}, coulombic efficiency

increased from 89.3% to 93.1%. Coulombic efficiency from the vacuum impregnated electrode remained higher throughout cycling, but is noticeably higher and more stable at specific currents ≤2.0 A g^{-1}. At 0.2 A g^{-1}, measured between cycle 71-80, coulombic efficiency from the as-manufactured electrode increased from 50.4% to 64.5%, while the increase was from 88.8% to 90.6% with the impregnated electrode. It should be noted that the small variability in capacity and efficiency between cycles at a given high specific current (ca. >10 A g^{-1}) is likely to be due to measurement errors as a result of the fast charge discharge times. For example, at 40.0 A g^{-1} discharge occurs in 1.43 seconds, so that a high measurement rate of 80 data points per second was required.

Figure 7.5 shows the voltage drop between charge and discharge potential as function of specific current. The data was taken from the 10th cycle at a given specific current between the 61st and 120th cycle for the as manufactured electrode, and between the 61st and 200th cycle for the impregnated electrode. For both electrodes, the IR-drop increases linearly. The IR-drop form the as-manufactured TiO_2 electrode increased from 4.5 mV at 0.2 A g^{-1} to 137.3 mV at 6.0 A g^{-1}, while the impregnated electrode increased from 1.1 mV at 0.2 A g^{-1} to 166.6 mV at 40.0 A g^{-1}. The voltage profiles from the vacuum impregnated electrode between 0.2 A g^{-1} to 4.0 A g^{-1} are given by Figure 7.6 (a), with Figure 7.6 (b) showing the profiles when cycled between 10.0 A g^{-1} to 40.0 A g^{-1}. The voltage profiles are observed to be similar, irrespective of the specific current used.

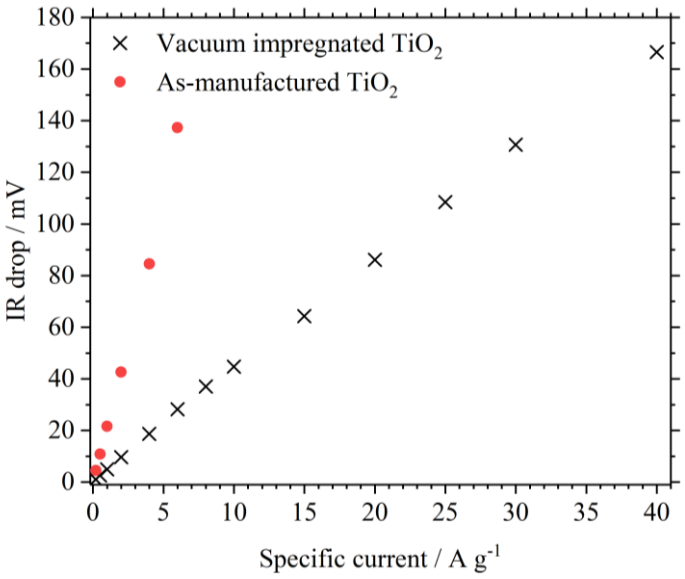

Figure 7.5. IR-drop between charge and discharge, vs specific current, from an as-manufactured (red circle) and impregnated TiO_2 (black cross) electrode cycled against an SCE reference between +0.4 V to -1.0 V in 1 mol dm^{-3} $AlCl_3$/1 mol dm^{-3} KCl.

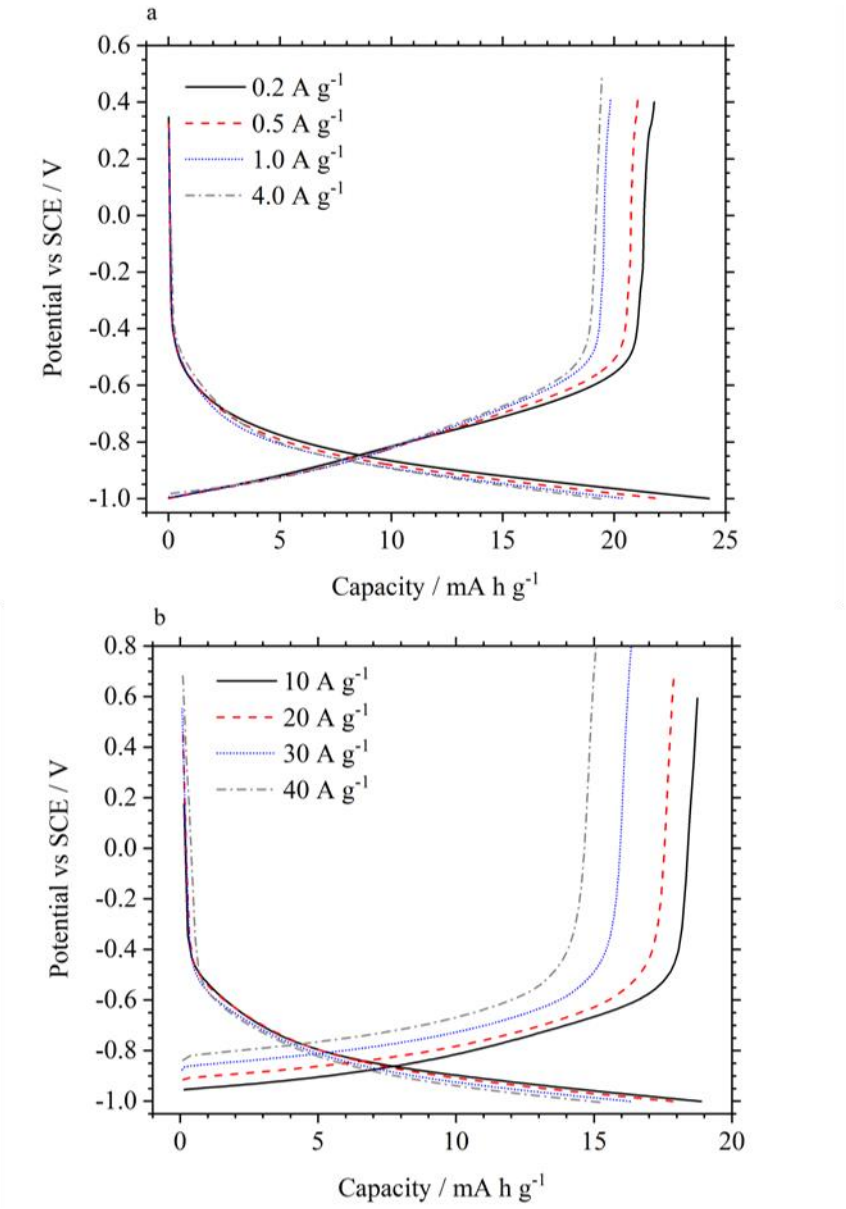

Figure 7.6. Voltage profiles of a vacuum impregnated TiO_2 electrode cycled in 1 mol dm^{-3} $AlCl_3$/1 mol dm^{-3} KCl against an SCE reference between specific currents of (a) 0.2 A g^{-1} to 4.0 A g^{-1} and (b) 10.0 A g^{-1} to 40.0 A g^{-1}.

The results presented in Figure 7.4 and Figure 7.6 show that though there is a negligible change in the discharge capacity of the vacuum impregnated electrode, compared to previous TiO_2 electrodes, there is a clear improvement to rate capability. This is likely due to greater electrode-electrolyte contact, where electrode pores previously inaccessible to electrolyte, as a result of surface tension and the hydrophobicity of the nanopowder electrode, are filled with electrolyte due to the removal of air and creation of low pressure voids within the electrode. The relative stability of the voltage profiles and capacity, where discharge capacity drops by <25% over an order of

magnitude increase in specific current, provides evidence that charge storage from these TiO_2 electrodes in aqueous Al^{3+} electrolyte are predominantly capacitive or surface controlled reactions.

It should also be noted that the experiment was performed on electrodes with relatively high mass loadings, of 6.5 mg cm^{-2} and 6 mg cm^{-2} for the vacuum impregnated and as-manufactured TiO_2 electrodes, respectively (achieving these mass loadings will be discussed further in the next section). Therefore, cycling the 8 cm^2, vacuum impregnated electrode at 40.0 A g^{-1} corresponds to a high current density of 260 mA cm^{-2}. This high specific current is considerably higher than the next highest reported by Lahan et al [137], where a capacity of approximately 15 mA h g^{-1} was measured at 6.25 A g^{-1}, while the coulombic efficiency can be estimated from the reported voltage profile to be only approximately 50%. The size and mass loading of the TiO_2 electrode are also likely to be higher than reported in the literature, where measurements are often performed on very small and thin electrodes - an important point when considering electrode manufacture scale-up. For example, Lahan et al [137] present no information on electrode size or thickness, while Kazazi et al [136] performed measurements on their TiO_2 nanospheres on electrodes with a 10 mm diameter (< 1 cm^2) without an indication of mass loading. Comparing to a relatively high performing aqueous lithium supercapacitor device, Pazhamalai [166] presented a graphene/MnHCF device capable of 31 Wh kg^{-1} at 3.2 kW kg^{-1}, which corresponded to a current density of only 5 mA cm^{-2} based on the mass of MnHCF.

7.1.2 Vacuum impregnation of CuHCF

The same vacuum impregnation procedure was also performed on a CuHCF electrode with a mass loading of 8.8 mg cm^{-2}. Performance was characterised in a 3-electrode cell through constant current cycling in 1 mol dm^{-3} $AlCl_3$/1 mol dm^{-3} KCl between 0.4 V to 1.0 V vs SCE. These results were then compared to an as-manufactured CuHCF electrode with a mass loading of 8.0 mg cm^{-2}. Figure 7.7 shows the charge and discharge capacities of the two electrodes during the initial 50-60 cycles with 10 cycles being performed at various specific currents.

Figure 7.8 (a) shows the charge discharge profile from an as-prepared CuHCF electrode being cycled at specific currents of 1.0, 2.0, 4.0 and 6.0 A g^{-1}, while Figure 7.8 (b) shows the charge-discharge profiles of a vacuum impregnated electrode being cycled between 1.0 A g^{-1} to 8.0 A g^{-1}. Figure 7.7 shows that both electrodes demonstrate a stable capacity throughout with coulombic efficiency being close to 100% after the 1st cycle. The as-manufactured electrode demonstrates a reversible capacity of 42.9 mA h g^{-1}, which drops to 34.2 mA h g^{-1} at 4.0 A g^{-1}. At 6.0 A g^{-1}, capacity is only 14.1 mA h g^{-1}. At 1.0 A g^{-1}, the capacity of the vacuum impregnated electrode is higher at 47.1 mA h g^{-1}.

Incremental reductions in capacity are observed with increasing specific current, where capacity drops from 33.0 mA h g^{-1} at 6.0 A g^{-1} to 28.1 mA h g^{-1} at 8.0 A g^{-1}. Figure 7.8 shows the expected increase in potential hysteresis, with increasing specific current, between charge and discharge.

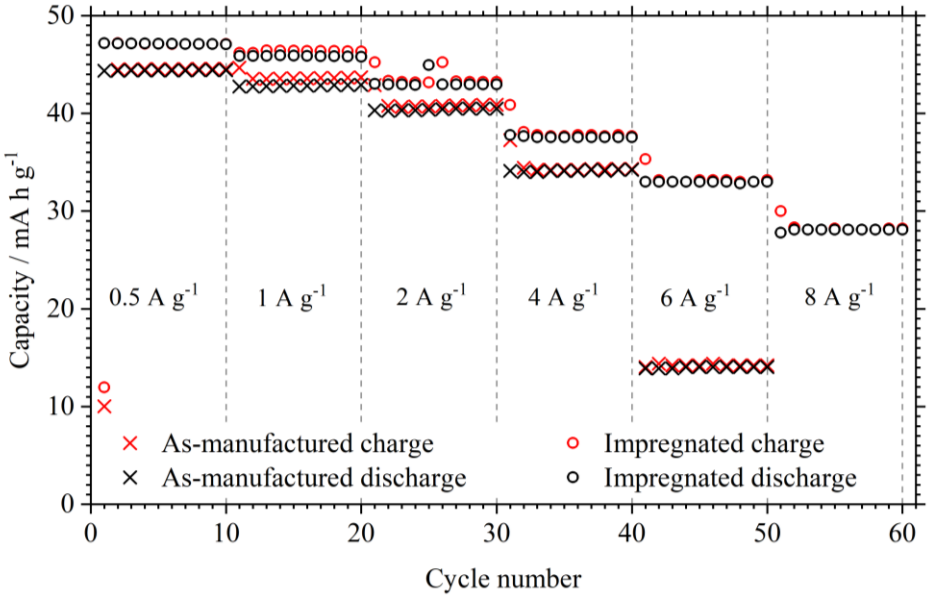

Figure 7.7. Charge and discharge capacity from the first 60 cycles of an-manufactured (crosses) and vacuum impregnated (circle) CuHCF electrode in 1 mol dm^{-3} $AlCl_3$/1 mol dm^{-3} KCl.

Figure 7.9 plots the potential hysteresis, defined as the difference between the average charge and average discharge potentials, against the specific current used during cycling. For both electrodes, the potential hysteresis increases linearly with increasing specific current. At 0.5 A g^{-1}, a hysteresis of 40.2 mV and 57.8 mV was measured from the vacuum impregnated and as-manufactured CuHCF electrode, respectively. These values increase to 351.3 mV at 8.0 A g^{-1} from the impregnated electrode and to 547.3 mV at 6.0 A g^{-1} from the as-manufactured electrode.

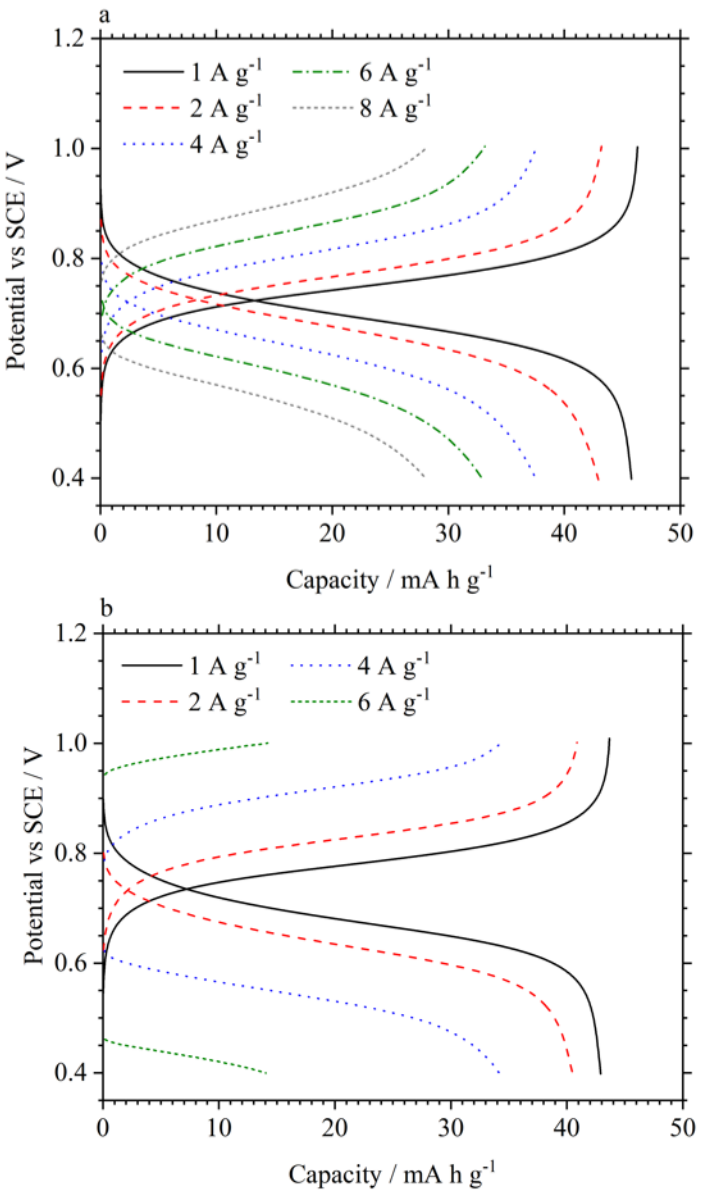

Figure 7.8. Charge-discharge profiles of a vacuum impregnated electrode (a) and an as-prepared CuHCF electrode (b). Both were cycled galvanostatically between 0.4 V to 1.0 V vs SCE in 1 mol dm^{-3} $AlCl_3$/1 mol dm^{-3} KCl.

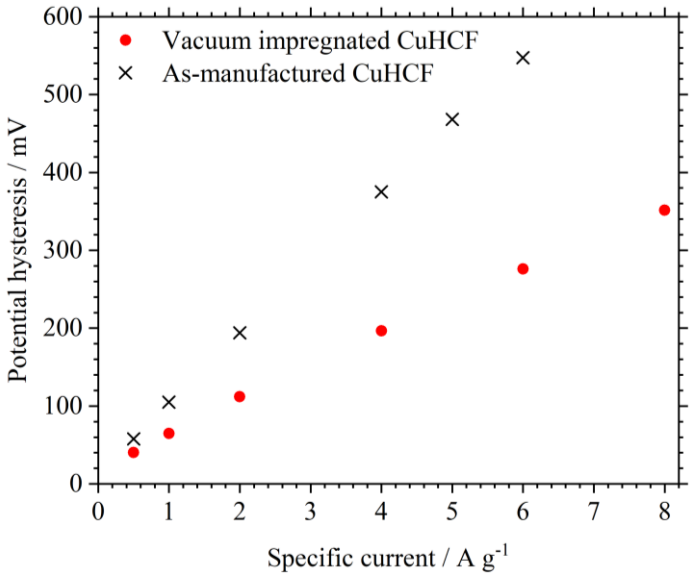

Figure 7.9. Potential hysteresis from an as-prepared CuHCF (black-cross) and a vacuum impregnated electrode (red-dot) cycled in 1 mol dm^{-3} $AlCl_3$/1 mol dm^{-3} KCl.

At the high rates of 40.0 A g^{-1}, the capacity and potential hysteresis from CuHCF would limit cell performance. Alternative materials that can maintain capacity at these high currents would therefore be required for an efficient, high power cell, though specific currents as high as 40 A g^{-1} are rarely reported. Manganese oxides may be a potential option with important characteristics such as low cost and toxicity. Feng et al demonstrated high rate capability from a manganese oxide electrode cycled between 0 V to 1 V vs SCE in 1 mol dm^{-3} Na_2SO_4 [214]. The electrode maintained a capacity of approximately 60 mA h g^{-1} at 50 C (1 C = 200 mA g^{-1}), though voltage profiles were omitted such that a large potential hysteresis may have been present at higher rates. Nevertheless, the results obtained from both the TiO_2 and CuHCF electrodes in the previous sections demonstrate the applicability of the vacuum impregnation process for improving the performance of electrodes in aqueous electrolytes.

7.2 Polymer binders and electrode manufacture techniques

7.2.1 Binder options

This section provides a brief comparison and discussion of the binder options available for the manufacture of composite electrodes. Polyvinylidene fluoride (PVDF) is a widely used binder in the literature as well as in commercial Li-ion batteries. However, concerns exist over the toxicity,

environmental impact and potential carcinogenic effects of N-Methyl-2-pyrrolidone (NMP), which is required as a solvent. As such, Nafion, which can make use of propanol and water as solvents, was used as the default binder for the construction of TiO_2 and CuHCF electrodes. Nevertheless, performance differences between electrodes using PVDF and Nafion was briefly explored, since good electrode adhesion is vital for electrode performance. A TiO_2 electrode was constructed using 5.0 wt% carbon black and 7.5 wt% PVDF dissolved in NMP. Additional water and propanol was then added and the ink magnetically stirred for 30 minutes before being sonicated for 30 minutes. The resulting ink was then coated onto carbon polymer current collectors and left to dry overnight in a fume cupboard. Table 7.1 gives the discharge capacity and coulombic efficiency of TiO_2 electrodes, at 0.2, 1.0 and 4.0 A g^{-1}, using either PVDF, Nafion or a Nafion/PTFE mix as binders. Using PVDF as binder results in discharge capacities of 27.6, 27.4 and 24.5 mA h g^{-1} at 0.2, 1.0 and 4.0 A g^{-1}. AS eluded to in section 6.4.1, the discharge capacities of electrodes using PVDF as a binder are therefore higher than previous electrodes using only Nafion as binder, especially at 4.0 A g^{-1}. The improvements to capacity may be the result of greater adhesion of electrode constituents, to each other and or the current collector, resulting in lower resistance through the electrode. Factors such as electrode wettability may also be altered with the use of PVDF. Additionally, PTFE was explored as a potential binder with an electrode using a PTFE/Nafion mix presenting similar performance to a Nafion only electrode. The electrodes described in Table 7.1 had mass loadings between 2.8 mg cm^{-2} and 3.1 mg cm^{-2}. However, using 6 wt% Nafion/4 wt% PTFE did allow for mass loadings as high as 6.5 mg cm^{-2}, as described in section 7.1.1.

Table 7.1. Typical discharge capacity and coulombic efficiency of TiO_2 electrodes using either PVDF, Nafion or a Nafion/PTFE mix as binders. Electrodes were cycled in 1 mol dm^{-3} $AlCl_3$/1 mol dm^{-3} KCl to a minimum potential of -1.0 V vs SCE.

	Discharge capacity / mA h g^{-1} (coulombic efficiency)		
Binder used	**0.2 A g^{-1}**	**1.0 A g^{-1}**	**4.0 A g^{-1}**
PVDF 7.5%/PTFE 2.5%	27.6 (84.5%)	27.4 (93.5%)	24.5 (99.9%)
Nafion 7.5%	23.5 (91.8%)	20.9 (98.4%)	16.2 (99.2%)
Nafion 6%/PTFE 4%	25.1 (77.6%)	20.1 (95.3%)	15.8 (98.4%)

While the use of PVDF may be difficult due to concerns over its toxicity and environmental impact, improvements to electrode performance are possible through changes to the electrode ink composition, namely, the binder used. This was also demonstrated in section 6.4.1, where an electrochemically treated electrode using PVDF as binder allowed for further improvements to capacity (30.5 mA h g^{-1} at 1.0 A g^{-1}).

7.2.2 Electrode spray coating

A number of coating techniques exist, in both the literature and industry, for the application of electrode inks. A popular method involves the creation of a soft electrode pellet, using PTFE as the binder, before pressing the electrode into a disk under pressure. Electrodes are then often dried at elevated temperatures. Homogenous dispersion of active materials can be difficult using this method since PTFE often results in the creation of thicker pastes as opposed to inks. The method used throughout has been the manual coating of electrode inks, using Nafion as the binder, with any excess allowed to drip off, before electrodes are laid flat and allowed to dry at ambient conditions. Additional layers are then added once previous applications have dried. Spray coating can allow for greater uniformity of the coatings as well as more control over the mass loading applied, though some variance in the application of coatings is inevitable without automating the process.

Four TiO_2 electrode inks were prepared using a similar process described in section 3.2.2 but with two of the electrodes spray-coated using a Badger air brush 350 in conjunction with a Clarke Wiz mini air compressor. Inks were sprayed at a pressure between 2 – 2.5 bar. The four electrodes prepared from two ink compositions via drip or spray coating are named E_1, E_2, E_3 and E_4 and are summarised in Table 7.2. E_1 refers to the drip-coated electrode using an ink composition of 87.5 wt% TiO_2, 7.5wt% Nafion and 5 wt% carbon black. E_2 refers to an electrode using the same ink composition but spray coated as opposed to drip coated. E_3 refers to the drip-coated electrode with an ink composition of 85 wt% TiO_2, 6 wt% Nafion, 4 wt% PTFE and 5 wt% carbon black, while E_4 refers to the spray-coated electrode also using this ink composition. An additional 15 minute sonication of the inks was also employed before application in order to disperse PTFE. To maintain consistency between ink preparations, this was also applied to inks without PTFE. Figure 7.10 shows photographic images of the four electrodes. From left to right are E_1, E_2, E_3 and E_4. Relatively even coatings can be seen for all the electrodes. E_2, which was prepared by spray coating an ink using 7.5 wt% Nafion, has a lighter colour than the other 3 electrodes, while the coating had a more powdery texture. This indicated comparatively poor adhesion to the carbon polymer current collector.

Table 7.2. Summary of the two ink compositions used to compare spray and drip coating inks.

Electrode	Coating method	Ink composition
E_1	Drip coated	87.5 wt% TiO_2, 7.5 wt% Nafion, 5.0 wt% carbon black
E_2	Spray coated	87.5 wt% TiO_2, 7.5 wt% Nafion, 5.0 wt% carbon black
E_3	Drip coated	85.0 wt% TiO_2, 6.0 wt% Nafion, 4.0 wt% PTFE, 5.0 wt% carbon black
E_4	Spray coated	85.0 wt% TiO_2, 6.0 wt% Nafion, 4.0 wt% PTFE, 5.0 wt% carbon black

Figure 7.10. From left to right are photographic images of E_1, E_2, E_3 and E_4.

Figure 7.11 (a) shows the discharge capacity from these electrodes during the first 10 cycles performed at 1.0 A g^{-1} in 1 mol dm^{-3} $AlCl_3$/1 mol dm^{-3} KCl. The discharge capacity of E_1 increases from 10.4 mA h g^{-1} to 14.5 mA h g^{-1}, while E_2 has a much lower discharge capacity of 1.4 mA h g^{-1}. E_3 had the highest initial discharge capacity, increasing from 20.2 mA h g^{-1} to 22.8 mA h g^{-1}, while E_4 increased from 8.8 mA h g^{-1} to 12.8 mA h g^{-1}. The coulombic efficiencies of E_1, E_3 and E_4 reached 85.5%, 91.1% and 65.2% respectively. Spray-coating electrodes without the addition of PTFE

resulted in almost negligible discharge capacities. A possible reason could be that during the spray process a certain amount of dissolved Nafion is vaporised, so that the deposited electrode has a lower Nafion percentage than the ink. While reducing the spray pressure may reduce this effect, the minimum possible pressure of approximately 2 – 2.5 bar was already being used. However, the spray painting of electrode inks was possible, though the addition of PTFE was required to obtain comparable results and no discernible performance improvement was observed. Indeed, the best performance over the 1st 10 cycles was obtained from a drip-coated electrode using 6 wt% Nafion/4 wt% PTFE as opposed to 7.5 wt% Nafion only. In conjunction with the figures shown in Table 7.1, it can be suggested that there remains room for further optimisation of electrode ink compositions.

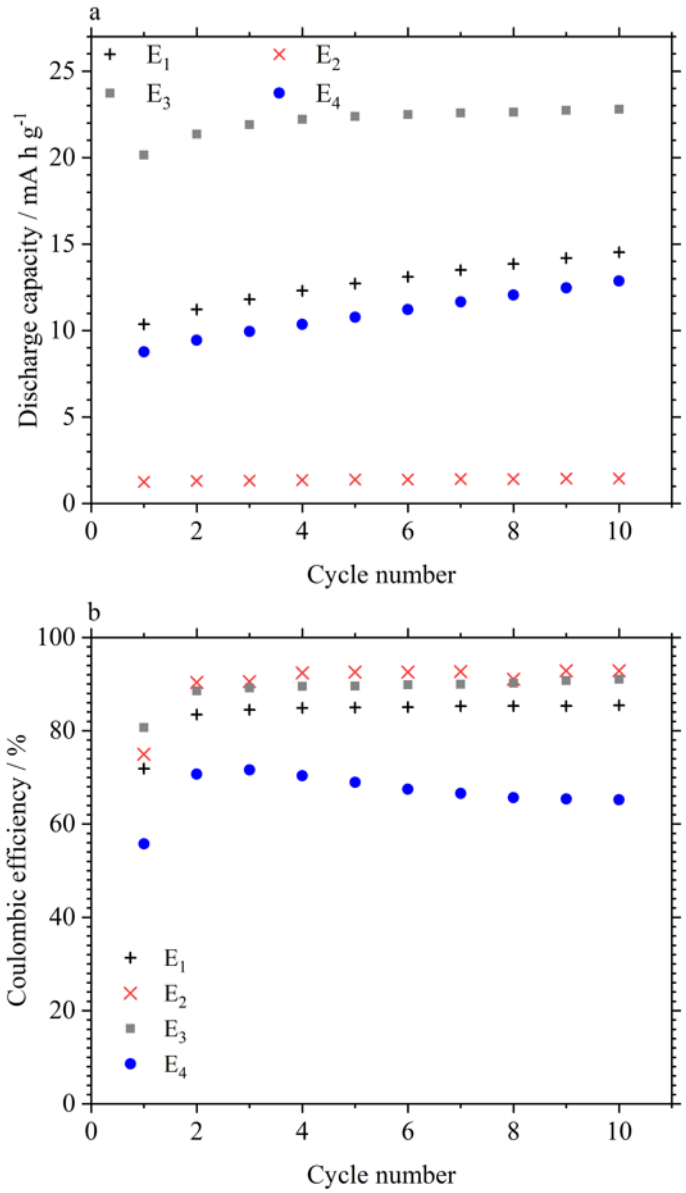

Figure 7.11. Comparison of the discharge capacity (a) and coulombic efficiency (b) of TiO_2 electrodes, during the first 10 cycles at 1.0 A g^{-1}. E_1 was drip coated using 7.5 wt% Nafion. E_2 was spray-coated using 7.5 wt% Nafion. E_3 was drip-coated using 6 wt% Nafion/4 wt% PTFE. E_4 was spray coated using 6 wt% Nafion/4 wt% PTFE.

7.3 Carbon black percentage

Throughout the project, the amount of carbon black (CB) used has been 5 wt%. However, cycling at higher rates may require higher percentages of conductive additive with much of the literature, regarding composite insertion and capacitive electrodes, using 10 wt% conductive additive as a default. To probe this more systematically, electrodes were manufactured with 2.5, 5.0, 7.5 and 10.0 wt% carbon black. 6.0 wt% Nafion and 4.0 wt% PTFE were used as binders. Electrodes were cycled between 0.4 V and -1.0 V vs SCE in 1 mol dm^{-3} $AlCl_3$/1 mol dm^{-3} KCl at specific currents of 0.2 A g^{-1} and 2.0 A g^{-1} after an initial 80 cycles at specific currents between 0.2 A g^{-1} to 3.0 A g^{-1}. Table 7.3 gives the discharge capacity and coulombic efficiencies of the four electrodes. At 0.2 A g^{-1}, a discharge capacity of 24.6 mA h g^{-1} is measured with 5.0 wt% CB. This is 6.8% and 11.7% lower when using 7.5 wt% and 2.5 wt% CB respectively. Coulombic efficiency is also highest using 5.0 wt% CB, measured at 87.9% compared to 83.8% and 76.5% for 7.5 wt% and 2.5 wt% CB electrodes, respectively. Performance using 10 wt% CB was considerably worse, resulting in a capacity of 10.5 mA h g^{-1} and a coulombic efficiency of 20.0%. At 2.0 A g^{-1}, coulombic efficiencies for electrodes with 2.5, 5.0 and 7.5 wt% CB are between 97.5% and 98.1%. Discharge capacity is again highest for 5.0 wt% CB at 19.9 mA h g^{-1}. Using 7.5 wt% CB results in a lower discharge capacity of 15.2 mA h g^{-1} with 10.9 mA h g^{-1} measured from the electrode using 2.5 wt% carbon black. While a capacity of 18.4 mA h g^{-1} was measured from the electrode using 10.0 wt% CB, coulombic efficiency was only 86.6%. These results suggest that an optimal carbon black percentage exists at approximately 5.0 wt%.

Table 7.3.* Discharge capacity and coulombic efficiency of TiO_2 electrodes with differing percentages of carbon black additive when cycled in 1 mol dm^{-3} $AlCl_3$/1 mol dm^{-3} KCl at 0.2 A g^{-1} and 2.0 A g^{-1}. Data corresponds to the 90th and 100th cycle for each electrode.

	0.2 A g^{-1}		2.0 A g^{-1}	
Carbon black percentage / %	**Discharge capacity/mA h g^{-1}**	**Coulombic efficiency/%**	**Discharge capacity/mA h g^{-1}**	**Coulombic efficiency/%**
2.5	19.3	76.5	10.9	97.5
5.0	24.6	87.9	19.9	98.6
7.5	23.0	83.8	15.2	98.1
10.0	10.5	21.0	18.4	86.6

.

7.4 Conclusions

The work in this chapter shows that a number of ink and electrode manufacturing parameters affect electrode performance. Further work would require a systematic approach to optimise factors such as the carbon black percentage, mass loading, ink application process, binder type and binder percentage. However, the work presented in this chapter provides compelling evidence that the capacity from as-manufactured TiO_2 electrodes (using commercial powders) is limited to less than 30 mA h g^{-1}, irrespective of ink composition. A vacuum impregnation technique was also presented and was shown to improve the rate capability of TiO_2 in aqueous Al^{3+} electrolyte by forcing electrolyte to fill voids within the electrode to improve contact between electrolyte and electrode. In this work, it improved the rate capability of both TiO_2 and CuHCF. A vacuum impregnated TiO_2 electrode was able to maintain a capacity of >15 mA h g^{-1} at the very high specific current of 40 A g^{-1} (260 mA cm^{-2}) with nearly 100% coulombic efficiency. As previously stated, this specific current is considerably higher than the next highest reported by Lahan et al [137] and improves upon the current density (5 mA cm^{-2}) of a high performing aqueous lithium supercapacitor device (31 Wh kg^{-}

* Data was taken during a mini-project for a post-graduate student, Ben Craig. I set out the scope for this work and provided supervision for electrode manufacturing, electrochemical cell set-up, software/hardware use and analysis of data.

[1] at 3.2 kW kg^{-1}), reported by Pazhamalai et al [166] by nearly two orders of magnitude [166]. The impregnation technique was repeated on a CuHCF electrode. The increased rate capability also measured from CuHCF suggests the possibility of repeating this simple technique on various electrode materials and electrolytes. Certainly, it would be interesting to observe whether the rate capability of higher capacity electrodes can be similarly improved.

Chapter 8 Conclusions and future work

The work presented in this thesis followed three core lines of study. The first revolved around a proof-of-concept cell; the second around understanding the storage mechanism and performance characteristics of TiO_2 as a negative electrode; and the third consisted of improving the performance of TiO_2, which has desirable characteristics in terms of material availability, cost, non-toxicity and environmental benignity.

A cell consisting of TiO_2, CuHCF and 1 mol dm^{-3} $AlCl_3$/1 mol dm^{-3} KCl electrolyte was constructed and its performance characterised, while a 2-cell battery was also shown to function with the use of a bipolar electrode. While cells functioned in $AlCl_3$ only, energy efficiency improved with the addition of KCl due to the more facile intercalation of K^+ into CuHCF, as expected from the literature and preliminary results. The cell could therefore be considered a dual-ion chemistry, requiring Al^{3+} for charge storage at TiO_2 and K^+ for improving the performance of CuHCF. A single cell was shown to be capable of 1750 cycles when cycled at 20 C (333 mA g^{-1}) and energy efficiency between 70-80% throughout, though specific energy was low at ca. 14 mW h g^{-1}. A separate cell, cycled at various specific C-rates demonstrated reasonable power capability, producing a specific energy of >16 W h kg^{-1} at 0.3 kW kg^{-1} and maintained >14.5 W h kg^{-1} at 2.6 kW kg^{-1}. Cell failure was due to the degradation of CuHCF, despite 28000 cycles being possible in a 3-electrode cell, tested over nearly 6 weeks. This was due to the <100% coulombic efficiency of TiO_2, which resulted in the consistent overcharging of CuHCF. As a result, a second potential plateau was observed during galvanostatic cycling. The mechanism for this plateau was at least partially electrochemically reversible and therefore unlikely to be due to O_2 evolution only, though was likely to have caused some dissolution of the electrode, given the yellow colour of the electrolyte after full cell cycling and the presence of Fe^{3+}, which was confirmed using UV-vis spectroscopy. Therefore, the section highlights the importance of full cell characterisation and that the primary limitation of the cell chemistry arises from the <100% coulombic efficiency of TiO_2. This meant that a number of questions relating to CuHCF remained open for future study. For example, the electrochemical reaction behind the 2nd plateau or the effect of crystallinity and shape homogeneity of the synthesised CuHCF on electrode performance.

Subsequent chapters focussed on the characterisation of TiO_2 electrodes in aqueous Al^{3+}-containing electrolytes. Charge storage was found to be due to Al^{3+} rather than H^+, while negligible charge capacity was measured from electrolytes containing Na^+, K^+ or Mg^{2+}. It was demonstrated that electrodes manufactured using TiO_2 nanopowders could provide rate capability comparable to supercapacitor electrodes, where a capacity of nearly 20 mA h g^{-1} could be maintained at C-rates of

360C (7.2 A g^{-1}). Given the high rate capability but relatively low capacity, it was possible that charge storage was due to a surface controlled mechanism, such as the adsorption of Al^{3+} onto TiO_2 causing the reduction of Ti^{4+} to Ti^{3+}. This was further explored through CV scans over a range of scan rates, which demonstrated a capacitive or surface controlled contribution to charge storage.

It was also explicitly shown that coulombic efficiency decreased with specific current, suggesting a time-dependent self-discharge mechanism. Previous publications overlooked any discussion of this, despite coulombic efficiencies of <100% being clear from their presented voltage profiles. Purging electrolytes with dry N_2 improved coulombic efficiency due to the removal of dissolved O_2, which would otherwise oxidise Ti^{3+} within the charged TiO_2 electrode. Electrode self-discharge also increased with decreasing pH, suggesting H_2 evolution as another cause of inefficiency, despite cyclic voltammetry not showing H_2 evolution at potentials < -1.3 V vs SCE. This could also explain the appearance of electrode cracking, shown via SEM images after ca. 5000 cycles, where H_2 bubbles could force loss of contact between electrode particles and the electrode coating with the current collector. As a result, purging the electrolyte with H_2 resulted in a small decrease in the rate of self-discharge. Furthermore, analysis of OCP self-discharge profiles showed a $t^{1/2}$ dependence, suggesting a diffusion limited process, which could be attributed to the diffusion of O_2 or H^+ through the electrode. At high specific currents of >1 A g^{-1}, the existence of charge redistribution was also shown to exist, due to inhomogeneous charging of the electrode, though this was not a major cause of inefficiency. Further work should certainly be carried out to fully understand the causes of inefficiency and self-discharge. For example, while N_2 or H_2 purged electrolytes were used, experiments were still carried out in air with cells covered with parafilm and tape to limit exposure. Therefore, the presence of O_2 within the electrolyte could not be entirely ruled out.

In an attempt to improve the performance of TiO_2 in aqueous $AlCl_3$, an electrochemical doping technique was applied to electrodes. The only other TiO_2 electrode for aqueous Al-ion batteries that demonstrated high coulombic efficiency came from a black TiO_2. XPS suggested the presence of Ti^{3+} as well as hydrogen and nitrogen bonds. However, electrochemical treatment would be considerably simpler than the solution plasma process method used to produce the black TiO_2. The electrochemical treatment of TiO_2 was carried through holding the electrode -1.4 V vs SCE for 15 minutes in 1 mol dm^{-3} KOH. The treatment did improve coulombic efficiency, especially at low specific currents of 0.2 A g^{-1} and 0.5 A g^{-1}, though coulombic efficiency still decreased with decreasing specific current. XPS analysis of treated electrodes showed no evidence of Ti^{3+}, which could suggest that any Ti^{3+} formed, was oxidised upon contact with air or that doping occurred within the bulk. However, Mott-Schottky plots showed a three order of magnitude decrease in C^{-2} from a treated electrode, suggesting an increase in the electron carrier number. Further work should be carried to out to ascertain whether the treatment resulted in the presence of Ti^{3+}, oxygen

vacancies or other dopants such as K^+. Because Ti^{3+} is paramagnetic, EPR measurements would give rise to signal if Ti^{3+} were present within TiO_2. Additionally, UV-vis could measure any change in band gap energy, though again the ex-situ nature of these techniques may result in the re-oxidation of any surface Ti^{3+}.

The final chapter brought together a number of electrode manufacture parameters that affected electrode performance, primarily of TiO_2 electrode performance. Of particular interest, was the use of a vacuum impregnation technique to improve electrolyte impregnation into the electrode. The technique allowed for a considerable improvement to the rate capability of both TiO_2 and CuHCF electrodes, which had high mass loadings of approximately 6.5 mg cm^{-2} and 8.8 mg cm^{-2}, respectively. A capacity of approximately 20 mA h g^{-1} was measured from TiO_2 at a specific current of 1 A g^{-1}, which dropped by only 25% when cycled at the very high specific current of 40 A g^{-1}. The mass loading of the electrode meant the corresponding current density was 260 mA cm^{-2}. These specific current and current density values are considerably higher than most pseudocapacitive materials presented in the literature. The rate capability of CuHCF was also improved, though less drastically. A capacity of 33 mA h g^{-1} was measured from the vacuum impregnated electrode at 6 A g^{-1}, compared to only 14 mA h g^{-1} from the as-manufactured electrode when cycled at the same specific current.

The primary novel outputs of this work relate to a better understanding of TiO_2 used as a negative electrode in aqueous Al^{3+}-containing electrolytes, as well as the techniques investigated for improving performance, i.e. the electrochemical treatment and vacuum impregnation. Electrodes were demonstrated to have superior rate capability and cycle lives to previously reported TiO_2 electrodes. Furthermore, the thesis reiterates the importance of considering full cell systems, where any discrepancy between electrode efficiencies or performance can lead to the accelerated degradation of the opposite electrode and therefore the cell. Nevertheless, TiO_2, which is an abundant, chemically stable and non-toxic material, showed promising rate capability and reasonable cycle life. Given the relatively low capacities, a higher cycle life would be necessary for its use to be attractive in high rate applications. Use in aqueous intercalation, hybrid or dual-ion cells would also require a better understanding and improvement of coulombic efficiency at low specific currents and should be the primary focus of any future study.

8.1 Future work

The conclusions presented above as well as within the main body of the text highlight various aspects of this project that require further work and experimentation. Specific lines of work are outlined here.

- For determining the working ion within TiO_2 i.e. Al^{3+}, H^+ or K^+ and the stoichiometry of working ion intercalated (or more likely adsorbed) per unit charge storage, a quartz microbalance experiment can be devised. Active material can be applied to a quartz substrate to be used as a working electrode in a 3-electrode set-up. Combining electrochemical and quartz microbalance measurements is then achieved through overlapping a DC voltage with a high frequency AC voltage. Mass changes due to adsorption/desorption species during charge and discharge changes the resonant frequency of the quartz and can therefore help elucidate the species responsible for charge storage [180]. Calculating the quantity of Al^{3+} adsorption at TiO_2 electrodes could also allow for an estimation of the electron transfer stoichiometry and therefore the underlying reaction responsible for charge storage. The experiment could also be used to confirm the preferential intercalation of K^+ over Al^{3+} for CuHCF. Further clarifying the charge storage mechanism of TiO_2 in aqueous Al^{3+} containing electrolytes could also make use of in-situ XRD or TEM. X-ray absorption spectroscopy could also be used to provide insight into the redox state of Ti at various states of charge or after the electrochemical reduction protocol outlined in Chapter 6.
- To further examine the causes of self-discharge at the TiO_2 electrode, chronoamperometric experiments should be performed. Here, the potential of a TiO_2 electrode is held at a constant value, for example at -1.0 V vs SCE, and the current decay measured. A plot of the current decay against $t^{-1/2}$ can be used in conjunction with the Cottrell equation, assuming a linear plot, to determine a diffusion co-efficient and help elucidate the species responsible for self-discharge. The Cottrell equation was given in section 5.3.3 by Equation (5.3). As shown in Section 5.3, the relatively low coulombic efficiency of TiO_2 is partially due to the evolution of H_2 at negative potentials. This would fundamentally limit the cycle life and usability of a full cell aqueous Al-ion system. Therefore, experiments should also be performed in a fully controlled environment, i.e. with fully de-oxygenated electrolytes as well as use of an inert atmosphere for electrode manufacture, cell construction and electrochemical testing.

- Further work can be carried out on the effect of particle size, surface area, pore size and pore size distribution of TiO_2 particles on their performance in Al^{3+} containing aqueous electrolytes i.e. capacity, efficiency, rate capability etc.
- Chapter 6 presented experiments detailing the effect of an electrochemical treatment on the performance of TiO_2. It was suggested that the improved performance was a result of the treatment was due to self-doping of the TiO_2 causing a shift in the flat band potential and an increase in the electron donor density. It would be interesting to expand this work by performing UV-vis and EPR measurements to determine whether it resulted in the introduction of Ti^{3+} or O_2 vacancies. Furthering this, other methods of doping, for example via the reduction of TiO_2 in a H_2 atmosphere or through metal doping during synthesis, should be explored and their effects on performance metrics, especially coulombic efficiency, quantified. In addition, there is scope to optimise the electrochemical reduction protocol, for example, through changes to the electrolyte, reduction potential or reduction time.
- Similarly, while some variety of electrode ink preparation techniques were tested and outlined in Chapter 7, optimisation of parameters including the type and ratio of binder, conductive additive and solvent could be carried out. A fully consistent and repeatable ink coating technique would also be desirable.

Appendix A

A.1 Future work for improving capacity – titanate nanotube electrodes

Commercially available TiO_2 powders have been used within this work, guaranteeing availability. It also reduces the possibility of variations in synthesised materials from separate batches thus improving quality control and repeatability. Scaling electrode size is also more easily achievable and are more likely to be cost effective in comparison to synthesis methods for novel nanostructures. However, while good rate capability and reasonable cycle life have been achieved using commercial TiO_2 nanopowders, capacity still remains relatively low. Synthesis of nanostructures such as nanotubes and nanosheets provides a possible route to improve capacity. Titanate nanotubes (TiNTs) were therefore synthesised by a hydrothermal method and tested as electrodes in aqueous Al^{3+} electrolytes. This hydrothermal method should lend itself to scalability more readily than other nanotube synthesis routes, such as titanium foil anodisation, which has been previously used for aqueous Al-ion cells.

A.2 Synthesis of titanate nanotubes

Synthesis of nanotubes closely followed the reflux method reported by Bavykin et al [215]. KOH was added to 250ml 10 mol dm^{-3} NaOH to achieve a 1:25 ratio of KOH to NaOH. The solution was transferred to a PTFE autoclave and 25.6 g of p25 TiO_2 (Alfa-Aesar) added to the solution. A reflux was set-up and the magnetically stirred solution heated to 120°C with a temperature of 120-140°C maintained for 48 hours using a heating mantle. The solution was allowed to cool to room temperature and transferred to a separate PTFE bottle. Additional water was mixed in with the solution before allowing sediment to settle before carefully discarding the excess water. This washing process was repeated until the solution reached a pH of 9.1. 0.1 mmol dm^{-3} HCl was then added to bring down the pH to 1.8 and convert sodium titanate nanotubes to poly-titanic acid, $H_2Ti_nO_{2n+1}$. The process of decanting and washing with water was repeated to bring conductivity down to 25 $\mu S\ cm^{-1}$. The sediment was allowed to settle for a final time, excess water removed, and the sediment dried in an oven at 100°C for 24 hours. Calcined nanotubes were prepared by heating at 450°C for an additional 8 hours.

A.3 XRD and TEM characterisation

Figure A.1 (a) shows the XRD patterns of synthesised titanate nanotubes dried at 100°C for 24 hours (top) and nanotubes calcined for an additional 8 hours at 450°C (bottom). Careful indexing of the peaks and crystal structure of the nanotubes was not carried out. However, the pattern obtained from calcined nanotubes resembles that of anatase TiO_2 with characteristic peaks at 25.16°, 37.9°, 48.1° and a broad double peak at 54.0 and 55.0°. Figure A.1 (b) gives a TEM image of the dried nanotubes*. The image shows the length of the nanotubes exceeding 100 nm with diameters being approximately 5 nm.

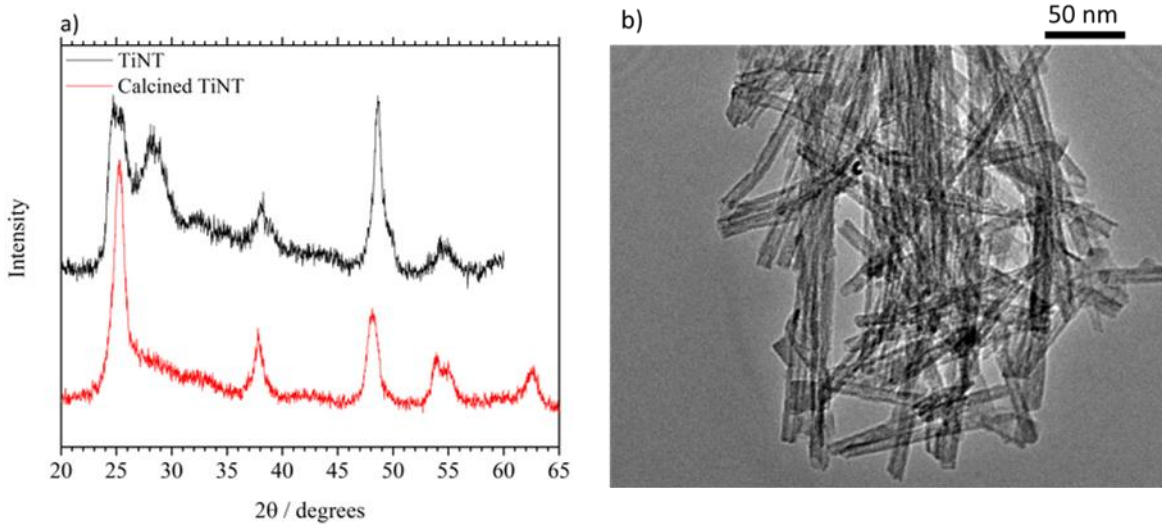

Figure A.1. (a) XRD patterns of synthesised titanate nanotubes dried at 100°C for 24 hours and nanotubes calcined for an additional 8 hours at 450°C. (b) TEM image of dried titanate nanotubes.

A.4 Electrochemical screening of titanate nanotubes

Electrodes were manufactured as previously described, using dried nanotubes and calcined nanotubes in place of TiO_2 powders. The electrodes were cycled in 1 mol dm^{-3} $AlCl_3$/1 mol dm^{-3} KCl between +0.4 V to -1.0 V vs SCE. Figure A.2 (a) shows the 1st 40 cycles from the dried nanotube electrode, with cycles performed at 0.5, 1.0 and 2.0 A g^{-1}. Cycling at 1.0 A g^{-1} gave rise to an initial discharge capacity of 35.3 mA h g^{-1}, which increased to 63.6 mA h g^{-1} on the 3rd cycle with coulombic efficiency increasing from 78.6% to 83.4%. Discharge capacity then decreased to 42.8 mA h g^{-1} during the 10th cycle at 1.0 A g^{-1}. Between the 11th and 20th cycle performed at 0.5 A g^{-1}, discharge

* TEM image was produced by post-doctoral researcher Dr Rachel McKerracher.

capacity decreased from 44.1 mA h g^{-1} to 22.2 mA h g^{-1}. Discharge capacity then decreased from 14.5 mA h g^{-1} to 10.0 mA h g^{-1} during cycles 21-30 at 2.0 A g^{-1} and dropped to below 10 mA h g^{-1} between the 30th and 40th cycle at 1.0 A g^{-1}. Figure A.2 (b) gives the discharge capacity and coulombic efficiency from the calcined nanotube electrode. Discharge capacity increased from 17.0 mA h g^{-1} to 30.6 mA h g^{-1} during the 1st 10 cycles at 1.0 A g^{-1} with coulombic efficiency increasing from 65.3% to 86.0%. During the next 10 cycles, at 0.5 A g^{-1}, discharge capacity increased initially from 32.4 mA h g^{-1} to 33.4 mA h g^{-1} decreasing again to 31.3 mA h g^{-1} by cycle 20. Coulombic efficiency increased throughout these 10 cycles from 76.8% to 82.3%. Cycling at 2.0 A g^{-1}, performed between cycle 21-30, discharge capacity decreased slightly from 26.8 mA h g^{-1} to 25.9 mA h g^{-1}, while coulombic efficiency remained relatively stable at approximately 95%. At 4.0 A g^{-1}, coulombic efficiency and discharge capacity are approximately 16.5 mA h g^{-1} and 98%. Between cycles 41-60 preformed again at 1.0 A g^{-1}, discharge capacity decreases from 21.5 mA h g^{-1} to 19.7 mA h g^{-1} and coulombic efficiency remains around 93-94%. Figure A.2 (b) shows the cycling regime being repeated, with another 10 cycles performed at each of the specific currents of 0.5, 2.0, 4.0 then 1.0 A g^{-1}. By cycle 100, at 1.0 A g^{-1}, discharge capacity had decreased to 12.9 mA h g^{-1}. Figure A.3 (a) gives the voltage profile of the non-calcined TiNT electrode at cycle 10 and 40 (1.0 A g^{-1}). Figure A.3 (b) provides the profile from the calcined electrode at cycles 10 and 50 (1.0 A g^{-1}), showing a cleaner profile compared to the non-calcined electrode that more closely resembles the profiles previously obtained from the anatase nanopowders. Figure A.2 and Figure A.3 show that the calcined nanotubes provide more stable capacity compared to the dried, non-calcined nanotubes. A capacity of approximately 26 mA h g^{-1} obtained at 4.0 A g^{-1} is also higher than the 18 mA h g^{-1} obtained from 5 nm TiO_2 at the same specific current. However, capacity still degrades considerably faster compared to the nanopowders used previously.

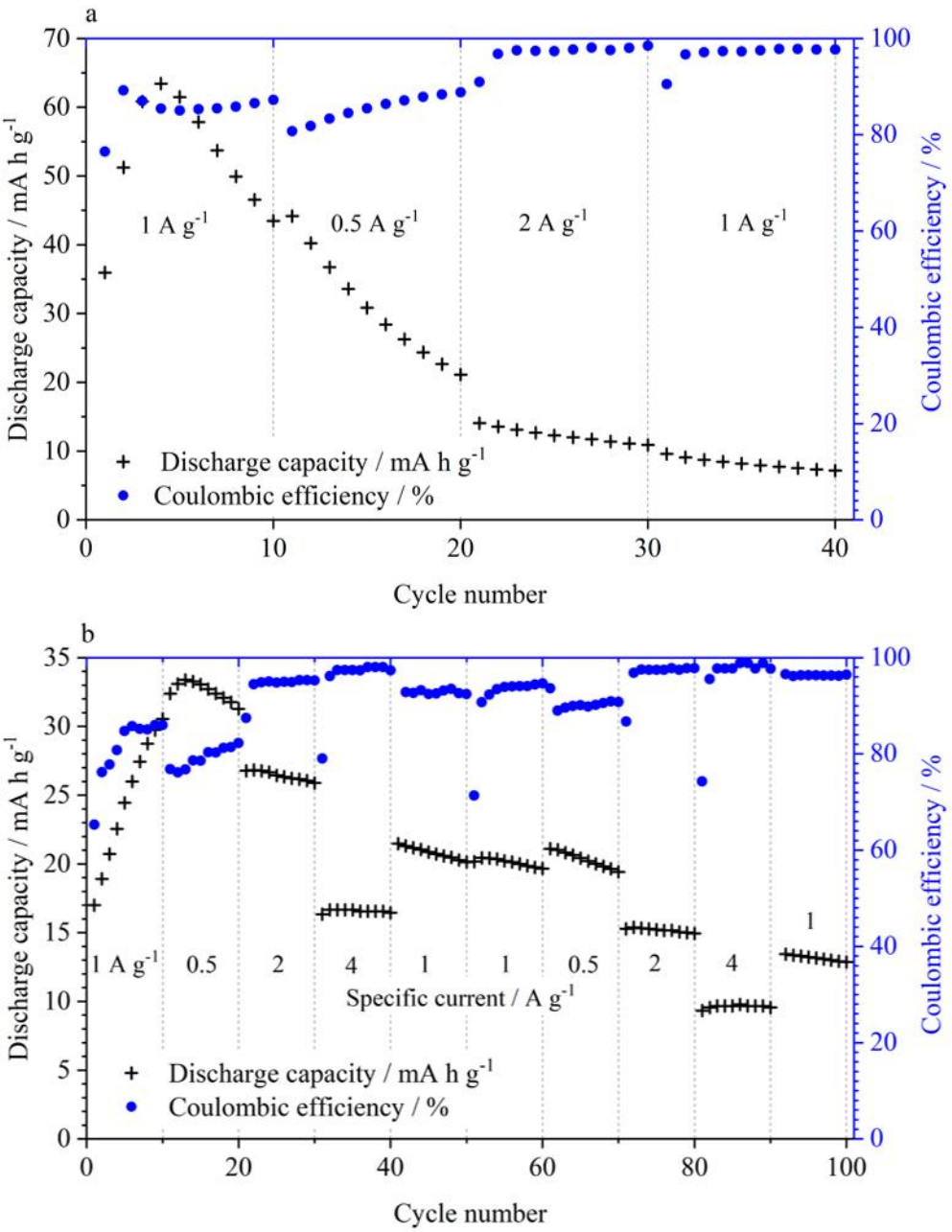

Figure A.2. (a) Discharge capacity and coulombic efficiency of a dried nanotube electrode during the initial 40 cycles. (b) Discharge capacity and coulombic efficiency from a calcined nanotube electrode during the initial 100 cycles at specific currents between 0.5 A g^{-1} to 4.0 A g^{-1}.

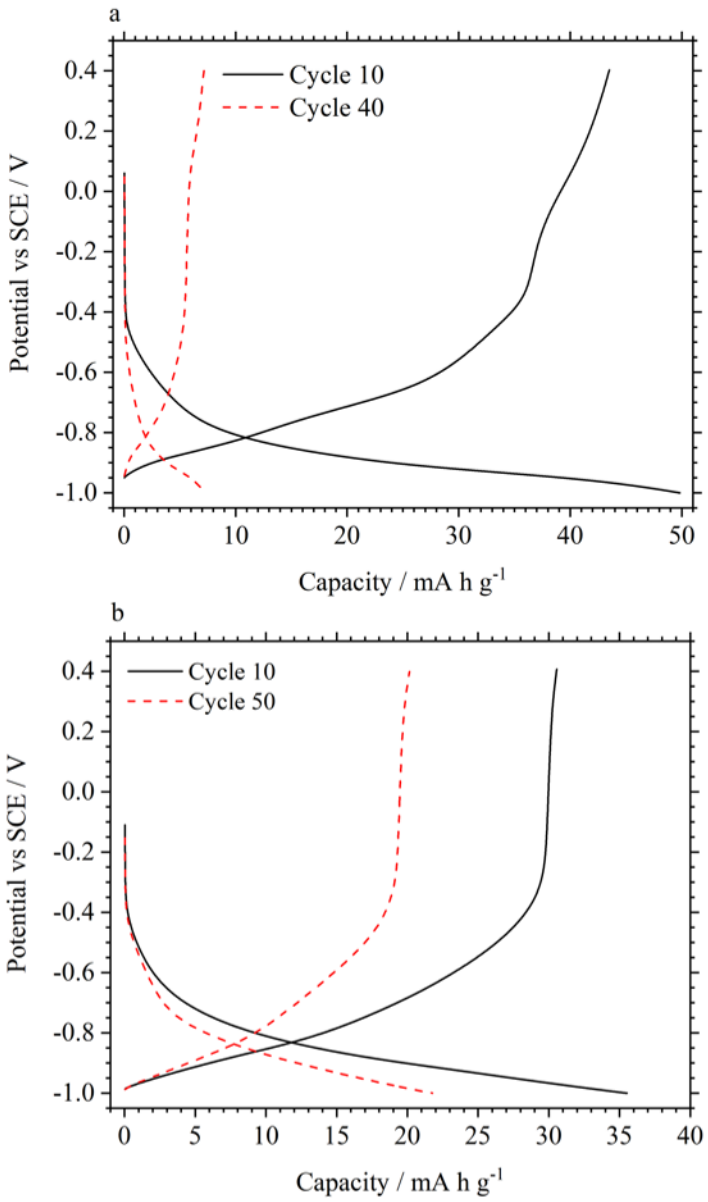

Figure A.3. a) Voltage profile from the 10th and 40th cycles, performed at 1.0 A g^{-1}, of the dried nanotube electrode. (b) Voltage profile from the 10th and 50th cycle, at 1.0 A g^{-1}, of the dried nanotube electrode.

A.5 Conclusions

This section shows the potential for improved capacity from TiNTs over commercial TiO_2 powders. However, the reduced stability over cycling is problematic. Certainly, further work should be done to better characterise the TiNTs in terms of surface area, pore size, tube dimensions as well as the charge storage and degradation mechanisms. The crystal phase and stoichiometry of the synthesised nanotubes were also not characterised in detail. XRD did show the crystallinity of

calcined nanotubes to be relatively poor, which may well affect electrochemical performance and stability over cycling. SEM images of manufactured nanotubes were not taken and would be necessary to observe any potential damage to the nanotube structure as a result of high speed shear mixing. Synthesis of TiO_2 nanostructures with control over parameters including surface area, pore size, dimensions and crystallinity could help elucidate both charge storage and degradation mechanisms. However, synthesis of novel nanostructures was not the emphasis of this work and given the relatively low stability of electrode performance during cycling, it was decided that studies would focus on commercially available TiO_2 powders.

References

1. *Climate Change Act 2008*. 2008: UK.

2. Li, J., et al., *Toward Low-Cost, High-Energy Density, and High-Power Density Lithium-Ion Batteries.* JOM, 2017. **69**(9): p. 1484-1496.

3. Manthiram, A., *An Outlook on Lithium Ion Battery Technology.* ACS Central Science, 2017. **3**(10): p. 1063-1069.

4. Centre, T.A.P., *TOWARDS 2040: A GUIDE TO AUTOMOTIVE PROPULSION TECHNOLOGIES*. 2018: Coventry, UK.

5. Matthey, J., *Our Guide to Batteries 3rd Edition.* 2015.

6. Choi, J.W. and D. Aurbach, *Promise and reality of post-lithium-ion batteries with high energy densities.* Nature Reviews Materials, 2016. **1**: p. 16013.

7. Stan, A.I., et al. *Lithium ion battery chemistries from renewable energy storage to automotive and back-up power applications — An overview*. in *2014 International Conference on Optimization of Electrical and Electronic Equipment (OPTIM)*. 2014.

8. Sakti, A., et al., *A techno-economic analysis and optimization of Li-ion batteries for light-duty passenger vehicle electrification.* Journal of Power Sources, 2015. **273**: p. 966-980.

9. A. Nelson, P., et al., *Modeling the performance and cost of lithium-ion batteries for electric-drive vehicles*. 2011.

10. Ayad, M.Y., M. Becherif, and A. Henni, *Vehicle hybridization with fuel cell, supercapacitors and batteries by sliding mode control.* Renewable Energy, 2011. **36**(10): p. 2627-2634.

11. Wachsman, E.D. and K.T. Lee, *Lowering the Temperature of Solid Oxide Fuel Cells.* Science, 2011. **334**(6058): p. 935-939.

12. Un-Noor, F., et al., *A Comprehensive Study of Key Electric Vehicle (EV) Components, Technologies, Challenges, Impacts, and Future Direction of Development.* Energies, 2017. **10**(8): p. 1217.

13. Khaligh, A. and Z. Li, *Battery, Ultracapacitor, Fuel Cell, and Hybrid Energy Storage Systems for Electric, Hybrid Electric, Fuel Cell, and Plug-In Hybrid Electric Vehicles: State of the Art.* IEEE Transactions on Vehicular Technology, 2010. **59**(6): p. 2806-2814.

14. Pischinger, S., C. Schönfelder, and J. Ogrzewalla, *Analysis of dynamic requirements for fuel cell systems for vehicle applications.* Journal of Power Sources, 2006. **154**(2): p. 420-427.

15. DOE. *DOE Energy Storage Database*. 2018 17-07-2018]; Available from: https://www.energystorageexchange.org/projects.

16. Joseph H. Eto, J.U., Peter Mackin, Ron Daschmans, Ben Williams, Brian Haney, Randall Hunt, Jeff Ellis *Use of Frequency Response Metrics to Assess the Planning and Operating Requirements for Reliable Integration of Variable Renewable Generation* 2010, Ernest Orlando Lawrence Berkeley National Laboratory: Berkeley, CA.

17. IRENA, *Battery storage for renewables: market status and technology outlook*. 2015, International Renewables Energy Agency.

18. Alex Eller, D.G., *Energy Storage Trends and Opportunities in Emerging Markets*. 2017, Navigant Consulting: Boulder, CO.

19. Chen, H., et al., *Progress in electrical energy storage system: A critical review.* Progress in Natural Science, 2009. **19**(3): p. 291-312.

20. Castillo, A. and D.F. Gayme, *Grid-scale energy storage applications in renewable energy integration: A survey.* Energy Conversion and Management, 2014. **87**: p. 885-894.

21. EPRI, *Electricity Energy Storage Technology Options A White Paper Primer on Applications, Costs, and Benefits*. 2010, Electric Power Research Institute: Palo Alto, CA.

22. Vazquez, S., et al., *Energy Storage Systems for Transport and Grid Applications.* IEEE Transactions on Industrial Electronics, 2010. **57**(12): p. 3881-3895.

23. Abbas A. Akhil, G.H., Aileen B. Currier, Benjamin C. Kaun, Dan M. Rastler, and A.L.C. Stella Bingqing Chen, Dale T. Bradshaw, and William D. Gauntlett, *DOE/EPRI 2013 Electricity Storage Handbook in Collaboration with NRECA*. 2013, Sandia National laboratories: Albuquerque, NM.

24. Barton, J.P. and D.G. Infield, *Energy storage and its use with intermittent renewable energy.* IEEE Transactions on Energy Conversion, 2004. **19**(2): p. 441-448.

25. Dong, L., et al., *Flexible electrodes and supercapacitors for wearable energy storage: a review by category.* Journal of Materials Chemistry A, 2016. **4**(13): p. 4659-4685.

26. Yong, S., et al., *Flexible solid-state fabric based supercapacitor.* Journal of Physics: Conference Series, 2015. **660**(1): p. 012074.

27. Jost, K., et al., *Carbon coated textiles for flexible energy storage.* Energy & Environmental Science, 2011. **4**(12): p. 5060-5067.

28. Pasta, M., et al., *Aqueous supercapacitors on conductive cotton.* Nano Research, 2010. **3**(6): p. 452-458.

29. Yu, Y., et al., *Waterproof, Ultrahigh Areal-Capacitance, Wearable Supercapacitor Fabrics.* Advanced Materials, 2017. **29**(19): p. 1606679.

30. Liubing, D., et al., *Breathable and Wearable Energy Storage Based on Highly Flexible Paper Electrodes.* Advanced Materials, 2016. **28**(42): p. 9313-9319.

31. Ostfeld, A.E., et al., *High-performance flexible energy storage and harvesting system for wearable electronics.* Scientific Reports, 2016. **6**: p. 26122.

32. Wei, Z., et al., *Fiber-Based Wearable Electronics: A Review of Materials, Fabrication, Devices, and Applications.* Advanced Materials, 2014. **26**(31): p. 5310-5336.

33. Holland, A., et al., *An aluminium battery operating with an aqueous electrolyte.* Journal of Applied Electrochemistry, 2018. **48**(3): p. 243-250.

34. Li, W., J.R. Dahn, and D.S. Wainwright, *Rechargeable Lithium Batteries with Aqueous Electrolytes.* Science, 1994. **264**(5162): p. 1115-1118.

35. Kim, H., et al., *Aqueous Rechargeable Li and Na Ion Batteries.* Chemical Reviews, 2014. **114**(23): p. 11788-11827.

36. Wang, Y., et al., *Ultra-low cost and highly stable hydrated FePO4 anodes for aqueous sodium-ion battery.* Journal of Power Sources, 2018. **374**: p. 211-216.

37. Wang, L.-P., et al., *Prussian blue nanocubes as cathode materials for aqueous Na-Zn hybrid batteries.* Journal of Power Sources, 2017. **355**: p. 18-22.

38. Helbig, C., et al., *Supply risks associated with lithium-ion battery materials.* Journal of Cleaner Production, 2018. **172**: p. 274-286.

39. Ellingsen, L., et al., *Environmental Screening of Electrode Materials for a Rechargeable Aluminum Battery with an AlCl3/EMIMCl Electrolyte.* Materials, 2018. **11**(6): p. 936.

40. Larcher, D. and J.M. Tarascon, *Towards greener and more sustainable batteries for electrical energy storage.* Nature Chemistry, 2014. **7**: p. 19.

41. Kushnir, D. and B.A. Sandén, *The time dimension and lithium resource constraints for electric vehicles.* Resources Policy, 2012. **37**(1): p. 93-103.

42. Cheng, X.-B., et al., *Toward Safe Lithium Metal Anode in Rechargeable Batteries: A Review.* Chemical Reviews, 2017. **117**(15): p. 10403-10473.

43. Rahman, M.A., X. Wang, and C. Wen, *High Energy Density Metal-Air Batteries: A Review.* Journal of The Electrochemical Society, 2013. **160**(10): p. A1759-A1771.

44. Ma, Z., et al., *A review of cathode materials and structures for rechargeable lithium–air batteries.* Energy & Environmental Science, 2015. **8**(8): p. 2144-2198.

45. Arumugam, M., C. Sheng-Heng, and Z. Chenxi, *Lithium–Sulfur Batteries: Progress and Prospects.* Advanced Materials, 2015. **27**(12): p. 1980-2006.

46. Ruopian, F., et al., *More Reliable Lithium-Sulfur Batteries: Status, Solutions and Prospects.* Advanced Materials, 2017. **29**(48): p. 1606823.

47. Lars, B., O. Martin, and K. Stefan, *Carbon Materials for Lithium Sulfur Batteries—Ten Critical Questions.* Chemistry – A European Journal, 2016. **22**(22): p. 7324-7351.

48. Ji, X., K.T. Lee, and L.F. Nazar, *A highly ordered nanostructured carbon–sulphur cathode for lithium–sulphur batteries.* Nature Materials, 2009. **8**: p. 500.

49. Burke, A., *R&D considerations for the performance and application of electrochemical capacitors.* Electrochimica Acta, 2007: p. 1083–1091.

50. *Our guide to batteries*. 2012.

51. Nykvist, B. and M. Nilsson, *Rapidly falling costs of battery packs for electric vehicles.* Nature climate change Letters, 2015. **5**: p. 329-332.

52. *Cost and performance of EV batteries*. 2012, Element Energy Limited: Cambridge.

53. Nelson, P.A., et al., *Modeling the Performance and Cost of Lithium-Ion Batteries for Electric-Drive Vehicles*. 2012, Argonne National Laboratory: Argonne.

54. Nitta, N., et al., *Li-ion battery materials: present and future.* Materials Today, 2015. **18**(5): p. 252-264.

55. *Advanced Clean Transit Battery Cost for Heavy-Duty Electric Vehicles (Discussion Draft)*. 2016.

56. Tie, S.F. and C.W. Tan, *A review of energy sources and energy management system in electric vehicles.* Renewable and Sustainable Energy Reviews, 2013. **20**: p. 82-102.

57. Soloveichik, G.L., *Battery Technologies for Large-Scale Stationary Energy Storage.* Annual Review of Chemical and Biomolecular Engineering, 2011. **2**: p. 503-527.

58. *Electrical Energy Storage*. 2011: Geneva.

59. EPRI, *Electricity energy storage options: A white paper on applications, costs and benefits*. 2010, EPRI: Palo Alto, CA.

60. Burke, A., *R&D considerations for the performance and application of electrochemical capacitors.* Electrochimica Acta, 2007. **53**(3): p. 1083-1091.

61. Grey, C.P. and J.M. Tarascon, *Sustainability and in situ monitoring in battery development.* Nature Materials, 2016. **16**: p. 45.

62. Tang, W., et al., *Aqueous rechargeable lithium batteries as an energy storage system of superfast charging.* Energy & Environmental Science, 2013. **6**(7): p. 2093-2104.

63. Ribière, P., et al., *Investigation on the fire-induced hazards of Li-ion battery cells by fire calorimetry.* Energy & Environmental Science, 2012. **5**(1): p. 5271-5280.

64. Hammami, A., N. Raymond, and M. Armand, *Runaway risk of forming toxic compounds.* Nature, 2003. **424**: p. 635.

65. Zafar, Z.A., et al., *Cathode materials for rechargeable aluminum batteries: current status and progress.* Journal of Materials Chemistry A, 2017. **5**(12): p. 5646-5660.

66. Antonio, E.G., et al., *An Overview and Future Perspectives of Aluminum Batteries.* Advanced Materials, 2016. **28**(35): p. 7564-7579.

67. Zhu, Y., et al., *Electrochemical Techniques for Intercalation Electrode Materials in Rechargeable Batteries.* Accounts of Chemical Research, 2017. **50**(4): p. 1022-1031.

68. Liu, C., Z.G. Neale, and G. Cao, *Understanding electrochemical potentials of cathode materials in rechargeable batteries.* Materials Today, 2016. **19**(2): p. 109-123.

69. Massé, R.C., et al., *Energy storage through intercalation reactions: electrodes for rechargeable batteries.* National Science Review, 2017. **4**(1): p. 26-53.

70. Manthiram, A. and J. Choi, *Chemical and structural instabilities of lithium ion battery cathodes.* Journal of Power Sources, 2006. **159**(1): p. 249-253.

71. Thomas, B., et al., *The Electrochemistry of Nanostructured Titanium Dioxide Electrodes.* ChemPhysChem, 2012. **13**(12): p. 2824-2875.

72. Jiang, F. and P. Peng, *Elucidating the Performance Limitations of Lithium-ion Batteries due to Species and Charge Transport through Five Characteristic Parameters.* Scientific Reports, 2016. **6**: p. 32639.

73. J Bard, A. and L. R. Faulkner, *Electrochemical methods : fundamentals and applications / Allen J. Bard, Larry R. Faulkner*. Vol. 18. 1980.

74. Berckmans, G., et al., *Cost Projection of State of the Art Lithium-Ion Batteries for Electric Vehicles Up to 2030.* Energies, 2017. **10**(9): p. 1314.

75. Linda Gaines, R.C., *Costs of Lithium-Ion Batteries for Vehicles*. 2000, Argonne National Laboratory: Illinois.

76. P.A. Nelson, K.G.G., I. Bloom, and D.W. Dees, *Modeling the Performance and Cost of Lithium-Ion Batteries for Electric-Drive Vehicles.* Argonne National Laboratory, Chemical sciences and Engineering Division, 2011.

77. Shabbir Ahmed, P.N., Naresh Susarla, Dennis Dees, *Automotive Battery Cost Using BatPaC.* IEA Workshop on Batteries for Electric Mobility, Paris, 2018: p. Argonne National Laboratory.

78. Yuan, C., et al., *Manufacturing energy analysis of lithium ion battery pack for electric vehicles.* CIRP Annals, 2017. **66**(1): p. 53-56.

79. Li, W., J.R. Dahn, and D.S. Wainwright, *Rechargeable lithium batteries with aqueous electrolyte.* Science, 1994. **264**: p. 1115-1118.

80. Mass´e, R.C., et al., *Energy storage through intercalation reactions: electrodes for rechargeable batteries.* National Science Review, 2016. **4**: p. 26-53.

81. Jiang, F. and P. Peng, *Elucidating the Performance Limitations of Lithium-ion Batteries due to Species and Charge Transport through Five Characteristic Parameters.* Scientific Reports, 2016. **6**.

82. Alias, N. and A.A. Mohamad, *Advances of aqueous rechargeable lithium-ion battery: A review.* Journal of Power Sources, 2015. **274**: p. 237-251.

83. Kim, H., et al., *Aqueous Rechargeable Li and Na Ion Batteries.* Chemical Reviews, 2014. **114**: p. 11788−11827.

84. Luo, J.-Y., et al., *Raising the cycling stability of aqueous lithium-ion batteries by eliminating oxygen in the electrolyte*. Vol. 2. 2010. 760-5.

85. Ruffo, R., et al., *Electrochemical behavior of LiCoO2 as aqueous lithium-ion battery electrodes.* Electrochemistry Communications, 2009. **11**(2): p. 247-249.

86. Zhao, M., et al., *Excellent rate capabilities of (LiFePO4/C)//LiV3O8 in an optimized aqueous solution electrolyte.* Journal of Power Sources, 2013. **232**: p. 181-186.

87. Qu, Q., et al., *Porous LiMn2O4 as cathode material with high power and excellent cycling for aqueous rechargeable lithium batteries.* Energy & Environmental Science, 2011. **4**(10): p. 3985-3990.

88. Sun, D., et al., *Long-lived Aqueous Rechargeable Lithium Batteries Using Mesoporous LiTi2(PO4)3@C Anode.* Scientific Reports, 2015. **5**: p. 17452.

89. Luo, J.-Y., et al., *Raising the cycling stability of aqueous lithium-ion batteries by eliminating oxygen in the electrolyte.* Nature Chemistry, 2010. **2**: p. 760-765.

90. Mohan Rao, M., et al., *Electrochemical behaviour of solid lithium cobaltate (LiCoO2) and lithium manganate (LiMn2O4) in an aqueous electrolyte system.* Journal of Solid State Electrochemistry, 2001. **5**(1): p. 50-56.

91. Jayalakshmi, M., M. Mohan Rao, and F. Scholz, *Electrochemical Behavior of Solid Lithium Manganate (LiMn2O4) in Aqueous Neutral Electrolyte Solutions.* Langmuir, 2003. **19**(20): p. 8403-8408.

92. Köhler, J., et al., *LiV3O8: characterization as anode material for an aqueous rechargeable Li-ion battery system.* Electrochimica Acta, 2000. **46**: p. 59-65.

93. Zhang, Z., et al., *V2O5-SiO2 hybrid as anode material for aqueous rechargeable lithium batteries.* Ionics, 2016. **22**(9): p. 1593-1601.

94. Sun, D., et al., *Advanced aqueous rechargeable lithium battery using nanoparticulate LiTi2(PO4)3/C as a superior anode.* Scientific Reports, 2015. **5**: p. 10733.

95. Zhao, M., et al., *Characteristics and electrochemical performance of LiFe0.5Mn0.5PO4/C used as cathode for aqueous rechargeable lithium battery.* Journal of Power Sources, 2012. **211**: p. 202-207.

96. He, P., et al., *Investigation on capacity fading of LiFePO4 in aqueous electrolyte.* Electrochimica Acta, 2011. **56**(5): p. 2351-2357.

97. Wang, Y.-g., et al., *Hybrid Aqueous Energy Storage Cells Using Activated Carbon and Lithium-Ion Intercalated Compounds.* Journal of the Electrochemical Society, 2006. **153**: p. 1425-1431.

98. Vujković, M., et al., *Gel-combustion synthesis of LiFePO4/C composite with improved capacity retention in aerated aqueous electrolyte solution.* Electrochimica Acta, 2013. **92**: p. 248-256.

99. Arrebola, J.C., et al., *Aqueous Rechargeable Lithium Battery Based on LiNi0.5Mn1.5O4 Spinel with Promising Performance.* Energy & Fuels, 2013. **27**(12): p. 7854-7857.

100. Zhou, D., et al., *Na2V6O16·0.14H2O nanowires as a novel anode material for aqueous rechargeable lithium battery with good cycling performance.* Journal of Power Sources, 2013. **227**: p. 111-117.

101. Suo, L., et al., *"Water-in-salt" electrolyte enables high-voltage aqueous lithium-ion chemistries.* Science, 2015. **350**(6263): p. 938-943.

102. Wang, Y.-g. and Y.-y. Xia, *Hybrid Aqueous Energy Storage Cells Using Activated Carbon and Lithium-Intercalated Compounds: I. The C／Li Mn 2 O 4 System.* Journal of The Electrochemical Society, 2006. **153**(2): p. A450-A454.

103. Dipan, K., et al., *The Emerging Chemistry of Sodium Ion Batteries for Electrochemical Energy Storage.* Angewandte Chemie International Edition, 2015. **54**(11): p. 3431-3448.

104. Sauvage, F., et al., *Study of the Insertion/Deinsertion Mechanism of Sodium into Na0.44MnO2.* Inorganic Chemistry, 2007. **46**(8): p. 3289-3294.

105. Whitacre, J.F., A. Tevar, and S. Sharma, *Na4Mn9O18 as a positive electrode material for an aqueous electrolyte sodium-ion energy storage device.* Electrochemistry Communications, 2010. **12**(3): p. 463-466.

106. Whitacre, J.F., et al., *An aqueous electrolyte, sodium ion functional, large format energy storage device for stationary applications.* Journal of Power Sources, 2012. **213**: p. 255-264.

107. Hou, Z., et al., *An aqueous rechargeable sodium ion battery based on a NaMnO2–NaTi2(PO4)3 hybrid system for stationary energy storage.* Journal of Materials Chemistry A, 2015. **3**: p. 1400.

108. Hou, Z., et al., *An aqueous rechargeable sodium ion battery based on a NaMnO2–NaTi2(PO4)3 hybrid system for stationary energy storage.* Journal of Materials Chemistry A, 2015. **3**(4): p. 1400-1404.

109. Zhang, Q., et al., *A High Rate 1.2V Aqueous Sodium-ion Battery Based on All NASICON Structured NaTi2(PO4)3 and Na3V2(PO4)3.* Electrochimica Acta, 2016. **196**: p. 470-478.

110. Zhou, H., Z. Ryan Tian, and S.S. Ang, *Improving the cycling stability of Na3V2(PO4)3 nanoparticle in aqueous sodium ion batteries by introducing carbon support.* Materials for Renewable and Sustainable Energy, 2016. **5**(1): p. 3.

111. Wessells, C.D., R.A. Huggins, and Y. Cui, *Copper hexacyanoferrate battery electrodes with long cycle life and high power.* Nature Communications, 2011. **2**: p. 550.

112. Wessells, C.D., et al., *The Effect of Insertion Species on Nanostructured Open Framework Hexacyanoferrate Battery Electrodes.* Journal of The Electrochemical Society, 2011. **159**(2): p. A98-A103.

113. Wessells, C.D., et al., *Nickel Hexacyanoferrate Nanoparticle Electrodes For Aqueous Sodium and Potassium Ion Batteries.* Nano Letters, 2011. **11**(12): p. 5421-5425.

114. Lu, K., et al., *A rechargeable Na-Zn hybrid aqueous battery fabricated with nickel hexacyanoferrate and nanostructured zinc.* JOURNAL OF POWER SOURCES, 2016. **321**: p. 257-263.

115. Wang, F., et al., *Aqueous Rechargeable Zinc/Aluminum Ion Battery with Good Cycling Performance.* ACS Applied Materials & Interfaces, 2016. **8**(14): p. 9022-9029.

116. Liang, C., et al., *Aqueous Batteries Based on Mixed Monovalence Metal Ions: A New Battery Family.* ChemSusChem, 2014. **7**(8): p. 2295-2302.

117. Chen, L., et al., *New-concept Batteries Based on Aqueous Li(+)/Na(+) Mixed-ion Electrolytes.* Scientific Reports, 2013. **3**: p. 1946.

118. Yao, H.-R., et al., *Rechargeable dual-metal-ion batteries for advanced energy storage.* Physical Chemistry Chemical Physics, 2016. **18**(14): p. 9326-9333.

119. Chen, L., et al., *New-concept Batteries Based on Aqueous Li+/Na+ Mixed-ion Electrolytes.* Scientific Reports, 2013. **3**: p. 1946.

120. Wang, F., et al., *Aqueous Rechargeable Zinc/Aluminum Ion Battery with Good Cycling Performance* ACS Applied Materials and interfaces, 2016. **8**: p. 9022–9029.

121. Chen, X. and S.S. Mao, *Titanium Dioxide Nanomaterials: Synthesis, Properties, Modifications, and Applications.* Chemical Reviews, 2007. **107**(7): p. 2891-2959.

122. Hoffmann, M.R., et al., *Environmental Applications of Semiconductor Photocatalysis.* Chemical Reviews, 1995. **95**(1): p. 69-96.

123. Ning, X., et al., *Outstanding supercapacitive properties of Mn-doped TiO2 micro/nanostructure porous film prepared by anodization method.* Scientific Reports, 2016. **6**: p. 22634.

124. Pirkanniemi, K. and M. Sillanpää, *Heterogeneous water phase catalysis as an environmental application: a review.* Chemosphere, 2002. **48**(10): p. 1047-1060.

125. Jiang, C., et al., *Particle size dependence of the lithium storage capability and high rate performance of nanocrystalline anatase TiO2 electrode.* Journal of Power Sources, 2007. **166**(1): p. 239-243.

126. Xu, Y., et al., *Nanocrystalline anatase TiO2: a new anode material for rechargeable sodium ion batteries.* Chemical Communications, 2013. **49**(79): p. 8973-8975.

127. Nguyen, N.T., et al., *Spaced TiO2 nanotube arrays allow for a high performance hierarchical supercapacitor structure.* Journal of Materials Chemistry A, 2017. **5**(5): p. 1895-1901.

128. Lu, X., et al., *Hydrogenated TiO2 Nanotube Arrays for Supercapacitors.* Nano Letters, 2012. **12**(3): p. 1690-1696.

129. Zhang, Y., et al., *Design and Synthesis of Hierarchical SiO2@C/TiO2 Hollow Spheres for High-Performance Supercapacitors.* ACS Applied Materials & Interfaces, 2017. **9**(35): p. 29982-29991.

130. Nam, K.W., et al., *The High Performance of Crystal Water Containing Manganese Birnessite Cathodes for Magnesium Batteries.* Nano Letters, 2015. **15**: p. 4071−4079.

131. Gu, X., et al., *First-Principles Study of H+ Intercalation in Layer-Structured LiCoO2.* The Journal of Physical Chemistry C, 2011. **115**(25): p. 12672-12676.

132. Deng, D., et al., *Green energy storage materials: Nanostructured TiO2 and Sn-based anodes for lithium-ion batteries.* Energy & Environmental Science, 2009. **2**: p. 818-837.

133. Liu, S., et al., *Aluminum storage behavior of anatase TiO2 nanotube arrays in aqueous solution for aluminum ion batteries†.* Energy and Environmental Science, 2012. **5**: p. 9743-9746.

134. Liu, Y., et al., *The electrochemical behavior of Cl−assisted Al3+insertion intotitanium dioxide nanotube arrays in aqueous solution for aluminumion batteries.* Electrochimica Acta, 2014. **143**: p. 340-346.

135. He, Y.J., et al., *Black mesoporous anatase TiO2 nanoleaves: a high capacity and high rate anode for aqueous Al-ion batteries.* Journal of Materials Chemistry A, 2014. **2**: p. 1721-1731.

136. Kazazi, M., P. Abdollahi, and M. Mirzaei-Moghadam, *High surface area TiO2 nanospheres as a high-rate anode material for aqueous aluminium-ion batteries.* Solid State Ionics, 2017. **300**: p. 32-37.

137. Lahan, H., et al., *Anatase TiO2 as an Anode Material for Rechargeable Aqueous Aluminum-Ion Batteries: Remarkable Graphene Induced Aluminum Ion Storage Phenomenon.* The Journal of Physical Chemistry C, 2017. **121**(47): p. 26241-26249.

138. Gonz´alez, J.R., et al., *Reversible intercalation of aluminium into vanadium pentoxide xerogel for aqueous rechargeable batteries†.* RSC Advances, 2016. **6**: p. 62157-62164.

139. Liu, S., et al., *Copper hexacyanoferrate nanoparticles as cathode material for aqueous Al-ion batteries.* Journal of Materials Chemistry, 2015. **3**: p. 959-962.

140. Zhong, W., et al., *Electrochemically conductive treatment of TiO2 nanotube arrays in AlCl3 aqueous solution for supercapacitors.* Journal of Power Sources, 2015. **294**: p. 216-222.

141. Song, S.H.K.K., et al., *Polymorphism-induced catalysis difference of TiO2 nanofibers for rechargeable Li–O2 batteries.* Journal of Materials Chemistry A, 2014. **2**: p. 19660-19664.

142. Amati, M., et al., *Electrical conductivity of cluster-assembled carbon/titania nanocomposite films irradiated by highly focused vacuum ultraviolet photon beams* Journal of Applied Physics, 2007. **101**.

143. Ramadoss, A. and S.J. Kim, *Improved activity of a graphene–TiO2 hybrid electrode in an electrochemical supercapacitor.* Carbon, 2013. **63**: p. 434-445.

144. Li, S., et al., *Three-dimensional hierarchical graphene/TiO2 composite as high-performance electrode for supercapacitor.* Journal of Alloys and Compounds, 2018. **746**: p. 670-676.

145. Yadav, P., et al., *Probing the electrochemical properties of TiO2/graphene composite by cyclic voltammetry and impedance spectroscopy*. Vol. 206. 2015.

146. Wessells, C.D., R.A. Huggins, and Y. Cui, *Copper hexacyanoferrate battery electrodes with long cycle life and high power.* nature Communications, 2011. **2**.

147. Vujković, M., et al., *THE INFLUENCE OF INTERCALATED IONS ON CYCLIC STABILITY OF V2O5/GRAPHITE COMPOSITE IN AQUEOUS ELECTROLYTIC SOLUTIONS: EXPERIMENTAL AND THEORETICAL APPROACH.* Electrochimica Acta, 2015. **176**: p. 130-140.

148. Conway, B.E., V. Birss, and J. Wojtowicz, *The role and utilization of pseudocapacitance for energy storage by supercapacitors.* Journal of Power Sources, 1997. **66**(1): p. 1-14.

149. Sharma, P. and T.S. Bhatti, *A review on electrochemical double-layer capacitors.* Energy Conversion and Management, 2010. **51**(12): p. 2901-2912.

150. Brousse, T., D. Bélanger, and J.W. Long, *To Be or Not To Be Pseudocapacitive?* Journal of The Electrochemical Society, 2015. **162**(5): p. A5185-A5189.

151. Chen, G.Z., *Supercapacitor and supercapattery as emerging electrochemical energy stores.* International Materials Reviews, 2017. **62**(4): p. 173-202.

152. Wang, J., et al., *Pseudocapacitive materials for electrochemical capacitors: from rational synthesis to capacitance optimization.* National Science Review, 2017. **4**(1): p. 71-90.

153. Augustyn, V., P. Simon, and B. Dunn, *Pseudocapacitive oxide materials for high-rate electrochemical energy storage.* Energy & Environmental Science, 2014. **7**(5): p. 1597-1614.

154. Li, J., Z. Tang, and Z. Zhang, *Layered Hydrogen Titanate Nanowires with Novel Lithium Intercalation Properties.* Chemistry of Materials, 2005. **17**(23): p. 5848-5855.

155. Hu, C.-C., et al., *Design and Tailoring of the Nanotubular Arrayed Architecture of Hydrous RuO2 for Next Generation Supercapacitors.* Nano Letters, 2006. **6**(12): p. 2690-2695.

156. Menzel, J., K. Fic, and E. Frackowiak, *Hybrid aqueous capacitors with improved energy/power performance.* Progress in Natural Science: Materials International, 2015. **25**(6): p. 642-649.

157. Zhou, L., et al., *Prussian blue as positive electrode material for aqueous sodium-ion capacitor with excellent performance.* RSC Advances, 2016. **6**(111): p. 109340-109345.

158. Fic, K., et al., *Around the thermodynamic limitations of supercapacitors operating in aqueous electrolytes.* Electrochimica Acta, 2016. **206**: p. 496-503.

159. Lu, K., et al., *An advanced aqueous sodium-ion supercapacitor with a manganous hexacyanoferrate cathode and a Fe3O4/rGO anode.* Journal of Materials Chemistry A, 2015. **3**(31): p. 16013-16019.

160. Zhao, F., et al., *Cobalt Hexacyanoferrate Nanoparticles as a High-Rate and Ultra-Stable Supercapacitor Electrode Material.* ACS Applied Materials & Interfaces, 2014. **6**(14): p. 11007-11012.

161. Pasta, M., et al., *Full open-framework batteries for stationary energy storage.* Nature Communications, 2014. **5**: p. 3007.

162. Yu, F., et al., *Electrochemical characterization of P2-type layered Na2/3Ni1/4Mn3/4O2 cathode in aqueous hybrid sodium/lithium ion electrolyte.* Ceramics International, 2017. **43**(13): p. 9960-9967.

163. Kumar, A., et al., *An efficient α-MnO2 nanorods forests electrode for electrochemical capacitors with neutral aqueous electrolytes.* Electrochimica Acta, 2016. **220**: p. 712-720.

164. Abbas, Q., et al., *Sustainable AC/AC hybrid electrochemical capacitors in aqueous electrolyte approaching the performance of organic systems.* Journal of Power Sources, 2016. **326**: p. 652-659.

165. Mostazo-López, M.J., et al., *Nitrogen doped superporous carbon prepared by a mild method. Enhancement of supercapacitor performance.* International Journal of Hydrogen Energy, 2016. **41**(43): p. 19691-19701.

166. Pazhamalai, P., et al., *Fabrication of high energy Li-ion hybrid capacitor using manganese hexacyanoferrate nanocubes and graphene electrodes.* Journal of Industrial and Engineering Chemistry, 2018. **64**: p. 134-142.

167. Liu, S., et al., *Facile Synthesis of Microsphere Copper Cobalt Carbonate Hydroxides Electrode for Asymmetric Supercapacitor.* Electrochimica Acta, 2016. **188**: p. 898-908.

168. Peng, H., et al., *High-Performance Asymmetric Supercapacitor Designed with a Novel NiSe@MoSe2 Nanosheet Array and Nitrogen-Doped Carbon Nanosheet.* ACS Sustainable Chemistry & Engineering, 2017. **5**(7): p. 5951-5963.

169. Peng, H., et al., *A novel aqueous asymmetric supercapacitor based on petal-like cobalt selenide nanosheets and nitrogen-doped porous carbon networks electrodes.* Journal of Power Sources, 2015. **297**: p. 351-358.

170. Ding, J., et al., *Peanut shell hybrid sodium ion capacitor with extreme energy–power rivals lithium ion capacitors.* Energy & Environmental Science, 2015. **8**(3): p. 941-955.

171. Hanna, O., et al., *Aqueous energy-storage cells based on activated carbon and LiMn2O4 electrodes.* Journal of Power Sources, 2017. **354**: p. 148-156.

172. Fic, K., et al., *Novel insight into neutral medium as electrolyte for high-voltage supercapacitors.* Energy & Environmental Science, 2012. **5**(2): p. 5842-5850.

173. Barzegar, F., et al., *Investigation of different aqueous electrolytes on the electrochemical performance of activated carbon-based supercapacitors.* RSC Advances, 2015. **5**(130): p. 107482-107487.

174. Li, S., et al., *Facile preparation and performance of mesoporous manganese oxide for supercapacitors utilizing neutral aqueous electrolytes.* RSC Advances, 2012. **2**(8): p. 3298-3308.

175. Andrew, B., *Ultracapacitor technologies and application in hybrid and electric vehicles.* International Journal of Energy Research, 2010. **34**(2): p. 133-151.

176. Bruce, P.G., B. Scrosati, and J.-M. Tarascon, *Nanomaterials for Rechargeable Lithium Batteries.* Angewandte Chemie, 2008. **47**: p. 2930-2946.

177. Liu, S., et al., *Aluminum storage behavior of anatase TiO2 nanotube arrays in aqueous solution for aluminum ion batteries.* Energy & Environmental Science, 2012. **5**(12): p. 9743-9746.

178. Liu, Y., et al., *The electrochemical behavior of Cl− assisted Al3+ insertion into titanium dioxide nanotube arrays in aqueous solution for aluminum ion batteries.* Electrochimica Acta, 2014. **143**: p. 340-346.

179. Zackrisson, M., L. Avellán, and J. Orlenius, *Life cycle assessment of lithium-ion batteries for plug-in hybrid electric vehicles – Critical issues.* Journal of Cleaner Production, 2010. **18**(15): p. 1519-1529.

180. Schoetz, T., et al., *Understanding the charge storage mechanism of conductive polymers as hybrid battery-capacitor materials in ionic liquids by in situ atomic force microscopy and electrochemical quartz crystal microbalance studies.* Journal of Materials Chemistry A, 2018. **6**(36): p. 17787-17799.

181. Liu, S., et al., *Copper hexacyanoferrate nanoparticles as cathode material for aqueous Al-ion batteries.* Journal of Materials Chemistry A, 2015. **3**(3): p. 959-962.

182. Pasta, M., et al., *A high-rate and long cycle life aqueous electrolyte battery for grid-scale energy storage.* Nature Communications, 2012. **3**: p. 1149.

183. Sang, S., et al., *The electrochemical behavior of TiO2-NTAs electrode in H+ and Al3+ coexistent aqueous solution.* Electrochimica Acta, 2016. **187**: p. 92-97.

184. He, Y.J., et al., *Black mesoporous anatase TiO2 nanoleaves: a high capacity and high rate anode for aqueous Al-ion batteries.* Journal of Materials Chemistry A, 2014. **2**(6): p. 1721-1731.

185. Zec, N., et al., *Electrochemical Performance of Anatase TiO2 Nanotube Arrays Electrode in Ionic Liquid Based Electrolyte for Lithium Ion Batteries.* Journal of The Electrochemical Society, 2017. **164**(8): p. H5100-H5107.

186. Moitzheim, S., S. De Gendt, and P.M. Vereecken, *Investigation of the Li-Ion Insertion Mechanism for Amorphous and Anatase TiO2 Thin-Films.* Journal of The Electrochemical Society, 2019. **166**(2): p. A1-A9.

187. Gao, H., et al., *Revealing the Rate-Limiting Li-Ion Diffusion Pathway in Ultrathick Electrodes for Li-Ion Batteries.* The Journal of Physical Chemistry Letters, 2018. **9**(17): p. 5100-5104.

188. Wagemaker, M., et al., *Two Phase Morphology Limits Lithium Diffusion in TiO2 (Anatase): A 7Li MAS NMR Study.* Journal of the American Chemical Society, 2001. **123**(46): p. 11454-11461.

189. Augustyn, V., et al., *High-rate electrochemical energy storage through Li+ intercalation pseudocapacitance.* Nature Materials, 2013. **12**: p. 518.

190. Yoon, S.-B. and K.-B. Kim, *Effect of poly(3,4-ethylenedioxythiophene) (PEDOT) on the pseudocapacitive properties of manganese oxide (MnO2) in the PEDOT/MnO2/multiwall carbon nanotube (MWNT) composite.* Electrochimica Acta, 2013. **106**: p. 135-142.

191. Zhong, C., et al., *A review of electrolyte materials and compositions for electrochemical supercapacitors.* Chemical Society Reviews, 2015. **44**(21): p. 7484-7539.

192. Andreas, H.A., *Self-Discharge in Electrochemical Capacitors: A Perspective Article.* Journal of The Electrochemical Society, 2015. **162**(5): p. A5047-A5053.

193. Kowal, J., et al., *Detailed analysis of the self-discharge of supercapacitors.* Journal of Power Sources, 2011. **196**(1): p. 573-579.

194. Oickle, A.M. and H.A. Andreas, *Examination of Water Electrolysis and Oxygen Reduction As Self-Discharge Mechanisms for Carbon-Based, Aqueous Electrolyte Electrochemical Capacitors.* The Journal of Physical Chemistry C, 2011. **115**(10): p. 4283-4288.

195. Takai, O., *Solution plasma processing (SPP)*, in *Pure and Applied Chemistry*. 2008. p. 2003.

196. Pitchaimuthu, S., et al., *Solution Plasma Process-Derived Defect-Induced Heterophase Anatase/Brookite TiO2 Nanocrystals for Enhanced Gaseous Photocatalytic Performance.* ACS Omega, 2018. **3**(1): p. 898-905.

197. Chen, X., L. Liu, and F. Huang, *Black titanium dioxide (TiO2) nanomaterials.* Chemical Society Reviews, 2015. **44**(7): p. 1861-1885.

198. Qiu, J., et al., *Hydrogenation Synthesis of Blue TiO2 for High-Performance Lithium-Ion Batteries.* The Journal of Physical Chemistry C, 2014. **118**(17): p. 8824-8830.

199. Shin, J.-Y., et al., *Oxygen-Deficient TiO2−δ Nanoparticles via Hydrogen Reduction for High Rate Capability Lithium Batteries.* Chemistry of Materials, 2012. **24**(3): p. 543-551.

200. He, H., et al., *Hydrogenated TiO2 film for enhancing photovoltaic properties of solar cells and self-sensitized effect.* Journal of Applied Physics, 2013. **114**(21): p. 213505.

201. Song, J., et al., *Electrochemically induced Ti3+ self-doping of TiO2 nanotube arrays for improved photoelectrochemical water splitting.* Journal of Materials Science, 2017. **52**(12): p. 6976-6986.

202. Zhou, H. and Y. Zhang, *Electrochemically Self-Doped TiO2 Nanotube Arrays for Supercapacitors.* The Journal of Physical Chemistry C, 2014. **118**(11): p. 5626-5636.

203. Zhou, Y., et al., *Stable Ti3+ Self-Doped Anatase-Rutile Mixed TiO2 with Enhanced Visible Light Utilization and Durability.* The Journal of Physical Chemistry C, 2016. **120**(11): p. 6116-6124.

204. Lu, H., et al., *Safe and facile hydrogenation of commercial Degussa P25 at room temperature with enhanced photocatalytic activity.* RSC Advances, 2014. **4**(3): p. 1128-1132.

205. Leshuk, T., et al., *Photocatalytic Activity of Hydrogenated TiO2.* ACS Applied Materials & Interfaces, 2013. **5**(6): p. 1892-1895.

206. Ren, R., et al., *Controllable Synthesis and Tunable Photocatalytic Properties of Ti(3+)-doped TiO(2).* Scientific Reports, 2015. **5**: p. 10714.

207. Wang, W., et al., *Hydrogenation temperature related inner structures and visible-light-driven photocatalysis of N–F co-doped TiO2 nanosheets.* Applied Surface Science, 2014. **290**: p. 125-130.

208. Gelderman, K., L. Lee, and S.W. Donne, *Flat-Band Potential of a Semiconductor: Using the Mott–Schottky Equation.* Journal of Chemical Education, 2007. **84**(4): p. 685.

209. Sellers, M.C.K. and E.G. Seebauer, *Measurement method for carrier concentration in TiO2 via the Mott–Schottky approach.* Thin Solid Films, 2011. **519**(7): p. 2103-2110.

210. Yu, P., C. Li, and X. Guo, *Sodium Storage and Pseudocapacitive Charge in Textured Li4Ti5O12 Thin Films.* The Journal of Physical Chemistry C, 2014. **118**(20): p. 10616-10624.

211. Yadav, P., et al., *Probing the electrochemical properties of TiO2/graphene composite by cyclic voltammetry and impedance spectroscopy.* Materials Science and Engineering: B, 2016. **206**: p. 22-29.

212. Lewandowski, A., et al., *Self-discharge of electrochemical double layer capacitors.* Physical Chemistry Chemical Physics, 2013. **15**(22): p. 8692-8699.

213. Yong, S., J. Owen, and S. Beeby, *Solid-State Supercapacitor Fabricated in a Single Woven Textile Layer for E-Textiles Applications.* Advanced Engineering Materials, 2018. **20**(5): p. 1700860.

214. Feng, M., et al., *Manganese oxide electrode with excellent electrochemical performance for sodium ion batteries by pre-intercalation of K and Na ions.* Scientific Reports, 2017. **7**(1): p. 2219.

215. Dmitry, V.B., et al., *An aqueous, alkaline route to titanate nanotubes under atmospheric pressure conditions.* Nanotechnology, 2008. **19**(27): p. 275604.